Transition metal complexes with tridentate ligands – a variety of properties

Dissertation

zur Erlangung des akademischen Grades einer Doktorin
der Naturwissenschaften (Dr. rer. nat.)
in der Bayreuther Graduiertenschule für Mathematik und Naturwissenschaften
(BayNAT)
der Universität Bayreuth

vorgelegt von

Katja Dankhoff
Aus Plauen
Bayreuth, 2019

This doctoral thesis was prepared at the department of chemistry at the University of Bayreuth from 11/2015 until 06/2019 and was supervised by Prof. Dr. Birgit Weber.

This is a full reprint of the dissertation submitted to obtain the academic degree of Doctor of Natural Sciences (Dr. rer. nat.) and approved by the Bayreuth Graduate School of Mathematical and Natural Sciences (BayNAT) of the University of Bayreuth.

Date of submission: 12.06.2019

Date of defence: 07.10.2019

Acting director: Prof. Dr. Markus Lippitz

Doctoral committee:

Prof. Dr. Birgit Weber (reviewer)

Prof. Dr. Jürgen Senker (reviewer)

Prof. Dr. Roland Marschall (chairman)

Prof. Dr. Rainer Schobert

„One never notices what has been done;
one can only see what remains to be done.“

Marie Curie

Contents

Danksagung

Zuerst möchte ich mich bei meiner Betreuerin Prof. Dr. Birgit Weber für die interessante Themenstellung, ihre Betreuung und die Unterstützung während dieser Arbeit bedanken. Vielen Dank für die stete Diskussionsbereitschaft, das Vertrauen in meine Arbeit und den akademischen Freiraum.

Bei meinen (ehemaligen) Arbeitskollegen Hannah Kurz, Sophie Schönfeld, Johannes Weihermüller und Ottokar Klimm möchte ich mich ebenfalls für die angenehme Arbeitsatmosphäre und die stete Hilfsbereitschaft bedanken. Besonderer Dank gilt meinem Laborkollegen Christoph Göbel, dafür, dass er diese ganze Arbeit gelesen hat und für die tägliche, gute Stimmung im Labor. Außerdem möchte ich Dr. Stephan Schlamp ein herzliches Dankeschön aussprechen, dass er mich während meiner Anfänge in dem Arbeitskreis tatkräftig unterstützt hat. Schön war es schon!

Ebenso sei den vielen Forschungspraktikanten und Bachelorstudenten, besonders aber Britta Reidelbach, Andreas Dürrmann, Lena Pfeifer und Sandra Schneider, für ihr Interesse und die wertvolle Arbeit gedankt. Auch wenn nicht immer alles wie geplant funktioniert hat, habe ich von euch viel gelernt.

Dem gesamten Lehrstuhl von Prof. Dr. Rhett Kempe möchte ich für die kollegiale Zusammenarbeit danken.

Ich danke Marlies Schilling, Heidi Maisel, Anna-Maria Dietel, Christine Fell, Dr. Ulrike Lacher, Kerstin Hannemann, Florian Puchtler und Marco Schwarzmann für die Unterstützung im administrativen, technischen und analytischen Bereich. Vielen Dank an das gesamte Team des Einkaufs, der Poststelle, der Werkstatt und der Glasbläserei.

Bei Prof. Dr. Rainer Schobert möchte ich mich für die gute Zusammenarbeit bedanken. Ein großes Dankeschön auch an Dr. Florian Schmitt, Matthias Rothemund, Madeleine Gold und Luisa Kober für die biochemischen Tests und für die Beantwortung meiner Fragen dazu.

Prof. Dr. Sonja Herres-Pawlis und Pascal Schäfer von der RWTH Aachen möchte ich ebenfalls für die gute Zusammenarbeit danken.

Bei den Kollegen aus der AC3 bedanke ich mich für die gute Nachbarschaft. Danke besonders an Dominik Greim, Robert Stäglich und Dr. Thomas Martin für das (gelegentliche) Feierabendbier.

Meinen Studienkolleginnen Tamara Bittner, Dr. Helen Grüninger, Katrin Spinnler, Gabriela Hahn und Julia Wollmann möchte ich sehr für die schöne Studien- und Promotionszeit danken. Danke für die vielen lustigen Stunden, sei es beim Protokoll schreiben, lernen, oder einfach nur beim Kaffee. Ohne euch wäre es in Bayreuth nur halb so schön gewesen!

Und natürlich möchte ich mich am meisten bei meiner Familie bedanken. Danke, dass ihr mich während meines Studiums so tatkräftig unterstützt habt. Danke Papa, dass du während meiner Schulzeit mit mir Formeln umgestellt hast, bis ich es (endlich) begriffen habe. Danke Mama, dass du einfach die Beste bist. Danke für die vielen Ratschläge und deine unendliche Geduld. Ich habe so unglaublich viel von dir gelernt. Danke Konny für die vielen Ausflüge, die unzähligen Stunden, die wir zusammen gekocht haben und dafür, dass du einfach die beste Schwester bist. Ohne euch wäre ich nicht die, die ich heute bin und dafür kann ich euch nicht genug danken.

List of abbreviations

bipy	2,2’-bipyridine
d	day(s)
DMSO	dimethyl sulfoxide
EI	electron ionization
EMSA	electrophoretic mobility shift assay
EtBr	ethidium bromide
EtOH	ethanol
h	hour(s)
HS	high spin
IC_{50}	inhibitory concentration
ICP-MS	inductively coupled plasma-mass spectrometry
J	coupling constant
LIESST	light induced excited spin state trapping
LS	low spin
MALDI	matrix assisted laser desorption ionisation
MeOH	methanol
min	minute(s)
MS	mass spectrometry
MTT	3-(4,5-dimethylthiazol-2-yl)-2,5-diphenyltetrazolium bromide
NBT	nitroblue tetrazolium
NMR	nuclear magnetic resonance
OAc	acetate
P4AE	parallel fourfold aryl embrace
P	spin pairing energy
PDI	polydispersity index
PLA	polylactide
ppm	parts per million
ROP	ring-opening polymerisation
ROS	reactive oxygen species
RT	room temperature

SCO	spin crossover
SQUID	superconduction quantum interference device
ST	spin transition
T	temperature
$T_{1/2}$	temperature, at which half of the molecules changed their spin state
TGA	thermogravimetric analysis
ToF	time of flight
γ_{HS}	molar fraction of molecules in the HS state
δ	chemical shift
ΔH	enthalpy
ΔG	Gibb's free energy
Δ_O	octahedral ligand field splitting
ΔS	entropy
τ	structural/Addison parameter
Σ	octahedral distortion parameter
μ_B	Bohr magneton number
μ_{SO}	spin-only moment
μ_{eff}	effective magnetic moment
χ_M	molar susceptibility

1. Summary

The aim of this thesis was the synthesis and characterisation of new Cu(II), Zn(II), Fe(II) and Fe(III) complexes with tridentate, Schiff base-like ligands. Their magnetic behaviour (Cu and Fe) was investigated, as well as their catalytic activity (Zn), and cytotoxicity (Cu). The ligands are derived from the Jäger type; those are normally rigid, tetradentate, and provide an $N_2O_2^{2-}$ or N_4^{2-} coordination sphere around the metal centre. The tridentate N_2O ligands on the other hand are more flexible due a methylene group. The coordination geometries (e.g. square planar/pyramidal, trigonal bipyramidal, octahedral) are similar to those realised by tetradentate ligands, but the coordination of additional co-ligands (anions or solvent molecules) in *cis* position is possible. Another advantage of these ligands is the enhanced stability of octahedral, mononuclear complexes compared to those derived from the tetradentate ligands.

The synthesis of the ligands was established and carried out in one step by condensation of 2-picolylamine and the corresponding keto-enol ether. Fe(II) and Fe(III) complexes were synthesised and characterised with regard to their potential spin crossover behaviour. The coordination geometry is octahedral and in case of Fe(III) as central metal atom varying anions were used to determine their influence on the spin transition. The single crystal X-ray structures of five Fe(III) and one Fe(II) complex could be obtained. The Fe(II) compounds stay mostly high spin, the majority of Fe(III) complexes on the other hand show SCO behaviour. The transition from HS to LS is mostly rather gradual over a large temperature range, indicating low cooperativity between the metal centres. In the case of $[Fe(L1)_2]ClO_4$ a parallel fourfold aryl embrace interaction was found in the crystal structure of the complex. Therefore the packing is very dense and the volume change required for a SCO is prevented. The isostructural pair $[Fe(L2)_2]ClO_4$ and $[Fe(L2)_2]BF_4$ allowed the direct evaluation of the size of the anion on the transition temperature. Both complexes show an abrupt ST which is shifted to lower temperatures for the larger perchlorate anion. Strong hydrogen bonds from a methyl group of one ligand to the keto group of another ligand explain the abrupt SCO. No direct influence of the anion on the SCO behaviour was seen in the other cases. The electrochemical properties of the Fe complexes were measured, quasi-reversible processes between −0.40 and −0.51 V (vs. $Ag/AgNO_3$) take place, corresponding to the redox process Fe(II) ↔ Fe(III). The values are independent of the oxidation state of the starting material.

The Cu(II) complexes with varying anions were synthesised as well. Single crystal X-ray structures revealed that most of the compounds crystallised as dimers, with the Cu(II) centres coordinated by one tridentate ligand and connected via the anions. This resulted in a square pyramidal coordination sphere. It was found that anions with more than one donor atom (such as acetate or nitrate) coordinate mostly with only one of those. The magnetism of the compounds were investigated as dimeric Cu(II) complexes can show magnetic exchange interactions like superexchange. In almost all cases either weak ferro- or antiferromagnetic interactions were found and no direct relation between the structure and the magnetism could be established. The complex $[(\mu\text{-}1,1\text{-}NO_3)(\mu\text{-}1,3\text{-}NO_3)(CuL1)_2]$ showed a rather strong superexchange, which can be explained with the slightly different structure of the compound. One of the two nitrate anions is bridging the metal centres with two instead of one oxygen atom. This results in a larger bridging angle for the other anion and therefore a better overlap of the p orbital of the oxygen and the magnetic orbital of the Cu(II) centres.

Not only the magnetic properties of the compounds were of interest, the potential of 18 Cu(II) substances as anticancer agents was investigated as well. Complexes with different side chains were chosen and additional substituents at the pyridine ring were introduced. Most compounds showed moderate activity against the tested cancer cell lines with IC_{50} values between 10 and 50 µM. Two complexes with methoxy or methyl groups in 4-position on the pyridine ring and only ester groups on the chelate cycle were very active with IC_{50} values below 10 µM. The closely related compounds with a cyanide side chain on the other hand showed no activity, pointing towards a combination of steric and electronic effects. The possible mechanism of action of those complexes was investigated. No correlation with the formation of reactive oxygen species could be detected, but the inhibition of the enzyme topoisomerase I, which plays a crucial part in the supercoiling of the DNA, was found.

It was found that the Zn(II) complexes are capable of catalysing the ring opening polymerisation of lactide. The dimeric compounds were obtained by the reaction of zincacetate and the tridentate ligands. The metal centre is coordinated by one tridentate ligand and two acetates are bridging the two zinc atoms. The complexes were tested with regard to their catalytic behaviour in the ROP of non-purified *rac*-lactide in melt at 150 °C. A coordination-insertion mechanism was proposed and the resulting molecular weight of the polymer in combination with end group analysis revealed that the monomeric species is the catalytically active one. This also explains an induction phase in the beginning of the polymerisation. The cytotoxicity of one complex

against five different cell lines was investigated. With IC_{50} values > 100 µM the compound can be considered non-hazardous to health.

2. Zusammenfassung

Das Ziel der vorliegenden Arbeit war die Synthese und Charakterisierung neuer Cu(II), Zn(II), Fe(II) und Fe(III) Komplexe mit dreizähnigen, Schiff-Base ähnlichen Liganden. Das magnetische Verhalten (Cu und Fe) wurde untersucht, ebenso die katalytische Aktivität (Zn) und die Zytotoxizität (Cu). Die Liganden stammen vom Jäger Typ ab; diese sind normalerweise starr, vierzähnig und bilden eine $N_2O_2^{2-}$ oder N_4^{2-} Koordinationsumgebung um das Metallzentrum. Die dreizähnigen N_2O-Liganden hingegen sind durch die Methylengruppe flexibler. Die verschiedenen Koordinationsgeometrien (z.B. quadratisch planar/pyramidal, trigonal bipyramidal, oktaedrisch) sind ähnlich der, die mit den vierzähnigen Liganden realisiert werden können. Jedoch ist die Koordination von zusätzlichen Co-Liganden (Anionen oder Lösungsmittelmolekülen) in *cis* Position möglich. Ein weiterer Vorteil dieser dreizähnigen Liganden ist die erhöhte Stabilität von okteadrischen, mononuklearen Komplexen verglichen mit denen der vierzähnigen Liganden.

Eine einstufige Ligandensynthese, der Kondensation von 2-Picolylamin und dem entsprechenden Keto-Enol Ether, wurde etabliert. Fe(II) und Fe(III) Komplexe wurden hergestellt und hinsichtlich ihres möglichen Spin Crossover Verhaltens untersucht. Es wird eine oktaedrische Koordinationsgeometrie um das Metallzentrum beobachtet und im Fall von Fe(III) wurden verschiedenen Anionen verwendet, um deren Einfluss auf den Spinübergang zu untersuchen. Einkristallstrukturen von fünf Fe(III) und einem Fe(II) Komplex konnten erhalten werden. Die Fe(II) Verbindungen bleiben meist im High Spin Zustand, die Mehrheit der Fe(III) Komplexe zeigen hingegen SCO Verhalten. Der Übergang vom HS zum LS Zustand ist meist graduell und über einen großen Temperaturbereich gestreckt, was auf eine geringe Kooperativität zwischen den Metallzentren hinweist. Im Fall von $[Fe(L1)_2]ClO_4$ wurde eine starke „parallel fourfold aryl embrace“ Wechselwirkung in der Kristallstruktur des Komplexes gefunden. Diese sorgt für eine sehr dichte Packung und die Volumenänderung, die für einen SCO nötig ist, wird verhindert. Das isostrukturelle Paar $[Fe(L2)_2]ClO_4$ und $[Fe(L2)_2]BF_4$ erlaubt eine direkte Untersuchung des Einflusses der Größe des Anions auf die Übergangstemperatur. Beide Komplexe zeigen einen abrupten Spinübergang, der im Falle des größeren Perchlorations zu tieferen Temperaturen verschoben ist. Starke Wasserstoffbrückenbindungen zwischen der Methylgruppe des einen Liganden und einem

Ketosauerstoff eines anderen Liganden erklären den abrupten SCO. In den anderen Fällen konnte kein direkter Einfluss der Anionen auf das SCO Verhalten gefunden werden. Die elektrochemischen Eigenschaften der Verbindungen wurden untersucht, es finden quasi-reversible Übergänge zwischen −0.40 und −0.51 V (gegen $Ag/AgNO_3$) statt, diese können dem Redoxprozess Fe(II) ↔ Fe(III) zugeordnet werden. Diese Werte sind unabhängig von der Oxidationsstufe des Ausgangsmaterials.

Die Cu(II) Komplexe wurden ebenfalls mit unterschiedlichen Liganden hergestellt. Röntgeneinkristallstrukturanalyse zeigte, dass die meisten Verbindungen als Dimere kristallisieren, in denen die Cu(II) Zentren von den dreizähnigen Liganden koordiniert und durch die Anionen verbrückt werden. Dies resultiert in einer quadratisch-pyramidalen Koordinationsgeometrie. Anionen mit mehr als einem möglichen Donoratom (zum Beispiel Acetat oder Nitrat) koordinieren in den meisten Fällen mit nur einem dieser Atome. Der Magnetismus der Verbindungen wurde untersucht, da dimere Cu(II) Komplexe magnetische Austauschwechselwirkungen, wie den Superaustausch, aufweisen können. In fast allen Fällen wurden entweder schwache ferro- oder antiferromagnetische Wechselwirkungen gefunden und es konnte kein direkter Zusammenhang zwischen der Struktur und dem Magnetismus hergestellt werden. Der Komplex $[(\mu\text{-}1,1\text{-}NO_3)(\mu\text{-}1,3\text{-}NO_3)(CuL1)_2]$ zeigte einen vergleichsweise starken Superaustausch, welcher sich mit der leicht unterschiedlichen Struktur der Verbindung erklären lässt. Eines der beiden Nitrationen verbrückt mit zwei anstelle von einem Sauerstoffatom. Dies führt zu einem größeren Bindungswinkel für das andere Anion und damit zu einer besseren Überlappung des p-Orbitals des Sauerstoffs mit des magnetischen Orbitals der Cu(II) Zentren.

Nicht nur die magnetischen Eigenschaften der Verbindungen waren von Interesse, auch die Möglichkeit, die Cu(II) Substanzen als potentielles Mittel gegen Krebszellen zu nutzen, wurde untersucht. Es wurden Komplexe mit unterschiedlichen Seitengruppen ausgewählt und zusätzliche Substituenten am Pyridinring wurden eingeführt. Die meisten der 18 Verbindungen zeigten moderate Aktivitäten gegen die getesteten Krebszelllinien mit IC_{50} Werten zwischen 10 und 50 µM. Zwei Komplexe mit Methoxy- beziehungsweise Methylgruppen in 4-Position am Pyridinring und nur Estergruppen am Chelatring waren sehr aktiv mit IC_{50} Werten unter 10 µM. Die jeweiligen Verbindungen mit einer Cyanidseitengruppe zeigten hingegen keine Aktivität. Der mögliche Wirkmechanismus der Komplexe wurde untersucht. Es konnte keine Bildung von reaktiven Sauerstoffspezies detektiert werden, jedoch wurde die Inhibition des Enzyms

Topoisomerase I, welches eine entscheidende Rolle in der Superverdrillung der DNA spielt, gefunden.

Es wurde zudem festgestellt, dass die Zn(II) Komplexe in der Lage sind, die Ringöffnungspolymerisation von Lactid zu katalysieren. Die dimeren Substanzen wurden durch die Reaktion von Zinkacetat und den dreizähnigen Liganden erhalten. Das Metallzentrum ist von einem dreizähnigen Ligand umgeben und zwei Acetationen verbrücken die beiden Zinkatome. Die Komplexe wurden hinsichtlich ihrem katalytischen Verhalten in der ROP von nicht aufgereinigtem *rac*-Lactid bei 150 °C getestet in der Schmelze. Als Mechanismus wurde ein Koordinations-Insertions-Mechanismus vorgeschlagen und die erhaltenen Molekulargewichte in Kombination mit Endgruppenanalyse ergaben, dass die monomere Spezies die katalytisch aktive ist. Dies erklärt auch eine Induktionsphase zu Beginn der Polymerisation. Die Zytotoxizität eines Komplexes gegen fünf verschiedenen Zelllinien wurde untersucht. Mit IC_{50} Werten > 100 µM kann die Verbindung als gesundheitlich unbedenklich eingestuft werden.

3. Introduction

The design of new functional materials is a challenging and highly interesting field of research. In this regard, complexes are actively investigated since their properties can be easily tuned by the choice of the metal centre and design of the ligand(s). Coordination compounds with readily available 3d elements as central metal atom are actively investigated in the fields of magnetism, catalysis, or biological activity, just to mention a few examples.[1–6] The choice of ligand significantly influences the properties of the resulting complex. Monodentate ligands are often weakly coordinating and can be easily replaced and therefore result in a free coordination place, e.g. for catalysis.[7] Multidentate ligands usually result in stable complexes and by variation of the donor atoms (N, O, S, …) and/or the charge of the ligand the ligand field can be tuned.[8] Tridentate ligands offer a wide flexibility regarding their ligand structure and coordinated metal centres and therefore a variability in the resulting properties.[9–13]

3.1 Magnetism in first row transition metal complexes

Spin crossover (SCO) is a phenomenon that can occur in first row transition metal complexes with an electronic configuration of $d^{4–7}$. The metal centre is in the low spin (LS) state if the ligand field splitting Δ_O is much higher than the total spin pairing energy P, and in the high spin (HS) state if P is much higher than Δ_O. In case neither of these two conditions is clearly fulfilled, so if $\Delta_O \approx P$, a SCO is possible. The spin state of the complex can be switched between the HS state and the LS state by external stimuli such as temperature, pressure, or light irradiation (Figure 1). This leads to significant changes in the physical properties of the complex.[14,15] Most commonly investigated are complexes of Fe(II)[8, 16–19] and Fe(III)[20–22]. In the case of Fe(III) metal centres both spin states are paramagnetic with $S = 5/2$ (HS) and $S = 1/2$ (LS). Upon SCO the metal-ligand bond lengths shorten, as the antibonding e_g* orbitals are only occupied in the HS state. This leads to a smaller volume in the LS state. Also the colour of the complex differs in the two spin states.[14,15]

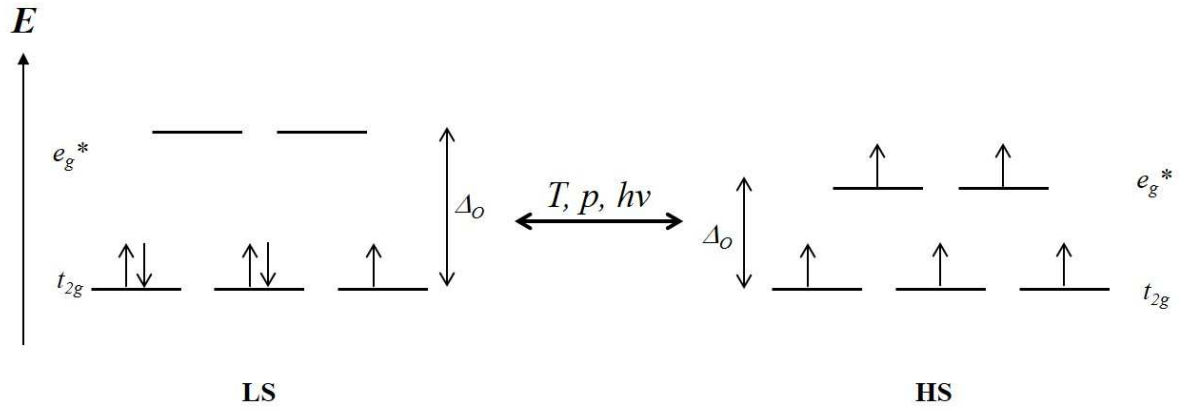

Figure 1. Schematic representation of SCO for a compound with a $3d^5$ electronic configuration. LS state (left), HS state (right).

Due to the significant changes SCO can be monitored by a number of different temperature dependent techniques. Magnetic measurements are the most useful, but also UV-Vis (in solid state or solution), single crystal/powder X-ray diffraction, IR/Raman spectroscopy, or Mössbauer spectroscopy are used.[23–26]

SCO is a thermodynamic process[27] driven by the Gibbs free energy *G*. The following equation describes the transition from the HS to the LS state, where *Δ* corresponds to the difference between the HS and the LS state:

$$\Delta G = \Delta H - T \cdot \Delta S$$

The transition temperature $T_{1/2}$ is the temperature at which half of the metal centres changed their spin state and is defined as $\Delta G = 0$ and therefore as:

$$T_{1/2} = {}^{\Delta H}/_{\Delta S}$$

In the HS state the enthalpy *H* is higher than in the LS state thus upon SCO *ΔH* is positive. The entropy *S* is higher in the HS state as well, which means that also *ΔS* is positive for a transition from the HS to the LS state. At lower temperature *H* is the dominating factor and therefore the LS state is energetically favoured, whereas at higher temperatures the dominating factor is the product $T \cdot \Delta S$, resulting in a stabilisation of the HS state.

There are different ways in which a SCO can occur: gradual and (in)complete, abrupt with or without hysteresis, a two-step transition with a plateau between the two steps, or a combination

of all of those (Figure 2). SCO can be influenced by many factors; the chosen ligand and metal centre are the most important ones and determine if a SCO can be observed. Also the solvent or anions are known to have a strong influence, as they can be involved in hydrogen bonding through the crystal lattice. Cooperative interactions through hydrogen bonds, van der Waals interactions, or π···π interactions can influence the ST as well. In most cases the stronger those interactions between the metal centres are the more abrupt the SCO is. Of course, in solution none of these interactions are present, so the ST is normally gradual and follows a Boltzmann distribution.[15,27]

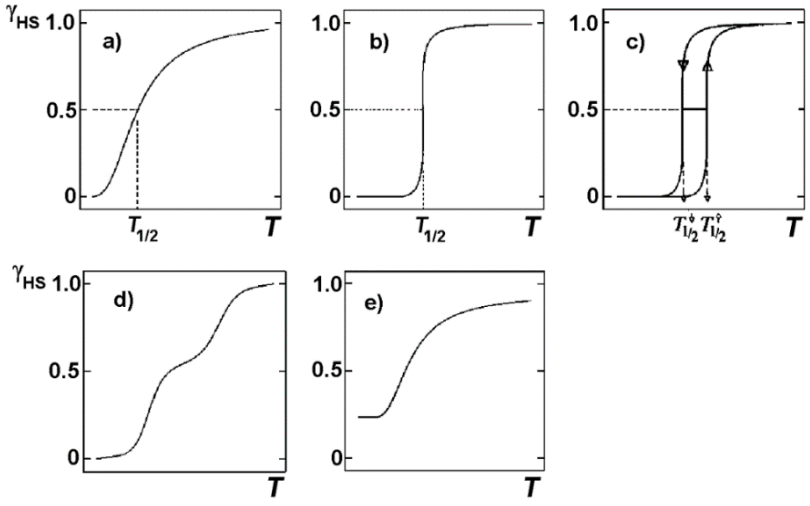

Figure 2. Different types of spin transition: a) gradual and complete, b) abrupt, c) abrupt with hysteresis, d) two-step, and e) gradual and incomplete.[15]

The spin transition cannot only be triggered by temperature, but also by light irradiation. This phenomenon is called Light Induced Excited Spin State Trapping (LIESST). Through light irradiation at low temperatures (usually below 10 K) a transition from the LS to the metastable HS state takes place. Upon warming the LS state is occupied again, the transition temperature is defined as T_{LIESST}.[28] In 2000, the first Fe(III) complex $[Fe(pap)_2]ClO_4 \cdot H_2O$ (Hpap = bis[2-hydroxyphenyl-(2-pyridyl-)methaneimine) showing this behaviour was reported by Sato *et al*.[29] The metal centre is coordinated by two Schiff base N_2O ligands and one perchlorate anion compensates the third positive charge. A complete ST with a 15 K wide hysteresis takes place between 165 and 180 K, strong π···π interactions between the tridentate ligands of two complexes are responsible for this cooperative behaviour. The LIESST temperature is slightly

above 100 K. Dominant π···π and/or parallel fourfold aryl embrace (P4AE) interactions are often responsible for cooperative ST in Fe(III) complexes of the quinolylsalicyladimine type.[21] In 2018, Hayami *et al.* reported four SCO complexes with varying aromatic counterions.[30] Those allowed them to tune the intermolecular coupling and therefore the ST. Three complexes also showed the LIESST effect, one with the highest conversion from LS to HS (59 %) reported for Fe(III) complexes so far.

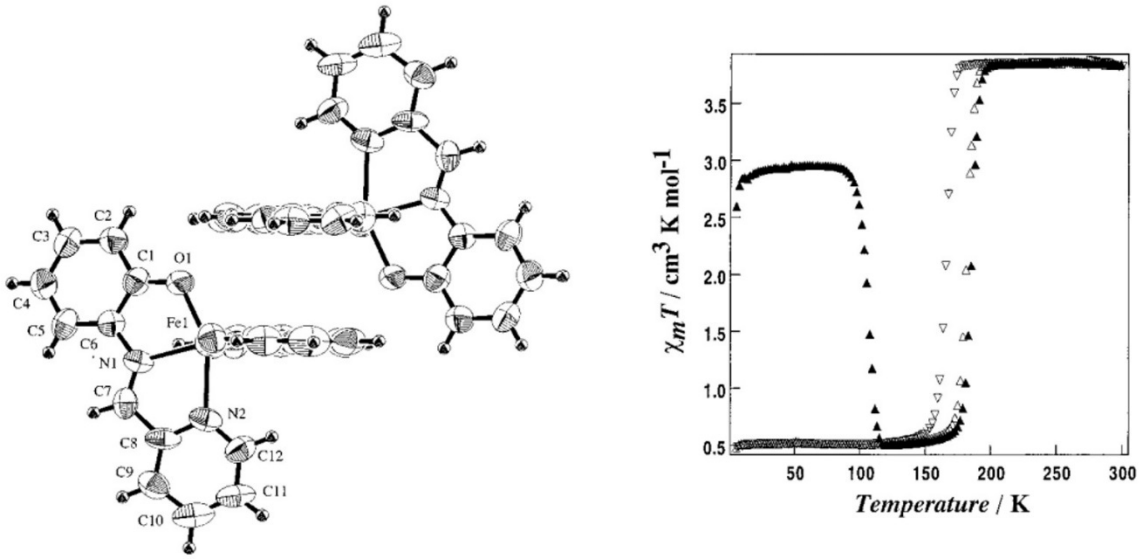

Figure 3. Crystal structure (left) and magnetic measurement (right) of $[Fe(pap)_2]ClO_4 \cdot H_2O$.[29]

Not only the SCO phenomenon can cause a change of magnetism with temperature, there are also magnetic exchange interactions that can lead to an increase or decrease of magnetisation with decreasing temperature. Dinuclear coordination compounds with a spin of $S = 1/2$ (like Cu(II)) which are bridged by diamagnetic linkers, such as acetate ions, can show magnetic exchange interactions leading to antiferromagnetic or ferromagnetic interactions.[31–33] For complexes with antiferromagnetic interactions the singlet state $S = 0$ is energetically more favourable than the triplet state $S = 1$. The energy difference between those two states is defined as coupling constant J. It is negative for antiferromagnetic materials and the spins of the metal centres align antiparallel (Figure 4, left), resulting in a decrease of magnetisation with decreasing temperature (Figure 5, right).[34]

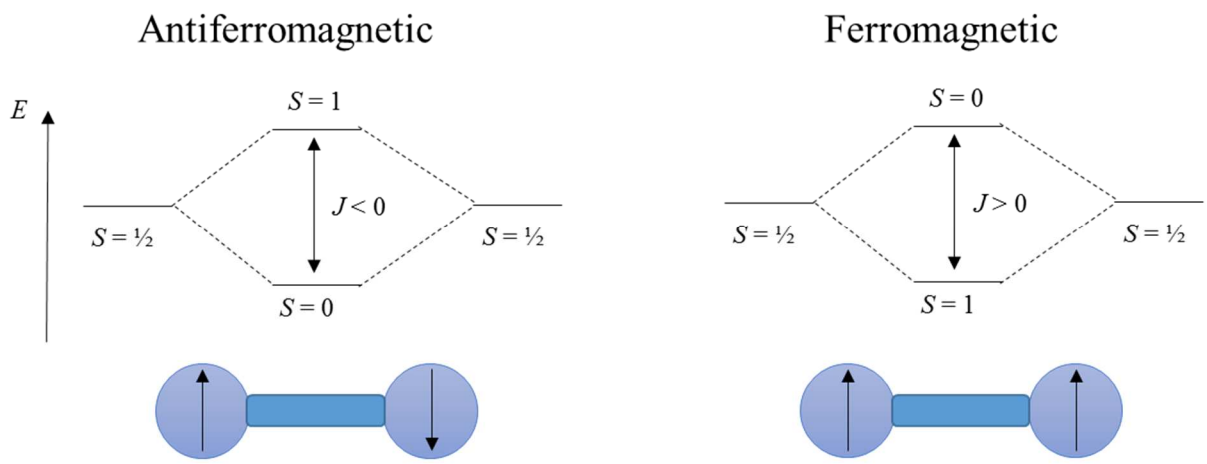

Figure 4. Schematic representation of antiferromagnetic (left) and ferromagnetic (right) interactions with the orientation of the spins of the metal centres.

A prominent example is the copper(II) acetate, $[Cu_2(OAc)_4(H_2O)_2]$. The two Cu(II) centres are bridged via the four acetate anions, leading to an overlap between the magnetic $d_{x^2-y^2}$ orbitals of the metal centres and the p orbitals of the oxygen atoms (Figure 5, left and middle). The electron exchange interaction through diamagnetic linkers is called superexchange; this leads to an antiferromagnetic coupling with a coupling constant $J = -296$ cm^{-1}.[31,34]

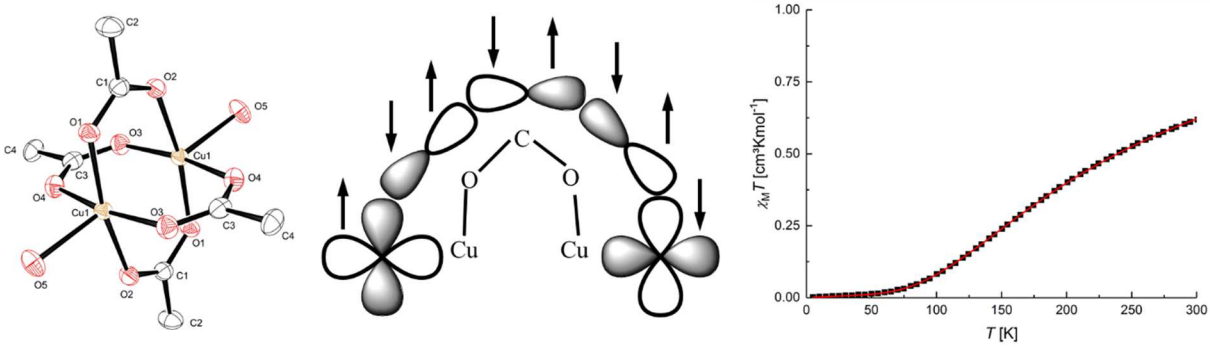

Figure 5. ORTEP drawing (left), magnetic orbitals of the Cu(II) centres and p orbitals of the bridging ligands (middle) with the orientation of the spins, and $\chi_M T$ vs. T plot of $[Cu_2(OAc)_4(H_2O)_2]$.

In complexes with ferromagnetic interactions the triplet state $S = 1$ is the ground state and therefore the coupling constant J is positive (Figure 4, right). The spins of the metal centres align parallel and the magnetisation is increasing with decreasing temperature (Figure 6, top right).[34] A well-known example is the heterobinuclear complex $[CuVO(fsa)_2en(MeOH)]$

($(fsa)_2en^{4-}$ = *N*,*N*'-(2-hydroxy-3-carboxybenzlidene)-1,2-diaminoethane).[35] The magnetic orbitals of the two metal centres, $d_{x^2-y^2}$ for Cu(II) and d_{xy} for V(IV), are orthogonal, therefore no superexchange can occur (Figure 6, top and bottom left). Hence, the coupling constant *J* is positive with a value of 118 cm^{-1}. If the V(IV) centre in this complex is exchanged with a Cu(II) centre the magnetic orbitals of the metal centres can overlap (Figure 6, bottom right), resulting in a strong antiferromagnetic interaction ($J = -650$ cm^{-1}).[34,35]

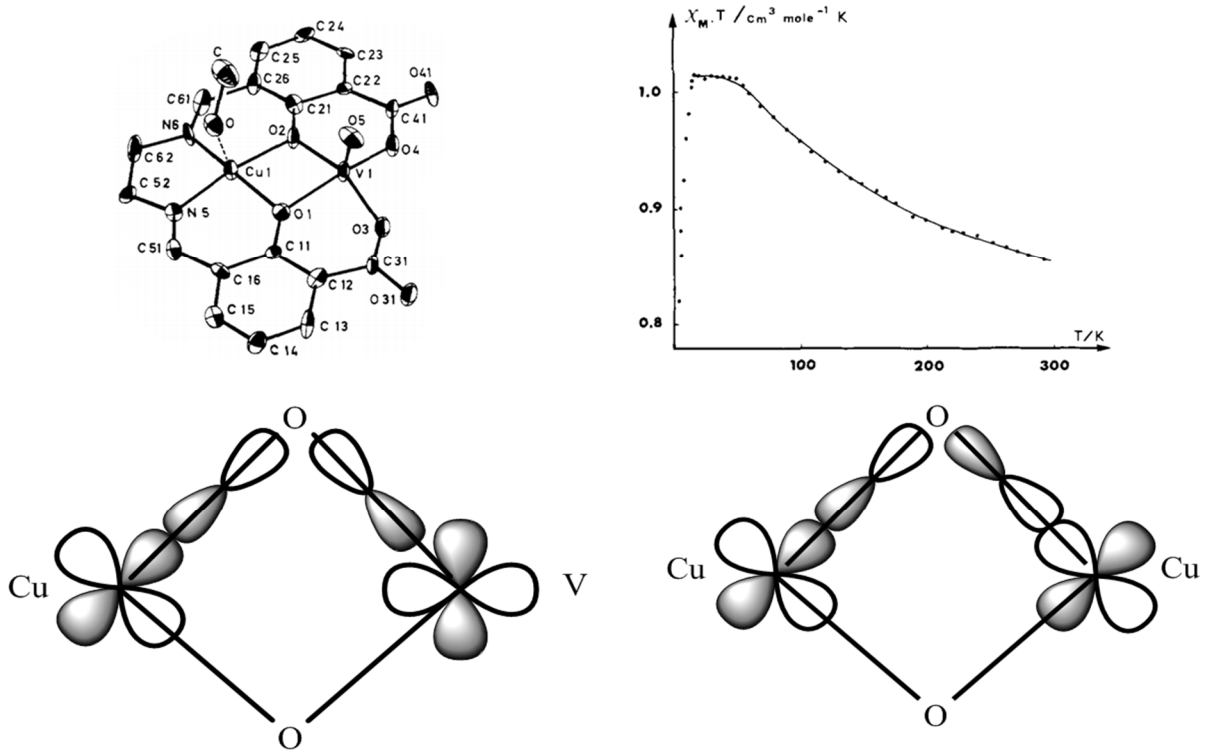

Figure 6. Structure (top left) and $\chi_M T$ vs. *T* plot of [CuVO$(fsa)_2$en(MeOH)] (top right). Relative symmetries of the magnetic orbitals of [CuVO$(fsa)_2$en(MeOH)] (bottom left) and [$Cu_2(fsa)_2$en(MeOH)] (bottom right).[34,35]

Not only the magnetic orbitals of the metal centres influence the kind and strength of magnetic exchange interactions, also the angle through which the metals are bridged has to be considered. Hatfield and Hodgson described the first magneto-structural correlation between the Cu–O–Cu angle in bis(hydroxido) bridged complexes and the nature and magnitude of the magnetic exchange interactions.[36] They proposed a linear relationship between the coupling constant *J* and the bridging angle. Ferromagnetic interactions were observed if this angle is smaller than 97.5° and antiferromagnetic interactions were found if the angle is larger than 97.5°. Also the magnitude of *J* increased; for a smaller angle stronger ferromagnetic interactions were observed

and for a bigger angle stronger antiferromagnetic interactions can be found. The bond lengths of the first coordination sphere and the M···M distances were found to have an impact on the magnetic exchange interactions as well.[34] The distortion parameter τ, also called Addison parameter[37], is an important structural factor in equatorial-axial complexes. It is calculated according to the following formula:

$$\tau = \frac{\beta - \alpha}{60°}$$

β and α are the two largest angles of the coordination sphere, and β > α. For an ideal square pyramidal coordination geometry it is 0, for a trigonal bipyramidal coordination sphere it is 1. Ribas *et al.* found in 2004 that for the maximal value of τ a minimal value of *J* was experimentally determined in equatorial-axial bridged Cu(II) azido complexes.[38]

Cu(II) complexes are not only investigated with regard to their interesting magnetic properties[39–41], copper is also an essential element and important for the development of organisms. As such it plays an important role in several enzymes (e.g. tyrosinase or catecholase).[6,7] Also, Cu(II) complexes are currently investigated as potential anticancer agents.[42]

3.2 Copper complexes as potential anticancer agents

Cancer still remains one of the leading causes of death in the world. About 1 in 6 fatalities are caused by cancer, and the disease was responsible for 9.6 million deaths in 2018 globally.[43] It can be treated by surgery, so removal of the affected tissue, radiotherapy, chemotherapy, or a combination of those. Treatment of cancer is proven to be difficult, as it is not a single disease; there are more than 200 different types of cancer as a result from different cellular effects. Therefore an effective treatment against one cancer type can be ineffective against another type.[44]

Normal cells have regulatory mechanism which control growth and multiplication. Those are lost in cancer cells, they become “rogue cells”. Specialised characteristics that differentiate one cell type (e.g. liver cell) from another (e.g. lung cell) are missing in those cells as well. This is

called loss of differentiation. Apoptosis, a built-in cellular self-destruction process, is the mechanism with which the body protects itself against abnormal or faulty cells. A series of different chemical signals helps cells to monitor themselves and in case any of these signals are missing, apoptosis takes place. This process is responsible for destroying cells that are leaving their normal tissue environment. Genetic changes of metastasing cancer cells allow them to avoid apoptosis. There are two distinct pathways for apoptosis: extrinsic and intrinsic. In case of the first, apoptosis results from external factors: the lack of growth factors or hormones, death activator proteins, which can bind to the cell membrane and trigger a signalling process resulting in apoptosis, or T-lymphocytes produced by the immune system. Those lymphocytes search for damaged cells and can perforate the cell membrane to inject an apoptosis-initiating enzyme. The intrinsic pathway may be triggered by factors like DNA damage (e.g. from exposure to chemicals, oxidative stress, or drugs). The cell detects the damage and increases the production of a tumour suppressor protein. This can trigger apoptosis at high enough concentrations. Cell death by apoptosis is also triggered by radiotherapy and many chemotherapy drugs.[42,44,45]

Chemotherapy is often used in combination with surgery and radiotherapy. The use of different chemotherapy drugs with various modes of action can lead to an increased efficiency, decreased toxicity, and evasion of drug resistance. Most of the traditional chemotherapy drugs act against targets present in normal and cancer cells. Therefore both, the effectiveness and selectivity, dependent on the fact, that cancer cells grow faster and therefore accumulate nutrients, synthetic building blocks, and drugs more quickly, resulting in a higher concentration of the drug in the cancer cells. Bone marrow cells grow rapidly as well leading to common side effects of chemotherapy like a weakening of the immune response and decreased resistance to infection. Cancer cells can have intrinsic or acquired resistance against chemotherapy drugs. While for an intrinsic resistance the cells show little response for the anticancer agent from the very start (e.g. due to poor uptake of the drug, slow growth rate and/or biochemical/genetic properties of the cell), cells with an acquired resistance are susceptible to the drug in the beginning, but become resistant over time. Acquired resistance may be caused by a mixture of drug-sensitive and drug-resistant cells in the tumour. The drug effects the sensitive cells, while leaving the resistant unaffected. Only one resistant cell is required for the growth of a new, now resistant to this specific drug, tumour. The cell in the centre of a tumour is often dormant and therefore intrinsically resistant. Another cause of resistance is mutation. The uptake of the drug by the cell can be decreased, or the synthesis of the target molecule may be increased. Some drugs

have to be activated in the cell in order to be efficient; the cell may adapt in a way, that those activation processes no longer take place. Also, the drugs can be expelled from the cell as soon as they enter; this may result in multi-drug resistance.[42,44,45]

The best-known coordination compound used as a chemotherapy drug is cis-platin (*cis*-diamminedichloridoplatinum(II)). It has to be activated in the cells; the two chlorides are replaced by DNA bases, this results in interstrand crosslinking and replication can no longer take place. Cis-platin is not very selective towards cancer cells, and they often acquire a resistance against this chemotherapy drug.[46–48] This is why there is a constant need for alternatives. Copper complexes are investigated during the last years[42,49–55], as they may have different mechanisms of action, biodistribution, and/or a lower toxicity than the commonly used platinum-based drugs. There is a chance that they may overcome intrinsic or acquired resistance and the poor chemoselectivity, and therefore have less side-effects.[42]

Copper complexes can interact with the DNA as well, e.g. through intercalation or the inhibition of enzymes responsible for replication and transcription. Intercalating drugs are compounds containing planar or heteroaromatic features. They can insert in the base pair layers of the DNA double helix, where the compounds are hold in place by van der Waals interactions. Further stabilisation can be achieved with the interaction of ionised groups on the drug with the charged phosphate groups of the DNA backbone. This insertion leads to the hindrance of transcription and replication and therefore to cell death. Consequences of intercalation are for example the deformation of the double helix or the hindrance of the unwinding of the double helix. The later prevents the synthesis of messenger RNA and therefore no transcription takes place.[42,44]

The Cu(II) complex of Hpyramol (Figure 7, left) [Cu(Pyrimol)Cl] (Figure 7, middle; the ligand Hpyramol oxidises upon coordination of the metal centre) exhibits high antitumour activity against cis-platin resistant and sensitive cancer cells.[56] The similar complex [Cu(L)(H_2O)(OAc)] (HL = *N*-2-pyridylmethylidene-2-hydroxy-5-chlorophenylamine, **Figure 7**, right) also oxidatively cleaves the DNA by the formation of reactive oxygen species (ROS). It inhibits the growth of cervix carcinoma cells (HeLa) in a dose-dependent matter; the free ligand showed no cytotoxicity.[57]

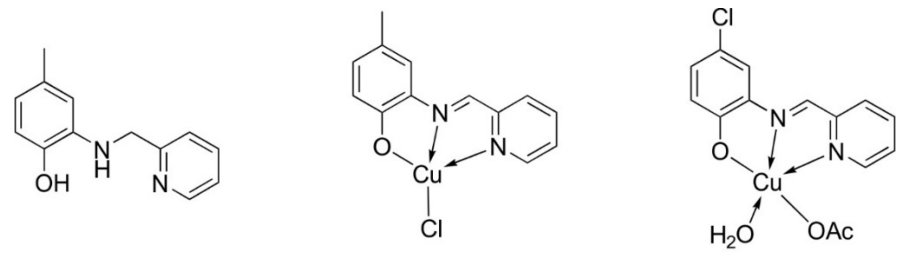

Figure 7. Hpyramol (left), [Cu(Pyrimol)Cl] (middle), and [Cu(L)(H_2O)(OAc)] (right).[56,57]

Another type of enzymes which are identified as clinical important targets are the topoisomerases.[42,44] They play a crucial part in the supercoiling process, where the DNA is coiled into a 3D shape so it can fit in the nucleus of the cell. This allows the efficient storage of DNA but it has to be uncoiled again for transcription and replication. The unwinding process leads to increased tension if the DNA is still supercoiled. Topoisomerases catalyse the passing of one stretch of DNA helix across another. The enzyme temporarily cleaves one (topoisomerase I) or both (topoisomerase II) strands of DNA helix to create a temporary gap and releases the strand(s) once the crossover has taken place. The uncoiling process is catalysed as well by topoisomerases therefore inhibition of those enzymes can effectively block transcription and replication. The topoisomerase II interacts with parts of the DNA where two regions of the double helix are in close proximity to each other. It binds to one helix and a tyrosine residue is used to nick both strands of the DNA. This temporary covalent bond between the enzyme and each strand stabilises the DNA. The strands are then pulled in opposite directions to create a gap, through which the intact DNA can pass. The enzyme reseals the strands and departs. Topoisomerase I acts similar to II, but cleaves only one strand of DNA. The relaxation of the torsional strain can be achieved by passing the intact strand through the nick (see Figure 8) or free rotation of the DNA about the uncleaved strand. As soon as the torsional strand has been relieved, the enzyme rejoins the cleaved strand of the DNA and departs.[58,59] Compounds targeting the topoisomerases can be divided into two groups: topoisomerase poisons and catalytic inhibitors. The poisons stabilise the reversible, covalent complex formed between the DNA and the enzyme, whereas catalytic inhibitors, which mostly target topoisomerase II, interfere in the catalytic cycle without trapping the covalent complex.[42,44]

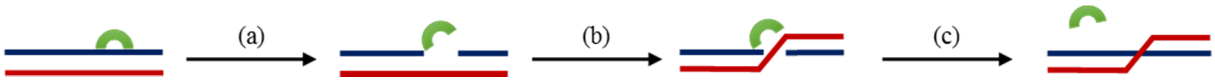

Figure 8. Schematic representation of DNA cleavage reaction catalyse by topoisomerase I. (a): DNA nicking, (b): strand passage, (c): resealing of the strand and departure of the enzyme.[58]

The two plumbagin (HL) derivative complexes $[Cu(L)_2]\cdot 2H_2O$ and $[Cu(L)(bipy)(H_2O)]_2(NO_3)_2\cdot 4H_2O$ (Figure 9) exhibit a high cytotoxicity against several human cancer cell lines and were more active than plumbagin. Both coordination compounds bind noncovalently to the DNA and mostly intercalated neighbouring DNA base pairs. They also inhibited topoisomerase I more efficiently than plumbagin.[60]

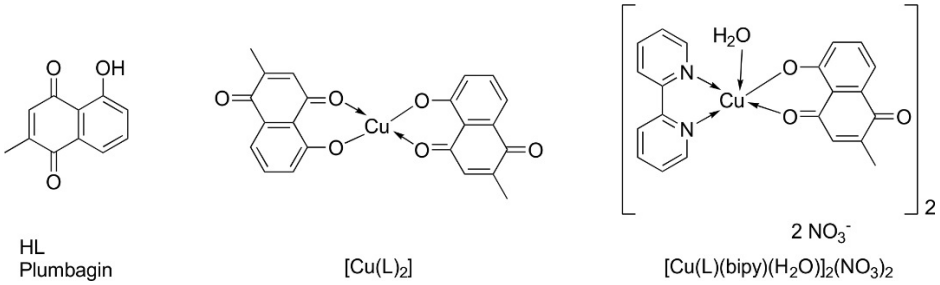

Figure 9. Structure of plumbagin (left), $[Cu(L)_2]\cdot 2H_2O$ (middle), and $[Cu(L)(bipy)(H_2O)]_2(NO_3)_2\cdot 4H_2O$ (right). Non-coordinating solvent molecules were omitted for clarity.[60]

3.3 Ring-opening polymerisation of lactide

Synthetic polymers have a huge impact on today's industry and everyday-life. Polyesters are one of the most versatile classes of those polymers, as they can be used in many different fields (fibres, plastics, coatings, …). Polylactide (PLA) is a biodegradable polymer, with a monomer (lactide acid or lactide) which can be obtained from annually renewable sources like corn or beets. It can be produced via the condensation of lactide acid or the ring-opening polymerisation (ROP) of lactide (cyclic dimer of lactide acid). ROP has many advantages: it leads to well controlled molecular weight, low polydispersity (PDI), and allows control over the stereochemistry of the product. A good catalyst for ROP has a metal centre, which is redox-inactive and an oxidation state between +2 and +4, inert to β-hydrogen atom abstraction from

the growing alkoxide polymer chain, and the complex should be inert towards ligand scrambling.[61,62]

Many metal based reactions follow the coordination-insertion mechanism. This is very well understood in the case of Al(O*i*-Pr)$_3$ as catalyst (Scheme 1). The first step (1) is the coordination of the monomer to the lewis-acidic metal centre. Afterwards (2) the monomer inserts into the Al–O*i*-Pr bond via nucleophilic addition of the O*i*-Pr group on the carbonyl oxygen. The ring-opening (step 3) proceeds via an acyl-oxygen cleavage. Hydrolysis of the O–Al bond leads to PLA.[62]

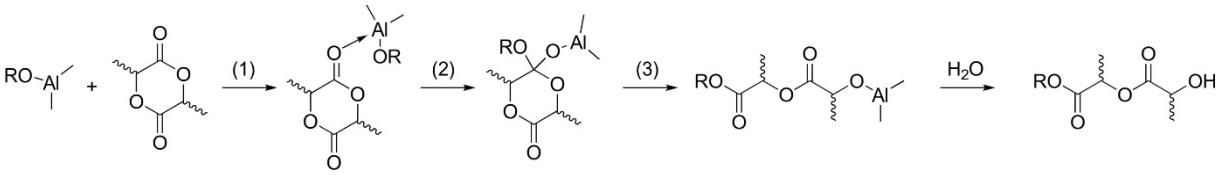

Scheme 1. Coordination insertion mechanism for the ROP of lactide with Al(O*i*-Pr)$_3$. RO refers to the initiating isopropyl group or the growing polymer chain.[62]

The catalyst mostly used is industry is Sn(Oct)$_2$.[63,64] It is not removed after the polymerisation in melt, and upon the compost degradation of PLA it accumulates.[65] As it is, like most tin compounds, thought to be harmful, a replacement has to be found.[66] Commonly investigated metal centres are Mg^{2+}, Al^{3+}, and Zn^{2+}.[67]

The dinuclear Zn(II) complex [$Zn_2L^{Et}(HMDS)_2$] (Figure 10, left) (L^{Et} is a bis(imino)diphenylamido macrocycle, HMDS = bis(trimethylsilyl)amido) shows a high activity in THF solution (c(*rac*-lactide) = 1 mol/L, 0.1 mol% catalyst) with turnover frequency values up to 60000 h^{-1}, resulting in M(polylactide) = 14000 g/mol, under immortal conditions (10 eq of isopropanol).[68] The complex has a folded conformation, this combines short intermetallic distances and open coordination sites with strong electron donation. A similar complex with O^iPr as anion shows a planar ligand conformation and the O^iPr groups are bridging the metal centres. This compound has a much lower activity compared to the HMDS complex, which has been explained with the lower flexibility of the macrocyclic ligand once the metal centres are bridged by additional co-ligands. The Zn(II) atoms in [$Zn_2L^{Et}(HMDS)_2$] are easily accessible for the monomer and therefore insertion and coordination are much faster.

The mononuclear complex [$ZnCl_2$(DMEGasme)] (**Figure 10,** right) (DMEGasme = 2-[(1,3-dimethylimidazolidin-2-ylidene)amino]benzoate) was investigated under industrial relevant conditions (polymerisation of technical grade *rac*-lactide in melt at 150 °C).[69] The rate constant was determined as $k_{app} = 1.26 \cdot 10^{-4}$ s^{-1} and polylactide with a molar mass of 69100 g/mol was obtained. The analogous bromide complex was as active as the chloride compound and produced chains with a higher molar mass (70400 g/mol). A coordination insertion mechanism was proposed and kinetic measurements revealed a fast first order behaviour with a polymerisation rate constant of k_p of $9.5 \cdot 10^{-2}$ $s^{-1}mol^{-1}L$.

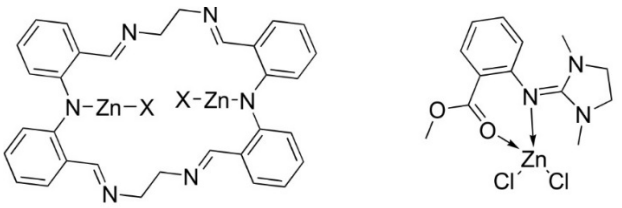

[$Zn_2L^{Et}(HMDS)_2$] [$ZnCl_2$(DMEGasme)]

Figure 10. Catalysts based on Zn(II) for the ROP of lactide. Left: [$Zn_2(L^{Et}(HMDS)_2$] X = $N(SiMe_3)_2$, right: [$ZnCl_2$(DMEGasme)].[68,69]

3.4 References

[1] E. Coronado, G. Mínguez Espallargas, *Chem. Soc. Rev.* **2013**, *42*, 1525–1539.

[2] P. Dechambenoit, J. R. Long, *Chem. Soc. Rev.* **2011**, *40*, 3249–3265.

[3] M. Kurmoo, *Chem. Soc. Rev.* **2009**, *38*, 1353–1379.

[4] V. Charra, P. de Frémont, P. Braunstein, *Coord. Chem. Rev.* **2017**, *341*, 53–176.

[5] E. I. Solomon, D. E. Heppner, E. M. Johnston, J. W. Ginsbach, J. Cirera, M. Qayyum, M. T. Kieber-Emmons, C. H. Kjaergaard, R. G. Hadt, L. Tian, *Chem. Rev.* **2014**, *114*, 3659–3853.

[6] T. Glaser, M. Heidemeier, S. Grimme, E. Bill, *Inorg. Chem.* **2004**, *43*, 5192–5194.

[7] S. Hazra, A. P. C. Ribeiro, M. F. C. Guedes da Silva, C. A. Nieto de Castro, A. J. L. Pombeiro, *Dalton Trans.* **2016**, *45*, 13957–13968.

[8] B. Weber, *Coord. Chem. Rev.* **2009**, *253*, 2432–2449.

[9] H. R. Bigmore, S. C. Lawrence, P. Mountford, C. S. Tredget, *Dalton Trans.* **2005**, 635–651.

[10] F. Silva, C. Fernandes, M. P. C. Campello, A. Paulo, *Polyhedron* **2017**, *125*, 186–205.

[11] R. L. Melen, L. H. Gade, in Topics in Organometallic Chemistry, eds. G. van Koten, R. Gossage, Springer, Cham, **2015**, vol. 54.

[12] D. Peng, X. Yan, C. Yu, S. Zhang, X. Li, *Polym. Chem.* **2016**, *7*, 2601–2634.

[13] J.-C. G. Bünzli, A.-S. Chauvin, H. K. Kim, E. Deiters, S. V. Eliseeva, *Coord. Chem. Rev.* **2010**, *254*, 2623–2633.

[14] P. Gütlich, H. A. Goodwin (editors); "Spin Crossover in Transition Metal Compounds I–III", *Topics in Current Chemistry*, **2004**.

[15] P. Gütlich, A. Hauser, H. Spiering, *Angew. Chem. Int. Ed. Engl.* **1994**, *33*, 2024–2054.

[16] M. H. Halcrow, *Coord. Chem. Rev.* **2009**, *253*, 2493–2514.

[17] J. Olguín, S. Brooker, *Coord. Chem. Rev.* **2011**, *255*, 203–240.

[18] G. A. Craig, O. Roubeau, G. Aromi, *Coord. Chem. Rev.* **2014**, *269*, 13–31.

[19] J. R. G. Mascarós, G. Aromi, M. Darawshehi, *Comptes Rendus Chimie* **2018**, *21*, 1209–1229.

[20] N. Nihei, T. Shiga, Y. Maeda, H. Oshio, *Coord. Chem. Rev.* **2007**, *251*, 221–249.

[21] D. J. Harding, P. Harding, W. Phonsri, *Coord. Chem. Rev.* **2016**, *313*, 38–61.

[22] M.-L. Boillot, B. Weber, *Comptes Rendus Chimie* **2018**, *21*, 1196–1208.

[23] J. S. Costa, *Comptes Rendus Chimie* **2018**, *21*, 1121–1132.

[24] J. A. Wolny, V. Schünemann, Z. Németh, G. Vankó, *Comptes Rendus Chimie* **2018**, *21*, 1152–1169.

[25] P. Gütlich, *Z. Anorg. Allg. Chem.* **2012**, *638*, 15–43.

[26] P. Gütlich, R. Link, A. Trautwein, "Mössbauer Spectroscopy and Transition Metal Chemistry", *Springer-Verlag Berlin Heidelberg New York* **1978**.

[27] W. Nicolazzi, A. Bousseksou, *Comptes Rendus Chimie* **2018**, *21*, 1060–1074.

[28] J.-F. Létard, G. Chastenet, P. Guionneau, C. Desplanches, in "Spin Crossover Materials", ed, M. H. Halcrow, Wiley, **2013**.

[29] S. Hayami, Z. Gu, M. Shiro, Y. Einaga, A. Fujishima, O. Sato, *J. Am. Chem. Soc.* **2000**, *122*, 7126–7127.

[30] A. Tsukiashi, M. Nakaya, F. Kobayashi, R. Ohtani, M. Nakamura, J. M. Harrowfield, Y. Kim, S. Hayami, *Inorg. Chem.* **2018**, *57*, 2834–2842.

[31] O. Kahn, Molecular Magnetism, VCH, New York, N. Y, **1993**.

[32] B. Sieklucka, D. Pinkowicz (eds.) "Molecular Magnetic Materials", Wiley, **2017**.

[33] C. Benelli, D. Gatteshi (eds.) "Introduction to Molecular Magnetism", Wiley, **2015**.

[34] J. Ferrando-Soria, J. Vallejo, M. Castellano, J. Martínez-Lillo, E. Pardo, J. Cano, I. Castro, F. Lloret, R. Ruiz-García, M. Julve, *Coord. Chem. Rev.* **2017**, *339*, 17–103.

[35] O. Kahn, J. Galy, Y. Journaux, J. Jaud, I. Morgenstern-Badarau, *J. Am. Chem. Soc.* **1982**, *104*, 2165–2176.

[36] H. van Crawford, H. W. Richardson, J. R. Wasson, D. J. Hodgson, W. E. Hatfield, *Inorg. Chem.* **1976**, *15*, 2107–2110.

[37] A. W. Addison, T. N. Rao, J. Reedijk, J. van Rijn; G. C. Verschoor, *J. Chem. Soc., Dalton Trans.* **1984**, 1349–1356.

[38] M. S. Ray, A. Ghosh, S. Chaudhuri, M. G. B. Drew, J. Ribas, *Eur. J. Inorg. Chem.* **2004**, 3110–3117.

[39] T. Limpke, C. Butenuth, A. Stammler, H. Bögge, T. Glaser, *Eur. J. Inorg. Chem.* **2017**, 3570–3579.

[40] W. X. C. Oliveira, C. B. Pinheiro, M. M. da Costa, A. P. S. Fontes, W. C. Nunes, F. Lloret, M. Julve, C. L. M. Pereira, *Cryst. Growth Des.* **2016**, *16*, 4094–4107.

[41] D. L. Reger, A. E. Pascui, E. A. Foley, M. D. Smith, J. Jezierska, A. Wojciechowska, S. A. Stoian, A. Ozarowski, *Inorg. Chem.* **2017**, *56*, 2884–2901.

[42] C. Santini, M. Pellei, V. Gandin, M. Porchia, F. Tisato, C. Marzano, *Chem. Rev.* **2014**, *114*, 815–862.

[43] World Health Organisation on Cancer, https://www.who.int/news-room/fact-sheets/detail/cancer, 25.04.2019

[44] G. L. Patrick "An Introduction to Medicinal Chemistry", 4th Edition, Oxford, **2009**.

[45] F. Tisato, C. Marzano, M. Porchia, M. Pellei, C. Santini, *Med. Res. Rev.* **2010**, *30*, 709–749.

[46] A. Basu, S. Krishnamurthy, *J: Nucleic Acids* **2010**, 1–16.

[47] R. H. Jones, P. A. Vasey, *Lancet Oncol.* **2003**, *4*, 738–747.

[48] Y. Jung, S. J. Lippard, *Chem, Rev.* **2007**, *107*, 1387–1407.

[49] J. N. Boodram, I. J. Mcgregor, P. M. Bruno, P. B. Cressey, M. T. Hemann, K. Suntharalingam, *Angew. Chem. Int. Ed.* **2016**, *55*, 2845–2850.

[50] Z. Ma, B. Zhang, M. F. C. Guedes da Silva, J. Silva, A. S. Mendo, P. V. Baptista, A. R. Fernandes, A. J. L. Pombeiro, *Dalton Trans.* **2016**, *45*, 5339–5355.

[51] S. K. Lee, K. W. Tan, S. W. Ng, *J. Inorg. Biochem.* **2016**, *159*, 14–21.

[52] W.-J. Lian, X.-T. Wang, C.-Z. Xie, H. Tian, X.-Q. Song, H.-T. Pan, X. Qiao, J.-Y. Xu, *Dalton Trans.* **2016**, *45*, 9073–9087.

[53] C. Spoerlein, K: Mahal, H. Schmidt, R. Schobert, *J. Inorg. Biochem.* **2013**, *127*, 107–115.

[54] A. Kurzwernhart, W. Kandioller, C. Bartel, S. Bächler, R. Trondl, G. Mühlgassner, M. A. Jakupec, V. B. Arion, D. Marko, B. K: Keppler, C. G. Hartinger, *Chem. Commun.* **2012**, *48*, 4839–4341.

[55] W. Zhou, X. Wang, M. Hu, C. Zhu, Z. Guo, *Chem. Sci.* **2014**, *5*, 2761–2770.

[56] S. Roy, P. U. Maheswari, M. Lutz, A. L. Spek, H. den Dulk, S. Barends, G. P. van Wetzel, F. Hartl, J. Reedijk, *Dalton Trans.* **2009**, 10846–10860.

[57] X. Qiao, Z.-Y. Ma, C. Z. Xie, F. Xue, Y.-W. Zhang, J.-Y. Xu, Z.-Y. Qiang, J.-S. Lou, G.-J. Chen, S.-P. Yan, *J. Inorg. Biochem.* **2011**, *105*, 728–737.

[58] M. Li, Y. Liu, *Genom. Proteom. Bioinf.* **2016**, *14*, 166–171.

[59] N. H. Dekker, V. V. Pybenkov, M. Duguet, N. J. Crisona, N. R. Cozzarelli, D. Bensimon, V. Croquette, *PNAS* **2002**, *99*, 12126–12131.

[60] Z.-F. Chen, M.-X. Tan, L. M. Liu, Y.-C. Liu, H.-S. Wang, B. Yang, Y. Peng, H.-G. Liu, H. Liang, C. Orvig, *Dalton Trans.* **2009**, 10824–10833.

[61] J. Wu, T.-L. Ya, C.-T. Chen, C.-C. Lin, *Coord. Chem. Rev.* **2006**, *250*, 602–626.

[62] M. J. Stanford, A. P. Dove, *Chem. Soc. Rev.* **2010**, *39*, 486–494.

[63] H. R. Kricheldorf, R. Dunsing, *Makromol. Chem.* **1986**, *187*, 1611–1625.

[64] J. W. Leenslag, A. J. Pennings, *Makromol. Chem.* **1987**, *188*, 1809–1814.

[65] A. Stjerndahl, A. Finne-Wistrand, A. C. Albertsson, C. M. Bäckesjö, U. Lindgren, *J. Biomed. Mater. Res., Part A* **2008**, *87A*, 1086–1091.

[66] H. R. Kricheldorf, *Chemosphere* **2001**, *43*, 49–54.

[67] Y. Sarazin, J.-F. Carpentier, *Chem. Rev.* **2015**, *115*, 3564–3614.

[68] A. Thevenon, C. Romain, M. S. Bennington, A. J. P. White, H. J. Davidson, S. Brooker, C. K. Williams, *Angew. Chem. Int. Ed.* **2016**, *55*, 8680–8685.

[69] P. M. Schäfer, M. Fuchs, A. Ohligschläger, R. Rittinghaus, P. McKeown, E. Akin, M. Schmidt, A. Hoffmann, M. A. Liauw, M. D. Jones, S. Herres-Pawlis, *ChemSusChem* **2017**, *10*, 3547–3556.

4. Synopsis

This thesis comprises three publications (Chapters 6–8), and two manuscripts (Chapters 9 and 10). The individual contributions to joint publications are summarised in Chapter 5.

This work deals with the synthesis of tridentate Schiff base-like ligands and their corresponding 3d metal complexes, namely Cu(II), Fe(II)/(III), and Zn(II). The tridentate ligands are derived from the Jäger type ligands and provide an *NNO* coordination sphere. Normally, the Weber group uses tetradentate Schiff base-like ligands. These are rigid and the resulting coordination spheres are limited to square planar, square pyramidal, or octahedral. Tridentate ligands are more flexible and can provide a wider range of coordination geometries, depending on the metal centre and possible co-ligands, e.g. solvent or coordinating anions. The general idea was to investigate these possibilities depending on the preferred coordination sphere of the metal centre and the resulting properties of the complexes.

The ligands were prepared by a simple condensation reaction between the commercially available 2-picolylamine and the corresponding keto-enol ether. Conversion with the respective metal salt and a base, needed for the deprotonation of the ligands, resulted in the formation of the 3d metal complexes. As expected, the Fe(II)/(III) complexes have an octahedral coordination sphere, whereas it is mostly square pyramidal for the Cu(II) and Zn(II) complexes (Figure 1).

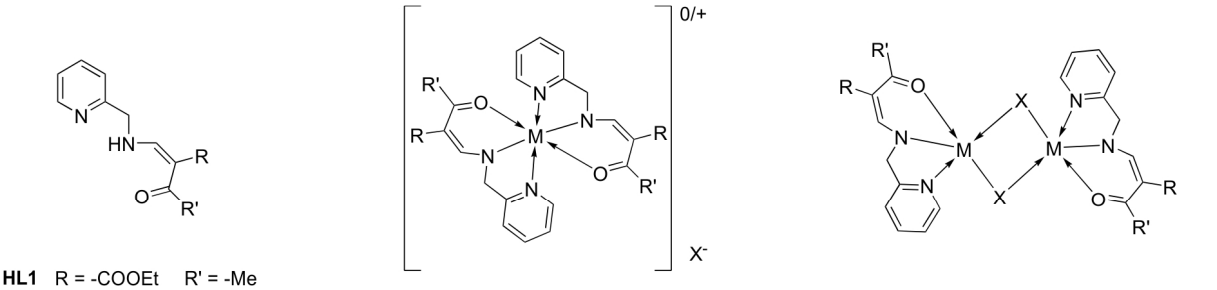

Figure 1. Structure of the ligands HL1–HL6 (left), the Fe(II)/Fe(III) complexes (middle), and Cu(II)/Zn(II) complexes.

In Chapter 6, the synthesis of six new ligands (HL1–HL6) and their Cu(II) complexes is described. The ligands, $CuSO_4$, and sodium methoxide were heated to reflux in dry methanol under an argon atmosphere to avoid the formation of $Cu(OH)_2$. This dark blue precursor solution was split in aliquots and the Cu(II) complexes were precipitated with an aqueous solution of an anion X^-. The metal centre is coordinated by one tridentate ligand, and the second positive charge is compensated by varying anions X^- (OAc^-, NO_3^-, Cl^-, I^-, NCS^-, and N_3^-). X-ray structures of four ligands and 22 Cu(II) complexes were obtained. Most of the Cu(II) complexes crystallised as dimers and the metal centres are bridged by the anions. For anions with more than one possible donor atom (e.g. NO_3^-) the coordination with only one of those is observed in most cases. The crystallisation of monomers (the fifth coordination place is occupied by a solvent molecule) or coordination polymers (the metal centres are either bridged by the anions to 1D chains or the –CN group of HL4 connects the Cu(II) ions) occurred as well. It was shown that for the dimeric complexes the Cu–X bond length and the Cu–X–Cu angle correlate well with the size of the anion. A smaller bridging anion leads to shorter bond lengths and larger angles. Powder X-ray diffraction was used to confirm the identical structures of the bulk complexes and the single crystals. The magnetic properties of the dimers were investigated, as Cu(II) complexes can show interesting magnetic behaviour such as superexchange. Most of the compounds are bridged by the anions in double axial-equatorial positions and have small coupling constants *J*, indicative of rather weak antiferromagnetic (*J* negative) or ferromagnetic (*J* positive) interactions. No direct correlation between the nature of the magnetic exchange interactions and the structural parameters, such as the Cu–X–Cu angle or the distortion parameter τ was found, making it difficult to predict those interactions. $[(\mu\text{-}I)_2(CuL5)_2]$ has the largest distortion parameter (0.28) and the second highest coupling constant (in absolute value) of $-7.36\ cm^{-1}$. The complex with the strongest superexchange ($J \approx -129\ cm^{-1}$) is $[(\mu\text{-}1,1\text{-}NO_3)(\mu\text{-}1,3\text{-}NO_3)(CuL1)_2]$ and has a different structure in the solid state (Figure 2) than the other dimeric Cu(II) complexes, the nitrate bridges at interlinking equatorial-equatorial and axial-axial positions at the adjacent Cu(II). One of the two nitrates coordinates with two oxygen instead of one, resulting in a much larger Cu–O–Cu angle of ≈143° for the second anion. This and the equatorial-equatorial coordination provide a better overlap between the magnetic $d_{x^2-y^2}$ orbital of the Cu(II) centre and the p orbital of the oxygen. Therefore the super exchange is much more pronounced than for the other complexes, resulting in this comparatively high coupling constant.

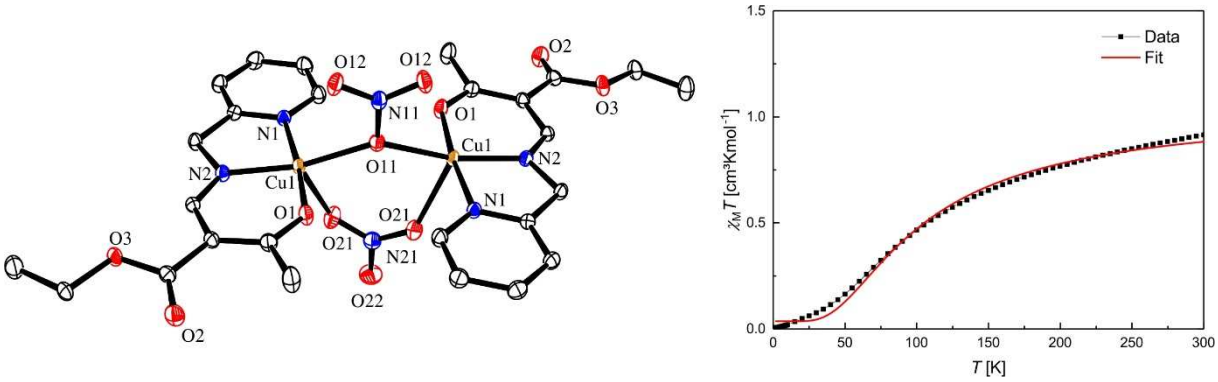

Figure 2. Complex [(μ-1,1-NO_3)(μ-1,3-NO_3)($CuL1)_2$] (left), thermal ellipsoids were drawn at 50 % probability level, hydrogen atoms were omitted for clarity. Right: $\chi_M T$ vs. *T* plot.

Selected coordination polymers were investigated as well considering their magnetic properties. The chloride bridged complex $[(\mu\text{-Cl})(CuL5)]_n$ showed weak ferromagnetic interactions, whereas for the –CN bridged complex $[CuL4(NO_3)]_n$ almost ideal Curie behaviour was observed. This indicates that, even though the cyanide chain coordinates in an equatorial position, the exchange pathway is too long.

Fe complexes can show interesting magnetic properties as well, a phenomenon called spin crossover. The spin state of the metal centre can be switch from the high spin to the low spin state by external stimuli, such as temperature. This was investigated in Chapters 7 and 8. The Fe(II) and Fe(III) complexes (with varying anions) were synthesised, characterised, and compared to the known $[Fe(bipy)_3]Cl_2$ and $[Fe(bipy)_3](PF_6)_3$ (bipy = 2,2'-bipyridine) in Chapter 7. The Fe(II) complexes were obtained by a ligand exchange reaction between $Fe(OAc)_2$ and the respective tridentate ligand under an argon atmosphere. The Fe(III) complexes were synthesised by reacting $Fe(NO_3)_3 \cdot 9H_2O$, sodium acetate, and the tridentate ligands. Afterwards the nitrate anion was exchanged by Cl^-, Br^-, I^-, BF_4^-, PF_6^-, or ClO_4^-. The X-ray structure of one Fe(II) complex, $[Fe(L6)_2]\cdot MeOH$, and three Fe(III) complexes ($[Fe(L1)_2]ClO_4$, $[Fe(L2)_2]PF_6 \cdot MeCN$, and $[Fe(L6)_2]ClO_4$) were obtained. The crystallographic data for the Fe(II) complex were of low quality, and therefore the complex was only discussed as general structural motif. The structures of the Fe(III) complexes were described in more detail. The spin state of $[Fe(L1)_2]ClO_4$ is HS at the measured temperature (133 K), the other two are LS. The spin states were attributed by the comparison of the bond lengths (as they are shorter in the LS state), the octahedral distortion parameter Σ (which is around 40° in the LS state and around 80° in the HS state), and the N_{py}–Fe–O angle (closer to 180° in the LS state). Several

intermolecular interactions were observed in the packing. The complex molecules form two layers, which are turned 180° with respect to each other. In the case of the two complexes in the LS state, the anions separate these layers. In $[Fe(L1)_2]ClO_4$, a strong P4AE (Parallel Fourfold Aryl Embrace), a combination of π···π and C–H···π interactions (see Figure 3), leaves no place for the anions between the layers. The magnetic measurements showed that the Fe(II) complexes remained mostly HS over the complete investigated temperature range (300–50 K), whereas out of the twelve Fe(III) complexes ten showed SCO behaviour. The spin transition is gradual in all cases, and mostly incomplete in the HS and the LS region. Two complexes show a small hysteresis: $[Fe(L1)_2]Br$ (6 K) and $[Fe(L1)_2]PF_6$ (5 K). The gradual nature of the SCO can be explained with the missing cooperativity between the Fe(III) centres, although several intermolecular interactions were observed in the crystal packing. The strong P4AE interaction in $[Fe(L1)_2]ClO_4$ is believed to prevent the occurrence of SCO, as the packing is very dense and a spin transition is always accompanied by a volume change. The complex $[Fe(bipy)_2]Cl_2$ undergoes an abrupt ST above 340 K. This process is irreversible and can be explained by the loss of solvent at elevated temperatures. On the other hand, $[Fe(bipy)_3](PF_6)_3$ is a pure LS complex. The difference in SCO behaviour of the Fe(II) and Fe(III) complexes can be explained with the different ligand field splitting; it increases with a higher oxidation state of the central metal atom, therefore for negatively charged ligands the ligand field of the Fe(III) complexes is in a region which allows a ST, whereas the Fe(II) complexes remain HS. For the neutral bidentate ligand bipy it is the opposite, the ligand field for the Fe(II) complex is in a region suitable for SCO, and the Fe(III) complex remains LS.

The complexes were investigated considering their properties in solution (UV-Vis spectroscopy and cyclic voltammetry) as well. The absorption maxima for the Fe(II) complexes are in the region of 450 nm, with an absorption coefficient that indicates a charge transfer process responsible for the colour of the complexes. The Fe(III) complexes show two absorption maxima (around 530 and 645 nm), which are independent of the used anion and only depend on the used tridentate ligand. The two maxima correspond to the HS and the LS state (respectively) of the iron(III) and indicate that a spin transition in solution is possible. Again, a charge transfer process is responsible for the colour of the complexes. The electrochemical behaviour was investigated with cyclic voltammetry. All Fe complexes with the tridentate ligands show quasi-reversible processes between −0.51 and −0.40 V, that correspond to the Fe(II)/Fe(III) redox process. Additionally an irreversible oxidation of the ligand above 1.1 V was observed as well. No significant influence of the counterions or the oxidation state of the

starting material on the redox potentials was found. The redox potential of the pair $[Fe(bipy)_3]^{2+}/[Fe(bipy)_3]^{3+}$ is at 0.72 V (reduction) and 0.83 V (oxidation). This shows again a strong impact of the different chelate ligands used (anionic and tridentate *vs.* neutral and bidentate).

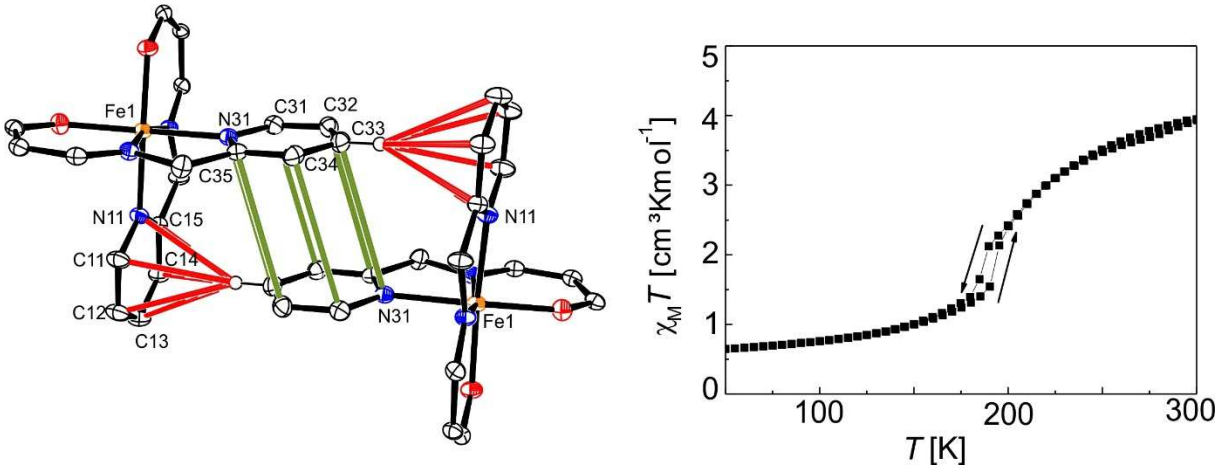

Figure 3. Left: Structure of $[Fe(L1)_2]ClO_4$ illustrating the P4AE interaction; ellipsoids were drawn at 50 % probability level, hydrogen atoms and side chains were omitted for clarity. Right: $\chi_M T$ vs. T plot of $[Fe(L1)_2]Br$.

So far, only gradual SCO was observed. This is different for the isostructural Fe(III) complexes $[Fe(L2)_2]BF_4$ and $[Fe(L2)_2]ClO_4$, that are discussed in Chapter 8. Both complexes crystallise in the orthorhombic space group $P2_12_12_1$ with one complex molecule and one anion per asymmetric unit. It was possible to obtain the single crystal structures of the two compounds in both, the HS and the LS state. The complexes show an abrupt ST above 100 K; the transition temperature $T_{1/2}$ is shifted by 30 K towards lower temperature for the perchlorate complex (145 K → 115 K). This shift can be explained by the size of the anion, as the perchlorate is slightly larger than the tetrafluoroborate anion and therefore stabilises the HS state. By comparing the structures in the HS and LS state it was seen that the volume change upon SCO is smaller for $[Fe(L2)_2]ClO_4$ (2.3 %) than it is for $[Fe(L2)_2]BF_4$ (2.8 %). The packing of the complex molecules in the crystal is similar to the SCO active iron(III) complexes described in Chapter 7: two layers of molecules are formed, which are turned 180° with respect to each other and are separated by the anions. Several intermolecular interactions are observed in the packing of the crystals, therefore a Hirshfeld surface analysis was performed to identify significantly strong/short contacts. There are dominant H···O interactions between a keto oxygen of one

ligand and a methyl group of another ligand (see Figure 4). A chain of molecules along [100] is formed by these non-classical hydrogen bonds. These interactions are a possible explanation for the very cooperative and therefore abrupt ST compared to the other Fe(III) complexes, that were discussed in Chapter 7.

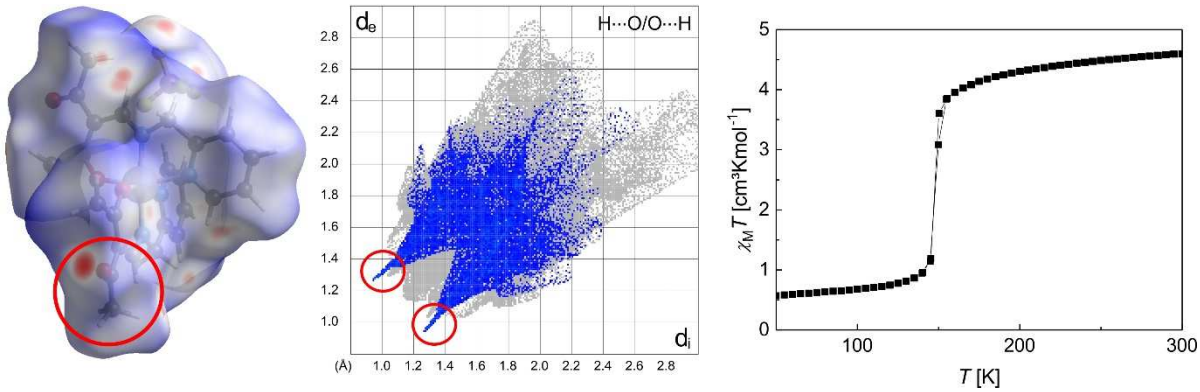

Figure 4. Hirshfeld surface (left) and 2D fingerprint plot (middle) of $[Fe(L2)_2]BF_4$ in the HS state. The red circle is highlighting the area of strong C–H···O interactions. Right: $\chi_M T$ vs. T plot of $[Fe(L2)_2]BF_4$.

So far, the focus of this work was on the magnetic properties of the complexes. Compounds with additional weakly binding ligands can also show interesting catalytic or biological activity. In Chapter 9, the dinuclear Zn(II) complexes were investigated considering their potential application as catalysts for the ring opening polymerisation of lactide. The white complexes were obtained by an easy complexation reaction between $Zn(OAc)_2{\cdot}2H_2O$ and the tridentate ligands. It was possible to obtain the single crystal X-ray structures of the two complexes [(μ-1,1-OAc)(μ-1,3-OAc)$(ZnL1)_2$] and [(μ-1,1-OAc)(μ-1,3-OAc)$(ZnL5)_2$]. Both show the same general motif, the two Zn(II) atoms are coordinated by the tridentate ligands and bridged *via* two acetate anions, one is coordinating with only one oxygen atom, while the other is bridging the Zn(II) centres with both oxygen atoms. Zn complexes of ligands HL1, HL2, HL4, HL5, and HL6 were tested regarding their activity in the ring opening polymerisation of non-purified *rac*-lactide in melt at a temperature of 150 °C. Due to the high fluorescence of complex [ZnL4OAc] it was not possible to perform a kinetic study. For the other four complexes polymerisation data were obtained. Compound [(μ-1,1-OAc)(μ-1,3-OAc)$(ZnL5)_2$] was the slowest catalyst with an apparent rate constant k_{app} one order of magnitude lower than the other three complexes (10^{-4} *vs.* 10^{-3} s^{-1}). This is due to the higher steric demand of the phenyl groups at the chelate cycle, making the access of the lactide more difficult. A coordination-insertion

mechanism was proposed; an induction phase takes place at the beginning, during which the dissociation of the dinuclear complex into a monomeric species leads to the formation of the active species. This was further supported by the fact that the obtained molar masses are much closer to the theoretically calculated molar masses if each Zn atom propagates a chain. Also, analysis of the polylactide by MALDI-ToF confirmed that the monomeric complex is attached to a chain end. ^{1}H NMR showed that only atactic polymers are formed. TGA revealed that the complexes are stable up to 225 °C, a temperature higher than the typical industrial conditions (180–200 °C). Complex [ZnL2OAc] was investigated considering its cytotoxicity towards one melanoma, two colon carcinoma, one cervix carcinoma, and one non-malignant human fibroblast cell lines. It showed no cytotoxicity towards any of these cell lines with IC_{50} values >100 µM and can be considered non-hazardous to health. This study points out that those Zn complexes have a high potential to replace the toxic $Sn(Oct)_2$ catalyst which is currently used for ring opening polymerisation of lactide in industry.

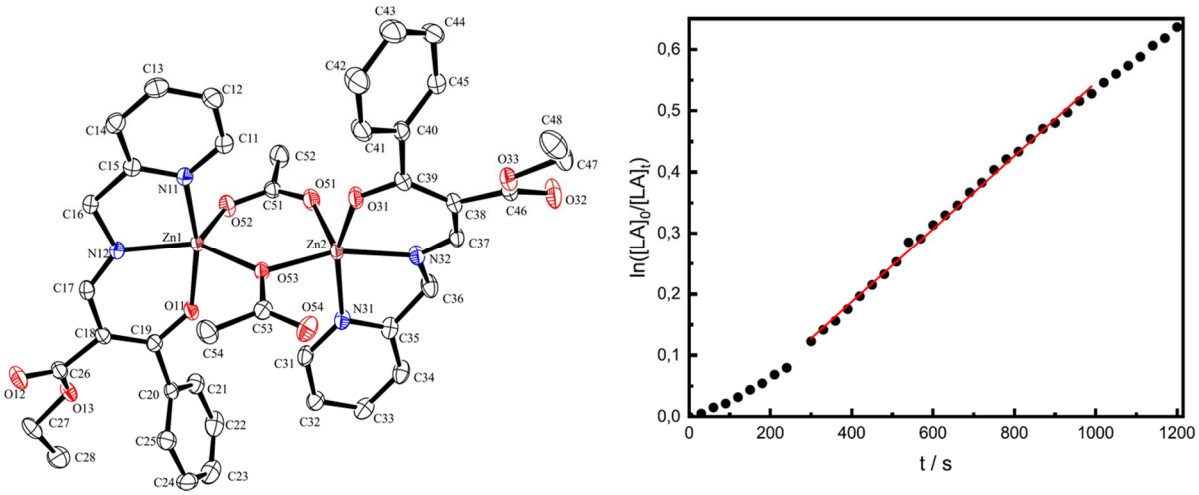

Figure 5. Structure (left) of [(µ-1,1-OAc)(µ-1,3-OAc)(ZnL5)$_2$] and semi-logarithmic plot (right) of the polymerisation of non-purified *rac*-LA with [(µ-1,1-OAc)(µ-1,3-OAc)(ZnL5)$_2$] [M]/[I] = 500:1, 150 °C, 260 rpm, conversion determined by *in situ* Raman spectroscopy, showing the induction phase at the beginning of the polymerisation.

In Chapter 10, the Cu(II) complexes were investigated considering their possible application as anticancer agents. The influence of the anion was analysed by testing complexes of ligand HL1 with different anions (NO_3^-, Cl^-, Br^-, and NCS^-). The effect of the side chains on the chelate cycle on the cytotoxic activity was examined by choosing Br^- as anion for the complexes of HL1–HL6. Additionally, substituents (4-OMe, 4-Cl, 4-Me, 5-Me, 6-Me) on the pyridine ring

were introduced to further alter the electronic environment of the central metal atom, and thus influence the cytotoxic activity. Only ligands of the type HL3 and HL4 were synthesised with substituents on the pyridine ring. X-ray structure analysis of four of the new complexes shows that unlike the examples with unsubstituted pyridine-rings (always square pyramidal coordination sphere) a square planar coordination is observed. In all cases short interactions between the Cu centre and a π system of a neighbouring ligand are observed (see Figure 6). UV-Vis spectroscopy and conductivity measurements were performed in water and/or DMSO to investigate if the anion coordinates to the Cu(II) centre in solution, which is especially of interest for the dimeric complexes. The absorption maxima only depend on the tridentate ligand and not the anion in aqueous solution, and in both solvents the conductivity was higher compared to the pure solvent. Therefore it was concluded that the anion does not coordinate to the metal centre and that the dimeric complexes are in fact monomeric and cationic species in solution. The low magnitude of the absorption coefficient ε (10^2) indicates a d–d transition responsible for the colour. The electrochemical behaviour of the complexes was investigated as well. Mostly irreversible Cu(II) → Cu(I) processes were found below −0.4 V. The anodic processes are ill-defined and correspond to oxidation processes of the ligand. The compounds were investigated with regard to their cytotoxic activity and were therefore tested against different cancer cell lines: one melanoma, two colon carcinoma, and one cervix carcinoma. Most complexes were moderately active against the cell lines with IC_{50} values > 10 µM. Two compounds showed high activity with IC_{50} values < 10 µM: complexes of the type HL3 with 4-OMe and 4-Me as substituents on the pyridine ring [Cu($^{4\text{-OMe}}$L3)Br] and [Cu($^{4\text{-Me}}$L3)Br]. The respective compounds of the type HL4 were not active against the cancer cell lines (IC_{50} > 50 µM). $CuSO_4$ was also tested and less active than most Cu(II) complexes. The uptake of the most active complexes was investigated using ICP-MS. Their cytotoxic activity nicely correlates with the Cu concentration in the cells; a higher Cu content in the cells leads to a lower IC_{50} value. The possible mode of action of the complexes was investigated. No direct interaction with the DNA was observed, and also only a tiny generation of reactive oxygen species was detected. It was found that the complexes inhibit the enzyme topoisomerase I which is a clinical important target for anticancer drugs. Again, $CuSO_4$ was tested as well and showed no inhibition.

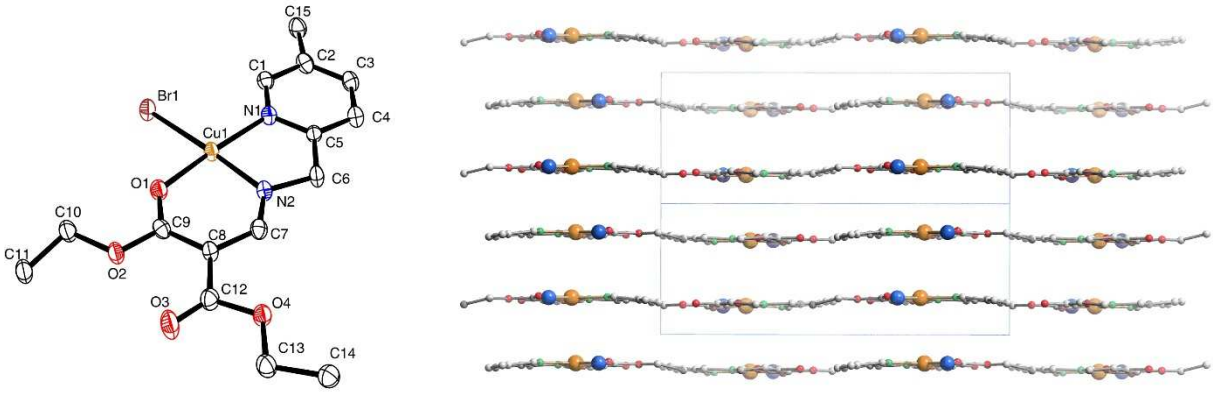

Figure 6. Asymmetric unit (left) and packing in the crystal along [101] (right) of [Cu($^{5\text{-Me}}$L3)Br].

In summary, the new tridentate *NNO* Schiff base-like ligands (middle Figure 7) have a wide variety of interesting properties ranging from magnetic exchange interaction (Cu, top left Figure 7) over spin crossover (Fe, bottom left Figure 7) to catalysts for the ring-opening polymerisation of lactide (Zn, bottom right Figure 7) and possible anti-cancer agents (Cu, top right Figure 7). Compared to the tetradentate ligands used by the Weber group, the observed coordination geometries are the same (square planar, square pyramidal, and octahedral) but due to the weakly binding co-ligands in cases of Zn(II) and Cu(II) complexes a free coordination place is easily accessible. This allows the Zn(II) compounds to act as catalysts for the ROP of lactide, which is not possible for Zn(II) complexes with the tetradentate ligands. The Cu(II) coordination compounds can show superexchange due to the bridging anions, a behaviour that is not observed with the tetradentate ligands. Also, their water solubility is much higher thus allowing the investigation of their cytotoxicity. In case of Fe(II)/Fe(III) complexes only the Fe(III) complexes with the tridentate ligands show SCO behaviour, whereas the Fe(II) complexes with the tetradentate ligands and an N_4O_2 coordination sphere are SCO active.

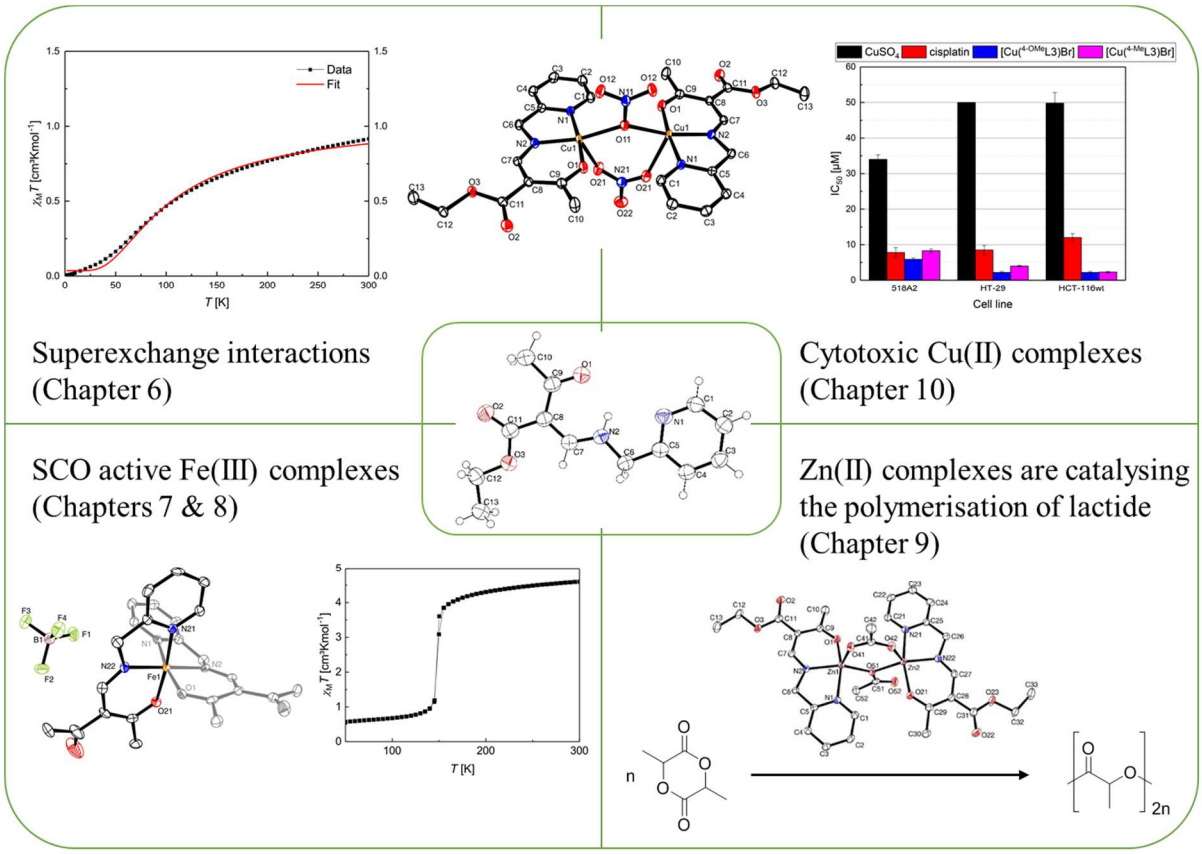

Figure 7. Overview of the different properties of the complexes with the new tridentate ligands depending on the metal centre.

5. Individual contributions to joint publications

The results of this thesis were obtained in collaboration with others and are published, accepted, or to be submitted as explained below. In this chapter, the contributions of all co-authors are specified. The asterisk denotes the corresponding author(s).

Chapter 6

This work was published in CrystEngComm (*CrystEngComm* **2018**, *20*, 818–828) with the title:

"Novel Cu(II) complexes with *NNO*-Schiff base-like ligands : structures and magnetic properties"

Katja Dankhoff and Birgit Weber*

I synthesised and characterised all the ligands and complexes in this work, carried out the magnetic measurements, solved the crystal structures, and wrote the publication. Birgit Weber supervised this work, was involved in scientific discussions, wrote the introduction, and corrected the manuscript.

Chapter 7

This work was published in Zeitschrift für anorganische und allgemeine Chemie (*Z. Anorg. Allg. Chem.* **2018**, *644*, 1839–1848) with the title:

"Iron(II) and Iron(III) Complexes of Tridentate *NNO* Schiff Base-like Ligands – X-ray Structures and Magnetic Properties"

Katja Dankhoff, Sandra Schneider, René Nowak, and Birgit Weber*

The complexes with the tridentate ligands were synthesised and characterised by me or Sandra Schneider during a practical course. I carried out the magnetic measurements, measured and solved the crystal structures, and wrote the publication. René Nowak synthesised and

characterised the iron(II) complex of 2,2'-bipyridine. Birgit Weber supervised this work, was involved in scientific discussions, wrote the introduction, and corrected the manuscript.

Chapter 8

This work was published in Dalton Transactions (*Dalton Trans.* **2019**, DOI: 10.1039/c9dt00846b) with the title:

"Isostructural iron(III) spin crossover complexes with a tridentate Schiff base-like ligand: X-ray structures and magnetic properties"

Katja Dankhoff and Birgit Weber*

I synthesised and characterised the complexes discussed in this work, carried out the magnetic measurements, measured and solved the crystal structures, and wrote the publication. Birgit Weber supervised this work, was involved in scientific discussions, wrote the introduction, and corrected the manuscript.

Chapter 9

This work was published in ChemistryOpen (*ChemistryOpen* **2019**, *8*, 1020–1026) with the title:

"Towards new robust Zn(II) complexes for the ring-opening polymerisation of lactide under industrial relevant conditions"

Pascal M. Schäfer, Katja Dankhoff, Matthias Rothemund, Agnieszka N. Ksiazkiewicz, Andrij Pich, Rainer Schobert, Birgit Weber* and Sonja Herres-Pawlis*

Pascal M. Schäfer carried out the polymerisation of lactide, the kinetic investigations, and wrote the manuscript. I synthesised and characterised the complexes used as catalysts, measured and solved the crystal structures, and wrote this part of the manuscript. Matthias Rothemund carried out the cell tests. Agnieszka N. Ksiazkiewicz carried out the MALDI measurements. Andrij

Pich, Rainer Schobert, Birgit Weber, and Sonja Herres-Pawlis supervised this work, were involved in scientific discussions, and corrected the manuscript.

Chapter 10

This work was published in Dalton Transactions (*Dalton Trans.* **2019**, *48*, 15220–15230) with the title:

"Copper(II) complexes with tridentate Schiff base-like ligands: solid state and solution structures and anticancer effects"

Katja Dankhoff, Madeleine Gold, Luisa Kober, Florian Schmitt, Lena Pfeifer, Andreas Dürrmann, Hana Kostrhunova, Matthias Rothemund, Viktor Brabec, Rainer Schobert* and Birgit Weber*

The complexes and ligands discussed in this work were synthesised and characterised by me, Lena Pfeifer, or Andreas Dürrmann during their bachelor thesis. I measured and solved the crystal structures and wrote the manuscript. Madeleine Gold, Luisa Kober, Florian Schmitt, and Matthias Rothemund carried out the cell tests. Hana Kostrhunova carried out the uptake studies of selected complexes using ICP-MS. Viktor Brabec, Rainer Schobert, and Birgit Weber supervised this work, were involved in scientific discussions, and corrected the manuscript.

6. Novel Cu(II) complexes with *NNO*-Schiff base-like ligands : structures and magnetic properties

Katja Dankhoff and Birgit Weber*

Department of Chemistry, University of Bayreuth, Universitätsstr. 30, 95440 Bayreuth, Germany. E-mail: weber@uni-bayreuth.de; Tel: +49(0)921552555

Published in: *CrystEngComm* **2018**, *20*, 818–828. (DOI: 10.1039/C7CE02007D)

Abstract: We present a series of six new tridentate Schiff base-like ligands, derived from 2-picolylamine, providing an *NNO* coordination sphere. Their corresponding Cu(II) complexes were synthesised with a range of varying counter anions (OAc^-, NO_3^-, Cl^-, I^-, NCS^-, and N_3^-). The results from single X-ray structure analyses of four ligands and 22 Cu(II) complexes are presented. The majority of the complexes crystallised as dimers with the anion bridging the Cu(II) centres in a μ-fashion; depending on the substituents at the ligand and the counter ion the formation of coordination polymers or mononuclear complexes is also possible. Temperature dependent magnetic measurements revealed that the exchange interactions between the Cu(II) centres depend on the nature of the bridging ligand (axial/equatorial), the Cu–X–Cu angle, and the distortion between a square pyramidal and a trigonal bipyramidal coordination sphere, explicable by assuming a superexchange.

6.1 Introduction

The design of functional materials is a great challenge for synthetic chemists. With regard to this, oligonuclear complexes and coordination polymers that are built through self-assembly of metal centres and polytopic ligands are actively investigated. Depending on their structure,

intriguing properties in the field of magnetism, catalytic or biological activity, or sensing applications can be found.[1] Tridentate ligands are widely used in many different fields of coordination chemistry due to their wide variability and also flexibility with regard to the ligand structures, coordinated metal centres, and the related physical and chemical properties.[2] In the case of metal centres that prefer an octahedral coordination sphere, usually mononuclear complexes of the general formula $[ML_2]^{n+}$ are obtained. Some of those complexes show an interesting magnetic bistability (e.g. spin crossover, SCO).[3,4] Additionally, for rigid tridentate ligands, control over either a facial (trispyrazolylmethane/-borate and related ligands) or a meridional coordination (terpyridine and related) is obtained. However, if a preferred coordination number of the metal centre is 4 or 5, as in the case of copper(II), the synthesis of mononuclear, dinuclear, or polymeric complexes is possible.[5,6] The different structural motifs will significantly influence the properties of the material. For coordination polymers and oligonuclear complexes different magnetic exchange interactions are possible.[6,7] Here it needs to be pointed out, that already small structural differences can significantly influence the magnetic properties.[8,9] Due to the S = ½ spin state of the copper(II) center systematic investigations on the influence of different bridging ligands on magnetic exchange interactions are possible.[10–13] One of the first prominent examples for a magnetostructural correlation of dinuclear μ-hydroxide-bridged copper(II) complexes was proposed by Hatfield and Hodgson.[14] The coupling constant J was found to strongly depend on the Cu–O–Cu angle of the dinuclear unit. For a more detailed discussion of the magnitude and nature of the exchange interactions in dinuclear and polymeric copper(II) complexes, the position of the bridging ligand (axial vs. equatorial) with regard to the magnetic orbital (usually $d_{x^2-y^2}$) has to be taken into account.[8,15] For penta-coordinated complexes with axial/equatorial bridging ligands the distortion parameter τ (ref. 16) that helps to distinguish between square pyramidal (τ = 0) and trigonal bipyramidal (τ = 1) complexes also needs to be considered.[17,18] Furthermore, mononuclear or dinuclear complexes with additional weakly binding (monodentate) ligands can show interesting biological or catalytic activity.[19] These complexes can be capable of activating oxygen and therefore oxidise phenol or catechol. This can be used to mimic the active site of tyrosinase or catecholase.[20] Other examples serve as active site for ethylene polymerisation[21] or are discussed as anticancer agents.[22] Here we present six new tridentate, 2-picolylamine derived *NNO* Schiff base-like ligands and their corresponding Cu(II) complexes. In combination with different anions a variety of Cu(II) complexes could be

obtained in an easy, three-step synthesis. Their X-ray structures and magnetic properties were compared.

6.2 Results and discussion

Synthesis

The Cu(II) complexes were synthesised in three steps (Scheme 1). First, the 2-picolylamine derived, tridentate Schiff base-like ligands (**HL1**–**HL6**) were synthesised, then treated with $CuSO_4$ under basic conditions to give the corresponding Cu(II) chelate complex which finally had its counter anion exchanged to afford either monomeric, dimeric, or polymeric Cu(II) complexes. For 22 of the 30 Cu(II) complexes thus obtained, the structures could be elucidated. An overview of the synthesised complexes is given in Table 1.

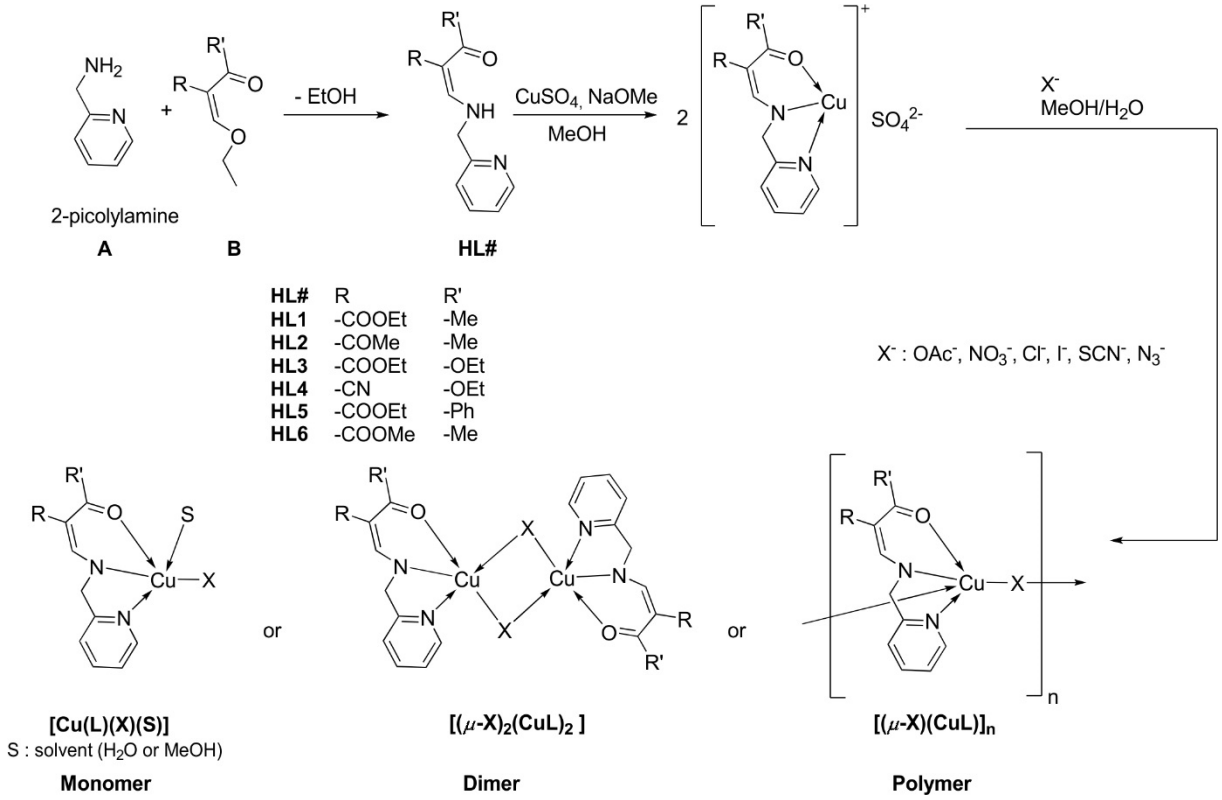

Scheme 1. General procedure for the synthesis of the ligands **HL1–HL6** and the corresponding Cu(II) complexes. The ligands were obtained in 50 to 98% yields, the yields of the Cu(II) complexes ranged from 13 to 79%.

Ligands. The new tridentate 2-((pyridin-2-yl)methylamino)-methylene-1,3-dicarbonyl ligands **HL1**–**HL6** were prepared by a condensation reaction between 2-picolyl amine **A** and the respective β-acylenol ether **B**. The ligands were obtained as white to slightly red powders and their identity and purity was confirmed by ^{1}H NMR spectroscopy, elemental analysis, mass spectrometry, and IR spectroscopy.

Cu(II) complexes. The reaction of the ligands **HL1**–**HL6** with $CuSO_4$ and sodium methoxide in methanol, acting as a base for the deprotonation of the ligand, resulted in dark blue solutions. These were split in aliquots and the respective Cu(II) complexes were precipitated by addition of an aqueous solution of the sodium or potassium salt of the desired anion. The resulting complexes were obtained as dark green to blue, fine crystalline powders. Their identity and purity was confirmed by means of elemental analysis, mass spectrometry, and IR spectroscopy. For some compounds only a few single crystals could be obtained, as either their solubility was too high (all complexes of the type $[CuL]_2SO_4$) or the obtained bulk material was not pure enough as to elemental analysis (for complexes with I^- or N_3^- as anion). In those cases only the results from single crystal X-ray structure analysis are presented.

Table 1. Overview of the synthesised complexes. Complexes of unknown structure were obtained as fine crystalline powders. For entries with "/" neither bulk material nor single crystals could be obtained.

ligand / anion	**L1**	**L2**	**L3**	**L4**	**L5**	**L6**
OAc^-	dimer	structure unknown	dimer	polymer	structure unknown	dimer
NO_3^-	dimer	monomer	structure unknown	polymer	dimer	structure unknown
Cl^-	dimer	dimer	dimer[b]	structure unknown	polymer	dimer
I^-	dimer[a]	/	/	/	dimer[b]	/
NCS^-	polymer	monomer	structure unknown	structure unknown	structure unknown	dimer
N_3^-	dimer[a]	dimer[a]	/	/	/	/
SO_4^{2-}	/	dimer[a]	dimer[a,b]	/	/	/

a Only obtained as single crystals. b Due to bad quality of the data the structures will only be discussed as general structural motif.

X-ray structure analysis

Crystals suitable for X-ray structure analysis were obtained for four ligands and 22 Cu(II) complexes. The crystallographic data were collected at 133 K and are given in the ESI, Table S1. ORTEP drawings of the ligands are shown in Fig. S1, and of selected complexes in Fig. 1. The remaining ORTEP drawings of the complexes are presented in Fig. S2 and S3, bond lengths and selected angles are given in Table S3.

Ligands. Colourless crystals suitable for X-ray structure analysis were obtained for ligands **HL1**, **HL5**, and **HL6** by slow evaporation of the mother liquor at room temperature, and of **HL4** directly from synthesis. For the free ligands two tautomers can be expected: the keto-enamine or the iminoenol form.[17] The results from X-ray structure analyses show that the ligands exist predominantly in the keto-enamine form. The length of the bond C7–C8 with an average value of 1.39 Å is clearly shorter and more in the order of a double bond, while the bond C8–C9 (1.45 Å on average) is significantly longer and more in the range expected for a single bond. The relevant bond lengths are given in Table S2. This is in agreement with other structures reported for similar tetradentate ligands of this Schiff base-like ligand type.[23,24]

Cu(II) complexes. The Cu(II) complexes with a onefold negatively charged anion crystallised with one counter ion and one tridentate ligand per copper centre whereas the complexes with sulfate crystallised with half a counter ion and one tridentate ligand per copper centre. In most cases the counter ion serves as additional ligand. With the exception of **2-SO$_4$** and **3-SO$_4$** the Cu(II) centre has a square pyramidal coordination sphere. The bond lengths between the Cu(II) centre and the donor atoms of the tridentate ligand show average values of 2.00 Å (Cu–N_{py}), 1.92 Å (Cu–N), and 1.93 Å (Cu–O), and are thus all in the same order of magnitude and similar to those of other Cu(II) complexes of related Schiff base-like ligands.[23]

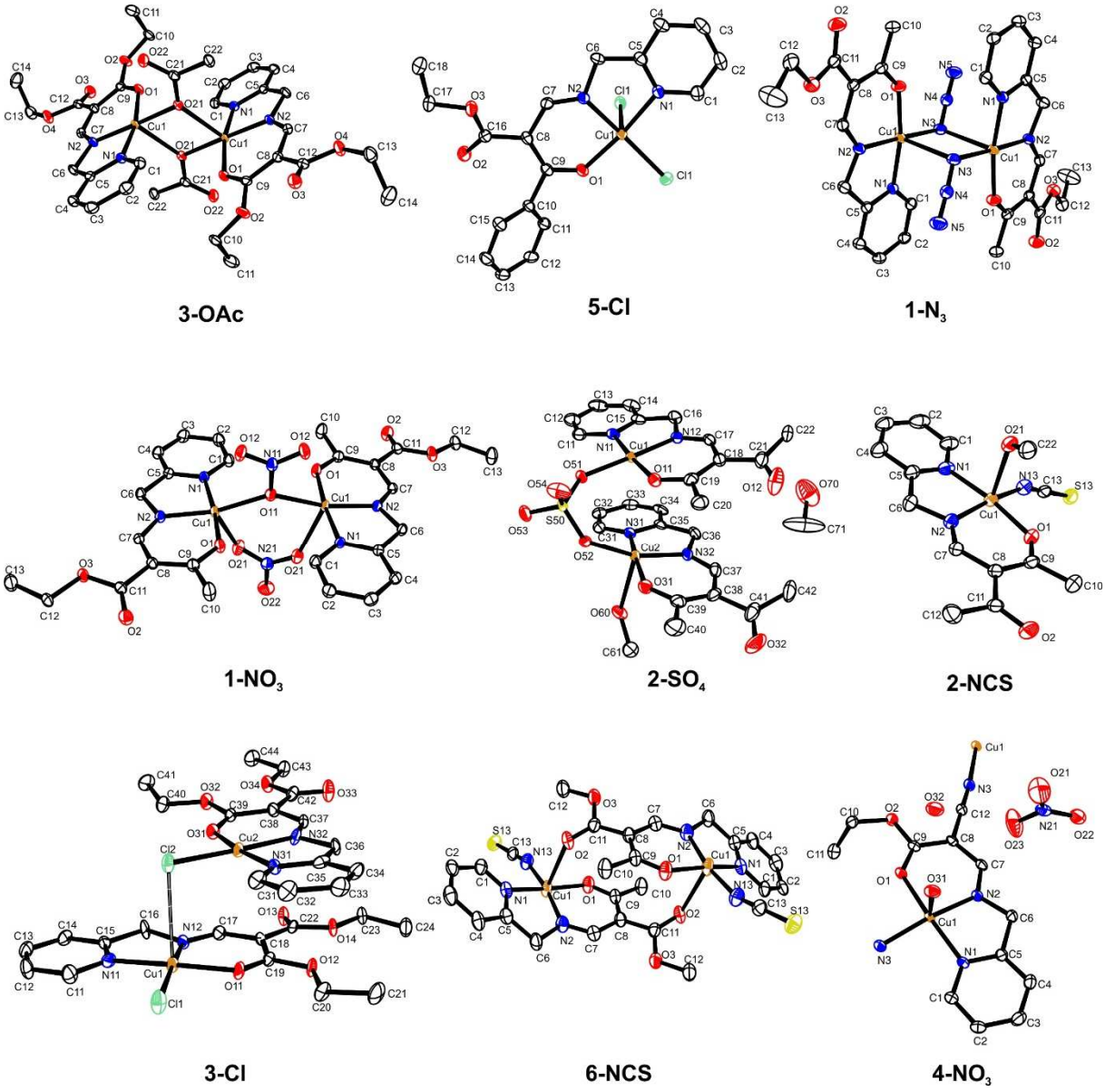

Fig. 1. ORTEP drawings of **3-OAc** (top left), **5-Cl** (top centre), **1-N$_3$** (top right), **1-NO$_3$** (middle left), **2-SO$_4$** (middle centre), **2-NCS** (middle right), **3-Cl** (bottom left), **6-NCS** (bottom centre), and **4-NO$_3$** (bottom right). Ellipsoids are drawn at 50% probability level. Hydrogen atoms were omitted for clarity.

Monomeric Cu(II) complexes. Two of the 27 complexes for which a crystal structure was obtained crystallised as monomers: **2-NO$_3$** and **2-NCS**. In both cases the Cu(II) centre has a square pyramidal coordination sphere, being coordinated by one tridentate ligand, the corresponding anion, and a solvent molecule, e.g. water for **2-NO$_3$** and methanol for **2-NCS**. An ORTEP picture of **2-NCS** is given in Fig. 2. Several intermolecular interactions between the ketone side chain, the anion, and the solvent molecules (one H_2O in **2-NO$_3$**) are apparent. For both complexes metallophilic interactions between one Cu centre and the chelate ring of

the tridentate ligand of a neighbouring complex can be observed. Details of all intermolecular interactions are given in Tables S4–S8.

Dimeric Cu(II) complexes. The majority of the Cu(II) complexes characterised by single crystal XRD have a dimeric structure (16 out of 22). Except for four of those dimers (**2-SO_4**, **3-Cl**, **3-SO_4**, and **6-NCS**), the overall structure of these compounds is similar. Each Cu(II) centre is coordinated by the tridentate ligand and the metal centres are bridged by two anions in a μ-fashion. The ligands are orientated *trans* towards each other. In cases where the bridging anions have more than one possible donor atom (such as OAc^-, NO_3^-, N_3^-) coordination with only one of these donor atoms is observed (with one exception: **1-NO_3**). While the bond lengths between the donor atoms of the chelate cycle and the Cu(II) centre are very similar for all complexes, the bond lengths to the bridging anion are asymmetric, one is shorter than the other. The bond lengths are very similar for complexes with the same bridging anion regardless of the side chains of the tridentate ligand. The Cu–X–Cu angle strongly depends on the bridging atoms, it is much closer to 90° for big anions (such as I^-) than for smaller atoms such as the oxygen of OAc^-. This angle is very similar for complexes with the same bridging anion and not depending on the side chains of the tridentate ligands. A graphic illustration of the Cu–X–Cu angle vs. Cu–X bond lengths is shown in Fig. 2. Several intermolecular interactions between the ketone/ester side chains, the anions, and the aromatic CH-groups of the pyridyl ring were identified for all complexes. In case of additional solvent molecules in the crystal packing, hydrogen bonds with them are observed. For example, in the packing of the complex **6-OAc** a chain of hydrogen bonds between the additional four water molecules lies along axis [100]. Interactions between the chelate ring of one complex and the pyridine ring or the Cu(II) centre of a neighbouring complex molecule were frequently observed. Details of all interactions are provided in Tables S4–S8. The coordination environment of the Cu(II) centre in **6-NCS** differs from that in previously described complexes. The tridentate ligand and the anion form a square planar coordination sphere around the metal centre, while the carbonyl oxygen of the ester side chain of an adjacent tridentate ligand occupies an axial coordination site of the Cu(II), resulting in a square-pyramidal coordination sphere. The complex also crystallised as a dimer.

The complexes $[CuL]_2(SO_4)$ were formed, but could not be obtained as pure materials due to their high solubility. However, crystals suitable for X-ray structure analysis were isolated of complexes **2-SO_4** and **3-SO_4**. The crystals of **3-SO_4** were of a low quality and therefore will be discussed only as a general structural motif. A square planar coordination sphere was observed

for both Cu(II) centres in **3-SO4**. Each Cu(II) centre is coordinated by the tridentate ligand and one oxygen atom of the anion. Two solvent molecules per asymmetric unit are present: one methanol and presumably one water, however the hydrogen atoms of the water molecule are not refined due to the low quality of the data. The Cu(II) centres in **2-SO4** have different coordination spheres: one Cu(II) centre has a square planar coordination sphere with one tridentate ligand and one oxygen of the SO_4^{2-}. The second Cu(II) centre has a square-pyramidal coordination sphere with one methanol molecule in axial position. One additional molecule of methanol per asymmetric unit is present as well. The distance between the Cu(II) centre and the SO_4^{2-} is similar to that between Cu(II) and the oxygen atom of other oxygen-bridged complexes.

The complex **3-Cl** also crystallised as a dimer, although the coordination is different. Unfortunately, the crystals obtained were of a low quality and therefore the structure can only be described as a motif, with no conclusions as to bond lengths and angles being drawn. The tridentate ligand and the chloride anion form a square-planar coordination around the metal centre. For one Cu(II) centre of the dimer the fifth coordination place is occupied by the chloride ion of another Cu(II) centre. For the second metal centre this is not the case, although a rather short metallophilic interaction between the Cu(II) centre and the chelate ring of the other complex molecule can be observed.

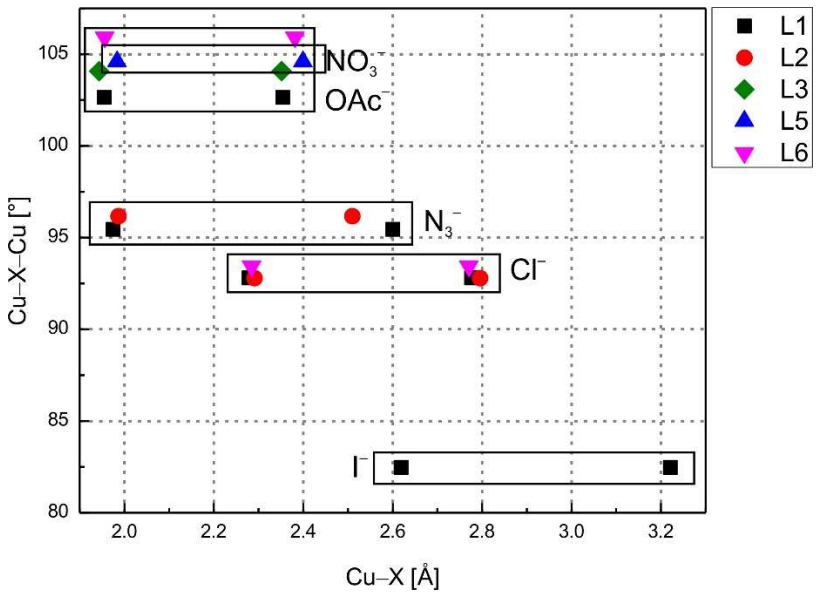

Fig. 2. Correlation of the Cu–X–Cu angles *vs.* Cu–X bond lengths for the Cu(II) complex dimers.

Cu(II) complex polymers. Four Cu(II) complexes crystallised as coordination polymers; two are μ-bridged via the anion (**1-NCS**, and **5-Cl**), and two complexes form a 1D chain via the –CN side chain of ligand L4 (**4-OAc** and **4-NO$_3$**). In **1-NCS** the anion is bridging to the nitrogen on one side and to the sulphur on the other side. The direction of the 1D chains is [100] for **1-NCS**, [010] for **4-OAc** and **4-NO$_3$**, and [001] for **5-Cl**. Complex **4-OAc** has presumably seven water molecules per asymmetric unit, but adding the corresponding hydrogen atoms led to an unstable refinement. Those water molecules separate the 1D chains from each other. Similar intermolecular interactions as for previously described complexes can be observed, all details are given in Tables S4–S8.

Powder X-ray diffraction

Powder X-ray diffraction of the dimeric complexes was done to confirm whether or not the X-ray structures obtained by slow diffusion and the complexes obtained from synthesis have the same structure. The calculated and measured spectra are given in Fig. S4 and S5. It can be seen that the patterns are almost identical for all measured complexes, with minor differences which can be explained with the different techniques and temperatures used to obtain the data.

Magnetism

The magnetic properties of all Cu(II) complexes that were obtained as bulk material were investigated. The central question was if exchange interactions mediated by the bridging ligands might be observable for the dimeric and polymeric complexes. Dimeric Cu(II) complexes are known to show either antiferromagnetic or ferromagnetic exchange interactions of very different magnitude, depending on the possible exchange pathways between the magnetic orbital (usually $d_{x^2-y^2}$, with the orbital lobes pointing towards the ligands with the shorter bond lengths) and the occurrence or absence of strict or accidental orthogonality. Which case is observed depends on several parameters such as the bridging mode, the Cu–X–Cu angle, the bridging ligand X, but also the distortion parameter τ,[8,11,17,18] as will be discussed in the following.

The temperature dependent magnetism was determined between 300 and 50 K for all complexes, and for selected complexes from 300 to 2 K. The values for μ_{eff} (μ_{eff} = effective Bohr magneton number, at 300 K), and $\chi_M T$ (χ_M = molar magnetic susceptibility, at 300 K, 50 K, and if measured, at 2 K) are given in Table S9. The effective Bohr magneton numbers (μ_{eff})

found were in good agreement with the calculated spin only values of μ_{SO} = 1.73 (monomer or polymer) and μ_{SO} = 2.45 (dimer). Plots of $\chi_M T$ vs. T for all complexes are given in Fig. S6–S9.

For the complexes discussed in this work, there are five different ways how the Cu(II) centres in the dimeric compounds are bridged, which can be relevant for the magnetic exchange pathways:

1) Interlinking equatorial–equatorial and axial–axial positions at the adjacent Cu(II) centres (**1-NO$_3$**)
2) Connecting equatorial–equatorial positions (**2-SO$_4$**)
3) Double axial–equatorial positions (e.g. **1-OAc** or **5-NO$_3$**)
4) Single axial–equatorial positions (**3-Cl**)
5) Double axial–axial positions (**6-NCS**).

The focus of this work was set on the complexes for which the bulk material and the single crystals have the same structure. Those were investigated down to 2 K to accurately determine a coupling constant between the Cu(II) centres and allow a magneto-structural correlation. As illustrated in Table 2, those complexes are bridged as explained in 1) or 3) above.

The $\chi_M T$ vs. T plot for **1-NO$_3$** is shown in Fig. 3 as a representative example. The fitting parameters for all investigated complexes (coupling constant J, g-value, and temperature independent paramagnetism TIP or the percentage of monomers α) are given in Table 2 together with selected structural parameters and examples from literature. For a dinuclear complex with two S = ½ centres, the Hamilton operator is

$$H = -JS_1S_2 \tag{1}$$

and the experimental values were fitted with one of the two following formulas[11]

$$\chi_M T = \frac{2 \cdot N_A \cdot g^2 \cdot \beta^2}{k \cdot \left(3 + exp\left(\frac{-J}{k \cdot T}\right)\right)} + TIP \cdot T \tag{2}$$

$$\chi_M T = \frac{2 \cdot N_A \cdot g^2 \cdot \beta^2}{k \cdot \left(3 + exp\left(\frac{-J}{k \cdot T}\right)\right)} \cdot (1 - \alpha) + \frac{N_A \cdot \beta^2 \cdot g^2}{2 \cdot k} \cdot \alpha \tag{3}$$

Since dimeric Cu(II) complexes can have monomeric impurities,[11,12,25] the percentage of monomers (α) has to be taken into account when performing the fit to obtain reasonable fitting

parameters (eqn (3), as was the case for **1-NO$_3$**). The magnetic data of the other complexes were fitted by taking TIP (temperature independent paramagnetism) into account, resulting in better fit of the experimental data.

It can be seen that the coupling constants of all complexes are very small ($< \pm 10$ cm^{-1}) except for **1-NO$_3$**. For this complex a rather negative coupling constant of $J = -129.5(19)$ cm^{-1} was determined, indicative of antiferromagnetic interactions. The difference between the coupling constant of **1-NO$_3$** and the other compounds can be explained based on the X-ray structures of the complexes. First of all, **1-NO$_3$** is the only complex where the Cu(II) centres are bridged in equatorial–equatorial and axial–axial positions by the anion (type 1 in Table 2). For such complexes a good overlap between the magnetic orbitals and the orbitals of the bridging ligand is possible that depends further on the bridging angle. Here, especially the equatorial–equatorial bridge (oxygen atom O11) needs to be considered. The angle Cu1–O11–Cu1 (143.39(9)°) is very large for **1-NO$_3$** and therefore a good overlap between the magnetic $d_{x^2-y^2}$ orbital of the Cu(II) centre and the p orbital of the oxygen atom of the counter ion is possible. This suggests a super exchange pathway[26] for **1-NO$_3$** with the Cu(II) centres coupling antiferromagnetically.

Table 2. Cu–X–Cu angles and distances, distortion parameter τ, coupling constants J, g-factors, temperature-independent paramagnetism TIP, and percentage of monomers α of selected Cu(II) complexes.

	Cu–X–Cu [°]	Cu–X [Å]	Type	τ	J [cm^{-1}]	g	TIP [cm^3mol^{-1}] α[%]	Ref.
1-OAc	102.65(6)	1.9549(15) 2.3542(14)	3	0.11	−2.581(3)	2.121(2)	$8.23(10)\cdot10^{-4}$ /	This work
1-NO_3	143.39(9)	2.3258(14) 2.6745(14)	1	0.14	−129.5(19)	2.383(9)	/ 3.4(5)	This work
1-Cl	92.81(4)	2.2786(11) 2.7766(12)	3	0.08	−1.060(13)	2.1325(10)	$3.68(5)\cdot10^{-4}$ /	This work
2-Cl	92.79(3)	2.2907(9) 2.7953(10)	3	0.13	−0.60(3)	2.140(2)	$6.19(9)\cdot10^{-4}$ /	This work
3-OAc	104.07(8)	1.9436(17) 2.3516(17)	3	0.15	−3.56(9)	2.178(7)	$11.2(3)\cdot10^{-4}$ /	This work
5-NO_3	104.59(6)	1.9836(14) 2.3997(15)	3	0.04	1.82(6)	2.113(2)	$4.69(9)\cdot10^{-4}$ /	This work
5-I	76[a]		3	0.28	−7.36(15)	2.122(8)	$5.3(4)\cdot10^{-4}$ /	This work
6-OAc	105.93(8)	1.9560(18) 2.3814(17)	3	0.10	−2.63(4)	2.139(3)	$10.00(15)\cdot10^{-4}$ /	This work
6-Cl	93.44(3)	2.2844(9) 2.7709(11)	3	0.17	4.8(11)	1.89(2)	$4.4(6)\cdot10^{-4}$ /	This work
[Cu_2(dpa)$_2$(NCO)$_4$]	98.8	1.966(2) 2.629(2)	3	0.19	3.14	2.06	/	[28]
[{Cu(Hdeg)$_2$}$_2$]	106.1(2)	1.957 2.263(3)	3	/	1.0	2.09	/	[29]
[Cu_2(dpp)$_2Cl_4$]	98.5 88.7	2.3043(12) 2.5600(13)	4	/	6.8(1) 1.0(1)	2.08(1) 2.06(1)	/	[30]
{[{Cu(bpca)}$_2$(H_2ppba)]·1.33DMF·0.66DMSO}$_n$	107.6(1)	1.964(3) 2.538(3)	3	/	1.70(1)	2.06(1)	/	[8]
Cu_2(5-Br-L)$_2$(CH_3COO)$_2$[b]	96.3(2)	2.003(4) 2.665(4)	3	/	−1.84(1)	2.10	/	[31]
[CuL'N_3]$_2$[c]	88.3			0.13	−2.63(1)	2.11	/	[32]

a Only approximate value, X-ray structure can only be discussed as motif. b L: *N*-methyl-*N'*-(5-bromosalicylidene)-1,3-propanediamine. c {*N*-[2-(Ethylamino)ethyl]-salicylaldimine}.

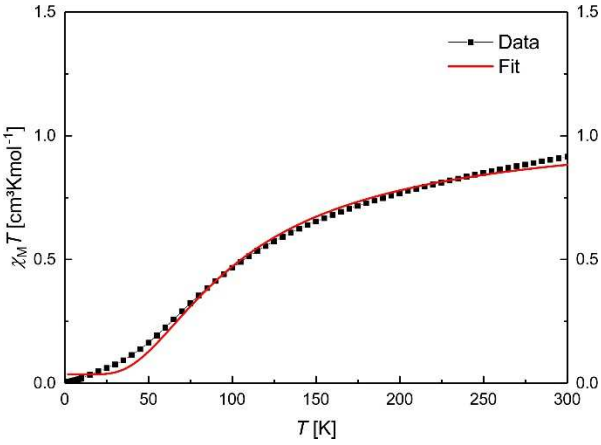

Fig. 3. $\chi_M T$ vs. T plot of **1-NO$_3$**. The black squares represent the reading points, the red line represents the fitted curve.

For the other complexes, the Cu(II) centres are bridged in double axial–equatorial fashion (type 3) and, additionally, the Cu–X–Cu angle is much closer to 90°. In these cases it is difficult to predict if very weak super exchange interactions are still possible (*J* negative) or if the magnetic orbitals are orthogonal (strict or accidental) to each other leading to ferromagnetic interactions (*J* positive).[13,27] Indeed, the complexes **1-OAc**, **3-OAc**, and **6-OAc** showed weak antiferromagnetic interactions with coupling constants of $J = -2.581(3)$ cm^{-1}, $J = -3.56(9)$ cm^{-1}, and $J = -2.63(4)$ cm^{-1}, respectively, whereas complex **5-NO$_3$** showed weak ferromagnetic interactions with $J = 1.82(6)$ cm^{-1}. In all complexes the Cu(II) centres are bridged via one oxygen atom and the Cu–O–Cu angles are 102.65(6)° (**1-OAc**), 104.07(8) (**3-OAc**), 105.93(8)° (**6-OAc**), and 104.59(6)° (**5-NO$_3$**). The Cu–X–Cu angle for the halide-bridged complexes is much closer to 90°, and no trend of the interactions can be recognised here, either. The chloride-bridged complexes show either weak ferro- or antiferromagnetic interactions. For such systems an additional parameter can be considered to obtain a magnetostructural correlation.[17,18] The distortion parameter τ (also called Addison parameter)[16] helps to distinguish between a square-pyramidal coordination geometry (τ close to 0) and a trigonal-bipyramidal coordination geometry (τ close to 1). The calculated values for the characterised complexes are given in Table 2. It can be seen that in all cases the coordination geometry is closer to square pyramidal with τ values between 0.04 and 0.28. Interestingly, for complex **5-I** with the maximum value of τ (0.28) the minimum value of J ($-7.36(15)$ cm^{-1}) is obtained for the presented complexes of type 3. This is in line with results previously reported in literature on similar systems[17] and can be explained with an improved overlap of the orbitals.

The complex **5-Cl** crystallised as polymer and was investigated as well. The interactions between the Cu(II) centres, which are bridged via the anion, are ferromagnetic, however, it was not possible to determine a coupling constant. The bridging mode can be assigned to type 4 (single equatorial–axial). Complex **4-NO_3** also crystallised as polymer, with the Cu(II) centres bridged via the –CN group of the ligand. For this complex an almost ideal Curie behaviour **(**Fig. S10) was observed (C = 0.46 cm^3 mol^{-1} K). Although the cyanide side chain coordinates in an equatorial position at the neighbouring Cu(II) centre, the exchange pathway is too long.

In conclusion, it is possible to determine parameters to predict the structure of the obtained copper(II) complexes. Dimers are formed by the majority of the complexes whereas monomers were only observed for complexes of the rather small and rigid ligand **L2**. Ligands with side chains that can serve as ligand for neighbouring metal centres, as in the case of **L4**, increase the probability for the formation of coordination polymers. Several factors need to be considered for a magneto-structural correlation: the type of interaction, the Cu–X–Cu angle and the distortion parameter τ were used in this manuscript. However, in some cases opposed effects with regard of sign and magnitude of coupling constant are possible and an in-depth explanation is not always possible.

6.3 Experimental section

Synthesis

MeOH was purified by distillation over Mg under argon. Ethoxymethylenethylacetoacetate, methoxymethylenacetylacetone, methoxymethylenmethylacetoacetate, and ethoxyphenylen-ethylacetoacetate were synthesised as already published.[33] All other chemicals were commercially available and used without further purification. ^{1}H NMR spectra were measured at room temperature and 300 MHz with a Varian INOVA 300. Elemental analysis were measured with a Vario EL III from Elementar Analysen-Systeme with acetanilide as standard. The samples were placed in a small tin boat. Mass spectra were recorded with a Finnigan MAT 8500 with a data system MASPEC II. IR spectra were recorded with a Perkin Elmer Spectrum 100 FT-IR spectrometer.

HL1. 2-Picolylamine (2 mL, 0.019 mol) was diluted in EtOH (5 mL) and ethoxymethylenethylacetoacetate (4.34 g, 0.023 mol) was added. The orange solution was heated to reflux for 1 h. After cooling to RT the solvent was removed under reduced pressure yielding a dark red oil. After one night at −28 °C the oil solidified. It was suspended in ice-cold diethyl ether (5 mL) and the resulting light orange solid was filtered and washed with ice-cold diethyl ether (10 mL). Yield: 4.22 g (248.28 g mol^{-1}, 88%). Elemental analysis ($C_{13}H_{16}N_2O_3$, %) found C 62.98, H 6.50, N 11.33; calcd. C 62.89, H 6.50, N 11.28. ^{1}H NMR (298 K, 300 MHz, $CDCl_3$): δ = 11.40 (1H, bs, –NH), 8.61 (1H, d^3, *J* = 3.8 Hz, 6-PyH), 8.14 (1H, d^3, *J* = 13.5 Hz, =CH), 7.73 (1H, dt^3, *J* = 7.7 Hz, *J* = 1.5 Hz, 4-PyH), 7.28 (1H, m, 5-PyH), 7.26 (1H, m, 3-PyH), 4.68 (2H, d^3, *J* = 6.1 Hz, 2-Py-CH_2), 4.21 (2H, q^3, *J* = 7.0 Hz, O=C–CH_2), 2.50 (3H, s, O=C–CH_3), 1.31 (3H, t^3, *J* = 7.1 Hz, –CH_2–CH_3) ppm. MS (EI, pos.) *m/z* (%): 248 ($C_{13}H_{16}N_2O_3$, 11), 93 (C_6H_6N, 100). IR: *ν* = 3203 (w, NH), 1693 (s, C=O), 1628 (s, C=O) cm^{-1}.

HL2. 2-Picolylamine (2 mL, 0.019 mol) was diluted in MeOH (5 mL) and methoxymethylenacetylacetone (3.27 g, 0.023 mol) was added. The yellow solution was heated to reflux for 1 h. After cooling to RT the solvent was removed under reduced pressure yielding an orange oil. After 12 d at −28 °C the now yellow solid was suspended in ice-cold diethyl ether (5 mL), filtered and washed with ice-cold diethyl ether (10 mL). Yield: 3.17 g (218.25 g mol^{-1}, 75%). Elemental analysis ($C_{12}H_{14}N_2O_2$, %) found C 65.99, H 6.48, N 12.88; calcd. C 66.04, H 6.47, N 12.88. ^{1}H NMR (298 K, 300 MHz, $CDCl_3$): δ = 11.42 (1H, s, –NH), 8.62 (1H, d^3, *J* = 4.2 Hz, 6-PyH), 7.95 (1H, d^3, *J* = 13.0 Hz, =CH), 7.75 (1H, dt^3, *J* = 7.64, *J* = 1.6 Hz, 4-PyH), 7.29 (2H, m, 5- & 3-PyH), 4.69 (2H, d^3, *J* = 6.1 Hz, 2-Py-CH_2), 2.50 (3H, s, O=CH_3), 2.30 (3H, s, O=CH_3) ppm. MS (EI, pos.) *m/z* (%): 218 ($C_{12}H_{14}N_2O_2$, 25), 93 (C_6H_6N, 100). IR: *ν* = 3169 (w, NH), 1608 (s, C=O) cm^{-1}.

HL3. 2-Picolylamine (2 mL, 0.019 mol) was diluted in EtOH (10 mL) and diethylethoxymethylenemalonate (6.49 g, 0.03 mol) was added. The orange solution was heated to reflux for 1 h. After cooling to RT the solvent was removed under reduced pressure yielding an orange oil. This oil was stored at −28 °C for one night, where it solidified. The yellow solid was suspended in ice-cold diethyl ether (10 mL), filtered, and washed with ice-cold diethylether (10 mL). Yield: 5.3 g (278.31 g mol^{-1}, 98%). Elemental analysis ($C_{14}H_{18}N_2O_4$, %) found C 60.24, H 6.51, N 10.04; calcd. C 60.42, H 6.52, N 10.07. ^{1}H NMR (298 K, 300 MHz, $CDCl_3$): δ = 9.60 (1H, s, –NH), 8.61 (1H, d^3, *J* = 4.5 Hz, 6-PyH), 8.12 (1H, d^3, *J* = 14.1 Hz, =CH), 7.75 (1H, dt^3, *J* = 7.54, *J* = 1.0 Hz, 4-PyH), 7.29 (2H, m, 5- & 3-PyH), 4.69 (2H, d^3, *J* = 6.0 Hz, 2-

Py-CH_2), 4.21 (4H, m, O=C–O–CH_2), 1.31 (6H, m, O=C–O–CH_2–CH_3) ppm. MS (EI, pos.) *m/z* (%): 278 ($C_{14}H_{18}N_2O_4$, 22), 232 ($C_{12}H_{13}N_2O_3$, 97), 93 (C_6H_6N, 100). IR: ν = 3290 (w, NH), 1677 (s, C=O), 1623 (s, C=O) cm^{-1}.

HL4. 2-Picolylamine (3 mL, 0.0291 mol) was diluted in EtOH (20 mL) and ethyl(ethoxymethylene)cyanoacetate (5.88 g, 0.0349 mol) was added. The yellow solution was heated to reflux for one hour. After cooling to RT the solution was stored at −28 °C for 14 d. A white, crystalline solid occurred, which was filtered and washed with EtOH. Yield: 4.16 g (231.25 g mol^{-1}, 62%). Elemental analysis ($C_{12}H_{13}N_3O_2$, %) found C 62.32, H 5.72, N 18.20; calcd. C 62.33, H 5.67, N 18.17. ^{1}H NMR (298 K, 300 MHz, $CDCl_3$): δ = 9.48 (1H, s, –NH), 8.63 (1H, m, 6-PyH), 8.01 (1H, d^3, *J* = 14.1 Hz, =CH), 7.77 (1H, m, 4-PyH), 7.33 (2H, m, 5- & 3-PyH), 4.69 (2H, d^3, *J* = 5.3 Hz, 2-Py-CH_2), 4.22 (H, m, O=C–O–CH_2), 1.30 (3H, m, O=C–O–CH_2–CH_3) ppm. MS (EI, pos.) *m/z* (%): 231 ($C_{12}H_{13}N_3O_2$, 50), 93 (C_6H_6N, 100). IR: *v* = 3266 (w, NH), 2204 (s, C≡N), 1695 (s, C=O) cm^{-1}.

HL5. 2-Picolylamine (1 mL, 0.0097 mol) was diluted in EtOH (5 mL) and ethoxyphenylenethylacetoacetate (2.89 g, 0.012 mol) was added. The yellow solution was heated to reflux for 1 h. After cooling to RT the solvent was removed under reduced pressure yielding a dark yellow oil. This oil was stored at −28 °C for 3 d. The now yellow solid was suspended in ice-cold diethyl ether (5 mL), filtered, and washed with ice-cold diethyl ether (10 mL). Yield: 2.92 g (310.35 g mol^{-1}, 97%). Elemental analysis ($C_{18}H_{18}N_2O_3$, %) found C 69.49, H 5.87, N 8.84; calcd. C 69.66, H 5.85, N 9.03. ^{1}H NMR (298 K, 300 MHz, $CDCl_3$): δ = 10.93 & 9.60 (0.6 & 0.3H, s, –NH), 8.61 (1H, d^3, *J* = 4.5 Hz, 6-PyH), 8.19 & 7.96 (0.6 & 0.4H, d^3, *J* = 13.8 Hz, =CH), 7.73 (1H, dt^3, *J* = 7.64, *J* = 0.9 Hz, 4-PyH), 7.57 (1H, d^3, *J* = 7.0 Hz, 5-PyH), 7.46–7.24 (6H, m, 3-PyH & 2-, 3-, 4-, 5-, & 6-PhH), 4.75 (2H, d^3, *J* = 6.2 Hz, 2-Py-CH_2), 4.00 (2H, q^3, *J* = 6.9 Hz, O=C–O–CH_2), 0.91 (3H, t^3, *J* = 7.0 Hz, O=C–O–CH_2–CH_3) ppm. MS (EI, pos.) *m/z* (%): 310 ($C_{18}H_{18}N_2O_3$, 30), 93 (C_6H_6N, 100). IR: *v* = 3223 (w, NH), 1676 (s, C=O), 1618 (s, C=O) cm^{-1}.

HL6. 2-Picolylamine (2.3 mL, 0.022 mol) was diluted in MeOH (5 mL) and methoxymethylenmethylacetoacetate (4.18 g, 0.026 mol) was added. The yellow solution was heated to reflux for 1 h. After cooling to RT the solvent was removed under reduced pressure yielding an orange oil. After 1 week at −28 °C the now orange solid was suspended in ice-cold diethyl ether (5 mL), filtered, and washed with ice-cold diethyl ether (10 mL). Yield: 2.43 g

(234.25 g mol^{-1}, 47%). Elemental analysis ($C_{12}H_{14}N_2O_3$, %) found C 61.53, H 6.05, N 12.05; calcd. C 61.53, H 6.02, N 11.96. ^{1}H NMR (298 K, 300 Hz, $CDCl_3$): δ = 11.42 (1H, s, –NH), 8.61 (1H, d^3, *J* = 4.2 Hz, 6-PyH), 8.14 (1H, d^3, *J* = 13.4 Hz, =CH), 7.75 (1H, dt^3, *J* = 7.74, *J* = 1.2 Hz, 4-PyH), 7.28 (2H, m, 5- & 3-PyH), 4.69 (2H, d^3, *J* = 6.2 Hz, 2-Py-CH_2), 3.72 (3H, s, O=C–O–CH_3), 2.49 (3H, s, O=C–CH_3) ppm. MS (EI, pos.) *m/z* (%): 234 ($C_{12}H_{14}N_2O_3$, 20), 93 (C_6H_6N, 100). IR: *v* = 3225 (w, NH), 1695 (s, C=O), 1638 (s, C=O) cm^{-1}.

General procedure for the synthesis of the Cu(II) complexes

1 g of the corresponding ligand, $CuSO_4$ (1.2 eq.), and sodium methoxide (1.2 eq.) were dissolved in MeOH (100 mL) under argon atmosphere and heated to reflux for 1 h, resulting in a dark blue solution. After cooling to RT the excess of $CuSO_4$ and sodium methoxide was removed by filtration. All further reactions were carried out in air. 20 mL of the dark blue solution were taken and the Cu(II) complexes were precipitated with an aqueous solution of the corresponding sodium or potassium salt of the anion (4 eq. in 20 mL). If no precipitate occurred, the solvent was removed under reduced pressure until a solid could be isolated. This solid was washed with water and MeOH and dried in air.

[(μ-1,1-OAc)$_2$(CuL1)$_2$] (1-OAc). Yield: 0.15 g blue powder (739.73 g mol^{-1}, 25%). Elemental analysis ($C_{30}H_{36}Cu_2N_4O_{10}\cdot H_2O$, %) found C 47.39, H 5.42, N 7.35; calcd. C 47.55, H 5.09, N 7.39. MS (EI, pos.) *m/z* (%): 369 ($C_{15}H_{18}CuN_2O_5$, 1), 309 ($C_{13}H_{15}CuN_2O_3$, 10), 248 ($C_{13}H_{15}N_2O_3$, 14), 93 (C_6H_6N, 46). IR: *v* = 1684 (s, C=O), 1601 (s, C=O) cm^{-1}.

[(μ-1,1-NO$_3$)(μ-1,3-NO$_3$)(CuL1)$_2$] (1-NO$_3$). Yield: 0.22 g dark blue crystalline powder (745.65 g mol^{-1}, 37%). Elemental analysis ($C_{26}H_{30}Cu_2N_6O_{12}$, %) found C 41.94, H 3.93, N 10.93; calcd. C 41.88, H 4.06, N 11.27. MS (EI, pos.) *m/z* (%): 372 ($C_{13}H_{15}CuN_3O_6$, 4), 309 ($C_{13}H_{15}CuN_2O_3$, 32), 248 ($C_{13}H_{15}N_2O_3$, 14), 93 (C_6H_6N, 100). IR: *v* = 1690 (s, C=O), 1608 (s, C=O) cm^{-1}.

[(μ-Cl)$_2$(CuL1)$_2$] (1-Cl). Yield: 0.20 g green, crystalline powder (692.54 g mol^{-1}, 36%). Elemental analysis ($C_{26}H_{30}Cl_2Cu_2N_4O_6$, %) found C 45.06, H 4.63, N 8.09; calcd. C 45.09, H 4.37, N 8.09. MS (EI, pos.) *m/z* (%): 345 ($C_{15}H_{18}ClCuN_2O_3$, 6), 309 ($C_{13}H_{15}CuN_2O_3$, 33), 248 ($C_{13}H_{15}N_2O_3$, 14), 93 (C_6H_6N, 100). IR: *v* = 1684 (s, C=O), 1606 (s, C=O) cm^{-1}.

[(μ-1,3-NCS)(CuL1)]$_n$ (1-NCS). Yield: 0.27 g dark green powder (368.90 g mol^{-1}, 91%). Elemental analysis ($C_{14}H_{15}CuN_3O_3S$, %) found C 41.94, H 3.93, N 10.93; calcd. C 41.88, H

4.06, N 11.27. MS (EI, pos.) *m/z* (%): 368 ($C_{14}H_{15}CuN_3O_3S$, 3), 309 ($C_{13}H_{15}CuN_2O_3$, 6), 248 ($C_{13}H_{15}N_2O_3$, 8), 93 (C_6H_6N, 100). IR: *v* = 2090 (s, NCS), 1668 (s, C=O), 1614 (s, C=O) cm^{-1}.

[CuL2(OAc)]·2H₂O (2-OAc). Yield: 0.09 g blue powder (375.87 g mol^{-1}, 26%). Elemental analysis ($C_{14}H_{16}CuN_2O_4 \cdot 2H_2O$, %) found C 45.24, H 5.31, N 7.42; calcd. C 44.74, H 5.36, N 7.45. MS (EI, pos.) *m/z* (%): 218 ($C_{12}H_{13}N_2O_2$, 93), 93 (C_6H_6N, 100). IR: *v* = 3366 (wb, OH), 1643 (s, C=O), 1615 (s, C=O) cm^{-1}.

[CuL2(NO₃)(H₂O)]·H₂O (2-NO₃). Yield: 0.22 g dark green, crystalline powder (378.83 g mol^{-1}, 64%). Elemental analysis ($C_{12}H_{15}CuN_3O_6 \cdot H_2O$, %) found C 37.68, H 4.71, N 11.10; calcd. C 38.05, H 4.52, N 11.09. MS (EI, pos.) *m/z* (%): 279 ($C_{12}H_{13}CuN_2O_2$, 19), 216 ($C_{12}H_{13}N_2O_2$, 45), 93 (C_6H_6N, 100). IR: *v* = 3445 (wb, OH), 3084 (wb, OH), 1615 (s, C=O), 1578 (s, C=O) cm^{-1}.

[(μ-Cl)₂(CuL2)₂] (2-Cl). Yield: 0.17 g dark green powder (632.49 g mol^{-1}, 30%). Elemental analysis ($C_{24}H_{26}Cl_2Cu_2N_4O_4$, %) found C 45.68, H 4.19, N 8.84; calcd. C 45.58, H 4.14, N 8.86. MS (EI, pos.) *m/z* (%): 279 ($C_{12}H_{13}ClCuN_2O_2$, 10), 218 ($C_{12}H_{13}N_2O_2$, 46), 93 (C_6H_6N, 100). IR: *v* = 1647 (s, C=O), 1613 (s, C=O) cm^{-1}.

[CuL2(NCS)]·0.5H₂O (2-NCS). Yield: 0.22 g green, crystalline powder (346.87 g mol^{-1}, 69%). Elemental analysis ($C_{13}H_{13}CuN_3O_2S \cdot 0.5H_2O$, %) found C 44.91, H 3.71, N 12.19; calcd. C 44.88, H 4.06, N 12.08. MS (EI, pos.) *m/z* (%): 338 ($C_{13}H_{13}CuN_3O_2S$, 1), 216 ($C_{13}H_{13}N_3O_2$, 50), 93 (C_6H_6N, 100). IR: *v* = 2076 (s, NCS), 1650 (s, C=O), 1595 (s, C=O) cm^{-1}.

[(μ-1,1-OAc)₂(CuL3)₂]·2H₂O (3-OAc). Yield: 0.09 g dark blue, crystalline powder (835.81 g mol^{-1}, 15%). Elemental analysis ($C_{32}H_{40}Cu_2N_4O_{12} \cdot 2H_2O$, %) found C 45.90, H 6.68, N 5.47; calcd. C 45.99, H 6.70, N 5.31. MS (EI, pos.) *m/z* (%): 339 ($C_{14}H_{17}CuN_2O_4$, 17), ($C_{14}H_{17}N_2O_4$, 26), 232 ($C_{12}H_{12}N_2O_3$, 53). IR: *v* = 1690 (s, C=O), 1608 (s, C=O) cm^{-1}.

[CuL3(NO₃)] (3-NO₃). Yield: 0.08 g dark blue, crystalline powder (402.85 g mol^{-1}, 28%). Elemental analysis ($C_{14}H_{17}CuN_3O_7$, %) found C 41.80, H 3.91, N 10.45; calcd. C 41.74, H 4.25, N 10.43. MS (EI, pos.) *m/z* (%): 402 ($C_{14}H_{17}CuN_3O_7$, 8), 339 ($C_{14}H_{17}CuN_2O_4$, 23), 232 ($C_{12}H_{12}N_2O_3$, 72), 93 (C_6H_6N, 100). IR: *v* = 1654 (s, C=O), 1618 (s, C=O) cm^{-1}.

[(μ-Cl)₂(CuL3)₂] (3-Cl). Yield: 0.17 g green needles (752.60 g mol^{-1}, 32%), Elemental analysis ($C_{28}H_{34}Cl_2Cu_2N_4O_8$, %) found C 44.54, H 4.60, N 7.47; calcd. C 44.69, H 4.55, N 7.44. MS

(EI, pos.) *m/z* (%): 375 ($C_{14}H_{17}ClCuN_2O_4$, 12), 339 ($C_{14}H_{17}CuN_2O_4$, 15), 232 ($C_{12}H_{12}N_2O_3$, 56), 93 (C_6H_6N, 100). IR: ν = 1685 (s, C=O), 1623 (s, C=O) cm^{-1}.

[CuL3NCS]·1.5H$_2$O (3-NCS). Yield: 0.18 g green, crystalline powder (425.95 g mol^{-1}, 59%). Elemental analysis ($C_{15}H_{17}CuN_3O_4S·1.5H_2O$, %) found C 42.46, H 4.46, N 10.28; calcd. C 42.30, H 4.73, N 9.87. MS (EI, pos.) *m/z* (%): 398 ($C_{15}H_{17}CuN_3O_4S$, 1), 341 ($C_{14}H_{17}CuN_2O_4$, 2), 278 ($C_{15}H_{17}N_2O_4$, 20), 93 (C_6H_6N, 100). IR: ν = 2092 (s, NCS), 1674 (s, C=O), 1604 (s, C=O) cm^{-1}.

[(CuL4)(OAc)]$_n$ (4-OAc). Yield: 0.1 g dark green, crystalline powder (352.84 g mol^{-1}, 33%) Elemental analysis ($C_{14}H_{15}CuN_3O_5$, %) found C 47.64, H 4.50, N 12.01; calcd. C 47.66, H 4.29, N 11.91. MS (EI, pos.) *m/z* (%): 353 ($C_{14}H_{15}CuN_3O_4$, 1), 293 ($C_{12}H_{12}CuN_3O_2$, 5), 231 ($C_{12}H_{12}N_3O_2$, 38), 93 (C_6H_6N, 100). IR: ν = 2202 (s, C≡N), 1620 (s, C=O) cm^{-1}.

[(CuL4)(NO$_3$)]$_n$·1.5H$_2$O (4-NO$_3$). Yield: 0.26 g green, crystalline powder (382.82 g mol^{-1}, 79%). Elemental analysis ($C_{12}H_{12}CuN_4O_5·1.5H_2O$, %) found C 38.01, H 4.26, N 14.29; calcd. C 37.65, H 3.95, N 14.64. MS (EI, pos.) *m/z* (%): 355 ($C_{12}H_{12}CuN_4O_5$, 1), 292 ($C_{12}H_{12}CuN_3O_2$, 3), 231 ($C_{12}H_{12}N_3O_2$, 35), 93 (C_6H_6N, 100). IR: ν = 2223 (s, C≡N), 1636 (s, C=O) cm^{-1}.

[CuL4Cl] (4-Cl). Yield: 0.19 g green needles (329.54 g mol^{-1}, 67%). Elemental analysis ($C_{12}H_{12}ClCuN_3O_2$, %) found C 43.65, H 3.59, N 12.99; calcd. C 43.78, H 3.67, N 12.76. MS (EI, pos.) *m/z* (%): 328 ($C_{12}H_{12}ClCuN_3O_2$, 11), 292 ($C_{12}H_{12}CuN_3O_2$, 8), 231 ($C_{12}H_{12}N_3O_2$, 35), 93 (C_6H_6N, 100). IR: ν = 2201 (s, C≡N), 1627 (s, C=O) cm^{-1}.

[CuL4NCS]·0.5H$_2$O (4-NCS). Yield: 0.24 g green crystalline powder (360.88 g mol^{-1}, 78%). Elemental analysis ($C_{13}H_{12}CuN_4O_2S·0.5H_2O$) found C 43.09, H 3.49, N 15.49; calcd. C 43.27, H 3.63, N 15.53. MS (EI, pos.) *m/z* (%): 231 ($C_{12}H_{12}N_3O_2$, 35), 93 (C_6H_6N, 100). IR: ν = 2207 (s, C≡N), 2091 (NCS), 1636 (s, C=O) cm^{-1}.

[CuL5(OAc)] (5-OAc). Yield: 0.24 g dark blue powder (449.95 g mol^{-1}, 53%). Elemental analysis ($C_{20}H_{20}CuN_2O_5 ·H_2O$, %) found C 53.42, H 4.56, N 6.19; calcd. C 53.39, H 4.93, N 6.23. MS (ES, pos.) *m/z* (%): 310 ($C_{18}H_{17}N_2O_3$, 11), 93 (C_6H_6N, 75). IR: ν = 1691 (s, C=O), 1602 (s, C=O) cm^{-1}.

[(μ-1,1-NO$_3$)$_2$(CuL5)$_2$] (5-NO$_3$). 0.18 g dark blue, crystalline powder (869.79 g mol^{-1}, 32%). Elemental analysis ($C_{36}H_{34}Cu_2N_6O_{12}$, %) found C 49.77, H 4.31, N 9.37; calcd. C 49.71, H

3.94, N 9.66. MS (EI, pos.) *m/z* (%): 434 ($C_{18}H_{17}CuN_3O_6$, 1), 371 ($C_{18}H_{17}CuN_2O_3$, 5), 308 ($C_{18}H_{17}N_2O_3$, 18). IR: *v* = 1673 (s, C=O), 1605 (s, C=O) cm^{-1}.

[(μ-Cl)(CuL5)]$_n$ (5-Cl). Yield: 0.18 g dark green, crystalline powder (408.34 g mol^{-1}, 69%). Elemental analysis ($C_{18}H_{17}ClCuN_2O_3$, %) found C 52.84, H 4.19, N 6.86; calcd. C 52.94, H 4.20, N 6.86. MS (EI, pos.) *m/z* (%): 310 ($C_{18}H_{17}N_2O_3$, 29), 205 ($C_{11}H_{12}N_2O_2$, 42), 93 (C_6H_6N, 100). IR: *v* = 1693 (s, C=O), 1613 (s, C=O) cm^{-1}.

[(μ-I)$_2$(CuL5)$_2$] (5-I). Yield: 0.2 g dark green needles (999.60 g mol^{-1}, 32%). Elemental analysis ($C_{36}H_{34}Cu_2I_2N_4O_6$, %) found C 43.38, H 3.70, N 5.62; calcd. C 43.26, H 3.43, N 5.61. MS (EI, pos.) *m/z* (%): 308 ($C_{18}H_{17}N_2O_3$, 20), 93 (C_6H_6N, 100). IR: *v* = 1673 (s, C=O), 1613 (s, C=O) cm^{-1}.

[CuL5(NCS)]·0.5H$_2$O (5-NCS). Yield: 0.21 g blue-green powder (439.98 g mol^{-1}, 75%). Elemental analysis ($C_{19}H_{17}CuN_3O_3S\cdot 0.5H_2O$, %) found C 52.05, H 3.87, N 9.70; calcd. C 51.87, H 4.12, N 9.55. MS (EI, pos.) *m/z* (%): 308 ($C_{18}H_{17}N_2O_3$, 40), 93 (C_6H_6N, 100). IR: *v* = 2094 (s, NCS), 1671 (s, C=O), 1610 (s, C=O) cm^{-1}.

[(μ-1,1-OAc)$_2$(CuL6)$_2$]·4H$_2$O (6-OAc). Yield: 0.09 g dark blue, crystalline powder (783.73 g mol^{-1}, 14%). Elemental analysis ($C_{28}H_{32}Cu_2N_4O_{10}\cdot 4H_2O$, %) found C 43.15, H 5.23, N 7.34; calcd. C 42.91, H 5.14, N 7.15. MS (ES, pos.) *m/z* (%): 234 ($C_{12}H_{13}N_2O_3$, 27), 93 (C_6H_6N, 93). IR: *v* = 3533 (w, OH), 3397 (wb, OH), 1682 (s, C=O), 1616 (s, C=O) cm^{-1}.

[CuL6(NO$_3$)]·0.5MeOH (6-NO$_3$). Yield: 0.21 g dark blue, crystalline powder (374.60 g mol^{-1}, 66%). Elemental analysis ($C_{12}H_{13}CuN_3O_6$, %) found C 40.45, H 4.04, N 11.39; calcd. C 40.06, H 4.03, N 11.21. MS (EI, pos.) *m/z* (%): 358 ($C_{12}H_{13}CuN_3O_6$, 5), 295 ($C_{12}H_{13}CuN_2O_3$, 32), 234 ($C_{12}H_{13}N_2O_3$, 22), 93 (C_6H_6N, 100). IR: *v* = 1699 (s, C=O), 1616 (s, C=O) cm^{-1}.

[(μ-Cl)$_2$(CuL6)$_2$] (6-Cl). Yield: 0.19 g green, crystalline powder (664.49 g mol^{-1}, 34%). Elemental analysis ($C_{24}H_{26}Cl_2Cu_2N_4O_6$, %) found C 43.40, H 3.99, N 8.42; calcd. C 43.38, H 3.94, N 8.43. MS (EI, pos.) *m/z* (%): 331 ($C_{12}H_{13}ClCuN_2O_3$, 9), 295 ($C_{12}H_{13}CuN_2O_3$, 37), 234 ($C_{12}H_{13}N_2O_3$, 54), 93 (C_6H_6N, 100). IR: *v* = 1685 (s, C=O), 1613 (s, C=O) cm^{-1}.

[CuL6(NCS)]·0.3H$_2$O (6-NCS). Yield: 0.14 g dark green powder (360.87 g mol^{-1}, 45%). Elemental analysis ($C_{13}H_{13}CuN_3O_3S\cdot 0.3H_2O$, %) found C 42.37, H 3.74, N 11.78; calcd. C

42.56, H 3.94, N 11.45. MS (EI, pos.) *m/z* (%): 234 ($C_{12}H_{13}N_2O_3$, 28), 93 (C_6H_6N, 100). IR: *ν* = 2102 (s, NCS), 1684 (s, C=O), 1619 (s, C=O) cm^{-1}.

X-ray diffraction on single crystals

The X-ray analysis of all crystals was performed with a Stoe StadiVari diffractometer using graphite-monochromated MoKα radiation. The data were corrected for Lorentz and polarization effects. The structures were solved by direct methods (SIR-97)[34] and refined by fullmatrix least-square techniques against Fo^2–Fc^2 (SHELXL-97).[35] All hydrogen atoms were calculated in idealised positions with fixed displacement parameters. ORTEP-III[36] to illustrate molecule packing. CCDC 1566611–1566627 and 1566633–1566641 contain the supplementary crystallographic data for this paper.

Powder X-ray diffraction

Powder diffractograms were measured with a STOE StadiP Powder Diffractometer (STOE, Darmstadt) using Cu[Kα1] radiation with a Ge Monochromator, and a Mythen 1K Stripdetector in transmission geometry.

Magnetic measurements

Magnetic measurements on the compounds were carried out using a SQUID MPMS-XL5 from Quantum Design with an applied field of 5000 G, and in the temperature range from 300 to 50 K (or 2 K). The sample was prepared in a gelatine capsule held in a plastic straw. The raw data were corrected for the diamagnetic part of the sample holder and the diamagnetism of the organic ligand using tabulated Pascal's constants.[11]

6.4 Conclusions

We presented six new tridentate, *NNO* Schiff base-like ligands and their corresponding Cu(II) complexes with varying anions (OAc^-, NO_3^-, Cl^-, I^-, NCS^-, N_3^-, SO_4^{2-}). It was possible to obtain single crystals of four ligands and 22 Cu(II) complexes. The majority of the Cu(II) complexes where a structure was obtained crystallised as μ-bridged dimers with the tridentate

ligands oriented *trans* to each other. Selected complexes were investigated considering their magnetic properties. Most of the dimers have rather small coupling constants which are either ferro- or antiferromagnetic. No correlation between the X-ray structures of the complexes and the nature of the coupling constants could be found. Only compound **1-NO$_3$** has a rather high coupling constant of $J = -129.5(19)$ cm^{-1} compared to the other complexes. This difference can be explained with the bridging mode (type 1) and Cu–X–Cu angle, which is higher for **1-NO$_3$** (143.3(9)°) than it is for the other complexes (<106°). For complex **5-I** with the second smallest coupling constant ($J = -7.36(15)$ cm^{-1}) the largest distortion parameter ($\tau = 0.28$) was determined. Both factors support the overlap between the magnetic orbital of the Cu(II) centres ($d_{x^2-y^2}$) and the p-orbital of the anion, which leads to a greater coupling constant.

Conflicts of interest

There are no conflicts of interest to declare.

Acknowledgements

KD thanks the University Bayreuth Graduate School for financial support.

6.5 Notes and references

[1] (a) E. Coronado, G. Mínguez Espallargas, *Chem. Soc. Rev.* **2013**, *42*, 1525–1539; (b) P. Dechambenoit, J. R. Long, *Chem. Soc. Rev.* **2011**, *40*, 3249–3265; (c) M. Kurmoo, *Chem. Soc. Rev.* **2009**, *38*, 1353–1379; (d) M. Abrantes, A. A. Valente, I. S. Gonçalves, M. Pillinger, C. C. Romão, *J. Mol. Catal. A: Chem.* **2005**, *238*, 51–55; (e) Z. Sun, J. Chen, T. Tu, *Green Chem.* **2017**, *19*, 789–794; (f) T. Kitao, Y. Zhang, S. Kitagawa, B. Wang, T. Uemura, *Chem. Soc. Rev.* **2017**, *46*, 3108–3133.

[2] (a) D. L. Reger, *Comments Inorg. Chem.* **1999**, *21*, 1–28; (b) A. Thakur, D. Mandal, *Coord. Chem. Rev.* **2016**, *329*, 16–52; (c) H. R. Bigmore, S. C. Lawrence, P. Mountford, C. S. Tredget, *Dalton Trans.* **2005**, 635–651; (d) D. Kalden, A. Oberheide, C. Loh, H. Görls, S. Krieck, M. Westerhausen, *Chem. Eur. J.* **2016**, *22*, 10944–10959; (e) R.

García-Rodríguez, D. S. Wright, *Dalton Trans.* **2014**, *43*, 14529–14532; (f) S. Trofimenko, *J. Am. Chem. Soc.* **1966**, *88*, 1842–1844.

[3] W. Phonsri, C. G. Davies, G. N. L. Jameson, B. Moubaraki, J. S. Ward, P. E. Kruger, G. Chastanet, K. S. Murray, *Chem. Commun.* **2017**, *53*, 1374–1377.

[4] (a) H. A. Goodwin, in Spin Crossover in Transition Metal Compounds I-III, ed. P. Gütlich and H. A. Goodwin, Springer Berlin/Heidelberg, **2004**, vol. *233*, pp. 59–90; (b) G. J. Long, F. Grandjean, D. L. Reger, in Spin Crossover in Transition Metal Compounds I-III, ed. P. Gütlich and H. A. Goodwin, Springer Berlin/Heidelberg, **2004**, vol. *233*, pp. 91–122; (c) D. J. Harding, P. Harding, W. Phonsri, *Coord. Chem. Rev.* **2016**, *313*, 38–61; (d) S. Hayami, Y. Shigeyoshi, M. Akita, K. Inoue, K. Kato, K. Osaka, M. Takata, R. Kawajiri, T. Mitani, Y. Maeda, *Angew. Chem., Int. Ed.* **2005**, *44*, 4899–4903; (e) S. Hayami, R. Moriyama, A. Shuto, Y. Maeda, K. Ohta, K. Inoue, *Inorg. Chem.* **2007**, *46*, 7692–7694.

[5] (a) M. Das, S. Chattopadhyay, *J. Mol. Struct.* **2013**, *1051*, 250–258; (b) K. Chattopadhyay, B. K. Shaw, S. K. Saha, D. Ray, *Dalton Trans*. **2016**, *45*, 6928–6938; (c) A. Igashira-Kamiyama, M. Saito, S. Kodera, T. Konno, *Eur. J. Inorg. Chem.* **2016**, 2692–2695.

[6] V. Ovcharenko, S. Fokin, E. Chubakova, G. Romanenko, A. Bogomyakov, Z. Dobrokhotova, N. Lukzen, V. Morozov, M. Petrova, M. Petrova, E. Zueva, I. Rozentsveig, E. Rudyakova, G. Levkovskaya, R. Sagdeev, *Inorg. Chem.* **2016**, *55*, 5853–5861.

[7] J. Ferrando-Soria, J. Vallejo, M. Castellano, J. Martínez-Lillo, E. Pardo, J. Cano, I. Castro, F. Lloret, R. Ruiz-García, M. Julve, *Coord. Chem. Rev.* **2017**, *339*, 17–103.

[8] W. X. C. Oliveira, C. B. Pinheiro, M. M. da Costa, A. P. S. Fontes, W. C. Nunes, F. Lloret, M. Julve, C. L. M. Pereira, *Cryst. Growth Des.* **2016**, *16*, 4094–4107.

[9] (a) M.-C. Dul, E. Pardo, R. Lescouëzec, Y. Journaux, J. Ferrando-Soria, R. Ruiz-García, J. Cano, M. Julve, F. Lloret, D. Cangussu, C. L. M. Pereira, H. O. Stumpf, J. Pasán, C. Ruiz-Pérez, *Coord. Chem. Rev.* **2010**, *254*, 2281–2296; (b) B. Nowicka, T. Korzeniak, O. Stefańczyk, D. Pinkowicz, S. Chorąży, R. Podgajny, B. Sieklucka, *Coord. Chem. Rev.* **2012**, *256*, 1946–1971; (c) J. Mroziński, *Coord. Chem. Rev.* **2005**, *249*, 2534–2548; (d) C. Janiak, *Dalton Trans.* **2003**, 2781.

[10] (a) D. L. Reger, A. E. Pascui, E. A. Foley, M. D. Smith, J. Jezierska, A. Wojciechowska, S. A. Stoian, A. Ozarowski, *Inorg. Chem.* **2017**, *56*, 2884–2901; (b) D. Adner, M. Korb,

C. Lochenie, B. Weber, H. Lang, *Z. Anorg. Allg. Chem.* **2015**, *641*, 1243–1246; (c) T. Glaser, M. Heidemeier, S. Grimme, E. Bill, *Inorg. Chem.* **2004**, *43*, 5192–5194; (d) T. Glaser, M. Heidemeier, J. B. H. Strautmann, H. Bögge, A. Stammler, E. Krickemeyer, R. Huenerbein, S. Grimme, E. Bothe, E. Bill, *Chem. Eur. J.* **2007**, *13*, 9191–9206; (e) B. Weber, E. Kaps, K. Dankhoff, *Z. Anorg. Allg. Chem.* **2017**, *643*, 1593–1599.

[11] O. Kahn, Molecular Magnetism, VCH, New York, N. Y, **1993**.

[12] Z. Fang, J. P. Dürholt, M. Kauer, W. Zhang, C. Lochenie, B. Jee, H. B. Albada, N. Metzler-Nolte, A. Pöppl, B. Weber, M. Muhler, Y. Wang, R. Schmid, R. A. Fischer, B. Albada, *J. Am. Chem. Soc.* **2014**, *136*, 9627–9636.

[13] B. Weber, J. Obel, L. R. Lorenz, W. Bauer, L. Carrella, E. Rentschler, *Eur. J. Inorg. Chem.* **2009**, 5535–5540.

[14] H. van Crawford, H. W. Richardson, J. R. Wasson, D. J. Hodgson, W. E. Hatfield, *Inorg. Chem.* **1976**, *15*, 2107–2110.

[15] M. Friedrich, J. C. Gálvez-Ruiz, T. M. Klapötke, P. Mayer, B. Weber, J. J. Weigand, *Inorg. Chem.* **2005**, *44*, 8044–8052.

[16] A. W. Addison, T. N. Rao, J. Reedijk, J. van Rijn; G. C. Verschoor, *J. Chem. Soc., Dalton Trans.* **1984**, 1349–1356.

[17] M. S. Ray, A. Ghosh, S. Chaudhuri, M. G. B. Drew, J. Ribas, *Eur. J. Inorg. Chem.* **2004**, 3110–3117.

[18] M. S. Ray, A. Ghosh, R. Bhattacharya, G. Mukhopadhyay, M. G. B. Drew, J. Ribas, *Dalton Trans.* **2004**, 252–259.

[19] S. Hazra, A. P. C. Ribeiro, M. F. C. Guedes da Silva, C. A. Nieto de Castro, A. J. L. Pombeiro, *Dalton Trans.* **2016**, *45*, 13957–13968.

[20] (a) E. I. Solomon, D. E. Heppner, E. M. Johnston, J. W. Ginsbach, J. Cirera, M. Qayyum, M. T. Kieber-Emmons, C. H. Kjaergaard, R. G. Hadt, L. Tian, *Chem. Rev.* **2014**, *114*, 3659–3853; (b) C. Citek, S. Herres-Pawlis, T. D. P. Stack, *Acc. Chem. Res.* **2015**, *48*, 2424–2433; (c) J. N. Hamann, B. Herzigkeit, R. Jurgeleit, F. Tuczek, *Coord. Chem. Rev.* **2017**, *334*, 54–66; (d) A. Hoffmann, S. Binder, A. Jesser, R. Haase, U. Flörke, M. Gnida, M. Salomone Stagni, W. Meyer-Klaucke, B. Lebsanft, L. E. Grünig, S. Schneider, M. Hashemi, A. Goos, A. Wetzel, M. Rübhausen, S. Herres-Pawlis, *Angew. Chem.* **2014**, *126*, 305–310; (e) C. Wilfer, P. Liebhäuser, A. Hoffmann, H. Erdmann, O. Grossmann, L. Runtsch, E. Paffenholz, R. Schepper, R. Dick, M. Bauer, M. Dürr, I. Ivanović-Burmazović, S. Herres-Pawlis, *Chem. Eur. J.* **2015**, *21*, 17639–17649.

[21] S. C. Lawrence, B. D. Ward, S. R. Dubberley, C. M. Kozak, P. Mountford, *Chem. Commun.* **2003**, 2880–2881.

[22] C. Santini, M. Pellei, V. Gandin, M. Porchia, F. Tisato, C. Marzano, *Chem. Rev.* **2014**, *114*, 815–862.

[23] C. Lochenie, S. Schlamp, A. P. Railliet, K. Robeyns, B. Weber, Y. Garcia, *CrystEngComm* **2014**, *16*, 6213.

[24] (a) C. Lochenie, K. G. Wagner, M. Karg, B. Weber, *J. Mater. Chem. C* **2015**, *3*, 7925–7935; (b) C. Lochenie, J. Heinz, W. Milius, B. Weber, *Dalton Trans.* **2015**, *44*, 18065–18077.

[25] B. Bleaney, K. D. Bowers, *Proc. R. Soc. London, Ser. A* **1952**, *214*, 451–465.

[26] E. F. Hasty, T. J. Colburn, D. N. Hendrickson, *Inorg. Chem.* **1973**, *12*, 2414–2421.

[27] O. Kahn, J. Galy, Y. Journaux, J. Jaud, I. Morgenstern-Badarau, *J. Am. Chem. Soc.* **1982**, *104*, 2165–2176.

[28] J. Carranza, J. Sletten, F. Lloret, M. Julve, *J. Mol. Struct.* **2008**, *890*, 31–40.

[29] B. Cervera, R. Ruiz, F. Lloret, M. Julve, J. Cano, J. Faus, C. Bois, J. Mrozinski, *J. Chem. Soc., Dalton Trans.* **1997**, 395–402.

[30] H. Grove, J. Sletten, M. Julve, F. Lloret, *J. Chem. Soc., Dalton Trans.* **2001**, 2487–2493.

[31] B. Chiari, J. H. Helms, O. Piovesana, T. Tarantelli, P. F. Zanazzi, *Inorg. Chem.* **1986**, *25*, 2408–2413.

[32] M. S. Ray, A. Ghosh, S. Chaudhuri, M. G. B. Drew, J. Ribas, *Eur. J. Inorg. Chem.* **2004**, 3110–3117.

[33] L. Claisen, *Justus Liebigs Ann. Chem.* **1897**, *297*, 1–98.

[34] A. Altomare, M. C. Burla, M. Camalli, G. L. Cascarano, C. Giacovazzo, A. Guagliardi, A. G. G. Moliterni, G. Polidori, R. Spagna, *J. Appl. Crystallogr.* **1999**, *32*, 115–119.

[35] G. Sheldrick, *Acta Crystallogr., Sect. A: Found. Crystallogr.* **2008**, *64*, 112–122.

[36] (a) C. K. Johnson and M. N. Burnett, ORTEP-III, Oak-Ridge National Laboratory, Oak-Ridge, TN, **1996**; (b) E. Keller, Schakal-99, University of Freiburg, Freiburg, Germany, **1999**.

6.6 Supporting Information

Table S1. Crystallographic data for the ligands and complexes presented in this paper.

	HL1	**HL4**	**HL5**	**HL6**	**1-OAc**	**1-NO_3**	**1-Cl**	**1-I**
CCDC	1566611	1566612	1566613	1566614	1566615	1566619	1566623	1566633
formula	HL1	HL4	HL5	HL6	[(μ–1,1–OAc)$_2$(CuL1)$_2$]	[(μ–1,1–NO_3)(μ–1,3–NO_3)(CuL1)$_2$]	[(μ–Cl)$_2$(CuL1)$_2$]	[(μ–I)$_2$(CuL1)$_2$]
sum formula	$C_{13}H_{16}N_2O_3$	$C_{12}H_{13}N_3O_2$	$C_{18}H_{18}N_3O_3$	$C_{12}H_{14}N_2O_3$	$C_{30}H_{36}Cu_2N_4O_{10}$	$C_{26}H_{30}Cu_2N_6O_{12}$	$C_{26}H_{30}Cl_2Cu_2N_4O_6$	$C_{26}H_{30}I_2Cu_2N_4O_6$
M/ g mol^{-1}	248.28	231.25	310.34	234.25	739.70	745.64	692.54	875.44
crystal system	monoclinic	triclinic	triclinic	monoclinic	monoclinic	monoclinic	triclinic	monoclinic
space group	$P2_1/a$	$P-1$	$P-1$	$C2/c$	$P2_1/c$	$C2/c$	$P-1$	$P2_1/C$
crystal description	colourless block	colourless block	colourless block	colourless block	blue block	blue block	blue block	green block
a/ Å	7.339(5)	6.0280(4)	5.5863(5)	25.029(5)	7.5927(5)	12.7796(5)	7.3859(5)	7.8179(3)
b/ Å	14.815(5)	9.2207(6)	11.6567(11)	4.211(5)	23.9283(12)	13.8977(8)	9.1298(7)	14.6683(6)
c/ Å	11.777(5)	11.3737(7)	13.2094(12)	28.823(5)	8.5927(5)	16.9969(6)	10.3252(7)	13.0905(4)
α/ °	90	74.653(5)	71.808(7)	90	90	90	94.110(6)	90
β/ °	97.495(5)	75.243(5)	79.534(7)	129.016(5)	93.078(5)	105.798(3)	96.016(6)	92.391(3)
γ/ °	90	87.728(5)	77.545(7)	90	90	90	105.895(6)	90
V/ Å^3	1269.5(11)	589.26(7)	791.86(13)	2360(3)	1558.87(16)	2904.7(2)	662.26(8)	1499.85(10)
Z	4	2	2	8	2	4	1	4
ρ_{calcd}/gcm^{-3}	1.299	1.303	1.302	1.319	1.576	1.705	1.736	1.938
μ/ mm^{-1}	0.093	0.092	0.090	0.096	1.428	1.540	1.858	3.522
crystal size/ mm	0.149×0.128×0.230	0.266×0.182×0.137	0.162×0.137×0.362	0.186×0.210×0.203	0.135×0.115×0.097	0.118×0.093×0.088	0.120×0.105×0.093	0.101×0.077×0.063
F(000)	528	244	328	992	764	1528	354	852
T/ K	133(2)	133(2)	133(2)	133(2)	133(2)	133(2)	133(2)	133(2)
λ/ Å	Mo-K$_\alpha$ 0.71073	Mo-K$_\alpha$ 0.71073	Mo-K$_\alpha$ 0.71073	Mo-K$_\alpha$ 0.71073	Mo-K$_\alpha$ 0.71073	Mo-K$_\alpha$ 0.71073	Mo-K$_\alpha$ 0.71073	Mo-K$_\alpha$ 0.71073
Θ range/ °	1.7-28.0	1.92–28.42	1.9-28.1	1.7-28.0	1.70–27.98	2.22–26.62	2.00–28.40	2.08–27.62
Reflns. collected	7264	6744	6984	7104	3530	9232	6277	3516
Indep. reflns.(R_{int})	2852 (0.112)	2762 (0.031)	3448 (0.037)	2682 (0.083)	2653 (0.0403)	3429 (0.0237)	3054 (0.0820)	2940 (0.0314)
Parameters	163	154	208	154	208	210	181	181
$R1$ (all data)	0.0757	0.0421 (0.0560)	0.0512	0.0620	0.0307 (0.0483)	0.0251 (0.0335)	0.0609 (0.0701)	0.0205 (0.0273)
$wR2$	0.2103	0.1172	0.1397	0.2176	0.0618	0.0766	0.1742	0.0458
GooF	0.92	1.029	0.96	1.04	0.909	1.076	1.069	0.936

Table S1 (continued). Crystallographic data for the ligands and complexes presented in this paper.

	1-NCS	**1-N_3**	**2-NO_3**	**2-Cl**	**2-NCS**	**2-N_3**	**2-SO_4**	**3-OAc**
CCDC	1566635	1566638	1566620	1566624	1566636	1566639	1566640	1566616
formula	[(μ–1,3–NCS)(CuL1)]$_n$	[(μ–1,1–N_3)$_2$(CuL1)$_2$]	[CuL2(NO_3)(H_2O)]·H_2O	[(μ–Cl)$_2$(CuL2)$_2$]	[CuL2(SCN)(MeOH)]	[(μ–1,1–N_3)$_2$(CuL2)$_2$]	[(CuL2)$_2SO_4$]·MeOH	[(μ–1,1–OAc)$_2$(CuL3)$_2$]
sum formula	$C_{14}H_{15}CuN_3O_3S$	$C_{26}H_{30}Cu_2N_{10}O_6$	$C_{12}H_{15}CuN_3O_6$, H_2O	$C_{24}H_{26}Cl_2Cu_2N_4O_4$	$C_{14}H_{17}CuN_3O_3S$	$C_{24}H_{26}Cu_2N_{10}O_4$, 2($H_2O$)	$C_{25}H_{30}Cu_2N_4O_9S$, CH_4O	$C_{32}H_{40}Cu_2N_4O_{10}$, 2($H_2O$)
M/ g mol^{-1}	368.89	705.68	378.82	632.46	370.90	681.66	721.71	835.78
crystal system	monoclinic	monoclinic	monoclinic	triclinic	monoclinic	triclinic	monoclinic	triclinic
space group	$P2_1/n$	$C2/c$	$P2_1/c$	$P-1$	$P2_1/n$	$P-1$	$P2_1/c$	$P-1$
crystal description	blue block	blue needle	blue hexagon	blue block	blue block	blue block	blue green block	blue block
a/ Å	5.9027(5)	20.5772(11)	8.7846(4)	7.6352(5)	9.8474(5)	7.3993(4)	12.7600(18)	8.8660(6)
b/ Å	16.4411(12)	19.5249(15)	18.8515(6)	9.0924(6)	15.5449(6)	9.3862(5)	16.897(3)	8.8511(6)
c/ Å	15.7542(13)	7.1596(4)	9.0280(4)	9.5031(6)	10.2348(6)	10.6959(5)	13.781(2)	12.7620(8)
α/ °	90	90	90	91.652(5)	90	105.369(4)	90	94.241(5)
β/ °	98.344(6)	94.083(4)	99.363(3)	98.150(5)	92.590(4)	99.166(4)	102.639(11)	104.942(5)
γ/ °	90	90	90	107.858(5)	90	97.860(4)	90	108.277(5)
V/ Å^3	1512.7(2)	2869.2(3)	1475.14(11)	619.77(7)	1565.11(14)	694.52(6)	2899.3(7)	905.63(11)
Z	4	4	4	1	4	1	4	1
ρ_{calcd}/ g cm^{-3}	1.620	1.634	1.706	1.695	1.574	1.630	1.653	1.532
μ/ mm^{-1}	1.597	1.543	1.523	1.971	1.544	1.590	1.603	1.247
crystal size/ mm	0.112×0.051×0.045	0.145×0.071×0.068	0.145×0.103×0.096	0.124×0.074×0.043	0.155×0.102×0.067	0.098×0.091×0.059	0.170×0.115×0.114	0.169×0.107×0.080
F(000)	756	1448	780	322	764	350	1488	434
T/ K	133(2)	133(2)	133(2)	133(2)	133(2)	133(2)	133(2)	133(2)
λ/ Å	Mo-K$_\alpha$ 0.71073	Mo-K$_\alpha$ 0.71073	Mo-K$_\alpha$ 0.71073	Mo-K$_\alpha$ 0.71073	Mo-K$_\alpha$ 0.71073	Mo-K$_\alpha$ 0.71073	Mo-K$_\alpha$ 0.71073	Mo-K$_\alpha$ 0.71073
Θ range/ °	1.82–28.49	1.99–28.36	2.16–27.65	2.17–28.08	2.39–28.46	2.02–26.62	1.76–26.00	1.68–26.61
Reflns. collected	3520	3421	3572	2769	3689	3289	6861	4267
Indep. reflns.(R_{int})	2615 (0.0386)	2681 (0.0335)	3105 (0.0452)	2197 (0.0792)	3020 (0.1146)	2967 (0.0168)	4686 (0.0615)	3604 (0.0366)
Parameters	199	199	224	163	200	190	390	243
$R1$ (all data)	0.0313 (0.0517)	0.0277 (0.0413)	0.0250 (0.0311)	0.0454 (0.0563)	0.0746 (0.0659)	0.0256 (0.0294)	0.0468 (0.0742)	0.0309 (0.0397)
$wR2$	0.0632	0.0606	0.0639	0.1123	0.1957	0.0672	0.1030	0.0867
GooF	0.894	0.934	1.030	0.962	1.067	1.084	0.909	1.140

Table S1 (continued). Crystallographic data for the ligands and complexes presented in this paper.

	3-Cl	**3-SO_4**	**4-OAc**	**4-NO_3**	**5-NO_3**	**5-Cl**	**5-I**
CCDC	1566625	1566641	1566617	1566621	1566622	1566626	1566634
formula	$[CuL3Cl]_2$	$[(CuL3)_2SO_4]\cdot MeOH\cdot H_2O$	$[CuL4(OAc)]_n$	$\{[CuL4(H_2O)]\cdot NO_3\cdot H_2O\}_n$	$[(\mu$–1,1–$NO_3)_2(CuL5)_2]$	$[(\mu$–Cl)$(CuL5)]_n$	$[(\mu$–I$)_2(CuL5)_2]$
sum formula	$C_{28}H_{34}Cl_2Cu_2N_4O_8$	$C_{28}H_{34}Cu_2N_4O_{10}S$, CH_4O, H_2O	$C_{14}H_{15}CuN_3O_4$, $7(H_2O)$	$C_{12}H_{14}CuN_3O_3$, NO_3, H_2O	$C_{36}H_{34}Cu_2N_6O_{12}$	$C_{18}H_{17}ClCuN_2O_3$	$C_{36}H_{34}Cu_2I_2N_4O_6$
M/ g mol^{-1}	752.56	827.81	478.94	391.83	869.76	408.32	999.55
crystal system	monoclinic	triclinic	monoclinic	monoclinic	monoclinic	monoclinic	monoclinic
space group	$P2_1/n$	$P-1$	$P2_1/c$	$P2_1/c$	$P2_1/n$	Cc	$P2_1/n$
crystal description	green block	purple plate	blue plate	blue block	blue block	green block	green plate
a/ Å	10.9871(5)	6.7842(6)	6.8193(4)	9.0597(6)	10.2653(4)	12.9059(7)	10.3415(7)
b/ Å	20.1512(12)	15.8946(15)	11.6812(6)	14.5372(7)	8.8823(4)	18.9389(13)	9.2060(4)
c/ Å	13.9510(6)	15.9754(18)	28.7206(16)	11.8354(8)	20.2634(9)	7.6909(4)	19.3186(14)
α/ °	90	93.458(9)	90	90	90	90	90
β/ °	94.232(3)	96.606(8)	95.047(4)	95.232(5)	97.713(3)	115.017(4)	98.818(5)
γ/ °	90	97.754(8)	90	90	90	90	90
V/ Å^3	3080.4(3)	1690.5(3)	2278.9(2)	1552.26(7)	1830.89(14)	1703.47(18)	1817.5(2)
Z	8	2	4	4	2	4	2
ρ_{calcd}/ g cm^{-3}	1.623	1.622	1.355	1.677	1.578	1.592	1.826
μ/ mm^{-1}	1.610	1.394	1.012	1.452	1.235	1.459	2.919
crystal size/ mm	0.179×0.112×0.094	0.157×0.095×0.086	0.177×0.158×0.132	0.150×0.109×0.083	0.163×0.136×0.134	0.142×0.110×0.090	0.130×0.102×0.075
F(000)	1544	852	948	804	892	836	980
T/ K	133(2)	133(2)	133(2)	133(2)	133(2)	133(2)	133(2)
λ/ Å	Mo-K_α 0.71073	Mo-K_α 0.71073	Mo-K_α 0.71073	Mo-K_α 0.71073	Mo-K_α 0.71073	Mo-K_α 0.71073	Mo-K_α 0.71073
Θ range/ °	1.78–28.59	1.76–28.26	1.49–26.02	2.23–28.52	2.03–28.45	2.05–28.22	2.12–28.50
Reflns. collected	7232	7952	5514	3688	4324	2498	4329
Indep. reflns.(R_{int})	4234 (0.2943)	4466 (0.2163)	3886 (0.0791)	2876 (0.0312)	3240 (0.0405)	2368 (0.0354)	3384 (0.2146)
Parameters	397	451	262	233	253	226	226
$R1$ (all data)	0.0711 (0.1126)	0.1353 (0.1789)	0.0567 (0.0824)	0.0274 (0.0410)	0.0314 (0.0487)	0.0240 (0.0260)	0.1270 (0.1413)
$wR2$	0.1847	0.3285	0.1517	0.057	0.0687	0.0544	0.3393
GooF	0.956	1.137	0.999	0.906	0.913	1.033 (Flack 0.010(12))	1.372

Table S1 (continued). Crystallographic data for the ligands and complexes presented in this paper.

	6-OAc	**6-Cl**	**6-NCS**
CCDC	1566618	1566627	1566637
formula	$[(\mu\text{–}1,1\text{–}OAc)_2(CuL6)_2]\cdot 4H_2O$	$[(\mu\text{–}Cl)_2(CuL6)_2]$	$[(CuL6)SCN]_2$
sum formula	$C_{28}H_{32}Cu_2N_4O_{10}$, $4(H_2O)$	$C_{24}H_{26}Cl_2Cu_2N_4O_6$	$C_{26}H_{26}Cu_2N_6O_6S_2$
M/ g mol^{-1}	783.72	664.46	709.73
crystal system	orthorhombic	triclinic	monoclinic
space group	*P*bca	$P\bar{1}$	$P2_1/c$
crystal description	blue needle	green block	blue needle
a/ Å	8.7017(4)	7.5941(5)	12.3364(8)
b/ Å	18.0339(11)	9.0685(6)	13.4022(11)
c/ Å	21.7086(12)	10.0399(6)	8.6223(5)
α/ °	90	90.393(5)	90
β/ °	90	96.377(5)	97.437(5)
γ/ °	90	110.150(5)	90
V/ Å^3	3406.6(3)	644.33(7)	1413.57(17)
Z	4	1	2
ρ_{calcd}/ g cm^{-3}	1.528	1.712	1.668
μ/ mm^{-1}	1.320	1.906	1.705
crystal size/ mm	0.198×0.049×0.048	0.130×0.105×0.082	0.176×0.057×0.051
F(000)	1624	338	724
T/ K	133(2)	133(2)	133(2)
λ/ Å	Mo-K_α 0.71073	Mo-K_α 0.71073	Mo-K_α 0.71073
Θ range/ °	1.88–28.46	2.05–28.44	2.26–27.48
Reflns. collected	4130	3031	3338
Indep. reflns.(R_{int})	1910 (0.0705)	2347 (0.0786)	1756 (0.0997)
Parameters	233	172	190
$R1$ (all data)	0.0343 (0.0985)	0.0470 (0.0606)	0.0551 (0.1126)
$wR2$	0.0531	0.1161	0.1208
GooF	0.728	0.942	0.857

Fig. S1. ORTEP drawings of ligands **HL1** (top left), **HL4** (top right), **HL5** (bottom left), and **HL6** (bottom right). Ellipsoids were drawn at 50 % probability level.

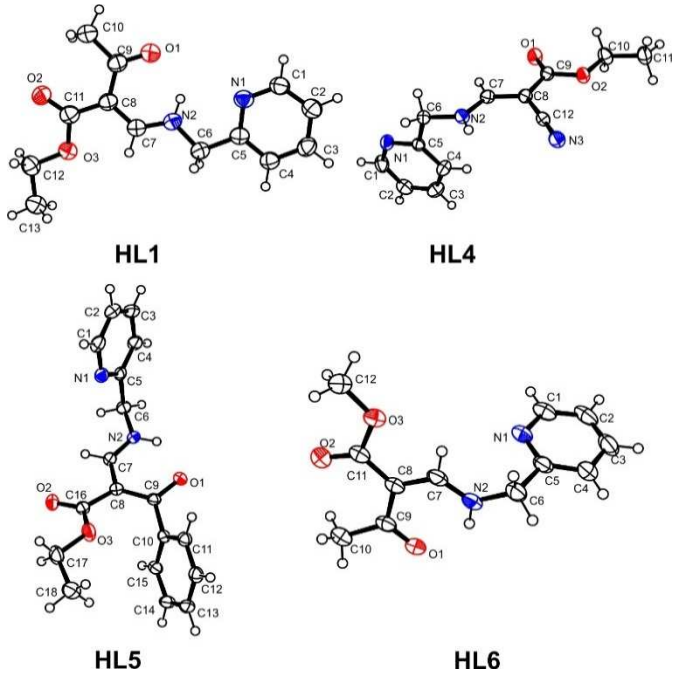

Table S2. Selected bond lengths / Å of the ligands **HL1**, **HL4**, **HL5**, and **HL6**.

	HL1	**HL4**	**HL5**	**HL6**
N2–C7	1.310(5)	1.3147(17)	1.312(2)	1.305(6)
C7–C8	1.391(4)	1.3805(18)	1.392(3)	1.391(4)
C8–C9	1.453(5)	1.4570(18)	1.442(3)	1.451(5)
C9–O1	1.243(4)	1.2155(16)	1.246(2)	1.245(4)

Fig. S2. ORTEP drawings of **1-Cl** (top left), **1-I** (top centre), **1-OAc** (top right), **1-NCS** (middle left), **2-N_3** (middle centre), **2-Cl** (middle right), **2-NO_3** (bottom left), **3-SO_4** (bottom centre), and **4-OAc** (bottom right). Ellipsoids are drawn at 50 % probability level. Hydrogen atoms and solvent molecules (**2-N_3**, **3-SO_4**, and **4-OAc**) were omitted for clarity.

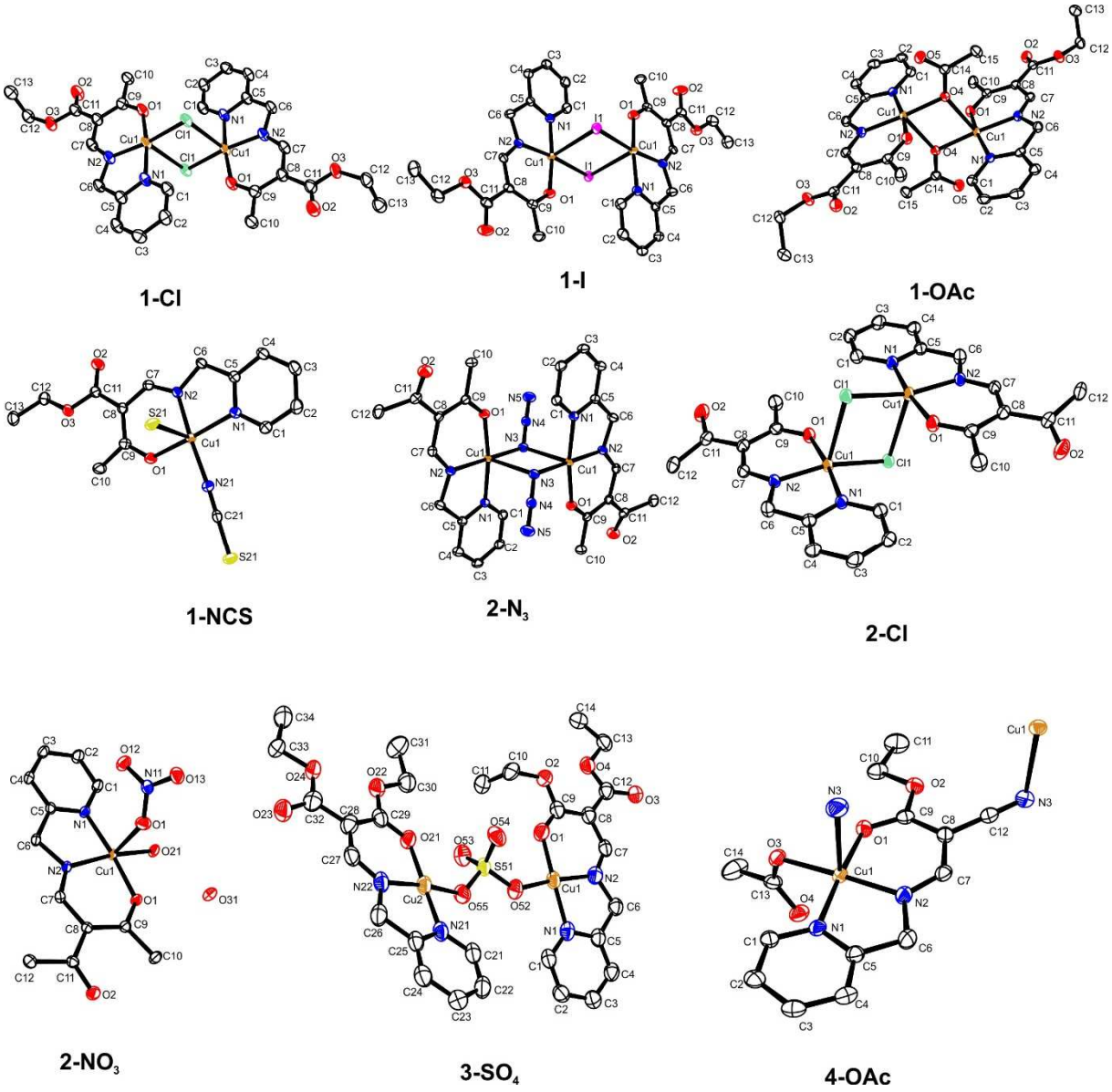

Fig. S3. ORTEP drawings of **5-NO$_3$** (top left), **5-I** (top right), **6-OAc** (bottom left), and **6-Cl** (bottom right). Ellipsoids are drawn at 50 % probability level. Hydrogen atoms and solvent molecules (**6-OAc**) were omitted for clarity.

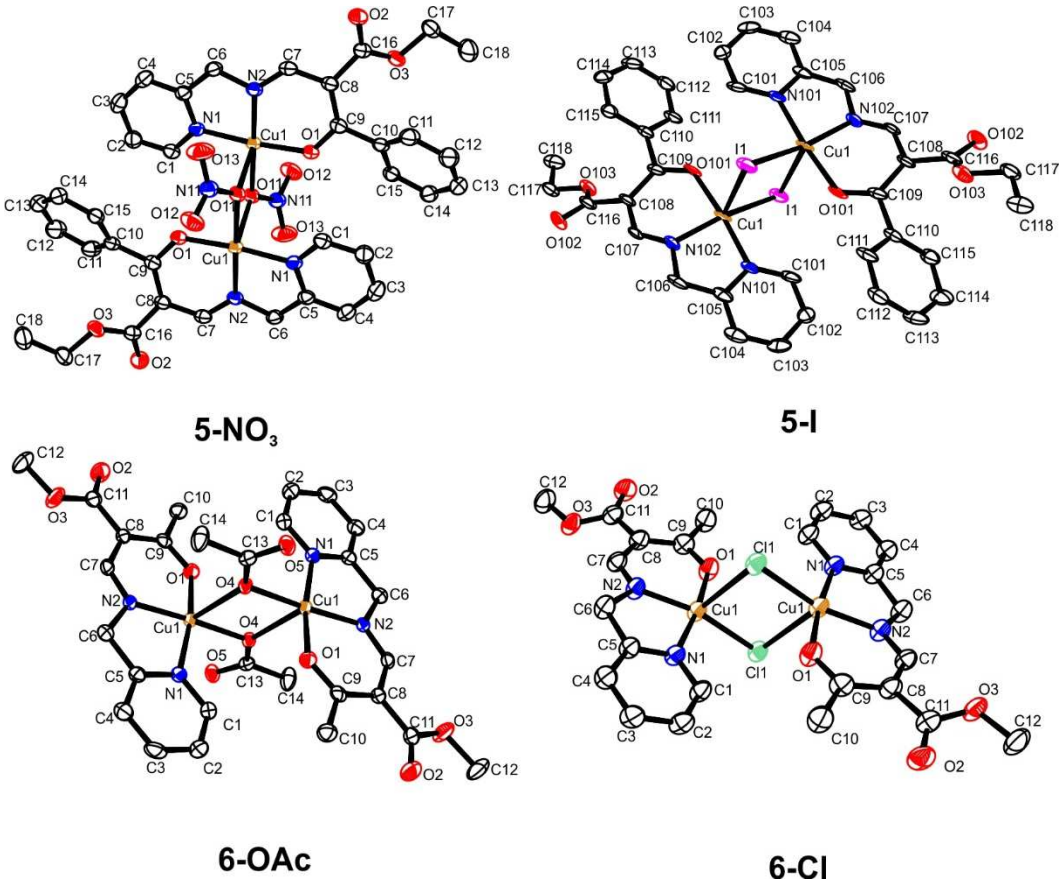

Table S3. Bond lengths/Å and angles/° of the coordination sphere of the complexes discussed in this work.

	Cu–N_{py}	Cu–N	Cu–O	Cu–X	Cu–Y	Cu–X–Cu	X–Cu–X
1-OAc	2.0052(17)	1.9255(16)	1.9411(17)	1.9549(15) 2.3542(14)	/	102.65(6)	77.35(5)
1-NO_3	1.9883(16)	1.9130(14)	1.9245(13)	2.3258(14) 2.6745(14)	/	143.39(9) 137.40(12) 121.7(2) (O–N–O)	84.54(6)
1-Cl	2.014(3)	1.925(4)	1.938(3)	2.2786(11) 2.7766(12)	/	92.81(4)	97.19(4)
1-I	2.001(2)	1.9296(18)	1.9189(18)	2.6187(4) 3.2212(4)	/	82.48(1)	97.52(1)
1-N_3	1.9918(16)	1.9278(17)	1.9103(14)	1.9745(17) 2.6005(15)	/	95.45(6)	84.55(6)
1-NCS	1.9995(18)	1.9162(19)	1.9296(16)	1.9420(19) (N) 2.9063(7) (S)	/	/	/
2-NO_3	1.9795(13)	1.9191(13)	1.9136(11)	2.3620(13)	1.9690(12) (H_2O)	/	/
2-Cl	1.999(3)	1.926(3)	1.929(3)	2.2907(9) 2.7953(10)	/	92.79(3)	87.21(3)
2-N_3	1.9973(14)	1.9233(15)	1.9266(12)	1.9868(15) 2.5097(15)	/	96.16(6)	83.84(6)
2-NCS	2.001(3)	1.920(3)	1.936(3)	1.944(4)	2.358(3) (MeOH)	/	/
2-SO_4	1.998(3) 1.990(3)	1.901(3) 1.920(3)	1.910(3) 1.926(3)	1.928(2) 1.955(3)	2.409(3) (Cu2, MeOH)	/	/
3-OAc	2.0084(18)	1.9213(18)	1.9562(15)	1.9436(17) 2.3516(17)	/	104.07(8)	75.93(7)
4-OAc	1.985(3)	1.919(3)	1.950(2)	1.962(2)	2.668(3) (–CN)	/	/
4-NO_3	1.9964(15)	1.9366(15)	1.9725(13)	/	2.2064(14) (H_2O) 1.9828(15) (–CN)	/	/
5-NO_3	1.9764(17)	1.9112(16)	1.9081(14)	1.9836(14) 2.3997(15)	/	104.59(6)	75.41(5)
5-Cl	2.030(3)	1.930(3)	1.944(2)	2.2539(8) 2.8230(9)	/	101.41(3)	102.43(3)
6-OAc	1.996(3)	1.920(3)	1.941(2)	1.9560(18) 2.3814(17)	/	105.93(8)	74.07(7)
6-Cl	2.004(3)	1.926(3)	1.932(2)	2.2844(9) 2.7709(11)	/	93.44(3)	86.56(3)
6-NCS	1.998(4)	1.916(4)	1.944(3)	1.940(5)	2.692(4) (–COOMe)	/	/

Table S4. Summary of the C–H···π / X–Y···π interactions of the ligands and complexes presented in this work.

		C_g	H···C_g/Å Y···C_g/Å	X–H···C_g/° X–Y···C_g/°	X···C_g/Å
HL1	C3–H3	N1–C1–C2–C3–C4–C5[a]	2.96	106	3.345(4)
HL5	C4–H4	C10–C11–C12–C13–C14–C15[b]	2.70	134	3.4289(3)
	C12–H12	N1–C1–C2–C3–C4–C5[c]	2.87	130	3.5592(3)
1-OAc	C6–H6A	Cu1–O1–C9–C8–C7–N2[d]	2.96	104	3.012(2)
1-NO_3	C6–H6A	Cu1–O1–C9–C8–C7–N2[e]	2.62	145	3.4855(18)
	C12–H12B	Cu1–O1–C9–C8–C7–N2[f]	2.59	154	3.513(2)
1-N_3	C12–H12A	N1–C1–C2–C3–C4–C5[g]	2.89	166	3.855(2)
1-NCS	C6–H6B	Cu1–O1–C9–C8–C7–N2[h]	2.65	150	3.549(3)
	C11–O2	N1–C1–C2–C3–C4–C5[h]	3.306(2)	96.01(14)	3.642(3)
2-Cl	C12–H12C	Cu1–O1–C9–C8–C7–N2[i]	2.93	139	3.725(4)
2-N_3	C10–H10B	Cu1–O1–C9–C8–C7–N2[j]	2.73	129	3.424(2)
2-NCS	C10–H10B	N1–C1–C2–C3–C4–C5[k]	2.77	91	2.917(3)
2-SO_4	C20–H20B	N11–C11–C12–C13–C14–C15[l]	2.61	137	3.391(4)
	C20–H20C	Cu2–O31–C39–C38–C37–N32[m]	2.69	118	3.260(4)
	C36–H36B	Cu1–O11–C19–C18–C17–N12[m]	2.70	123	3.349(4)
5-NO_3	C2–H2	C10–C11–C12–C13–C14–C15[n]	2.97	114	3.464(3)
5-Cl	C2–H2	C10–C11–C12–C13–C14–C15[o]	2.85	142	3.641(4)
	C11–H11	N1–C1–C2–C3–C4–C5[p]	2.61	129	3.288(4)
6-OAc	C6–H6A	Cu1–O1–C9–C8–C7–N2[q]	2.82	129	3.526(3)
	C12–H12C	Cu1–O1–C9–C8–C7–N2[r]	2.69	140	3.504(3)
6-NCS	C12–H12B	N1–C1–C2–C3–C4–C5[s]	2.83	130	3.520(7)

a: −1/2+x, 1/2−y, z; b: 2−x, −y, 1−z; c: 1−x, −y, 1−z; d: 2−x, 2−y, 1−z; e: −x, −y, −z; f: 1/2−x, 1/2−y, −z; g: 1/2−x, 1/2−y, 1−z; h: 1−x, −y, 1−z; i: 2−x, 1−y, 3−z; j: 2−x, 2−y, 1−z; k: 1/2−x, −1/2+y, 3/2−z; l: −x, −y, 1−z; m: x, y, z; n: −x, 1−y, 1−z; o: −1/2+x, 1/2+y, −1+z; p: x, −y, 1/2+z; q: 1−x, −y, −z; r: 1−x, 1−y, 1−z; s: 1−x, −1/2+y, −1/2−z.

Table S5. Selected distances and angles of the π–π and M– π interactions of the ligands and complexes presented in this work. $C_g(I)$ is the centroid of the ring number I, α is the dihedral angle between the rings, β is the angle between the vector $C_g(I) \rightarrow C_g(J)$ and the normal to ring I, γ is the angle between the vector $C_g(I) \rightarrow C_g(J)$ and the normal to ring J.

	$C_g(I)$	$C_g(J)$	C_g–C_g/Å	α/°	β/°	γ/°
HL4	N1–C1–C2–C3–C4–C5	N1–C1–C2–C3–C4–C5[a]	3.8849(9)	0.03(7)	19.2	19.2
1-Cl	Cu1–O1–C9–C8–C7–N2	Cu[b]	3.988	0	12.05	0
1-I	Cu1–O1–C9–C8–C7–N2	Cu[c]	3.621	0	17.21	0
1-N_3	Cu1–O1–C9–C8–C7–N2	Cu1–O1–C9–C8–C7–N2[d]	3.9849(9)	0.00(6)	31.4	31.4
	Cu1–O1–C9–C8–C7–N2	Cu[d]	3.505	0	6.47	0
2-NO_3	Cu1–O1–C9–C8–C7–N2	Cu[e]	3.481	0	10.58	0
2-Cl	N1–C1–C2–C3–C4–C5	N1–C1–C2–C3–C4–C5[f]	3.673(2)	0.00(18)	22.9	22.9
	Cu1–O1–C9–C8–C7–N2	N1–C1–C2–C3–C4–C5[g]	3.923(2)	1.75(15)	28.7	27.4
2-N_3	Cu1–O1–C9–C8–C7–N2	Cu1–O1–C9–C8–C7–N2[h]	3.8157(9)	0.02(6)	24.5	24.5
	Cu1–O1–C9–C8–C7–N2	Cu[h]	3.544	0	7.16	0
2-NCS	Cu1–O1–C9–C8–C7–N2	Cu[i]	3.560	0	28.35	0
2-SO_4	Cu1–O11–C19–C18–C17–N12	Cu2–N31–C35–C36–N32[i]	3.3578(19)	14.64(14)	9.8	22.8
	Cu1–O11–C19–C18–C17–N12	Cu1[j]	3.234	0	3.84	0
	N31–C31–C32–C33–C34–C35	Cu1[i]	3.461	0	27.33	0
3-OAc	N1–C1–C2–C3–C4–C5	Cu1–O1–C9–C8–C7–N2[k]	3.7700(14)	10.90(11)	30.5	21.4
4-NO_3	N1–C1–C2–C3–C4–C5	Cu[l]	3.823	0	19.87	0
5-NO_3	Cu1–N1–C5–C6–N2	N1–C1–C2–C3–C4–C5[m]	3.5718(11)	1.19(9)	10.2	9.5
5-Cl	Cu1–O1–C9–C8–C7–N2	Cu1–O1–C9–C8–C7–N2[n]	3.8568(17)	11.24(13)	27.7	25.8
	Cu1–O1–C9–C8–C7–N2	Cu[n]	3.493	0	2.29	0
6-NCS	N1–C1–C2–C3–C4–C5	N1–C1–C2–C3–C4–C5[o]	3.599(3)	0.0(2)	25.9	25.9

a: −x, −y, 1−z; b: −x, −y, 1−z; c: 2−x, 1−y, 1−z; d: 1/2−x, 1/2−y, 1−z; e: 1−x, −y, 1−z; f: 1−x, −y, 2−z; g: 2−x, 1−y, 2−z; h: 2−x, 2−y, 1−z; i: x, y, z; j: −x, −y, 1−z; k: 1−x, −y, 1−z; l: −x, −y, 1−z; m: −x, −y, 1−z; n: x, −y, 1/2+z; o: −x, −y, −1−z.

Table S6. Hydrogen bonds and angles of ligands and complexes presented in this work.

	Donor	Acceptor	D–H/Å	H···A/Å	D···A/Å	D–H···A/°
HL1	N2–H2	O1	0.88	1.98	2.622(4)	129
	N2–H2	N1	0.88	2.28	2.677(5)	107
	C2–H2A	O1[a]	0.95	2.53	3.236(5)	131
	C4–H4	O2[b]	0.95	2.44	3.266(5)	145
HL4	N2–H2A	N3[c]	0.88	2.14	2.9884(16)	162
	C4–H4	N2	0.95	2.56	2.884(2)	100
	C6–H6A	O1[d]	0.99	2.48	3.2701(16)	137
	C7–H7	O1[d]	0.95	2.38	3.2656(17)	155
HL5	N2–H2A	O1	0.88	2.04	2.6730(3)	128
	N2–H2A	O1[e]	0.88	2.24	2.9878(3)	143
	C2–H2B	O2[f]	0.95	2.46	3.3505(3)	156
	C11–H11	O1[g]	0.95	2.48	3.4256(3)	172
HL6	N2–H2	O1	0.88	2.02	2.650(4)	128
	N2–H2	O1[h]	0.88	2.28	3.012(5)	141
	C6–H6A	O1[i]	0.99	2.53	3.340(6)	139
	C6–H6B	N1[j]	0.99	2.58	3.414(6)	142
1-OAc	C2–H2	O2[k]	0.95	2.34	3.279(3)	115
	C6–H6A	O5[k]	0.99	2.52	3.305(2)	168
	C6–H6B	O5[l]	0.99	2.48	3.280(3)	137
	C7–H7	O5[k]	0.95	2.56	3.349(2)	141
1-NO_3	C6–H6A	O12[m]	0.99	2.56	3.179(2)	121
	C7–H7	O12[m]	0.95	2.37	3.179(2)	142
1-Cl	C3–H3	Cl[n]	0.95	2.73	3.535(5)	143
	C6–H6A	Cl[o]	0.99	2.71	3.552(5)	143
	C12–H12B	Cl[p]	0.99	2.81	3.406(4)	119
1-I	C4–H4	O2[q]	0.95	2.55	3.317(3)	138
	C6–H6A	O2[q]	0.99	2.57	3.321(3)	133
1-N_3	C6–H6B	N5[r]	0.99	2.59	3.497(3)	153
	C13–H13B	N5[s]	0.98	2.60	3.516(3)	155
1-NCS	C4–H4	O2[t]	0.95	2.44	3.255(3)	143
	C13–H13C	S21[u]	0.98	2.82	3.580(3)	135

a: −x, 1−y, −z; b: 1/2−x, −1/2+y, 1−z; c: 1−x, 1−y, −z; d: 1−x, 1−y, 1−z; e: 2−x, −y, 1−z; f: 1−x, −y, 1−z; g: 1−x, 1−y, 1−z; h: 3/2−x, 3/2−y, 1−z; i: 3/2−x, 1/2−y, 1−z; j: x, −1+y, z; k: 2−x, 1/2+y, 1/2−z; l: −1+x, y, z; m: −x, −y, −z; n: x, 1+y, z; o: −x, −y, 1−z; p: −1+x, y, −1+z; q: 2−x, −1/2+y, 3/2−z; r: 1/2−x, 1/2−y, 1−z; s: −1/2+x, 1/2−y, 1−z; t: 2−x, −y, 1−z; u: 3/2+x, 1/2−y, −1/2+z.

Table S7. Hydrogen bonds and angles of complexes presented in this work.

	Donor	Acceptor	D–H/Å	H···A/Å	D···A/Å	D–H···A/°
2-NO_3	O21–H21A	O31	0.775(19)	1.865(19)	2.6366(18)	173(3)
	O21–H21B	O2[a]	0.79(3)	1.93(3)	2.7355(16)	167(3)
	O31–H31A	O13[b]	0.75(3)	2.06(3)	2.8033(19)	170(2)
	O31–H31B	O11[c]	0.82(3)	2.06(3)	2.8385(18)	160(3)
	C1–H1	O2[a]	0.95	2.48	3.430(2)	177
	C6–H6A	O12[d]	0.99	2.56	3.2213(19)	124
	C7–H7	O12[d]	0.95	2.48	3.3396(19)	150
2-Cl	C2–H2	O2[e]	0.95	2.45	3.242(5)	140
	C3–H3	Cl1[f]	0.95	2.79	3.542(4)	137
	C6–H6A	O2[g]	0.99	2.82	3.350(5)	143
	C6–H6B	Cl1[h]	0.99	2.82	3.668(4)	144
2-N_3	C3–H3	O2[i]	0.95	2.53	3.266(2)	134
	C4–H4	N5[j]	0.95	2.55	3.251(2)	131
	C6–H6B	O2[k]	0.99	2.51	3.405(2)	151
2-NCS	O21–H21	O2[l]	0.84	1.91	2.742(4)	173
2-SO_4	O60–H60	O54[m]	0.84	1.85	2.682(5)	171
	O70–H70	O53[n]	0.84	1.95	2.765(6)	164
	C11–H11	O70[o]	0.95	2.33	3.190(6)	150
	C13–H13	012[p]	0.95	2.41	3.320(6)	159
	C14–H14	O31[n]	0.95	2.58	3.522(4)	171
	C16–H16A	O52[n]	0.99	2.33	3.275(4)	159
	C22–H22C	O70	0.98	2.42	3.294(9)	148
	C32–H32	O32[p]	0.95	2.49	3.382(5)	156
	C34–H34	O54[n]	0.95	2.57	3.511(5)	116
3-OAc	O31–H31A	O22	0.75(5)	2.12(5)	2.857(3)	167(5)
	O31–H31B	O3[q]	0.76(5)	2.25(5)	2.983(3)	164(5)
	C6–H6B	O22[r]	0.99	2.52	3.297(3)	135
	C10–H10A	O3[s]	0.99	2.53	3.335(3)	138

a: 1−x, 1/2+y, 1/2−z; b: −1+x, y, z; c: 1−x, −y, −z; d: 2−x, −y, 1−z; e: −1+x, −1+y, −1+z; f: x, −1+y−1+z; g: 2−x, 1−y, 3−z; h: 2−x, 1−y, 2−z; i: −1+x, −1+y, −1+z; j: x, y, −1+z; k: 2−x, 3−x, 1−z; l: 1/2−x, 1/2+y, 3/2−z; m: x, 1/2−y, 1/2+z; n: −x, −1/2+y, 3/2−z; o: −x, 1/2+y, 3/2−z; p: −1+x, y, z; q: 1+x, y, z; r: 1−x, −y, 1−z; s: 1−x, 1−y, 2−z.

Table S8. Hydrogen bonds and angles of complexes presented in this work.

	Donor	Acceptor	D–H/Å	H···A/Å	D···A/Å	D–H···A/°
4-OAc	C2–H2	N3[a]	0.95	2.53	3.248(5)	133
	C3–H3	O22	0.95	2.45	3.274(5)	145
4-NO$_3$	O31–H31A	O32	0.76(3)	2.01(3)	2.745(2)	164(3)
	O31–H31B	O22[b]	0.75(3)	2.08(3)	2.818(2)	170(3)
	O32–H32A	O22[c]	0.79(3)	2.09(3)	2.879(3)	171(3)
	O32–H32B	O23	0.79(3)	2.14(3)	2.881(3)	158(3)
	C2–H2	O22[d]	0.95	2.55	3.426(3)	153
5-NO$_3$	C4–H4	O12[e]	0.95	2.54	3.325(3)	140
	C6–H6B	O2[f]	0.99	2.59	3.405(2)	140
	C7–H7	O2[f]	0.95	2.48	3.338(2)	150
5-Cl	C3–H3	O2[g]	0.95	2.31	3.050(4)	135
	C13–H13	Cl1[h]	0.95	2.82	3.682(4)	151
6-OAc	O21–H21A	O2[i]	0.73(5)	2.12(5)	2.845(4)	173(5)
	O21–H21B	O31[j]	0.78(5)	1.95(5)	2.729(4)	175(5)
	O31–H31A	O21[k]	0.72(3)	2.07(4)	2.781(4)	170(4)
	O31–H31B	O5	0.80(4)	2.01(4)	2.800(3)	174(4)
	C2–H2	O21	0.95	2.52	3.460(4)	168
	C3–H3	O5[l]	0.95	2.40	3.319(4)	163
	C7–H7	O5[m]	0.95	2.46	3.281(3)	145
6-Cl	C3–H3	Cl1[n]	0.95	2.75	3.500(4)	137
	C6–H6B	Cl1[o]	0.99	2.67	3.546(4)	148

a: x, 1+y, z; b: 1−x, −1/2+y, 3/2−z; c: x, 1/2−y, 1/2+z; d: 1−x, −y, 1−z; e: −x, −y, 1−z; f: 1−x, −y, 1−z; g: −1/2+x, 1/2+y, −1+z; h: 1/2+x, −1/2−y, 1/2+z; i: 1/2−x, −y, −1/2+z; j: −x, 1/2+y, −1/2−z; k: 1/2−x, −1/2+y, z; l: 1/2−x, 1/2+y, z; m: 1−x, −y, −z; n: x, −1+y, z; o: 2−x, 1−y, −z.

Fig. S4. Powder X-ray diffraction spectra of **1-OAc**, **1-NO$_3$**, **1-Cl**, **2-Cl**, and **3-OAc**. Spectra were recorded at room temperature, the calculated spectra were obtained from the crystal data (133 K).

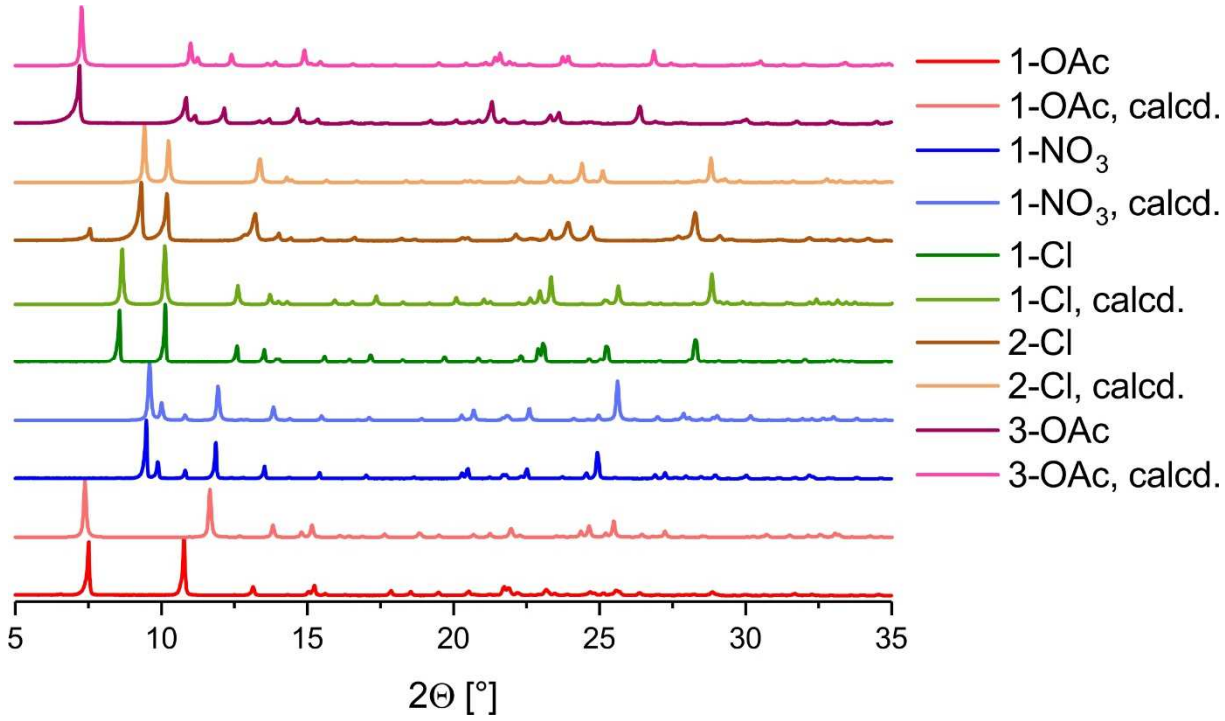

Fig. S5. Powder X-ray diffraction spectra **5-NO$_3$**, **5-Cl**, **5-I**, **6-OAc**, and **6-Cl**. Spectra were recorded at room temperature, the calculated spectra were obtained from the crystal data (133 K).

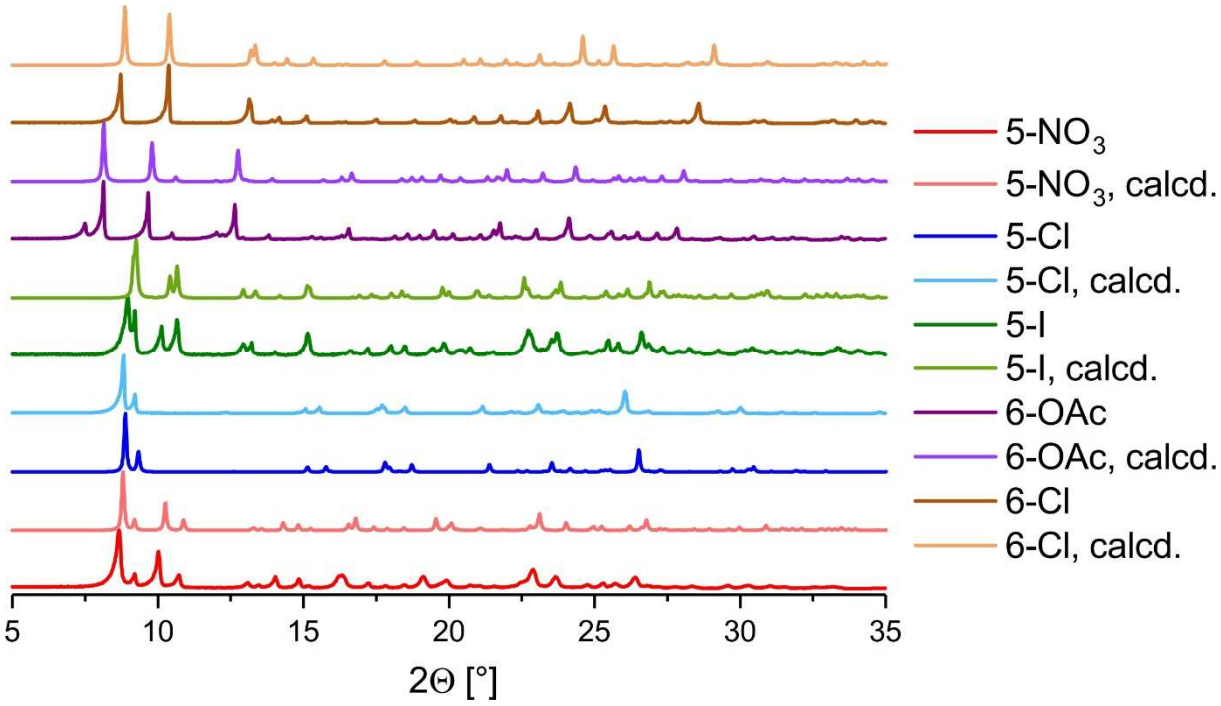

Table S9. Data of the magnetic measurements with μ_{eff} at 300 K, and $\chi_M T$ at 300 K, 50 K, and, if measured, 2 K.

	μ_{eff} [μ_B] (300 K)	$\chi_M T$ [$cm^3K^{-1}mol^{-1}$] (300 K)	$\chi_M T$ [$cm^3K^{-1}mol^{-1}$] (50 K)	$\chi_M T$ [$cm^3K^{-1}mol^{-1}$] (2 K)
1-OAc	2.95	1.09	0.88	0.39
1-NO$_3$	2.71	0.92	0.16	0.01
1-Cl	2.95	1.08	0.91	0.68
1-NCS	2.00	0.50	0.42	
2-OAc	2.07	0.54	0.40	
2-NO$_3$	2.23	0.62	0.50	
2-Cl	2.89	1.05	0.89	0.78
2-NCS	2.12	0.56	0.46	
3-OAc	3.18	1.27	0.95	0.20
3-NO$_3$	2.13	0.57	0.45	
3-Cl	2.92	1.06	0.92	
3-NCS	2.02	0.51	0.43	
4-OAc	2.17	0.59	0.47	
4-NO$_3$	2.10	0.55	0.44	0.41
4-Cl	2.03	0.51	0.44	
4-NCS	2.05	0.53	0.44	
5-OAc	2.07	0.53	0.43	
5-NO$_3$	2.81	0.99	0.88	1.01
5-Cl	2.04	0.52	0.46	0.69
5-I	3.18	1.26	0.86	0.14
5-NCS	2.15	0.58	0.45	
6-OAc	2.99	1.12	0.91	0.40
6-NO$_3$	2.17	0.59	0.48	
6-Cl	2.84	1.01	0.89	1.08
6-NCS	2.88	1.03	0.87	

Fig. S6. Plots of the $\chi_M T$ product *vs*. *T* for complexes **1-OAc** (top left), **1-Cl** (top right), **1-NCS** (middle left), **2-OAc** (middle right), **2-NO$_3$** (bottom left), and **2-Cl** (bottom right). The data points are black squares, the red line corresponds to the fit.

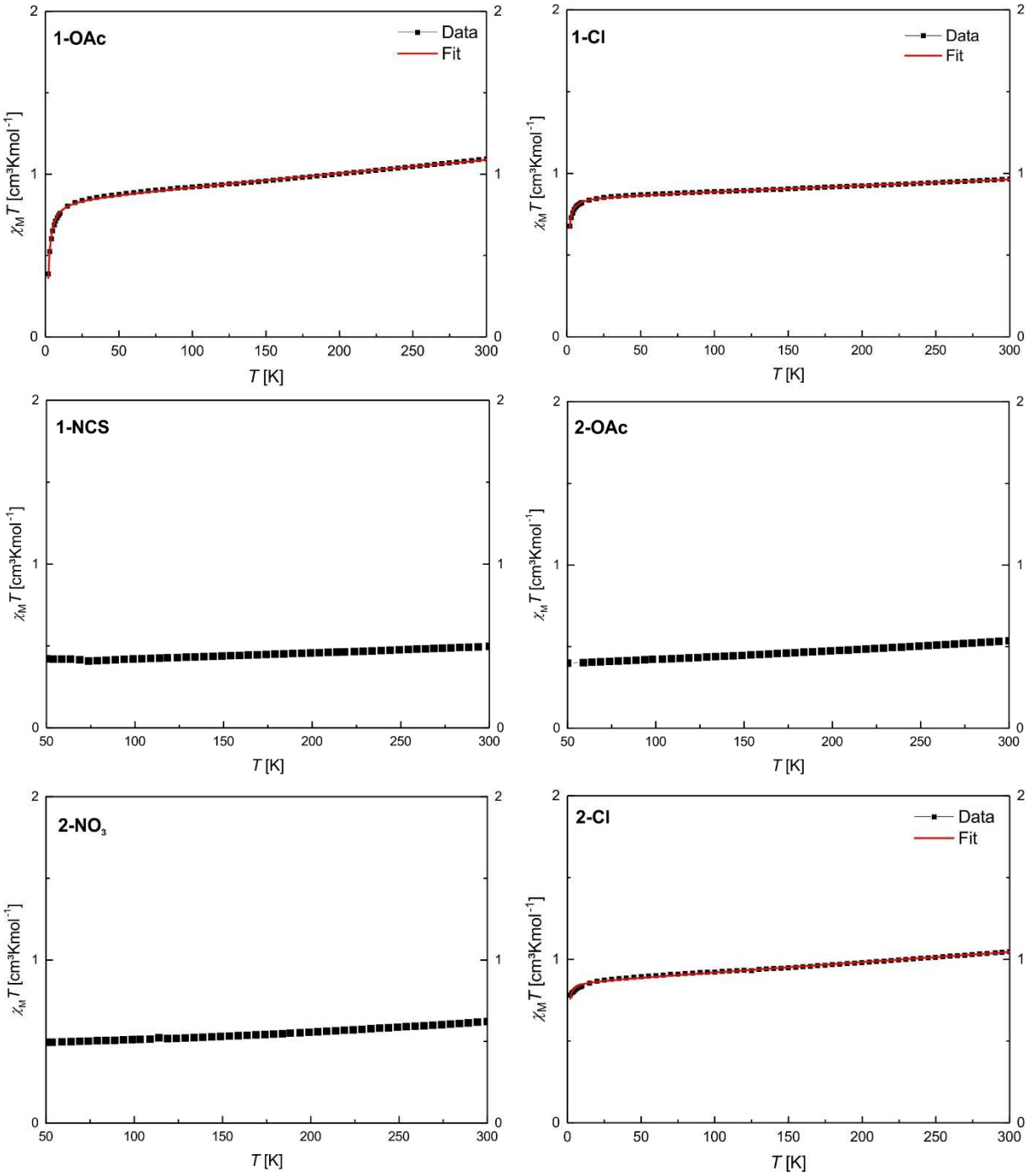

Fig. S7. Plots of the $\chi_M T$ product *vs*. *T* for complexes **2-NCS** (top left), **3-OAc** (top right), **3-NO3** (middle left), **3-Cl** (middle right), **3-NCS** (bottom left), and **4-OAc** (bottom right). The data points are black squares, the red line corresponds to the fit.

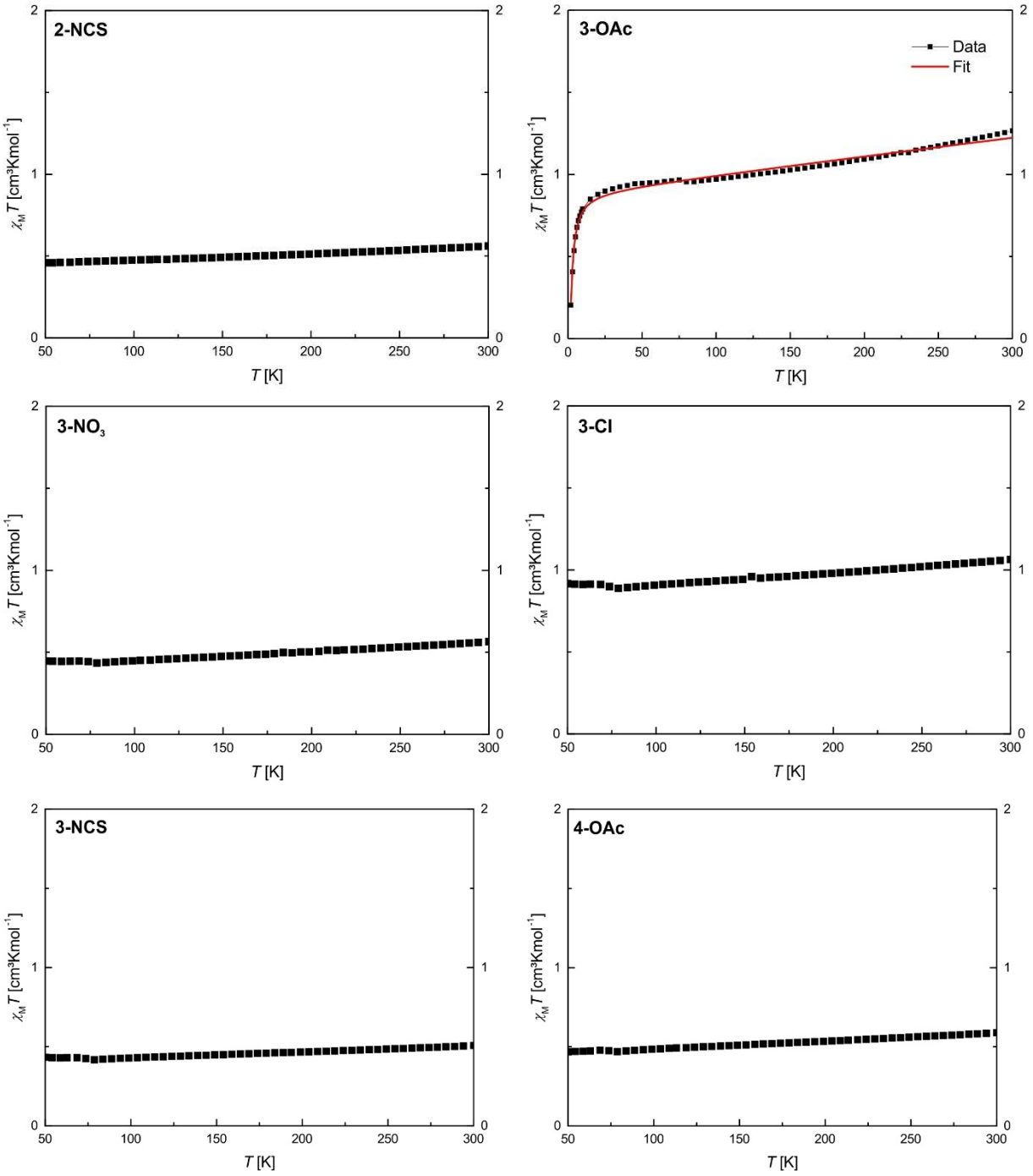

Fig. S8. Plots of the $\chi_M T$ product *vs*. *T* for complexes **4-NO3** (top left), **4-Cl** (top right), **4-NCS** (middle left), **5-OAc** (middle right), **5-NO3** (bottom left), and **5-Cl** (bottom right). The data points are black squares, the red lines corresponds to the fit.

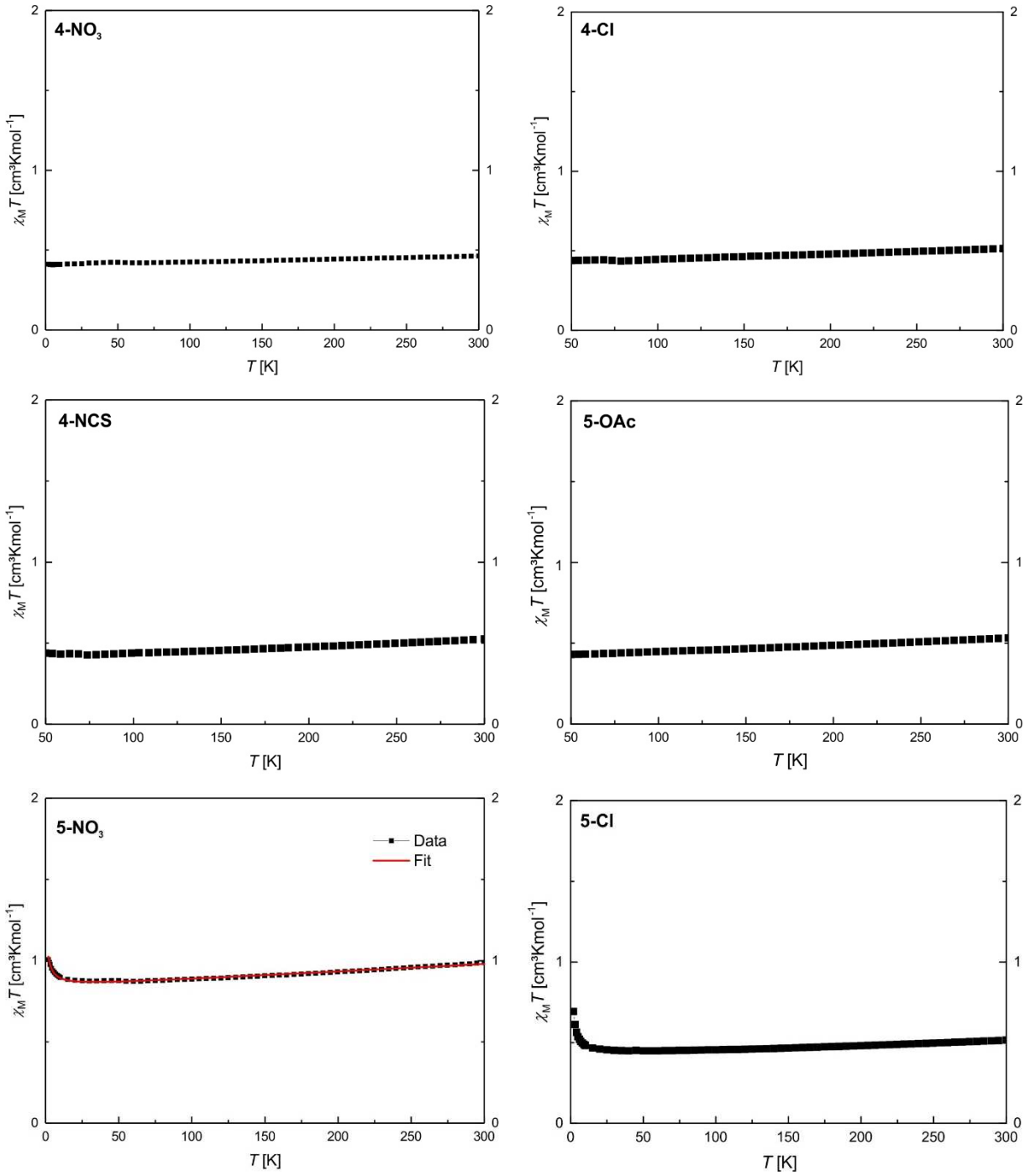

Fig. S9. Plots of the $\chi_M T$ product *vs*. *T* for complexes **5-I** (top left), **5-NCS** (top right), **6-OAc** (middle left), **6-NO$_3$** (middle right), **6-Cl** (bottom left), and **6-NCS** (bottom right). The data points are black squares, the red line corresponds to the fit.

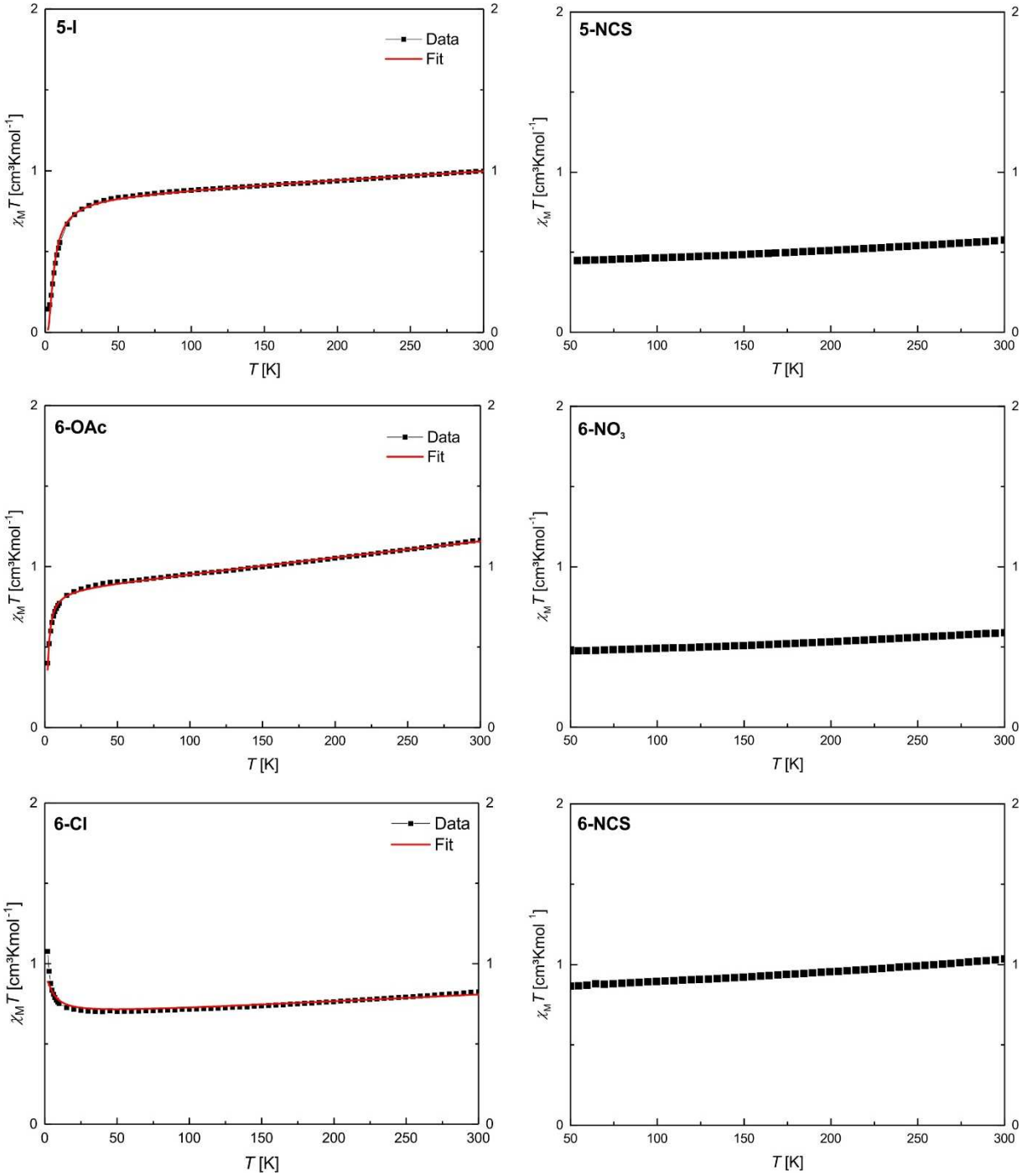

Fig. S10. Curie-plot of **4-NO3**.

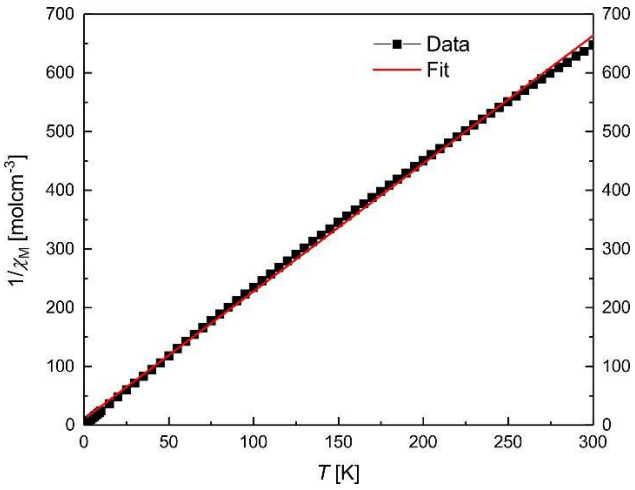

7. Iron(II) and Iron(III) Complexes of Tridentate *NNO* Schiff Base-like Ligands – X-ray Structures and Magnetic Properties

Katja Dankhoff, Sandra Schneider, René Nowak, and Birgit Weber*

Department Chemie, Universität Bayreuth, Universitätsstr. 30, 95440 Bayreuth, Germany. E-mail: weber@uni-bayreuth.de; Tel: +49(0)921552555

Published in: *Z. Anorg. Allg. Chem.* **2018**, *644*, 1839–1848. (DOI: 10.1002/zaac.201800359)

Dedicated to Professor Wolfgang Bensch on the Occasion of his 65th Birthday

Keywords: Schiff base ligands • Iron • Bipyridine • Magnetic Properties • Spin crossover

Abstract: A series of new $[Fe(L)_2]$ iron(II) and $[Fe(L)_2]X$ iron(III) complexes is presented with varying tridentate *NNO* coordinating Schiff base-like ligands (L^-) and different counterions (X^- = Cl^-, Br^-, I^- BF_4^-, PF_6^-, and ClO_4^-) in the case of the iron(III) complexes. The crystal structures of one iron(II) and three iron(III) complexes are discussed, as well as the magnetic properties of the complexes regarding the possibility of the observation of spin crossover. While the three iron(II) complexes are predominantly high spin, in the case of the iron(III) complexes spin crossover was observed for the majority of the complexes (10 out of 12). Additionally, the optical properties and electrochemical behavior in solution was investigated and the results are compared with related systems from literature.

7.1 Introduction

Spin crossover (SCO) compounds are an interesting class of materials, where the electronic configuration of a central metal atom can be switched between the high spin (HS) state and the low spin (LS) state by external stimuli such as temperature, pressure, or light.[1–3] The spin state of the central metal atom is HS, if the total spin pairing energy *P* is much higher than the ligand field splitting Δ_O or LS if Δ_O is much higher than *P*. In case neither of these two conditions is clearly fulfilled, a SCO is possible. This transition causes changes in the magnetic, optical, structural, and vibrational properties of the complex and can therefore be monitored by a number of different techniques, like temperature dependent magnetic susceptibility measurements, Mössbauer spectroscopy, UV/Vis spectroscopy, or single crystal/powder X-ray diffraction at different temperatures. The switching of the spin state and the resulting change in properties allows various possible applications as temperature/ pressure sensor or data storage.[4]

In the case of octahedral complexes, this phenomenon could be observed for any d^4–d^7 electron configuration. However, due to the significantly higher ligand field splitting Δ_O for 4d and 5d central metal atoms, it is predominantly observed for 3d complexes. Here, the most frequently investigated are based on iron as metal atom. Upon SCO, iron(II) complexes change from the paramagnetic HS state (S = 2) to the diamagnetic LS state (S = 0), whereas for iron(III) complexes both, the HS state (S = 5/2) and the LS state (S = 1/2), are paramagnetic. In the last decades, about 90% of all spin crossover complexes investigated were iron(II) complexes due to the pronounced changes in magnetism (diamagnetic/paramagnetic) and related properties (fluorescence,[5] conductivity,[6] liquid crystal phase transition,[7] just to mention few examples) that can be observed. Also, the structural changes often observed for iron(II) SCO complexes allowed the observation of spin crossover with hysteresis around room temperature quite frequently.[8]

However, in recent years the focus shifted back to the more stable iron(III) complexes as the iron(II) complexes are often very air sensitive.[9] This development is accelerated by reports on iron(III) systems with wide hysteresis.[10,11] In the case of iron(II) the most frequently observed donor atom set is N_6,[1–3] and although there are examples with an N_4O_2[12,13] or N_4S_2[14] donor atom set, they are comparatively rare. In the case of iron(III) complexes, spin crossover is more

frequently observed for systems with an N_4O_2 coordination sphere, which in their vast majority use Schiff base ligands.[9,15–17] So far, only few examples are reported where both, the iron(II) and iron(III) with the same ligand set are synthesized.[12,13]

Due to the higher positive charge of iron(III) compared to iron(II), the ligand field splitting Δ_O is expected to be larger in the case of iron(III) complexes, if the same ligands are used. However, as the spin pairing energy is much higher in the case of iron(III),[18] no general statements can be made for the impact of a mere change of the oxidation state at the central iron atom on the spin state of the complex.[15] Herein we present a series of new iron(II) and iron(III) complexes with anionic tridentate *NNO* Schiff base-like ligands. The impact of the oxidation state of the central metal atom on the spin state for those complexes is discussed. Please note that most of the iron(III) spin crossover complexes have negatively charged chelating ligands. One hypothesis is, that the negative charge is necessary to reach the higher ligand field splitting needed to compensate for the larger spin paring energy.[15] Thus the question arises if the negative charge of the ligand is necessary for the synthesis of iron(III) SCO complexes. We decided to use the $[Fe(bipy)_3]^{2+/3+}$ system with bipy = 2,2'-bipyridine as neutral bidentate *NN* ligand for comparison. The spin crossover behavior of trisdiimine iron(II) complexes is well understood by now and a very simple and straight forward approach to predict the spin state of such complexes was recently proposed.[19] Some examples for SCO active tris(bipyridine) iron(II) complexes are already reported in literature,[20] whereas for the corresponding iron(III) complexes only very limited data is available. Thus, the corresponding complex was synthesized and characterized herein as well.

7.2 Results and discussion

Synthesis

The general synthesis pathway of the iron(II) and iron(III) complexes is given in Scheme 1. An overview over all synthesized complexes together with the used abbreviations is given in Table 1 together with some examples from literature for comparison.

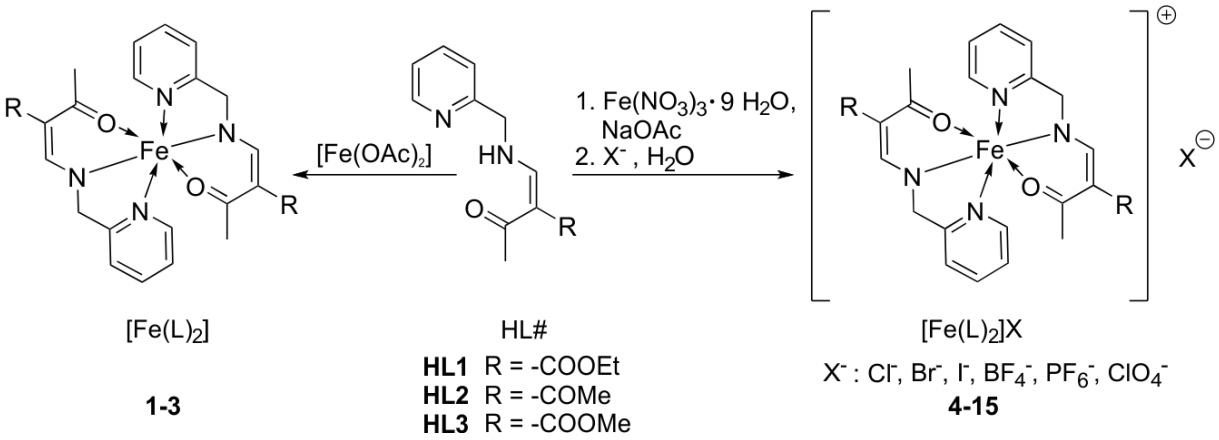

Scheme 1. General synthesis pathway for the iron(II) and iron(III) complexes presented in this work.

The tridentate ligands HL1 – HL3 were synthesized as described previously.[21] The corresponding iron(II) complexes $[Fe(L)_2]$ (**1**–**3**) were obtained by a reaction of iron(II) acetate and two equiv. of the respective tridentate ligand in ethanol (HL1) or methanol (HL2 and HL3). The acetate anion acts as a base for the deprotonation of the ligand. The orange to dark red iron(II) complexes were obtained directly from the synthesis with 0.5 to 1 solvent molecules associated. For the synthesis of the iron(III) complexes $[Fe(L)_2]X$ (**4**–**15**), iron(III) nitrate nonahydrate, sodium acetate, and the respective ligand were heated to reflux in ethanol (HL1) or methanol (HL2 and HL3) to obtain a dark purple solution. This solution was split in aliquots and the dark purple iron(III) complexes were precipitated with an aqueous solution of the desired anion. For comparison purpose, the pair $[Fe(bipy)_3]Cl_2 \cdot 2H_2O$ (**16**) and $[Fe(bipy)_3](PF_6)_3 \cdot 2H_2O$ (**17**) was synthesized as well following literature procedures.[24,25] The two complexes with bipy as neutral, bidentate ligand were obtained as dark blue (**17**) and pink (**16**) powder. The purity of all complexes was confirmed with elemental analysis, mass spectrometry, and IR spectroscopy.

Table 1. Overview of the synthesized iron(II) and iron(III) complexes, and their SCO behavior with $T_{1/2}$ and $\chi_M T$ at 300 and 50 K. For comparison purpose, some examples from literature are given as well.

	Compound	SCO behavior	$T_{1/2}$ /K	$\chi_M T$ /cm^3 K mol^{-1} (300 K)	μ_{eff} (300 K)	$\chi_M T$ /cm^3 K mol^{-1} (50 K)	Literature
1	$[Fe(L1)_2]\cdot 0.5EtOH$	HS	/	3.53	5.32	3.41	this work
2	$[Fe(L2)_2]\cdot 0.5MeOH$	HS	/	3.24	5.10	2.67	this work
3	$[Fe(L3)_2]\cdot MeOH$	HS	/	3.22	5.07	3.17	this work
16	$[Fe(bipy)_3]Cl_2\cdot 2H_2O$	abrupt, irreversible[a)]	377	0.07 / 3.13	0.76 / 5.01	0.03	this work
4	$[Fe(L1)_2]Cl\cdot 4H_2O$	gradual	206	3.93	5.62	0.62	this work
	$[Fe(qsal\text{-}Cl)_2]$[f)]	abrupt, two steps	308, 316	/	/	/	[12]
5	$[Fe(L1)_2]Br\cdot 2H_2O$	gradual with hysteresis	↓185 ↑191	3.95	5.62	0.65	this work
6	$[Fe(L1)_2]PF_6\cdot H_2O$	gradual with hysteresis	↓230 ↑235	3.94	5.61	0.69	this work
7	$[Fe(L1)_2]BF_4\cdot H_2O$	HS	/	4.62	6.08	4.43	this work
8	$[Fe(L1)_2]ClO_4$	HS	/	4.28	5.86	4.08	this work
9	$[Fe(L2)_2]I\cdot 2H_2O$	gradual	111	4.44	5.96	0.66	this work
10	$[Fe(L2)_2]PF_6\cdot H_2O$	gradual and incomplete	206	3.70	5.44	1.37	this work
11	$[Fe(L3)_2]Cl\cdot 3H_2O$	gradual	214	4.00	5.66	0.63	this work
12	$[Fe(L3)_2]Br\cdot 2H_2O$	gradual	211	3.95	5.63	0.71	this work
13	$[Fe(L3)_2]PF_6\cdot H_2O$	gradual and incomplete	250	2.84	4.77	0.74	this work
14	$[Fe(L3)_2]BF_4\cdot H_2O$	gradual with two steps	211 / 86	4.24	5.83	0.68	this work
15	$[Fe(L3)_2]ClO_4$	gradual and incomplete	181	3.93	5.61	1.22	this work
17	$[Fe(bipy)_3](PF_6)_3\cdot 2H_2O$	LS[b)]	/	0.81	2.55	0.56	this work
	$[Fe(bzpa)_2]ClO_4$[c)]	gradual and incomplete	≈230	/	/	/	[22]
	[Fe(qsal-I)$_2$]OTf·EtOH[d)]	abrupt with hysteresis	↓139 ↑252	/	/	/	[11]
	$[Fe(qsal)_2]BS\cdot MeOH$[e)]	abrupt, two steps	205 and 195	4.39	/	0.50 (10 K)	[17]
	$[Fe(qsal)_2][(C_6F_3I_3)Cl]$	gradual	268	4.15 (400 K)	/	0.57 (2 K)	[16]
	$[Fe(acpa)_2]ClO_4$[g)]	abrupt/gradual	250	/	/	/	[23]

a) Associated with solvent loss. b) The complex decomposes during sample preparation and measurement. c) Hbzpa = (1-benzoylpropen-2-yl)(2-pyridylmethyl)amine. d) qsal-I = 5-I-N-(8-quinolyl)salicylaldimine. e) q-sal = *N*-(8-quinolyl)salicylaldimine, BS = benzenesulfonate. f) qsal-Cl = 5-Cl-N-(8-quinolyl)salicylaldimine. g) Hacpa = *N*-(1-acetyl-2-propylidene)(2-pyridylmethyl)amine.

Single Crystal Structure Analysis

Crystals suitable for single-crystal X-ray structure analysis were obtained for the iron(II) complex **3** and the iron(III) complexes **8**, **10**, and **15**. For the iron(III) complexes the amount of solvent included in the crystal packing differs from the bulk complexes. As this can also influence the magnetic properties, the samples are denoted as **8a**, **10a**, and **15a**. The crystallographic data of the compounds were collected at 133 K and are given in Table S1 (Supporting Information). ORTEP drawings of the complexes are shown in Figure 1, whereas selected bond lengths and angles are summarized in Table 2. All complexes crystallized with two tridentate *NNO* Schiff base-like ligands being coordinated to the central iron atom, resulting in an octahedral N_4O_2 coordination sphere.

Iron(II) Complexes. Crystals suitable for X-ray structure analysis of **3** were obtained by storing the mother liquor at 8 °C. The complex crystallizes in the triclinic space group $P\bar{1}$ with two molecules of the complex and two methanol per asymmetric unit. An ORTEP drawing is given in Figure 1 (top left). Due to the low quality of the crystal and the crystallographic data this complex can only be discussed as a general structural motif, therefore no conclusions towards bond lengths, angles, or intermolecular interactions are drawn.

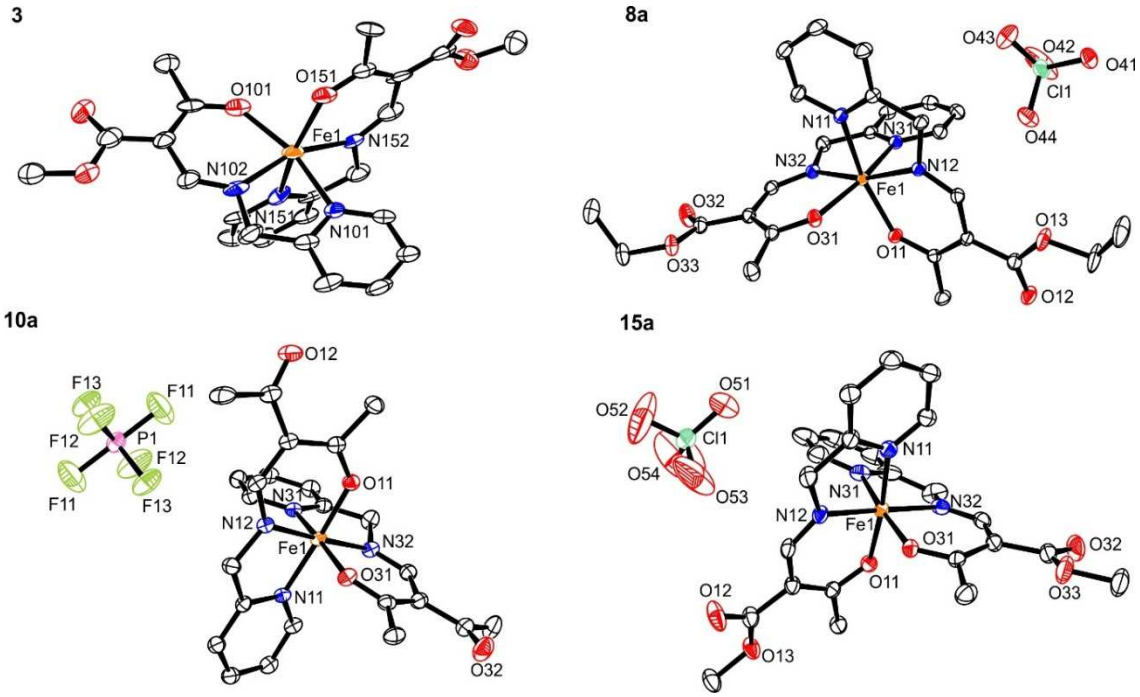

Figure 1. ORTEP drawings of **3** (top left), **8a** (top right), **10a** (bottom left), and **15a** (bottom right). Hydrogen atoms, solvent molecules, and disorder are omitted for clarity. Ellipsoids are drawn at 50% probability level.

Iron(III) Complexes. Crystals suitable for X-ray structure analysis of **8a**, **10a**, and **15a** were obtained by slow diffusion of diethyl ether into an acetonitrile solution of the complex.

Complex **8a** crystallizes in the triclinic space group $P\bar{1}$ with one complex and one anion per asymmetric unit. The last carbon atom of the ethyl ester of one tridentate ligand (C23) in **8a** is disordered into two positions (Figure S1, Supporting Information). During refinement, electron density of solvent molecules was present. However, those solvent molecules could not be refined due to disorder. Therefore SQUEEZE from Platon[26] was used to remove 43 electrons per unit cell. π– π interactions between the pyridine rings of two different complex molecules and C–H– π interactions can be observed (see Figure 3 and discussion of the packing). Complex **10a** crystallizes in the monoclinic space group *I*2/c with one complex, two half molecules of PF_6^-, and one molecule of acetonitrile per asymmetric unit. Four fluorine atoms of the PF_6^- anions are disordered in at least two positions (Figure S2, Supporting Information). Complex **15a** crystallizes in the monoclinic space group $P2_1/c$ with one complex and one anion per asymmetric unit.

Table 2. Spin state, selected bond lengths, angles, and the octahedral distortion parameter of complexes **8a**, **10a**, and **15a**.

	S	Fe–N_{py} / Å	Fe–N / Å	Fe–O / Å	N_{py}–Fe–O / °	Σ / °
8a	5/2	2.1537(15)	2.0588(14)	1.9661(12)	161.06(5)	84
		2.1505(15)	2.0642(13)	1.9692(14)	160.29(5)	
10a	1/2	1.9567(19)	1.886(2)	1.8942(16)	175.19(8)	48
		1.9604(18)	1.916(2)	1.8930(18)	171.66(8)	
15a	1/2	1.9690(19)	1.9001(19)	1.8999(18)	174.14(8)	44
		1.957(2)	1.912(2)	1.8955(17)	174.61(9)	

In order to determine the spin state of the central iron(III) atoms, the N_{py}–Fe–O angle of the tridentate ligand was taken into account. It has an average value of 160.7° for **8a**, 173.4° for **10a**, and 174.4° for **15a**. This indicates that in **8a** the central iron(III) atom is in the high spin state, whereas in the other two complexes it is in the low spin state. The octahedral distortion parameter Σ was calculated as well (Table 2). It can be seen that the value differs significantly for **8a** (84°) from the values of **10a** and **15a** (48° and 44°, respectively). Those values support the assumption of the spin states. The bond lengths are in average also significantly longer in **8a** (2.15 Å N_{py}–Fe, 2.06 Å N–Fe, and 1.97 Å O–Fe) than in **10a** (1.96 Å N_{py}–Fe, 1.90 Å N–Fe,

and 1.89 Å O–Fe) and **15a** (1.96 Å N_{py}–Fe, 1.91 Å N–Fe, and 1.90 Å O–Fe). Those results are in line with the results from the magnetic measurements (see below), where **8** is a pure HS complex while for **10** and **15** an incomplete gradual spin crossover is observed. Please note that differences in the magnetic properties can be due to differences in the crystal packing. Several intermolecular interactions between the anion or solvent molecules and the tridentate ligands are observed for all complexes, as well as interactions between different tridentate ligands. Details of all intermolecular interactions are summarized in Table S2–S4 (Supporting Information). Pictures of the packing of the complexes in the crystal are shown in Figure 2 and discussed in more detail in the following.

In the case of complex **8a**, a π···π interaction between the pyridine ring N31–C31–C32–C33–C34–C35 [Cg–Cg 3.6622(11) Å] of two neighboring complex molecules in combination with C–H···π interaction between the aromatic hydrogen atom (C33–H33) and the pyridine ring of the same pair leads to a P4AE (Parallel Fourfold Aryl Embrace) motif,[27] that is illustrated in Figure 3. Further C–X···π interactions are observed between the keto oxygen of the ester side chain (C41–O32) and a pyridine ring, and between the $–CH_2$ group of the tridentate ligand (C36–H36B) and the six-membered ring made up by the central iron(III) atom and the chelate cycle of the ligand (Fe1–O31–C39–C38–C37–N32). Those interactions result in the formation of a 3D network of linked molecules; the details are summarized in Table S2 (Supporting Information). This network is further strengthened by several non-classical hydrogen bonds between C–H groups of the ligand and oxygen atoms of the perchlorate anion or the keto oxygen atoms of neighboring ligands (the details are given in Table S4, Supporting Information).

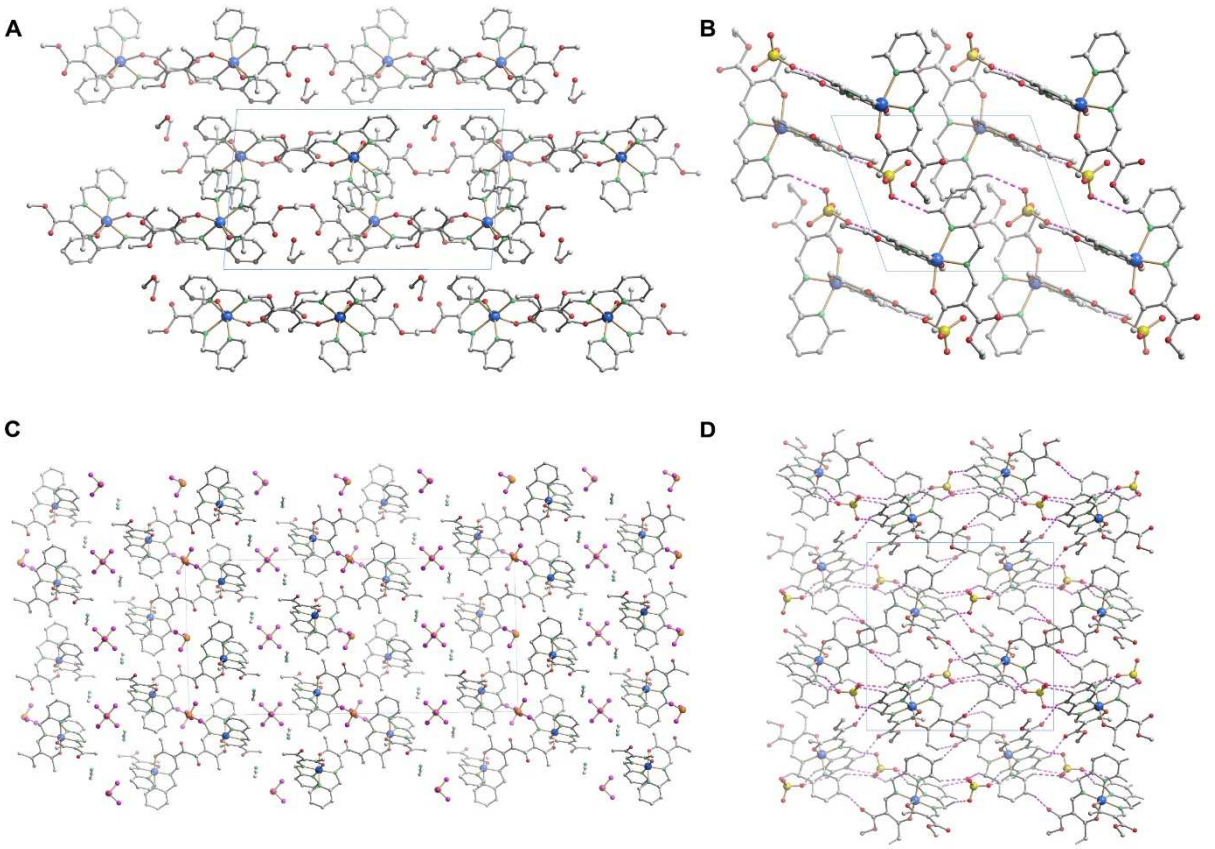

Figure 2. Molecular packing of **3** (top left, **A**, along [100]), **8a** (top right, **B**, along [001]), **10a** (bottom left, **C**, along [010]), and **15a** (bottom right. **D**, along [100]). Hydrogen atoms not involved in intermolecular interactions are omitted for clarity. Hydrogen bonds are drawn as pink, dashed lines.

For complex **10a**, four C–H···π interactions are observed in the molecule packing. One is between an aromatic C–H (C32–H32) group and the pyridine ring of another complex molecule (N11–C11–C12–C13–C14–C15); one involves a CH_2 group of the ester side chain (C40–H40B) and the pyridine ring of a neighboring complex (N31–C31–C32–C33–C34–C35); the other one is between the CH_2 group of the ester side chain (C22–H22A) and the six-membered ring made up by the central iron(III) atom and the chelate cycle of the ligand (Fe1–O11–C19–C18–C17–N12). The last C–H···π interaction is observed between the CH_3 group of the acetonitrile (C51–H51A) and a pyridine ring (N31–C31–C32–C33–C34–C35). A C–X···π interaction involving the keto oxygen atom of the side chain (C41–O32) and the pyridine ring of a neighboring ligand (N31–C31–C32–C33–C34–C35) is present as well. The details of those interactions are summarized in Table S2 (Supporting Information). As in the case of **8a**, a 3D network of linked molecules is built, where the counterions are included through several non-classical hydrogen bonds between C–H groups of the tridentate ligands or solvent molecules and the PF_6^- ions.

Some further non-classical hydrogen bonds to the keto oxygen atoms of the ligand are observed as well, all details are summarized in Table S4 (Supporting Information).

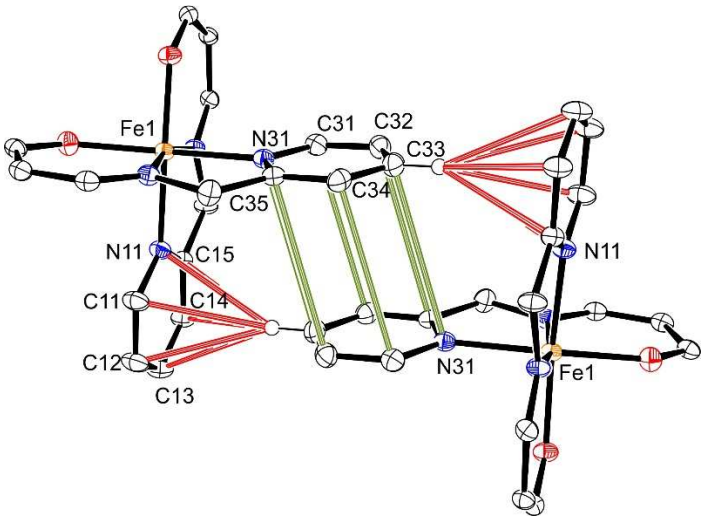

Figure 3. ORTEP drawing of **8a** illustrating the C–H···π and π···π interactions. Ellipsoids were drawn at 50% probability level. Hydrogen atoms and side chains are omitted for clarity.

In the case of **15a**, only one C–H···π interaction is observed, namely between the CH_2 group of the ester side chain (C42–H42A) and the six-membered ring made up by the central iron(III) atom and the chelate cycle of the ligand (Fe1–O31–C39–C38–C37–N32). Additionally, several non-classical hydrogen bonds involving the tridentate ligands as donor and the oxygen atoms of the anion or the keto groups as acceptor are present in the crystal packing. The details of those interactions are summarized in Tables S2 and S4 (Supporting Information). Again, a 3D network of interacting complexes is obtained.

In the packing of all three complexes two different layers of iron(III) sites can be observed, that are illustrated in Figure 4. The molecules in one layer are turned by 180° with respect to the second layer. In case of **10a** and **15a** the anions (and acetonitrile molecules) are separating those layers, whereas in the case of **8a** the strong P4AE interaction (π···π and C–H···π) leaves no space for the anions between the resulting pair of complex molecules. This could be one explanation for the difference in the magnetic behavior of the bulk complexes **8**, **10**, and **15**. Probably, the dense packing of **8a** in the crystal prevents the occurrence of spin crossover as the associated volume change is precluded. In the case of **10a** and **15a** this interaction is not observed, the packing is less dense and a gradual spin transition takes place. Please note that

there are several examples in literature, where P4AE interactions are believed to be responsible for abrupt SCO[12] – quite in contrast to our results presented herein.

Magnetic Measurements

The magnetic properties of all iron(II) and iron(III) complexes were investigated with a SQUID magnetometer at an applied field of 5000 G to analyze the spin state and follow a possible spin crossover. Different anions were used in the synthesis of the iron(III) complexes as they are known to significantly influence the packing of the molecules in the crystal and by this the magnetic properties. An overview of the SCO behavior of the complexes with the $\chi_M T$ values at 300 and 50 K is given in Table 1. The compilation is completed with the data obtained for magnetic measurements on the previously described $[Fe(bipy)_3]Cl_2 \cdot 2H_2O$ (**16**)[24] and $[Fe(bipy)_3](PF_6)_3 \cdot 2H_2O$ (**17**).[25] Although the two complexes are well known and have been described for many years, temperature dependent magnetic measurements are so far missing. This is especially interesting for $[Fe(bipy)_3]^{2+}$ that is known to be a stable LS complex in solution. The three ligands usually coordinate the central iron atom in an octahedral fashion with a very symmetric surrounding and a rather large ligand field splitting.[28] Therefore mostly diamagnetic complexes are generated. However, a reversible spin-crossover triggered by lattice water removal was recently reported by *Luo* et al. for $[Fe(44mBipy)_3](ClO_4)(SCN) \cdot 3H_2O$ (with 44mBipy = 4,4'-dimethyl-2,2'-bipyridine)[20] and we observed very recently a similar behaviour for chloride salts of other methyl-substituted bipyridines.[29]

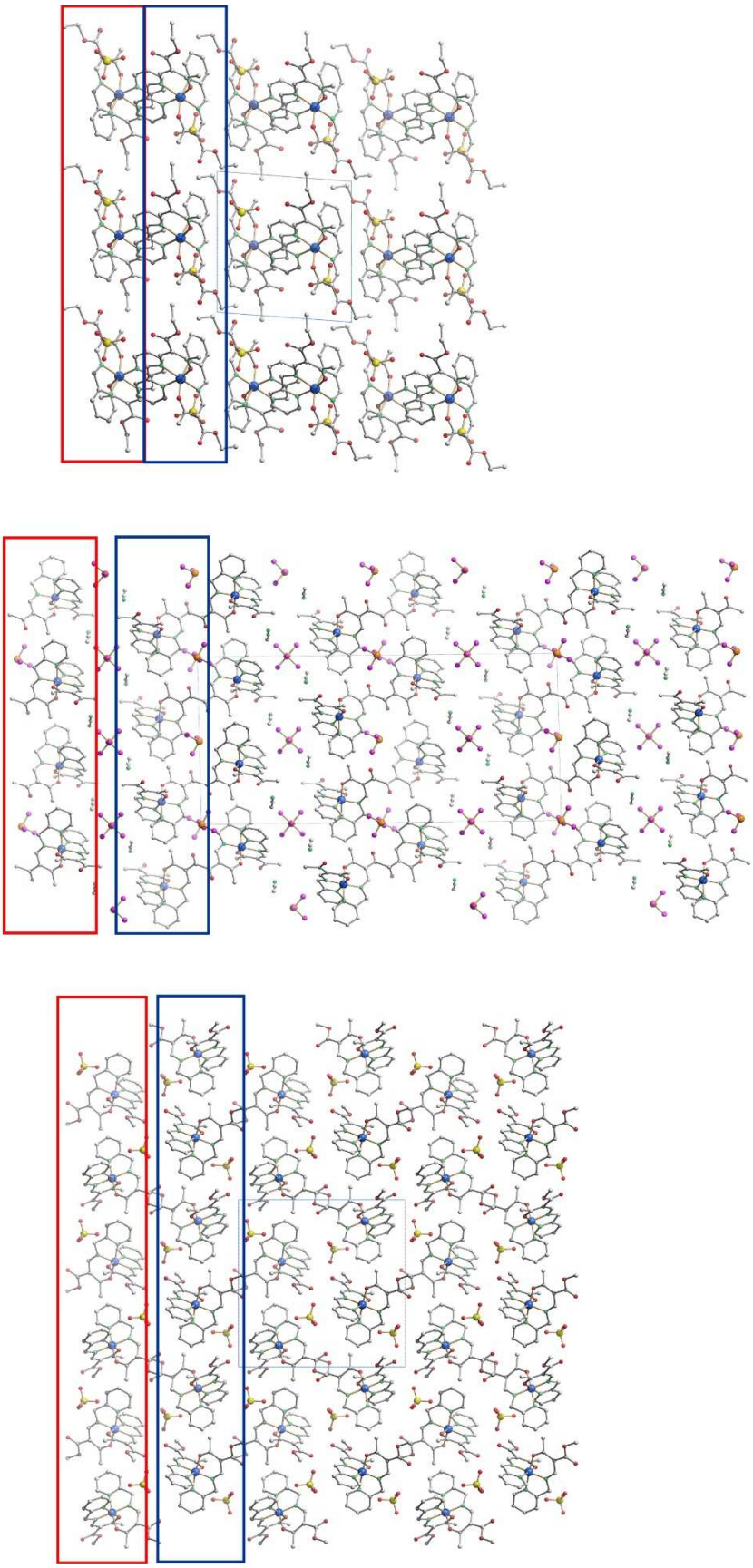

Figure 4. Packing of **8a** (top, along [100]), **10a** (middle, along [010]), and **15a** (bottom, along [100]). Hydrogen atoms are omitted for clarity. Red and blue boxes are highlighting the different iron(III) layers discussed in the text.

Iron(II) Complexes. In Figure 5, the $\chi_M T$ vs. T plot of **3** and **16** is shown as an example for a complex with a *NNO* coordinating anionic ligand and bipy as ligand. The $\chi_M T$ vs. T plots of **1** and **2** are shown in Figure S3 (Supporting Information). The iron(II) complexes with the anionic Schiff base-like ligand are essentially in the HS state in the whole temperature range investigated (300–50 K). The room temperature $\chi_M T$ product is in the range of 3.2–3.5 $cm^3 \cdot K \cdot mol^{-1}$ (see Table 1), typical for octahedral $S = 2$ systems with some orbital momentum contribution. Upon cooling, the $\chi_M T$ product does not change significantly for **1** and **3**. In the case of **2**, a slight gradual drop is observed around 100 K and the final $\chi_M T$ product at 50 K is 2.67 $cm^3 \cdot K \cdot mol^{-1}$. This could be an indication for a very incomplete SCO with about one fourth of the central iron atoms involved. As expected, **16** is diamagnetic with a $\chi_M T$ product of 0.07 $cm^3 \cdot K \cdot mol^{-1}$ at room temperature and the magnetic moment does not change upon cooling to 50 K. Upon heating, above 340 K an abrupt and complete transition to the HS state is observed and at 400 K a $\chi_M T$ product of 3.25 $cm^3 \cdot K \cdot mol^{-1}$ is observed, characteristic for HS iron(II). Upon subsequent cooling, the moment does not change significantly and the compound remains HS. This indicated, that the spin crossover is triggered by the removal of lattice solvent molecules as previously reported for related complexes.[20,29] As the measurements were made in gelatine capsule and the sample chamber of the SQUID is under vacuum, re-absorption of the water molecules is not possible. However, storage of the de-hydrated sample leads to a color change from the black HS state back to the pink LS state (see Figure 5).

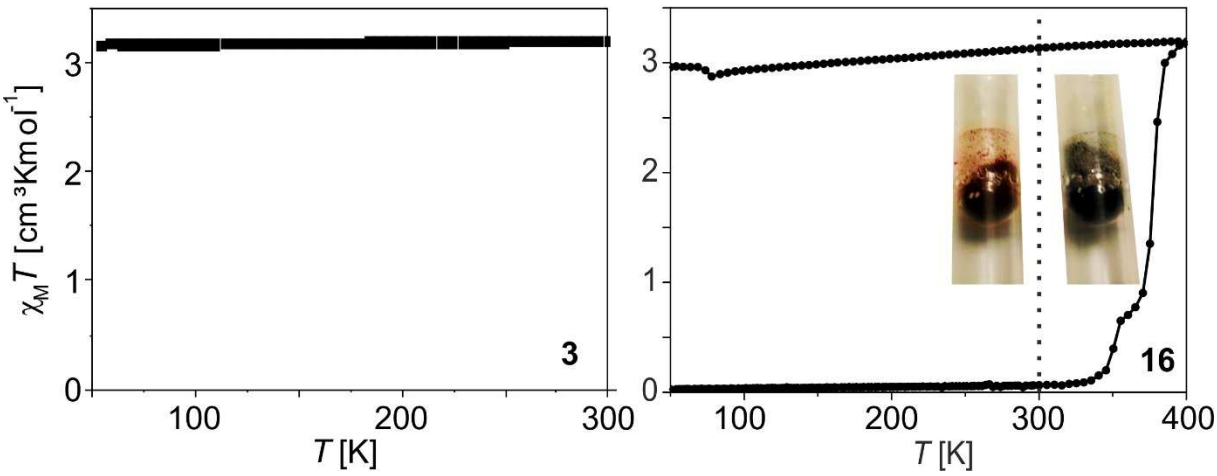

Figure 5. Plot of the $\chi_M T$ product vs. T for complex **3** (left) and **16** (right).

Iron(III) Complexes. In Figure 6, the $\chi_M T$ vs. T plot of **6** and **17** is shown as an example for an iron(III) complex with a *NNO* coordinating anionic ligand (**6**) and bipy as ligand (**17**). The $\chi_M T$ vs. T plots of the other iron(III) complexes are shown in Figures S5 and S6 (Supporting Information). Two of twelve iron(III) complexes (**7** and **8**) stay in the HS state over the complete temperature range (300–50 K). The room temperature $\chi_M T$ product is with 4.62 (**7**) and 4.28 (**8**) $cm^3 \cdot K \cdot mol^{-1}$ in the typical region for HS iron(III) complexes of this ligand type. All other complexes show gradual SCO that are in part incomplete, both, in the high and the low temperature region. As a consequence, the room temperature $\chi_M T$ product does not always reach to typical range for an HS iron(III) complex (around 4 $cm^3 \cdot K \cdot mol^{-1}$), especially for **13** the room temperature $\chi_M T$ product is with 2.84 $cm^3 \cdot K \cdot mol^{-1}$ significantly lower. The $\chi_M T$ product at 50 K is in most cases higher than the theoretically expected value for an iron(III) LS (S = ½) system. The details for each complex are summarized in Table 1. Compounds **5** and **6** show a gradual spin transition, however, with a 6 and 5 K wide hysteresis, respectively. The $T_{1/2}$ values are 185 (↓) and 191 (↑) K for **5** and 230 (↓) and 235 (↑) K for **6**. Complex **14** shows a gradual, two-step SCO behavior with $T_{1/2}$ = 211 and 86 K. The other complexes also exhibit gradual spin transitions with $T_{1/2}$ below 250 K. This gradual behavior can be explained with the missing cooperativity between the central metal atoms. Complex **17** with bipy as bidentate ligand stays in the LS state (50–400 K) with a $\chi_M T$ product (room temperature) of 0.81 $cm^3 \cdot K \cdot mol^{-1}$. This is slightly higher than expected for a pure LS central iron(III) atom, but can be explained with the rather unstable nature of the complex towards reduction.

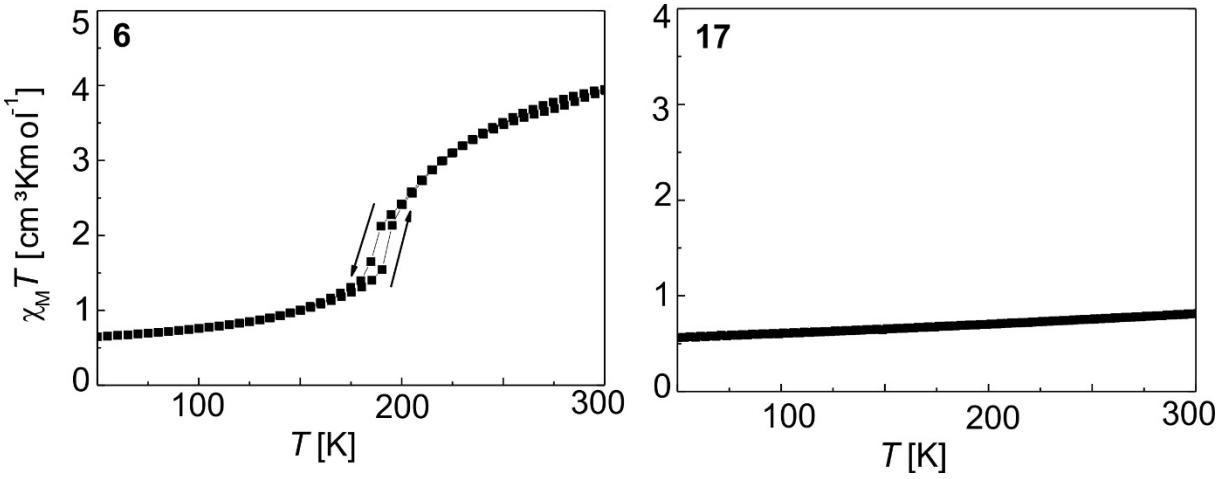

Figure 6. Plot of the $\chi_M T$ product vs. T for complex **6** (left) and **17** (right).

The difference in magnetic behavior of the iron(II) complexes, which are fully HS, and the iron(III) complexes, which are SCO active, can be explained with the different ligand field splitting allowed by the central metal atoms. This is in agreement with the spectrochemical series of the metal ions, as the ligand field splitting increases with an increase of the oxidation state of the central metal atom. Therefore Δ_O is in the region of SCO for the iron(III) complexes of this type, whereas the iron(II) complexes are HS. In the case of the bipyridine-based complexes the iron(II) complex shows spin crossover, while the iron(III) complex remains in the LS state. Thus for the complexes presented herein the differences in spin-pairing energy for iron(II) and iron(III) have no significant impact on the expected magnetic properties, independent of the nature of the ligand (negative charge or not). Again, it is of interest to compare the results with examples from literature. For the system with qsal-*X* (*X* = Cl, Br, I) as negatively charged three-dentate N_2O ligand, spin crossover is observed in the case of iron(II), whereas the corresponding iron(III) complexes are high spin.[12] The differences could be due to packing effects that are known for their strong impact on SCO properties.

UV/Vis and Cyclic Voltammetry

The complexes were investigated in acetonitrile solution with regard to their optical properties and electrochemical behavior. The absorption maxima λ_{max}, log ε, and the electrochemical properties of the complexes are given in Table 3. The UV/Vis spectra of the complexes are given in Figures S7–S9 (Supporting Information). It can be seen that the iron(II) complexes have one absorption maxima in the region of 450 nm, independent of the used ligand. The logarithm of the absorption coefficient ε indicates a charge transfer process as origin of this transition. The absorption of the iron(III) complexes depends only on the tridentate ligand. As expected, the complexes with the same Schiff base-like ligand and different anions have the same absorption maxima at 528 and 640 nm for ligand HL1, 542 and 650 nm for ligand HL2, and 542 and 650 nm for ligand HL3. Again, the differences between the three ligands are not very pronounced. As for the iron(II) complexes the logarithm of the absorption coefficient ε indicates a charge transfer process responsible for both transitions. It is possible that the absorption at ca. 530 nm corresponds to the HS species of the complex, and the absorption at ca. 640 nm to the LS species, as observed for related systems in literature.[30] This indicates that a spin transition is also possible in solution and indeed, a color change from purple to blue is observed when solutions of the complexes are cooled with liquid nitrogen. Temperature dependent UV/Vis spectroscopy is needed to further confirm this hypothesis.

Table 3. λ_{max}, log ε, and the electrochemical properties (in acetonitrile, 0.1 M NBu_4PF_6, 50 $mV \cdot s^{-1}$, vs. $Ag/AgNO_3$).

	λ_{max} /nm (log ε)	E_{red} /V	E_{ox} /V
1	442 (3.33)	−0.50	−0.37 / 1.21
2	451 (3.43)	−0.48	−0.37 / 1.20
3	451 (3.43)	−0.48	−0.37
4	528 (3.43) / 640 (3.15)	−0.45	−0.34 / 1.18
5	528 (3.46) / 640 (3.18)	−0.44	−0.37 / 1.21
6	528 (3.48) / 640 (3.21)	−0.46	−0.35 / 1.28
7	528 (3.45) / 640 (3.18)	−0.46	−0.36
8	528 (3.29) / 640 (3.03)	−0.45	−0.35
9	542 (3.46) / 650 (3.25)	−0.40	−0.33
10	542 (3.50) / 650 (3.29)	−0.41	−0.34
11	526 (3.44) / 636 (3.18)	−0.51	−0.36 / 1.10
12	526 (3.44) / 636 (3.18)	−0.48	−0.36 / 1.14
13	526 (3.49) / 636 (3.23)	−0.45	−0.37
14	526 (3.46) / 636 (3.20)	−0.49	−0.38
15	526 (3.47) / 636 (3.21)	−0.44	−0.36
17	[a]	0.72	0.83

a) It was not possible to measure the absorption of **17**, as the compound was immediately reduced to the iron(II) species upon dissolving in acetonitrile.

The electrochemical behavior of the iron complexes was investigated using cyclic voltammetry. The results are summarized in Table 3, the voltammograms are given in Figures S10–S12 (Supporting Information). All complexes (**1**–**15**) show quasi-reversible processes between –0.40 and –0.51 V, that correspond to the iron(II)/iron(III) redox process. The peak above 1.1 V can be attributed to the oxidation of the ligand, this process is irreversible. As expected, no major influence of the ligand or counterion on the electrochemical behavior is observed and the same results are obtained independent of the oxidation stage of the starting material. Additional oxidation and reduction peaks are observed in cases halide anions were used as counterions for the complexes. Complex **17** shows also a quasi-reversible process [iron(II)/iron(III)] at 0.72 V (reduction potential) and 0.83 V (oxidation potential), in good agreement with the values reported in literature (1.07 V vs. Ag/AgCl in 0.2 M NEt_4ClO_4/MeCN[31]). Please note the strong impact of the used chelate ligand on the redox potentials.

7.3 Conclusions

We presented 15 new iron(II) and iron(III) complexes with tridentate *NNO* Schiff base-like ligands. It was possible to isolate single crystals suitable for X-ray structure analysis of one iron(II) and three iron(III) compounds with different ligands and anions. The temperature dependent magnetic behavior of the complexes was studied and it was found that the iron(II) complexes stay HS, whereas the iron(III) complexes are spin crossover active. Ten of twelve iron(III) complexes show a rather gradual spin transition below 250 K. Hysteresis of 6 and 5 K were observed for compounds **5** and **6**, respectively. The gradual nature of the spin transition can be explained with the missing cooperativity between the central metal atoms, although several intermolecular interactions were observed in the crystal packings.

The complexes were investigated with regard to their optical properties, the absorption maxima depend on the tridentate ligand and the oxidation state of the central iron atom. The electrochemical properties were measured as well. One quasi-reversible process was found corresponding to the redox process iron(II)/iron(III), and one irreversible oxidation process of the ligand could be attributed. For comparison purpose, the pair $[Fe(bipy)_3]Cl_2 \cdot 2H_2O$ and $[Fe(bipy)_3](PF_6)_3 \cdot 2H_2O$ was characterized as well. Due to the stronger ligand field splitting, the iron(II) complex shows spin crossover above room temperature whereas the iron(III) complex remains in the low spin state. The differences are also reflected in different colors and redox potentials and follow the expectations from the spectrochemical series of the ligands and the metal atoms.

7.4 Experimental Section

The ligands HL1, HL2, and HL3,[21] iron(II)acetate,[32] and $[Fe(bipy)_3](PF6)_3$[25] were synthesized as published. All other chemicals were commercially available and used without further purification. Syntheses of iron(II) complexes were carried out in an argon atmosphere (5.0) using Schlenk tube techniques. In those cases MeOH and EtOH were saturated with argon for 30 min before use. CHN analyses were measured with a Vario El III from Elementar

AnalysenSysteme. Samples were prepared in a tin boat, and acetanilide was used as standard. Mass spectra were recorded with a Finnigan MAT 8500 with a data system MASPEC II. IR spectra were recorded with a Perkin–Elmer Spectrum 100 FT-IR spectrometer. TG was measured with Netzsch STA 449.

[Fe(L1)$_2$]·0.5EtOH (1): [Fe(OAc)$_2$] (0.2 g, 1.15 mmol) and HL1 (0.628 g, 2.53 mmol) were dissolved in EtOH (15 mL) and the orange solution was heated to reflux for 1 h. After cooling to room temperature and left to stand for 1 d, the orange precipitate was filtered, washed six times with 3 mL EtOH, and dried in vacuo. Yield: 0.45 g (573.46 g·mol^{-1}, 68%). $C_{26}H_{30}FeN_4O_6$·0.5EtOH: calcd. C 56.55, H 5.80, N 9.77; found C 56.16, H 5.60, N 9.99%; calcd. C 56.55, H 5.80, N 9.77%. MS (EI, pos.) *m*/*z* (%): 550 ($C_{26}H_{30}FeN_4O_6$, 100), 303 ($C_{13}H_{15}FeN_2O_3$, 35), 93 (C_6H_6N, 16). IR: ν = 1664 (s, C=O), 1585 (s, C=O) cm^{-1}. TG: up to 150 °C: –3.4% mass change (corresponds to the loss of 0.5 ethanol molecules, theory: –4.0 %), above 150 °C decomposition.

[Fe(L2)$_2$]·0.5MeOH (2): [Fe(OAc)$_2$] (0.2 g, 1.15 mmol) and HL2 (0.552 g, 2.53 mmol) were dissolved in MeOH (20 mL) and the red solution was heated to reflux for 1 h. After cooling to room temperature and left to stand for 1 d, the red, crystalline precipitate was filtered, washed once with 3 mL MeOH, and dried in vacuo. Yield: 0.28 g (506.36 g·mol^{-1}, 48%). $C_{24}H_{26}FeN_4O_4$·0.5MeOH: calcd. C 58.11, H 5.57, N 11.06%; found C 58.05, H 5.60, N 11.06%. MS (EI, pos.) *m*/*z* (%): 490 ($C_{24}H_{26}FeN_4O_4$, 100), 273 ($C_{12}H_{13}FeN_2O_2$, 93), 93 (C_6H_6N, 33). IR: ν = 1633 (s, C=O), 1562 (s, C=O) cm^{-1}. TG: up to 150 °C: –2.0% mass change (corresponds to the loss of 0.5 methanol molecules, theory: –3.2 %), above 150 °C decomposition.

[Fe(L3)$_2$]·MeOH (3): [Fe(OAc)$_2$] (0.2 g, 1.15 mmol) and HL3 (0.592 g, 2.53 mmol) were dissolved in MeOH (15 mL) and the red/brown solution was heated to reflux for 1 h. After cooling to room temperature and left to stand for 1 d, the orange precipitate was filtered, washed twice with 3 mL MeOH, and dried in vacuo. Yield: 0.25 g (554.38 g·mol^{-1}, 39%). $C_{24}H_{26}FeN_4O_6$·MeOH: calcd. C 54.16, H 5.45, N 10.11%; found C 53.91, H 5.39, N 10.12%. MS (EI, pos.) *m*/*z* (%): 522 ($C_{24}H_{26}FeN_4O_6$, 100), 289 ($C_{12}H_{13}FeN_2O_3$, 52), 93 (C_6H_6N, 23). IR: ν = 1664 (s, C=O), 1588 (s, C=O) cm^{-1}. TG: up to 150 °C: –1.2% mass change (corresponds to the loss of 0.25 methanol molecules, theory: –1.5 %), above 150 °C decomposition.

[Fe(bipy)$_3$]Cl$_2$·2H$_2$O (16): The complex was synthesized using standard procedures.[24] The product precipitated as pink powder with two water molecules.

General Synthesis of the Iron(III) Complexes: 1 g of the corresponding ligand (2 equiv.), iron(III) nitrate nonahydrate (1.2 equiv.), and sodium acetate (1.2 equiv.) were dissolved in 100 mL of ethanol (HL1) or methanol (HL2 and HL3) and the dark purple solution was heated to reflux for 1 h. This solution was split in aliquots (20 mL) and approximately half of the solvent was removed under reduced pressure. The iron(III) complexes were precipitate with an aqueous solution (20 mL) of the anion. This precipitate was filtered, washed with water and ethanol or methanol, and dried in vacuo.

[Fe(L1)$_2$]Cl·4H$_2$O (4): Yield: 0.28 g dark purple powder (657.90 g·mol^{-1}, 95%). $C_{26}H_{30}FeN_4O_6Cl·4H_2O$: calcd. C 47.47, H 5.82, N 8.52%; found C 47.09, H 5.96, N 9.03%. MS (EI, pos.) *m*/*z* (%): 550 ($C_{26}H_{30}FeN_4O_6$, 42), 93 (C_6H_6N, 100). IR: ν = 3395 (br. s, OH), 1702 (s, C=O), 1588 (s, C=O) cm^{-1}. TG: up to 150 °C: –9.2% mass change (corresponds to the loss of 4 water molecules, theory: –10.9 %), above 150 °C decomposition.

[Fe(L1)$_2$]Br·2H$_2$O (5): Yield: 0.12 g dark purple powder (630.30 g·mol^{-1}, 47%). $C_{26}H_{30}FeN_4O_6Br·2H_2O$: calcd. C 46.90, H 5.10, N 8.40%; found C 46.8, H 5.65, N 8.49%. MS (EI, pos.) *m*/*z* (%): 550 ($C_{26}H_{30}FeN_4O_6$, 7), 131 ($C_8H_7N_2$, 100), 93 (C_6H_6N, 82). IR: ν = 3421 (br. s, OH), 1702 (s, C=O), 1587 (s, C=O) cm^{-1}. TG: up to 150 °C: –3.5% mass change (corresponds to the loss of 1 water molecule, theory: –2.8 %), above 150 °C decomposition.

[Fe(L1)$_2$]PF$_6$·H$_2$O (6): Yield: 0.27 g dark purple powder (713.37 g·mol^{-1}, 95%). $C_{26}H_{30}FeN_4O_6PF_6·H_2O$: calcd. C 43.78, H 4.52, N 7.85%; found C 43.87, H 4.58, N 8.03%. MS (EI, pos.) *m*/*z* (%): 550 ($C_{26}H_{30}FeN_4O_6$, 28), 248 ($C_{13}H_{15}N_2O_3$, 14), 93 (C_6H_6N, 100). IR: ν = 1684 (s, C=O), 1591 (s, C=O) cm^{-1}. TG: up to 150 °C: –1.4% mass change (corresponds to the loss of 1 water molecule, theory: –2.5 %), above 150 °C decomposition.

[Fe(L1)$_2$]BF$_4$·H$_2$O (7): Yield: 0.22 g dark purple powder (655.21 g·mol^{-1}, 47%). $C_{26}H_{30}FeN_4O_6BF_4·H_2O$: calcd. C 47.66, H 4.92, N 8.55%; found C 48.19, H 5.10, N 8.25%. MS (EI, pos.) *m*/*z* (%): 550 ($C_{26}H_{30}FeN_4O_6$, 14), 248 ($C_{13}H_{15}N_2O_3$, 17), 93 (C_6H_6N, 100). IR: ν = 1685 (s, C=O), 1587 (s, C=O) cm^{-1}. TG: up to 150 °C: –2.8% mass change (corresponds to the loss of 1 water molecule, theory: –2.8 %), above 150 °C decomposition.

[Fe(L1)$_2$]ClO$_4$ (8): Yield: 0.19 g dark purple powder (649.84 g·mol^{-1}, 73%). IR: ν = 1685 (s, C=O), 1590 (s, C=O) cm^{-1}.

[Fe(L2)$_2$]I·2H$_2$O (9): Yield: 0.15 g dark purple powder (653.28 g·mol^{-1}, 59%). $C_{24}H_{26}FeN_4O_4I{\cdot}2H_2O$: calcd. C 44.13, H 4.63, N 8.58%; found C 44.59, H 4.21, N 8.55%. MS (EI, pos.) *m*/*z* (%): 490 ($C_{24}H_{26}FeN_4O_4$, 4), 93 (C_6H_6N, 100). IR: ν = 1577 (s, C=O), 1564 (s, C=O) cm^{-1}. TG: up to 182 °C: –2.6% mass change (corresponds to the loss of 1 water molecule, theory: –2.8 %), above 185 °C decomposition.

[Fe(L2)$_2$]PF$_6$·H$_2$O (10): Yield: 0.17 g dark purple powder (653.32 g·mol^{-1}, 63%). $C_{24}H_{26}FeN_4O_4PF_6{\cdot}H_2O$: calcd. C 44.12, H 4.32, N 8.58%; found C 43.86, H 4.29, N 8.40 %. MS (EI, pos.) *m*/*z* (%): 490 ($C_{24}H_{26}FeN_4O_4$, 2), 93 (C_6H_6N, 100). IR: ν = 1581 (s, C=O), 1567 (s, C=O) cm^{-1}. TG: up to 175 °C: –1.3% mass change (corresponds to the loss of 0.5 water molecule, theory: –1.4 %), above 175 °C decomposition.

[Fe(L3)$_2$]Cl·3H$_2$O (11): Yield: 0.09 g dark purple powder. (611.83 g·mol^{-1}, 32%). $C_{24}H_{26}FeN_4O_6Cl{\cdot}3H_2O$: calcd. C 47.11, H 5.27, N 10.86%; found C 46.94, H 5.34, N 10.77%. MS (EI, pos.) *m*/*z* (%): 522 ($C_{24}H_{26}FeN_4O_6$, 10), 93 (C_6H_6N, 22). IR: ν = 3436 (br. s, OH), 1703 (s, C=O), 1588 (s, C=O) cm^{-1}. TG: up to 150 °C: –10.5% mass change (corresponds to the loss of 3.5 water molecules, theory: –10.3 %), above 150 °C decomposition.

[Fe(L3)$_2$]Br·2H$_2$O (12): Yield: 0.04 g dark purple powder. (638.27g·mol^{-1}, 10%). $C_{24}H_{26}FeN_4O_6Br{\cdot}2H_2O$: calcd. C 45.16, H 4.74, N 8.78%; found C 45.57, H 4.60, N 9.42%. MS (EI, pos.) *m*/*z* (%): 234 ($C_{12}H_{13}N_2O_3$, 25), 93 (C_6H_6N, 100). IR: ν = 1703 (s, C=O), 1586 (s, C=O) cm^{-1}. TG: up to 150 °C: –6.8% mass change (corresponds to the loss of 2.5 water molecules, theory: –7.0 %), above 150 °C decomposition.

[Fe(L3)$_2$]PF6·H$_2$O (13): Yield: 0.14 g dark purple powder. (685.32 g·mol^{-1}, 41%). $C_{24}H_{26}FeN_4O_6PF_6{\cdot}H_2O$: calcd. C 42.06, H 4.12, N 8.18%; found C 42.33, H 4.15, N 8.45%. MS (EI, pos.) *m*/*z* (%): 522 ($C_{24}H_{26}FeN_4O_6$, 9), 93 (C_6H_6N, 100). IR: ν = 1697 (s, C=O), 1667 (s, C=O) cm^{-1}. TG: up to 150 °C: –2.2% mass change (corresponds to the loss of 1 water molecule, theory: –2.6%), above 150 °C decomposition.

[Fe(L3)$_2$]BF$_4$·H$_2$O (14): Yield: 0.13 g dark purple powder. (627.16 g·mol^{-1}, 42%). $C_{24}H_{26}FeN_4O_6BF_4{\cdot}H_2O$: calcd. C 45.96, H 4.50, N 8.93%; found C 45.42, H 4.75, N 8.74%. MS (EI, pos.) *m*/*z* (%): 522 ($C_{24}H_{26}FeN_4O_6$, 100), 93 (C_6H_6N, 43). IR: ν = 1705 (s, C=O), 1589 (s, C=O) cm^{-1}. TG: up to 150 °C: –1.5% mass change (corresponds to the loss of 0.5 water molecules, theory: –1.4 %), above 150 °C decomposition.

$[Fe(L3)_2]ClO_4$ (15): Yield: 0.18 g dark purple powder (621.79 g·mol^{-1}, 57%). IR: ν = 1707 (s, C=O), 1588 (s, C=O) cm^{-1}.

$[Fe(bipy)_3](PF_6)_3$ (17): The complex was synthesized using standard procedures.[25] The product precipitated as blue powder with 2 water molecules.

X-ray Diffraction on Single Crystals: The X-ray analysis was performed with a Stoe StadiVari diffractometer using graphite-monochromated Mo-*K*α radiation. The data were corrected for Lorentz and polarization effects. The structures were solved by direct methods (SIR-97)[33] and refined by full-matrix least-square techniques against $Fo^2–Fc^2$ (SHELXL-97).[34] All hydrogen atoms were calculated in idealized positions with fixed displacement parameters. ORTEP-III[35] was used for the structure representation, SCHAKAL-99[36] to illustrate molecule packing. Crystallographic data (excluding structure factors) for the structures in this paper have been deposited with the Cambridge Crystallographic Data Centre, CCDC, 12 Union Road, Cambridge CB21EZ, UK. Copies of the data can be obtained free of charge on quoting the depository numbers CCDC-1862181, CCDC-1862182, CCDC-1862183, and CCDC-1862184 (Fax: +44-1223-336-033; E-Mail: deposit@ccdc.cam.ac.uk, http://www.ccdc.cam.ac.uk).

Magnetic Measurements: Magnetic measurements on the compounds were carried out using a SQUID MPMS-XL5 from Quantum Design with an applied field of 5000 G, and in the temperature range from 300 to 50 K in settle mode. The complexes **16** and **17** were investigated up to 400 K. The sample was prepared in a gelatine capsule held in a plastic straw. The raw data were corrected for the diamagnetic part of the sample holder and the diamagnetism of the organic ligand using tabulated Pascal's constants.

Optical Properties: Absorbance spectra were obtained with an Agilent UV/Vis spectrophotometer 8453 (Agilent Technologies, USA) operating in a spectral range of 190–1100 nm. The spectra were measured at 298 K in quartz cells with 1 cm lightpath (Hellma, Germany).

Cyclic Voltammetry: Redox potentials were obtained with a CH Instruments Electrochemical Analyser (610E) in 0.1 M NBu_4PF_6/MeCN with a platinum electrode, referenced to 0.01 M $AgNO_3$ at room temperature with a scan rate of 50 mV·s^{-1}.

Supporting Information (see footnote on the first page of this article): Crystallographic data of **3**, **8a**, **10a**, and **15a**, magnetic measurements, UV-Vis spectra, cyclic voltammograms, and TG measurements can be found in the Supporting Information.

Acknowledgements

Financial support of the University of Bayreuth and the BayNAT graduate school is gratefully acknowledged.

7.5 References

[1] A. B. Gaspar, B. Weber, in *Molecular Magnetic Materials* (Eds.: B. Sieklucka, D. Pinkowicz), Wiley-VCH Verlag GmbH & Co. KGaA, Weinheim, Germany **2017**, 231–252.

[2] M. A. Halcrow (Ed.), *Spin-Crossover Materials*, John Wiley & Sons Ltd, Chichester **2013**.

[3] P. Gütlich, H. A. Goodwin (Eds.), *Topics in Current Chemistry, 233–235*, Springer Berlin / Heidelberg **2004**.

[4] a) K. Senthil Kumar, M. Ruben, *Coord. Chem. Rev.* **2017**, *346*, 176–205; b) A. D. Naik, L. Stappers, J. Snauwaert, J. Fransaer, Y. Garcia, *Small* **2010**, *6*, 2842–2846.

[5] a) C. Lochenie, K. Schötz, F. Panzer, H. Kurz, B. Maier, F. Puchtler, S. Agarwal, A. Köhler, B. Weber, *J. Am. Chem. Soc.* **2018**, *140*, 700–709; b) I. Suleimanov, O. Kraieva, J. Sánchez Costa, I. O. Fritsky, G. Molnár, L. Salmon, A. Bousseksou, *J. Mater. Chem. C* **2015**, *3*, 5026–5032; c) C.-F. Wang, R.-F. Li, X.-Y. Chen, R.-J. Wei, L.-S. Zheng, J. Tao, *Angew. Chem. Int. Ed.* **2015**, *54*, 1574–1577; d) H. J. Shepherd, C. M. Quintero, G. Molnár, L. Salmon, A. Bousseksou, in *Spin-Crossover Materials* (Ed.: M. A. Halcrow), John Wiley & Sons Ltd, Chichester **2013**, 347–373.

[6] a) C. Faulmann, K. Jacob, S. Dorbes, S. Lampert, I. Malfant, M.-L. Doublet, L. Valade, J. A. Real, *Inorg. Chem.* **2007**, *46*, 8548–8559; b) H.-Y. Wang, J.-Y. Ge, C. Hua, C.-Q. Jiao, Y. Wu, C. F. Leong, D. M. D_Alessandro, T. Liu, J.-L. Zuo, *Angew. Chem. Int.*

Ed. **2017**, *56*, 5465–5470; c) Y.-S. Koo, J. R. Galán-Mascarós, *Adv. Mater.* **2014**, *26*, 6785–6789.

[7] a) A. B. Gaspar, M. Seredyuk, *Coord. Chem. Rev.* **2014**, *268*, 41–58; b) P. N. Martinho, Y. Ortin, B. Gildea, C. Gandolfi, G. McKerr, B. O'Hagan, M. Albrecht, G. G. Morgan, *Dalton Trans.* **2012**, *41*, 7461–7463; c) S. Hayami, K. Kato, Y. Komatsu, A. Fuyuhiro, M. Ohba, *Dalton Trans.* **2011**, *40*, 2167–2169.

[8] a) S. Brooker, *Chem. Soc. Rev.* **2015**, *44*, 2880–2892; b) M. A. Halcrow, *Chem. Lett.* **2014**, *43*, 1178–1188; c) M. Seredyuk, M. C. Muñoz, M. Castro, T. Romero-Morcillo, A. B. Gaspar, J. A. Real, *Chem. Eur. J.* **2013**, *19*, 6591–6596; d) C. Lochenie, W. Bauer, A. P. Railliet, S. Schlamp, Y. Garcia, B. Weber, *Inorg. Chem.* **2014**, *53*, 11563–11572.

[9] D. J. Harding, P. Harding, W. Phonsri, *Coord. Chem. Rev.* **2016**, *313*, 38–61.

[10] S. Hayami, Z.-z. Gu, H. Yoshiki, A. Fujishima, O. Sato, *J. Am. Chem. Soc.* **2001**, *123*, 11644–11650.

[11] W. Phonsri, P. Harding, L. Liu, S. G. Telfer, K. S. Murray, B. Moubaraki, T. M. Ross, G. N. L. Jameson, D. J. Harding, *Chem. Sci.* **2017**, *8*, 3949–3959.

[12] W. Phonsri, D. S. Macedo, K. R. Vignesh, G. Rajaraman, C. G. Davies, G. N. L. Jameson, B. Moubaraki, J. S. Ward, P. E. Kruger, G. Chastanet, *Chem. Eur. J.* **2017**, *23*, 7052–7065.

[13] O. Iasco, E. Riviere, R. Guillot, M. Buron-Le Cointe, J.-F. Meunier, A. Bousseksou, M.-L. Boillot, *Inorg. Chem.* **2015**, *54*, 1791–1799.

[14] A. Arroyave, A. Lennartson, A. Dragulescu-Andrasi, K. S. Pedersen, S. Piligkos, S. A. Stoian, S. M. Greer, C. Pak, O. Hietsoi, H. Phan, *Inorg. Chem.* **2016**, *55*, 5904–5913.

[15] M.-L. Boillot, B. Weber, *C. R. Chim.* **2018**, DOI: 10.1016/j.crci.2018.01.006.

[16] I.-R. Jeon, O. Jeannin, R. Clérac, M. Rouzières, M. Fourmigué, *Chem. Commun.* **2017**, *53*, 4989–4992.

[17] A. Tsukiashi, M. Nakaya, F. Kobayashi, R. Ohtani, M. Nakamura, J. M. Harrowfield, Y. Kim, S. Hayami, *Inorg. Chem.* **2018**, *57*, 2834–2842.

[18] E. Knig, S. Kremer, *Theo. Chim. Acta* **1971**, *23*, 12–20.

[19] H. Phan, J. J. Hrudka, D. Igimbayeva, L. M. Lawson Daku, M. Shatruk, *J. Am. Chem. Soc.* **2017**, *139*, 6437–6447.

[20] Y.-H. Luo, L.-J. Yang, Q.-L. Liu, Y. Ling, W. Wang, B.-W. Sun, *Dalton Trans.* **2014**, *43*, 16937–16942.

[21] K. Dankhoff, B. Weber, *CrystEngComm* **2018**, *20*, 818–828.

[22] Y. Maeda, H. Oshio, K. Toriumi, Y. Takashima, *J. Chem. Soc., Dalton Trans.* **1991**, *11*, 1227–1235.

[23] S. Hayami, D. Urakami, Y. Yamamoto, K. Kato, Y. Kojima, S. Nakashima, K. Inoue, *Chem. Lett.* **2010**, *39*, 328–329.

[24] R. Nowak, E. A. Prasetyanto, L. de Cola, B. Bojer, R. Siegel, J. Senker, E. Rössler, B. Weber, *Chem. Commun.* **2017**, *53*, 971–974.

[25] R. E. DeSimone, R. S. Drago, *J. Am. Chem. Soc.* **1970**, *92*, 2343–2352.

[26] A. L. Spek, *PLATON* – A Multipurpose Crystallographic Tool, Utrecht University, Utrecht, The Netherlands **2008**.

[27] D. J. Harding, P. Harding, H. Adams, *Acta Crystallogr., Sect. E* **2008**, *64*, m1538.

[28] a) L. Pazderski, T. Pawlak, J. Sitkowski, L. Kozerski, E. Szłyk, *Magn. Reson. Chem.* **2010**, *48*, 450–457; b) Y. Garcia, P. Gütlich, in: *Topics in Current Chemistry*, *233–235* (Eds.: P. Gütlich, H. A. Goodwin), Springer Berlin / Heidelberg **2004**, 786.

[29] R. Nowak, *Dissertation*, Universität Bayreuth, Bayreuth **2017**.

[30] S. Schenker, A. Hauser, R. M. Dyson, *Inorg. Chem.* **1996**, *35*, 4676–4682.

[31] H. L. Chum, M. Rock, N. Y. Murakami, I. Jordan, T. Rabockai, *J. Electroanal. Chem.* **1977**, *76*, 277–285.

[32] B. Weber, R. Betz, W. Bauer, S. Schlamp, *Z. Anorg. Allg. Chem.* **2011**, *637*, 102–107.

[33] A. Altomare, M. C. Burla, M. Camalli, G. L. Cascarano, C. Giacovazzo, A. Guagliardi, A. G. G. Moliterni, G. Polidori, R. Spagna, *J. Appl. Crystallogr.* **1999**, *32*, 115–119.

[34] a) G. Sheldrick, *SHELXL-97*, University of Göttingen, Göttingen, Germany **1997**; b) G. Sheldrick, *Acta Crystallogr., Sect. A* **2008**, *64*, 112–122.

[35] a) C. K. Johnson, M. N. Burnett, *ORTEP-III*, Oak-Ridge National Laboratory, Oak-Ridge, TN **1996**; b) L. Farrugia, *J. Appl. Crystallogr.* **1997**, *30*, 565.

[36] E. Keller, *Schakal-99*, University of Freiburg, Freiburg, Germany **1999**.

7.6 Supporting Information

Table S1. Crystallographic data of the complexes presented in this work.

	8a	**10a**	**15a**	**3**
CCDC	1862182	1862183	1862184	1862181
sum formula	$C_{26}H_{30}FeN_4O_6$, ClO_4	$C_{24}H_{26}FeN_4O_4$, F_6P, C_2H_3N	$C_{24}H_{26}FeN_4O_6$, ClO_4	$C_{24}H_{26}FeN_4O_6$, CH_4O
M/ g mol^{-1}	649.84	676.36	621.79	554.38
crystal system	triclinic	monoclinic	monoclinic	triclinic
space group	$P\bar{1}$	$I2/c$	$P2_1/c$	$P\bar{1}$
crystal description	dark purple prism	purple plate	purple block	red plate
a/ Å	10.6724(4)	17.5376(8)	8.8991(6)	10.3791(10)
b/ Å	12.1462(5)	8.5840(4)	17.0675(8)	12.8918(15)
c/ Å	12.7400(5)	37.4666(15)	17.13478(8)	20.048(2)
α/ °	87.407(3)	90	90	94.526(9)
β/ °	70.186(3)	90.865(4)	101.188(5)	90.124(8)
γ/ °	70.671(3)	90	90	111.074(8)
V/ Å^3	1461.95(11)	5639.7(4)	2584.8(3)	2494.0(5)
Z	2	8	4	4
ρ_{calcd}/ g cm^{-3}	1.476	1.593	1.598	1.477
μ/ mm^{-1}	0.669	0.674	0.753	0.658
crystal size /mm	0.125×0.110×0.106	0.120×0.081×0.057	0.130×0.116×0.098	0.115×0.085×0.079
F(000)	674	2776	1284	1160
T/ K	133	133	133	133
λ/ Å	Mo-Kα 0.71073	Mo-Kα 0.71073	Mo-Kα 0.71073	Mo-Kα 0.71073
Θ range/ °	1.7–28.5	2.2–28.6	1.7–28.6	1.7–28.1
Reflns. collected	22010	11059	11273	23932
Indep. reflns.(R_{int})	6829 (0.031)	6707 (0.051)	6112 (0.037)	10996 (0.192)
Parameters	389	429	361	664
$R1$ (all data)	0.0333	0.0447	0.0456	0.1437
$wR2$	0.0989	0.1155	0.1309	0.4062
GooF	1.05	0.92	1.06	0.92

Figure S1. ORTEP drawing of **8a** including the disorder of the side chain. Ellipsoids were drawn at 50 % probability level. Hydrogen atoms were omitted for clarity.

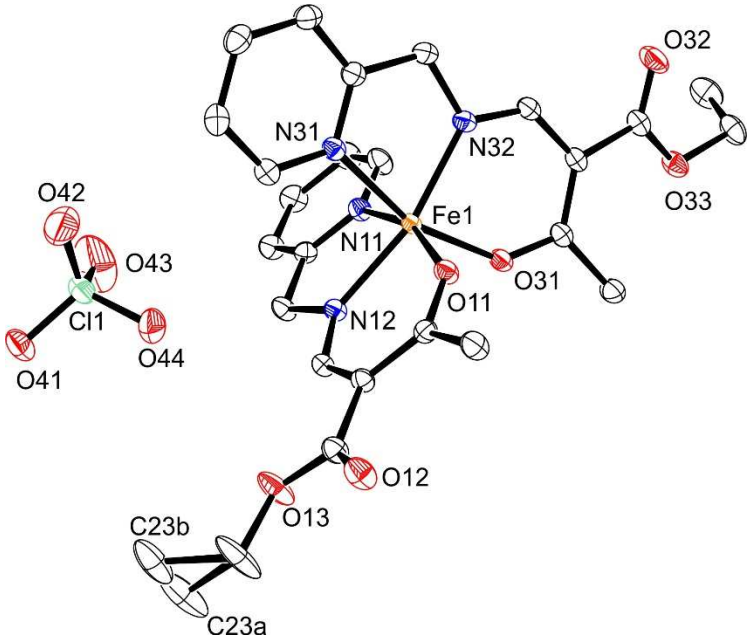

Figure S2. ORTEP drawing of **10a** including the disorder of the anion. Ellipsoids were drawn at 50 % probability level, hydrogen atoms were omitted for clarity.

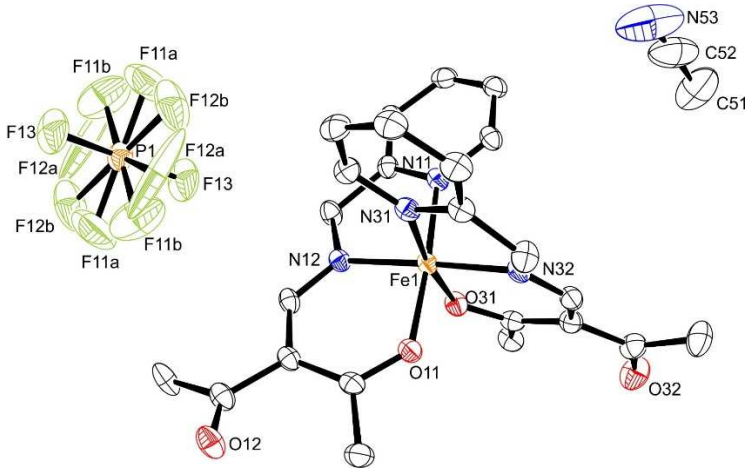

Table S2. Summary of the C–H···π / X–Y···π interactions of the complexes presented in this work.

		C_g	H···C_g/Å Y···C_g/Å	X–H···C_g/° X–Y···C_g/°	X···C_g/Å
8a	C33–H33	N11–C11–C12–C13–C14–C15[a]	2.72	173	3.662(2)
	C36–H36B	Fe1–O31–C39–C38–C37–N32[b]	2.87	141	3.691(2)
	C41–O32	N31–C31–C32–C33–C34–C35[b]	3.3029(17)	83.63(12)	3.389(2)
10a	C22–H22A	Fe1–O11–C19–C18–C17–N12[c]	2.83	143	3.661(3)
	C32–H32	N11–C11–C12–C13–C14–C15[d]	2.99	139	3.758(3)
	C40–H40B	N31–C31–C32–C33–C34–C35[e]	2.67	141	3.489(3)
	C51–H51A	N31–C31–C32–C33–C34–C35[e]	2.76	154	3.667(6)
	C41–O32	N31–C31–C32–C33–C34–C35[e]	3.644(2)	89.24(17)	3.829(3)
15a	C42–H42A	Fe1–O31–C39–C38–C37–N32[f]	2.77	170	3.738(4)

a: 1−x, 1−y, 1−z; b: 2−x, 1−y, 1−z; c: 1/2−x, ½+y, −z; d: x, 4+y, z; e: x, −1+y, z; f: 1−x, −y, 1−z.

Table S3. Selected distances and angles of the π– π and M– π interactions of the complexes presented in this work. C_g(I) is the centroid of the ring number I, α is the dihedral angle between the rings, β is the angle between the vector C_g(I) → C_g(J) and the normal to ring I, γ is the angle between the vector C_g(I) → C_g(J) and the normal to ring J.

	C_g(I)	C_g(J)	C_g–C_g/Å	α/°	β/°	γ/°
8a	N31–C31–C32–C33–C34–C35	N31–C31–C32–C33–C34–C35[a]	3.6622(11)	0.04(9)	18.6	18.6

a: 1−x, 1−y, 1−z.

Table S4. Hydrogen bonds and angles of complexes presented in this work.

	Donor	Acceptor	D–H/Å	H···A/Å	D···A/Å	D–H···A/°
8a	C12–H12	O12[a]	0.95	2.60	3.207(2)	122
	C13–H13	O12[a]	0.95	2.59	3.203(2)	123
	C14–H14	O41[b]	0.95	2.48	3.184(3)	131
	C16–H16A	O43	0.99	2.59	3.565(4)	170
	C16–H16A	O44	0.99	2.57	3.358(2)	136
	C16–H16B	O31[c]	0.99	2.52	3.445(2)	155
	C31–H31	O44	0.95	2.48	3.335(2)	150
	C32–H32	O42	0.95	2.56	3.255(3)	130
	C34–H34	O43[d]	0.95	2.54	3.473(4)	167
	C42–H42A	O12[e]	0.99	2.54	3.384(2)	144
10a	C16–H16A	F13	0.99	2.47	3.323(3)	144
	C22–H22A	O31[f]	0.98	2.54	3.378(3)	143
	C33–H33	F23B[g]	0.95	2.42	3.163(8)	135
	C36–H36A	F22B[h]	0.99	2.28	3.059(7)	134
	C51–H51C	O32[i]	0.98	2.22	3.183(6)	168
15a	C11–H11	O52[k]	0.95	2.53	3.129(5)	121
	C12–H12	O52[k]	0.95	2.46	3.087(5)	124
	C13–H13	O54[l]	0.95	2.55	3.396(7)	149
	C14–H14	O12[m]	0.95	2.41	3.198(4)	140
	C16–H16B	O53	0.99	2.46	3.298(9)	142
	C31–H31	O51	0.95	2.58	3.391(5)	143
	C32–H32	O32[n]	0.95	2.33	3.198(5)	151
	C36–H36A	O51[o]	0.99	2.53	3.427(5)	151
	C40–H40B	O32[b]	0.98	2.58	3.336(4)	134

a: x, y, −1+z; b: 1−x, −y, 1−z; c: 2−x, −y, 1−z; d: 1−x, 1−y, 1−z; e: 1+x, y, −z+1; f: 1/2−x, 1/2+y, −z; g: x, 1+y, z; h: 1−x, y, 1/2−z; i: 1/2+x, −5/2−y, z; k: 1/2+x, 1/2−y, −1/2+z; l: 1+x, y, z; m: 1−x, −y, 2−z; n: −1/2+x, 1/2−y, 1/2+z; o: −1/2+x, 1/2−y, −1/2+z.

Figure S3. Plots of the $\chi_M T$ product vs. T for the iron(II) complexes **1** (left) and **2** (right).

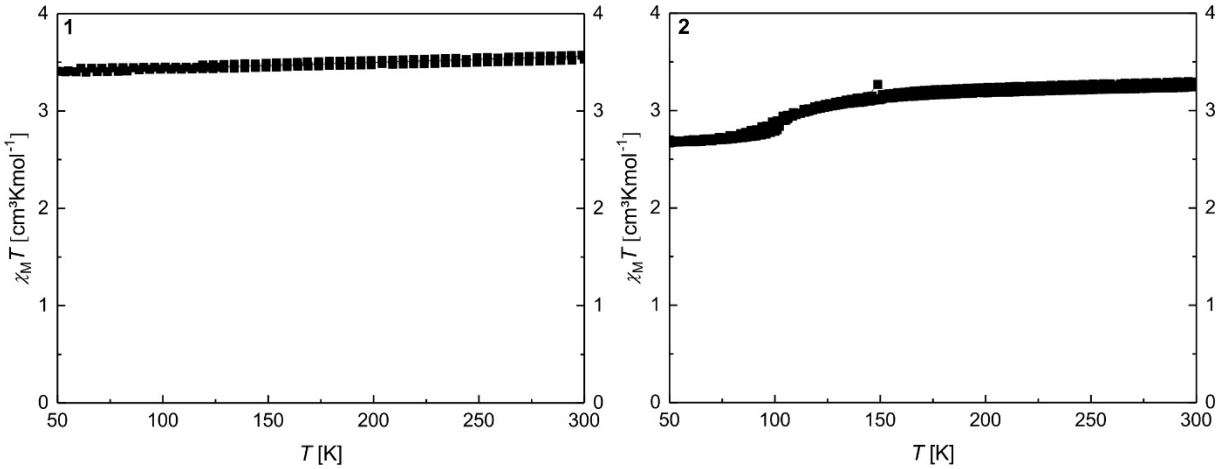

Figure S4. Plots of the $\chi_M T$ product vs. T for complexes **4** (top left), **6** (top right), **7** (middle left), **8** (middle right), **9** (bottom left), and **10** (bottom right).

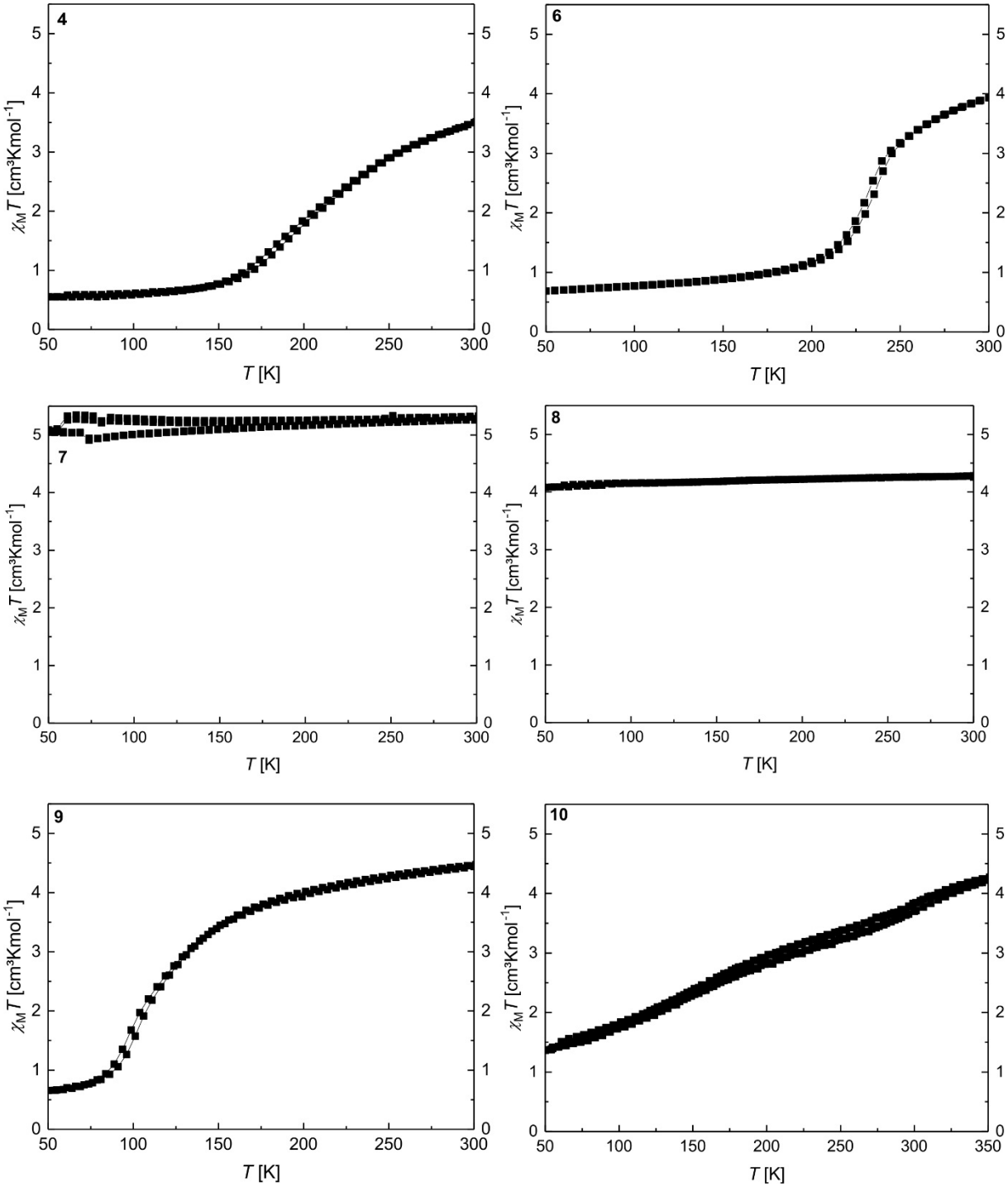

Figure S5. Plots of the $\chi_M T$ product vs. T for complexes **11** (top left), **12** (top right), **13** (middle left), **14** (middle right), and **15** (bottom).

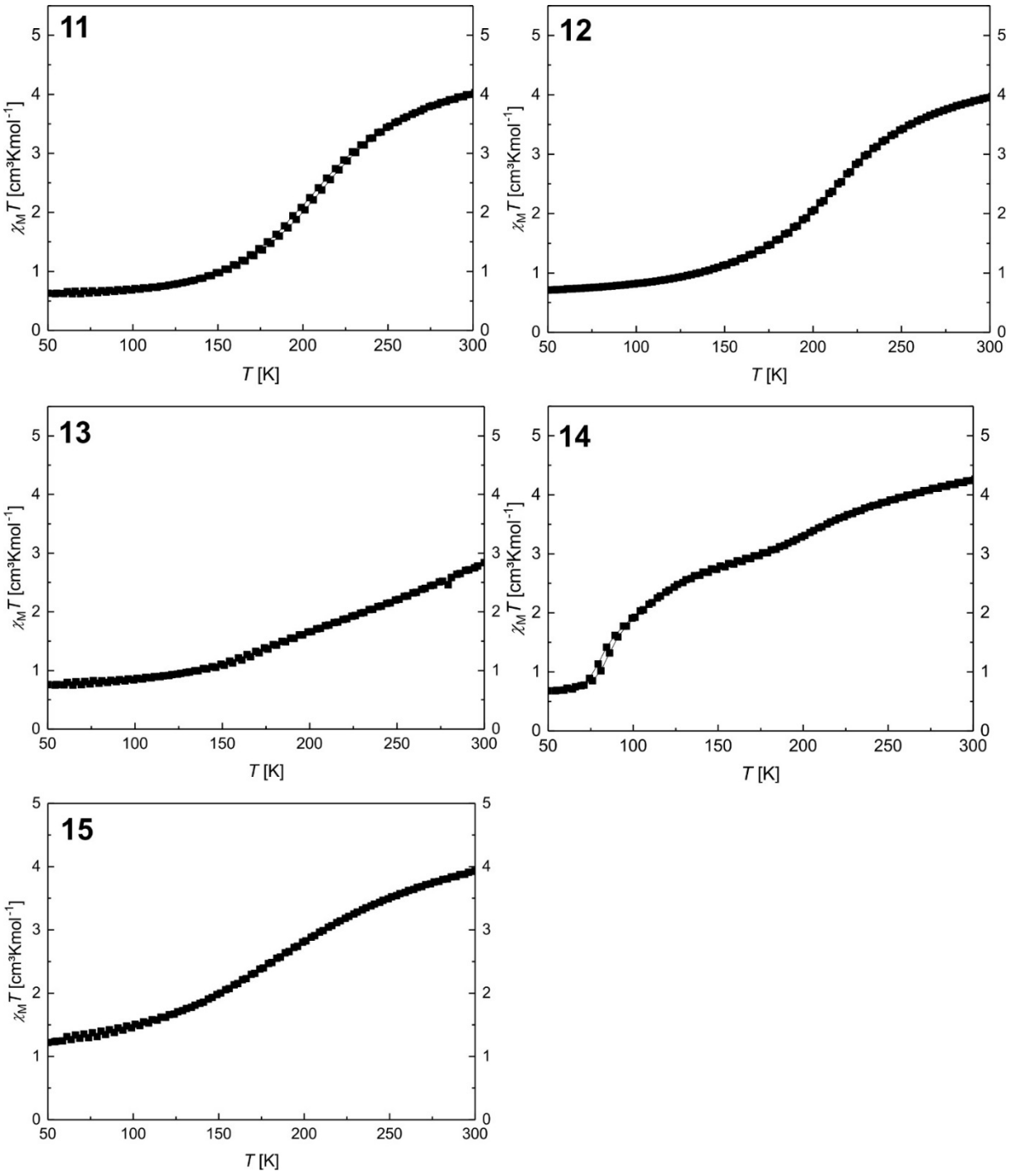

Figure S6. UV-Vis spectra of complexes **1** (top left), **2** (top right), **3** (middle left), **4** (middle right), **5** (bottom left), and **6** (bottom right).

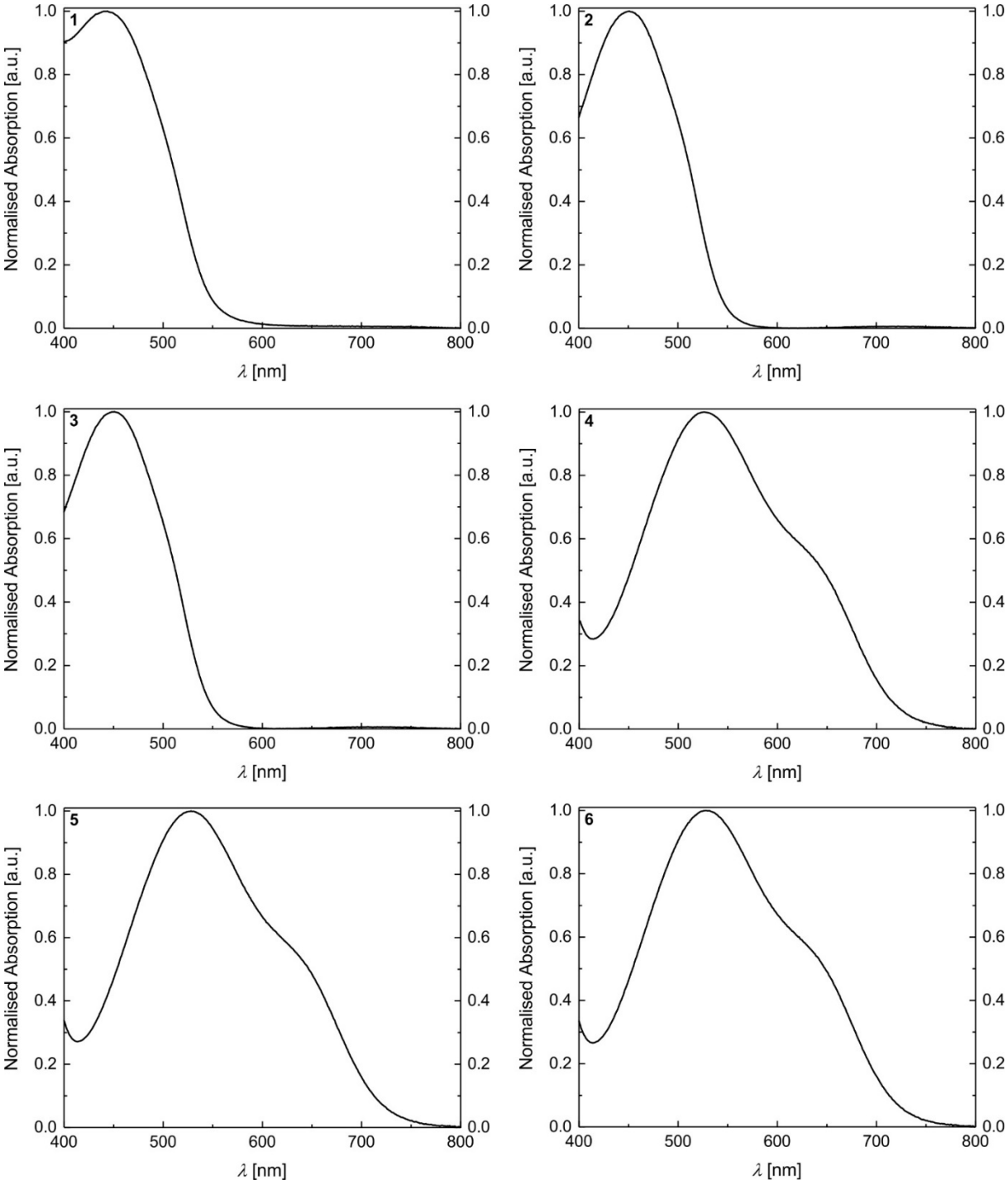

Figure S7. UV-Vis spectra of complexes **7** (top left), **8** (top right), **9** (middle left), **10** (middle right), **11** (bottom left), and **12** (bottom right).

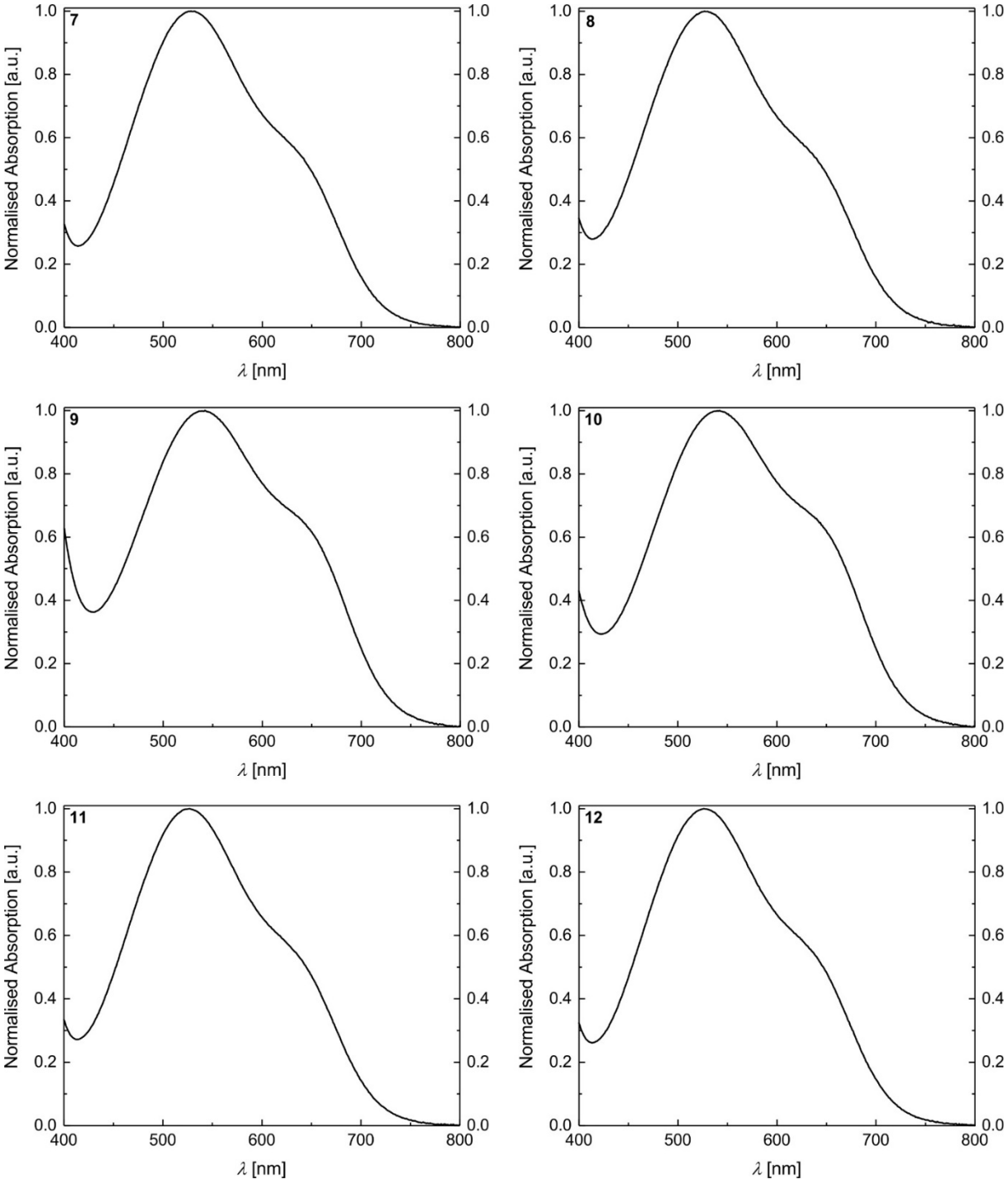

Figure S8. UV-Vis spectra of complexes **13** (top left), **14** (top right), and **15** (bottom).

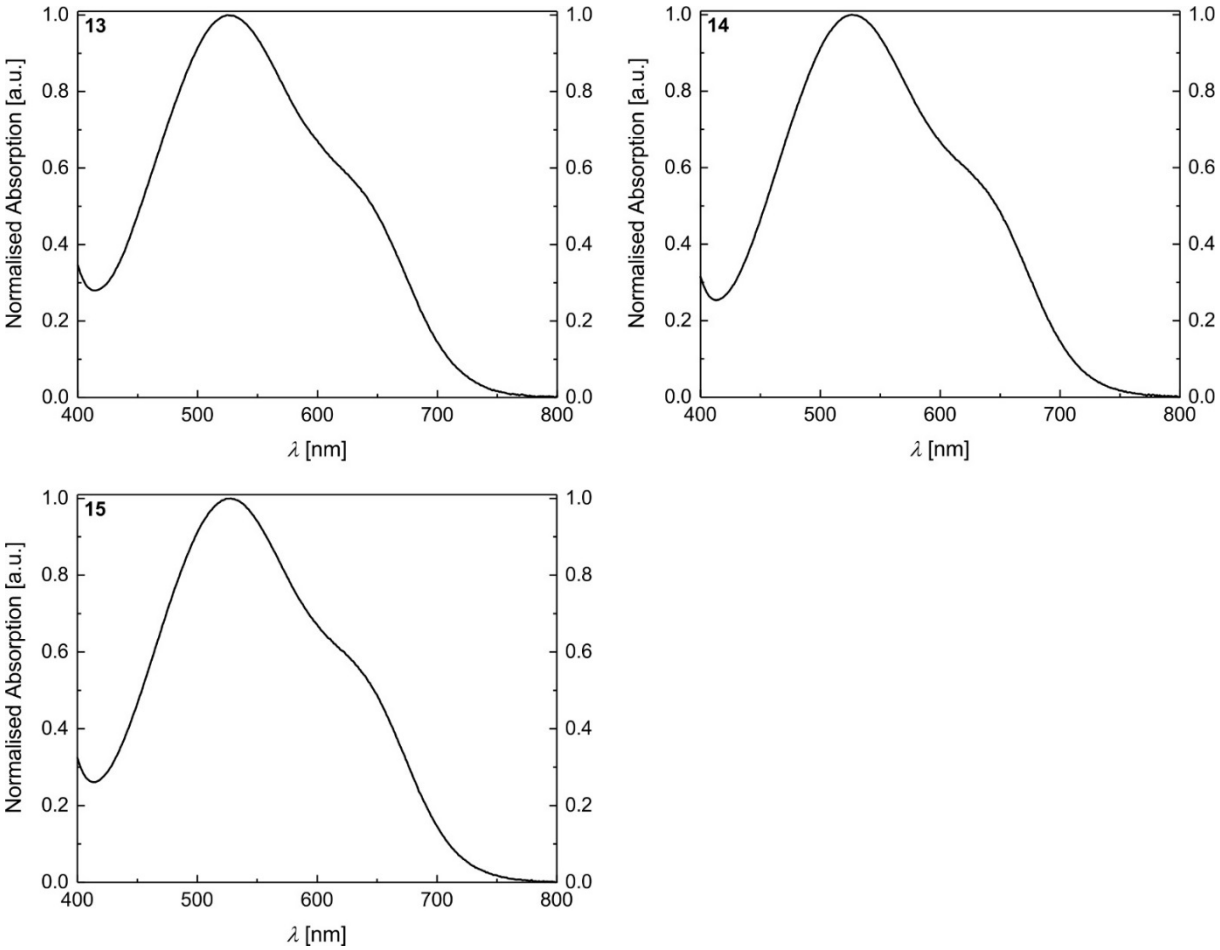

Figure S9. Cyclic voltammograms of complexes **1** (top left), **2** (top right), **3** (middle left), **4** (middle right), **5** (bottom left), and **6** (bottom right).

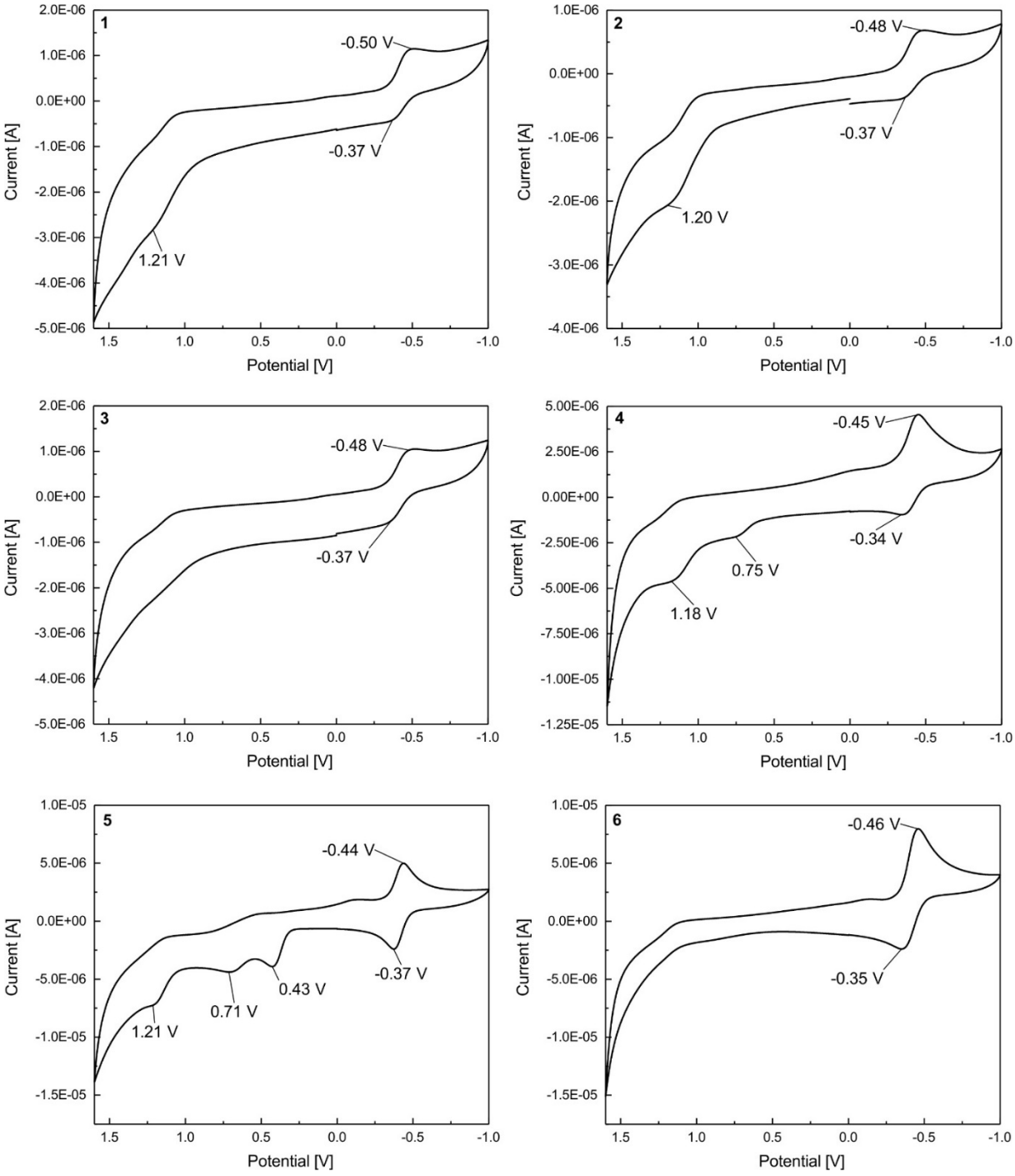

Figure S10. Cyclic voltammograms of complexes **7** (top left), **8** (top right), **9** (middle left), **10** (middle right), **11** (bottom left), and **12** (bottom right).

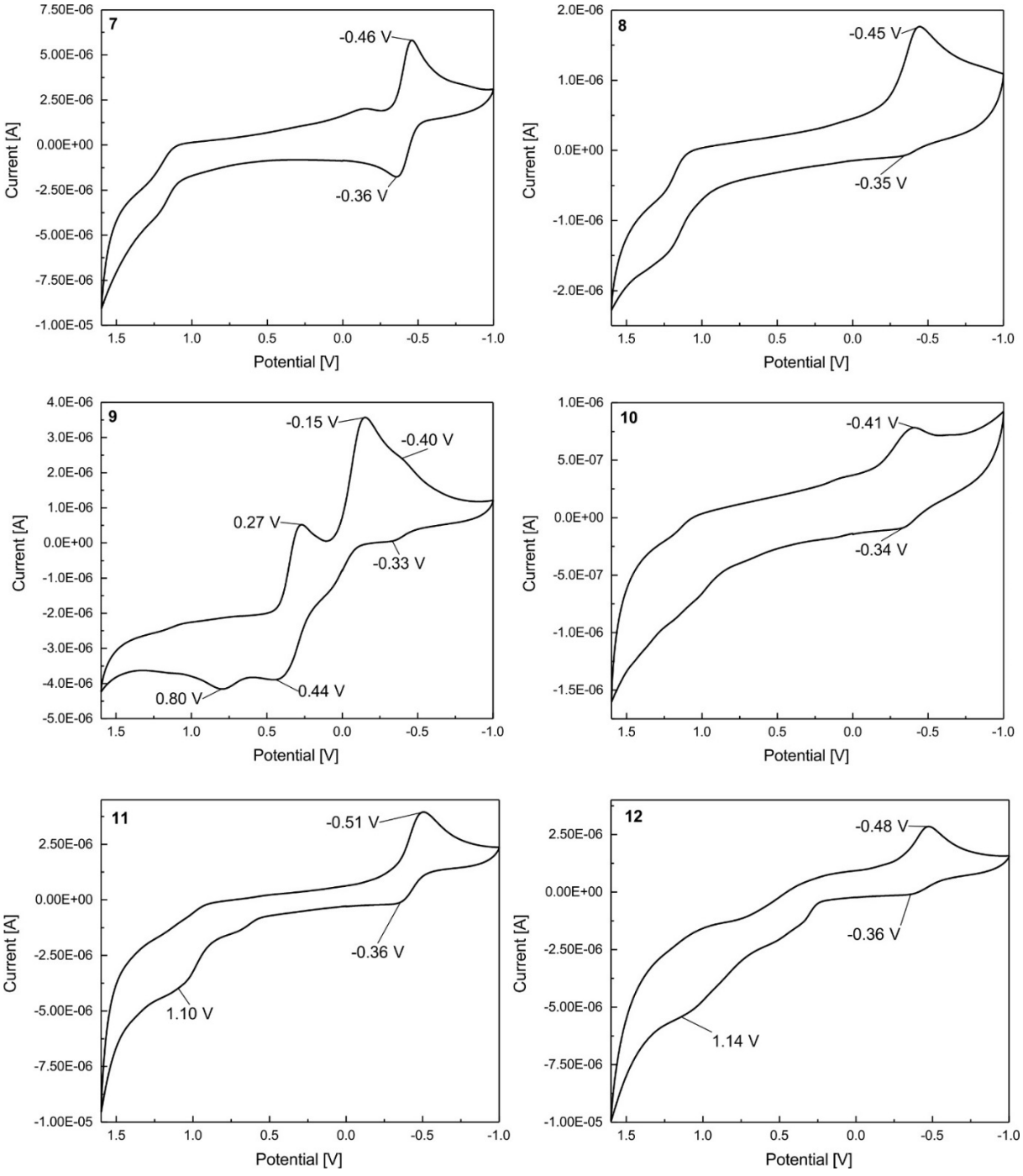

Figure S11. Cyclic voltammograms of complexes **13** (top left), **14** (top right), **15** (bottom left), and **17** (bottom right).

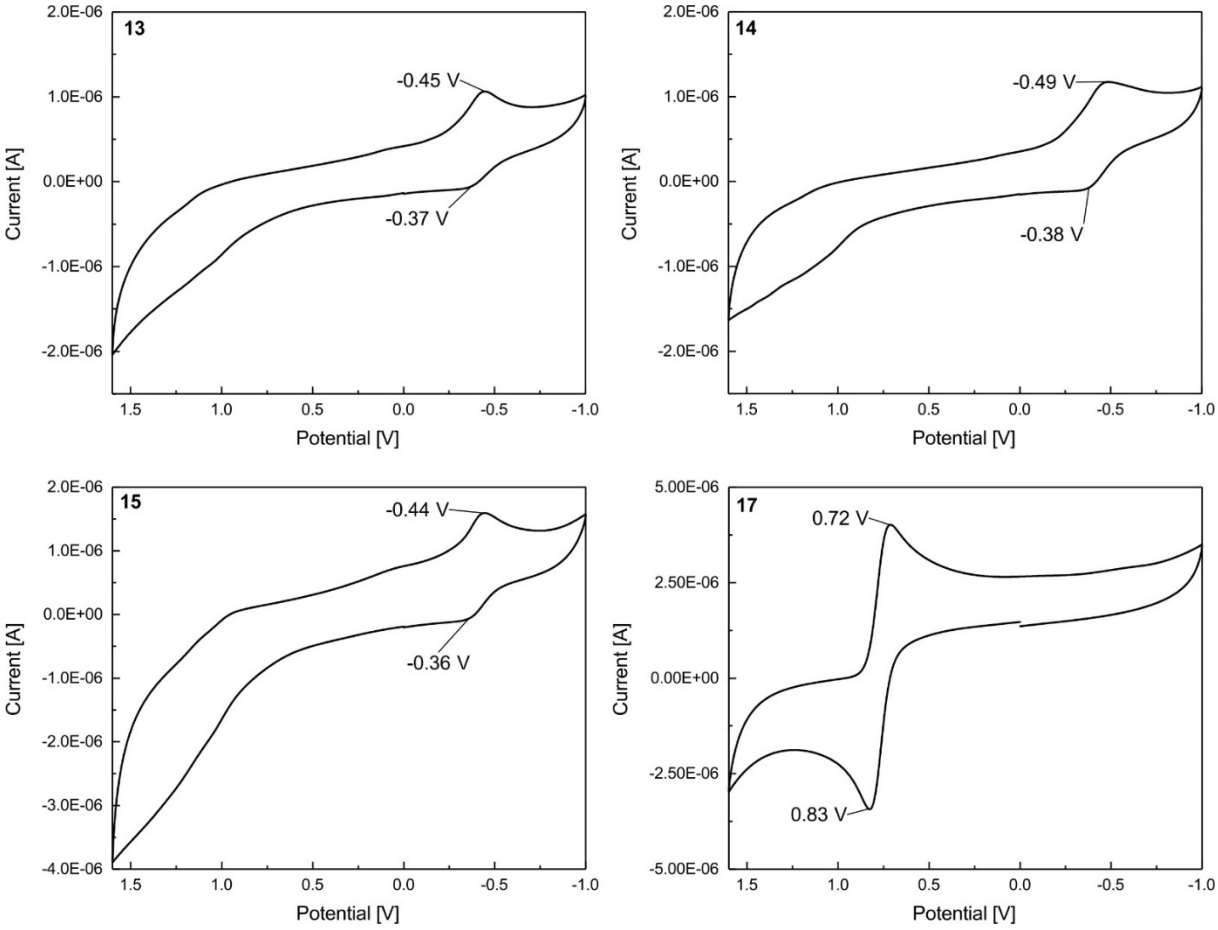

Figure S12. TG measurements of **1**–**6**.

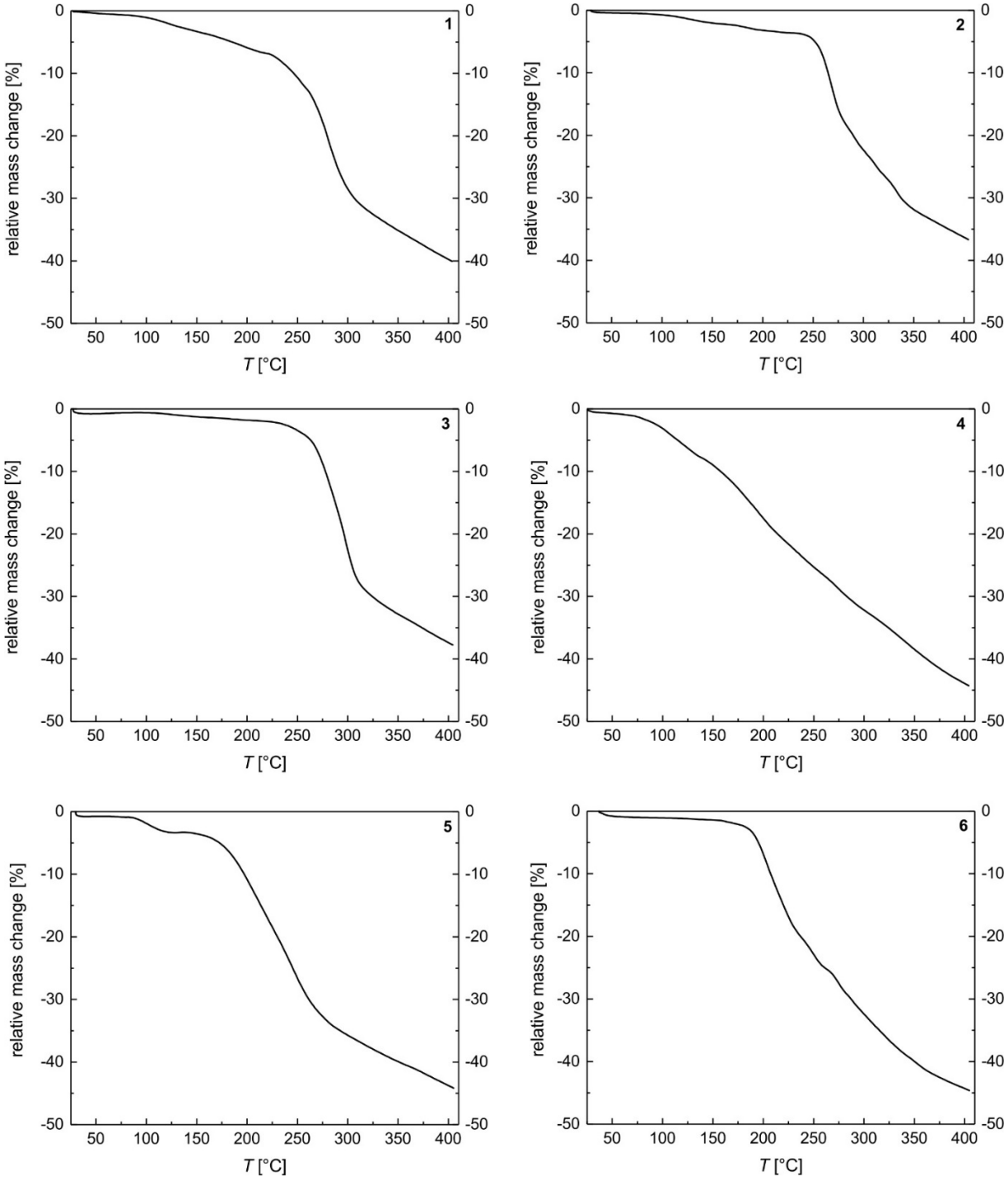

Figure S13. TG measurements of **7**–**14**.

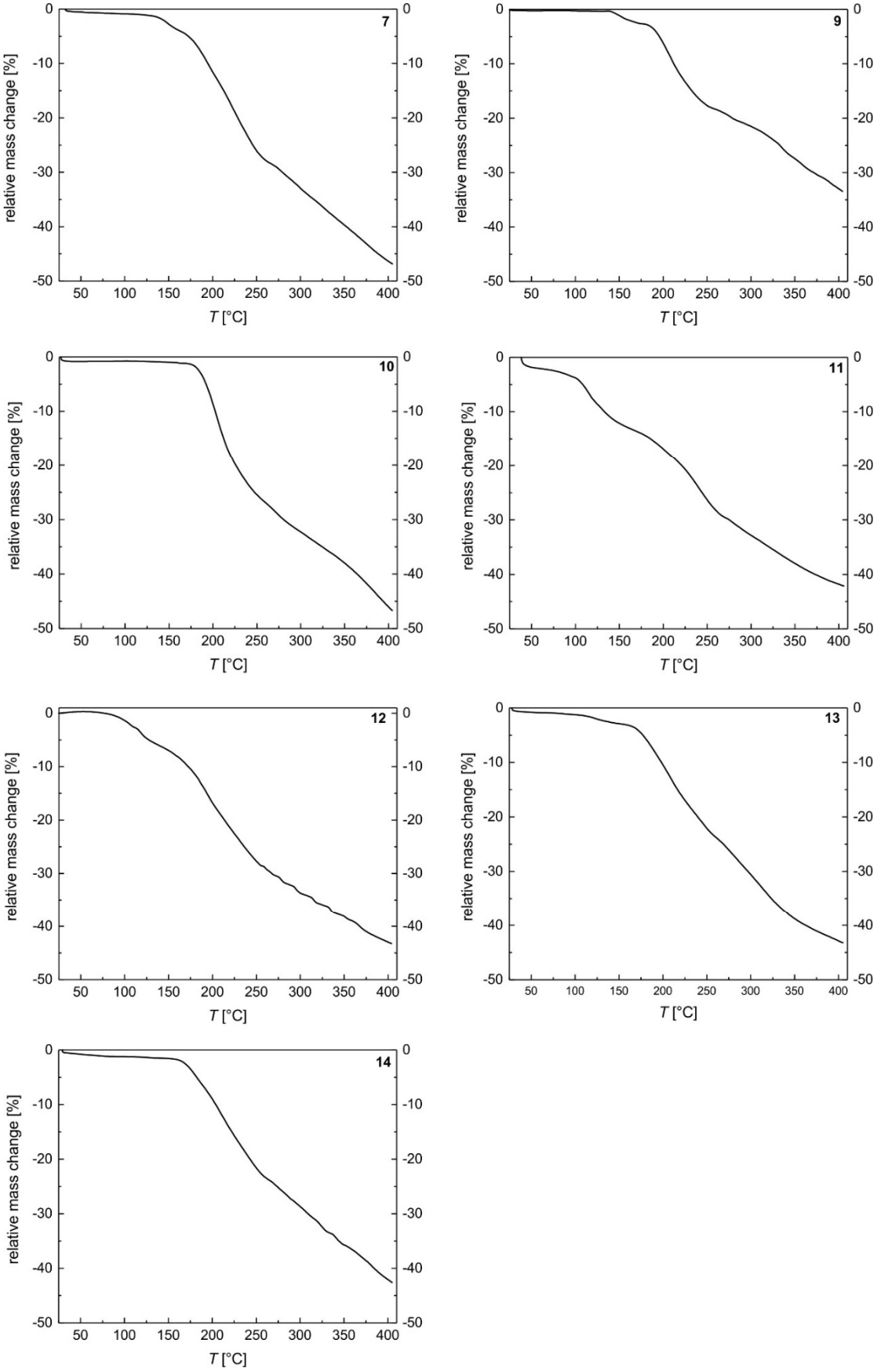

8. Isostructural iron(III) spin crossover complexes with a tridentate Schiff base-like ligand: X-ray structures and magnetic properties

Katja Dankhoff and Birgit Weber*

Department of Chemistry, University of Bayreuth, Universitätsstr. 30, 95447 Bayreuth, Germany. E-mail: weber@uni-bayreuth.de; Tel: +49 (0)921552555

Published in *Dalton Trans.* **2019**, DOI: 10.1039/c9dt00846b

Abstract: Here we present two isostructural iron(III) spin crossover complexes with the same tridentate ligand and perchlorate or tetrafluoroborate as counter ion. Single crystal X-ray structures in the high spin and low spin state were obtained for both complexes. An abrupt spin transition above 100 K is observed with the transition temperature depending on the size of the anion.

8.1 Introduction

Spin crossover (SCO) is an interesting phenomenon which can occur in 3d transition metal complexes with a d^{4-7} electronic configuration. The spin state of the metal centre can be switched between the high spin (HS) state and the low spin (LS) state by external stimuli such as temperature, pressure, or light irradiation. This results in significant changes in the structural, vibrational, magnetic, or optical properties of the material.[1] Due to the pronounced property changes in SCO compounds, various applications, such as data storage and/or

temperature/pressure sensors are possible.[2,3] For iron(III) complexes both spin states are paramagnetic with $S = 5/2$ (HS) and $S = 1/2$ (LS). Upon SCO the bond lengths shorten and the volume of the unit cell is smaller in the LS than in the HS state. In the case of iron(II) the structural and magnetic changes upon SCO are more pronounced with a paramagnetic ($S = 2$) HS state and a diamagnetic ($S = 0$) LS state. However, iron(II) complexes are often air sensitive. Therefore the focus has recently shifted towards the more stable iron(III) complexes.[4,5] Compared to the large amount of iron(II) spin crossover complexes, where systematic investigations on the impact of different parameters such as counter ions or the inclusion of solvent molecules on the spin crossover properties (hysteresis, control of transition temperature) are available,[3,6] in the case of iron(III) the data base is limited.

Recently, we published the synthesis and magnetic behaviour of iron(II) and iron(III) complexes with tridentate, Schiff base-like ligands. We found that the iron(II) complexes remain HS, whereas the iron(III) complexes show mostly gradual and incomplete SCO.[7] Here we report two isostructural iron(III) complexes with the same tridentate *NNO* Schiff base-like ligand, but different anions (BF_4^- and ClO_4^-) both showing a similar abrupt SCO. It is well known, that different anions alter the magnetic properties of iron(II) and iron(III) complexes.[8–11] In the case of iron(III) quinolylsalicyladimate complexes it was possible to tune the SCO properties through variation of the size of the counter ion, small anions stabilised the LS state whereas larger anions stabilised the HS state.[12] However, the opposite trend was observed for $[Fe(Him)_2(happen)]^+$ complexes.[13] Those examples show that it is difficult to establish general rules, especially since differences in size and shape of the anions often trigger differences in the crystal packing.

8.2 Results and discussion

Here we present a pair of isostructural complexes that allow a direct evaluation of the impact of anion size on the transition temperature. The complexes were synthesised using the same synthetic procedure as described previously.[7] The tridentate Schiff base-like ligand HL, iron(III) nitrate nonahydrate, and sodium acetate were dissolved in methanol and heated to reflux for one hour. The respective iron(III) SCO complexes $[Fe(L)_2]BF_4$ (**1**) or $[Fe(L)_2]ClO_4$

(**2**) were precipitated by adding an aqueous solution of the corresponding anion BF_4^- (**1**) or ClO_4^- (**2**) (Scheme 1).

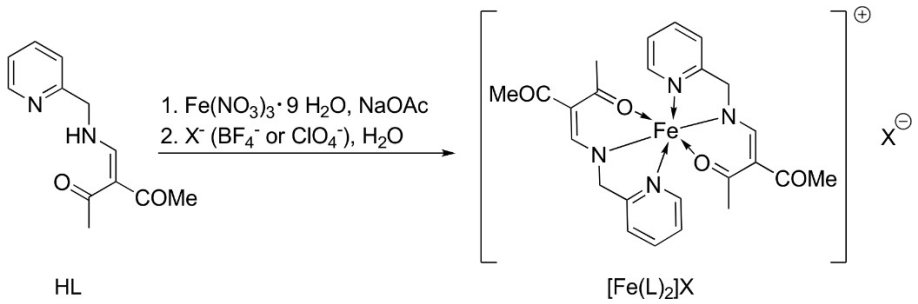

Scheme 1 Synthesis of the complexes discussed in this work and used abbreviations.

Crystals suitable for X-ray structure analysis were obtained by slow diffusion of diethyl ether into an acetonitrile solution of the coordination compound. The two iron(III) complexes crystallise in the orthorhombic space group $P2_12_12_1$ and the crystallographic data were determined at 175 K (**1-HS**), 150 K (**2-HS**), 133 K (**1-LS**), and 100 K (**2-LS**) and are summarised in the ESI, Table S1. An ORTEP drawing of **1** and **2** in the LS state is shown in Fig. 1, ORTEP drawings of both spin states of the complexes with a full numbering scheme is given in the ESI, Fig. S1 and S2. The asymmetric unit consists of one complex molecule and one anion for both complexes. The iron(III) centre is coordinated by two tridentate ligands in an octahedral fashion.

Selected bond lengths, angles, and the octahedral distortion parameter Σ of the coordination sphere are given in Table 1. The bond lengths are significantly shorter in the LS state than in the HS state (Fe–N_{py} 0.15 Å, Fe–N_{ax} 0.13 Å, and Fe–O 0.06 Å in average). In order to determine the spin state of the iron(III) centre the N_{py}–Fe–O angle was taken into account; it has an average value of 162° in the HS state and 173° in the LS state for both complexes. The calculated octahedral distortion parameter Σ supports this assumption, as it is much larger in the HS state (80° for **1-HS** and 84° for **2-HS**) than in the LS state (43° for **1-LS** and 44° for **2-LS**). This is in agreement with previously reported complexes of this type.[5,7]

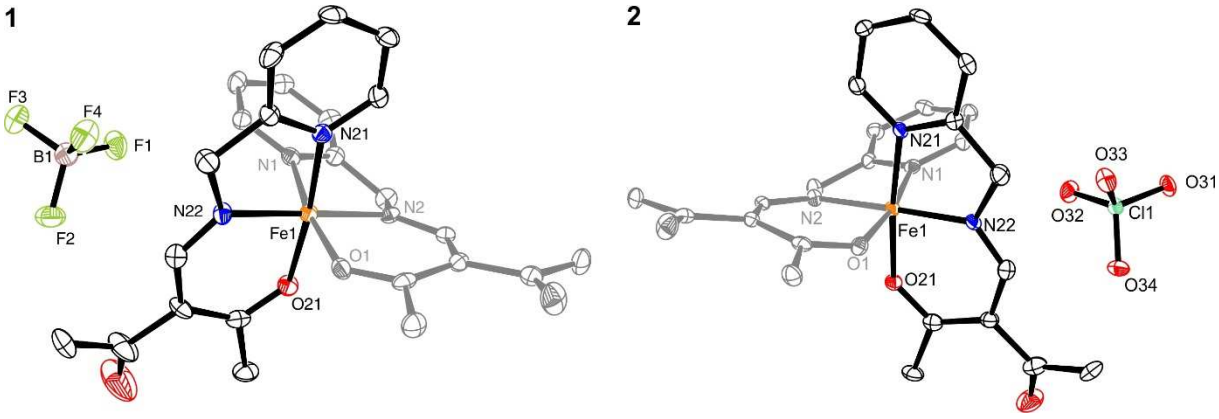

Fig. 1 ORTEP drawing of **1** (LS, left) and **2** (LS, right). Ellipsoids were drawn at 50% probability level. Hydrogen atoms were omitted for clarity.

Due to the occupation of the anti-bonding e_g* orbitals in the HS state the bond lengths within the first coordination sphere are significantly longer than in the LS state. The volume of the unit cell is 2.8% (**1**) and 2.3% (**2**) larger in the HS state compared to the LS state.

Table 1. Spin state, selected bond lengths [Å], angles [°], and the octahedral distortion parameter Σ [°] of complexes **1** and **2**.

	S	Fe–N_{py}	Fe–N_{ax}	Fe–O	N_{py}–Fe–O	Σ
1-HS	5/2	2.133(4)	2.028(3)	1.953(3)	161.69(14)	80
		2.108(4)	2.046(3)	1.956(3)	162.79(14)	
1-LS	1/2	1.982(4)	1.901(3)	1.902(3)	171.40(14)	43
		1.973(3)	1.912(3)	1.904(3)	174.11(15)	
2-HS	5/2	2.145(3)	2.030(3)	1.956(3)	160.84(12)	84
		2.114(3)	2.057(3)	1.954(3)	162.22(12)	
2-LS	1/2	1.978(3)	1.901(3)	1.904(2)	171.25(12)	44
		1.962(3)	1.911(3)	1.9040(19)	173.97(12)	

Several C–H···π interactions and hydrogen bonds are present in the crystal packing of the complexes. Details of those intermolecular interactions are summarised in Tables S2 and S3. As previously shown,[7] the complex molecules form two different layers in the crystal packing, with each layer being separated from the other by the anions. The molecules in the first layer are turned 180° with respect to the second layer (Fig. 2).

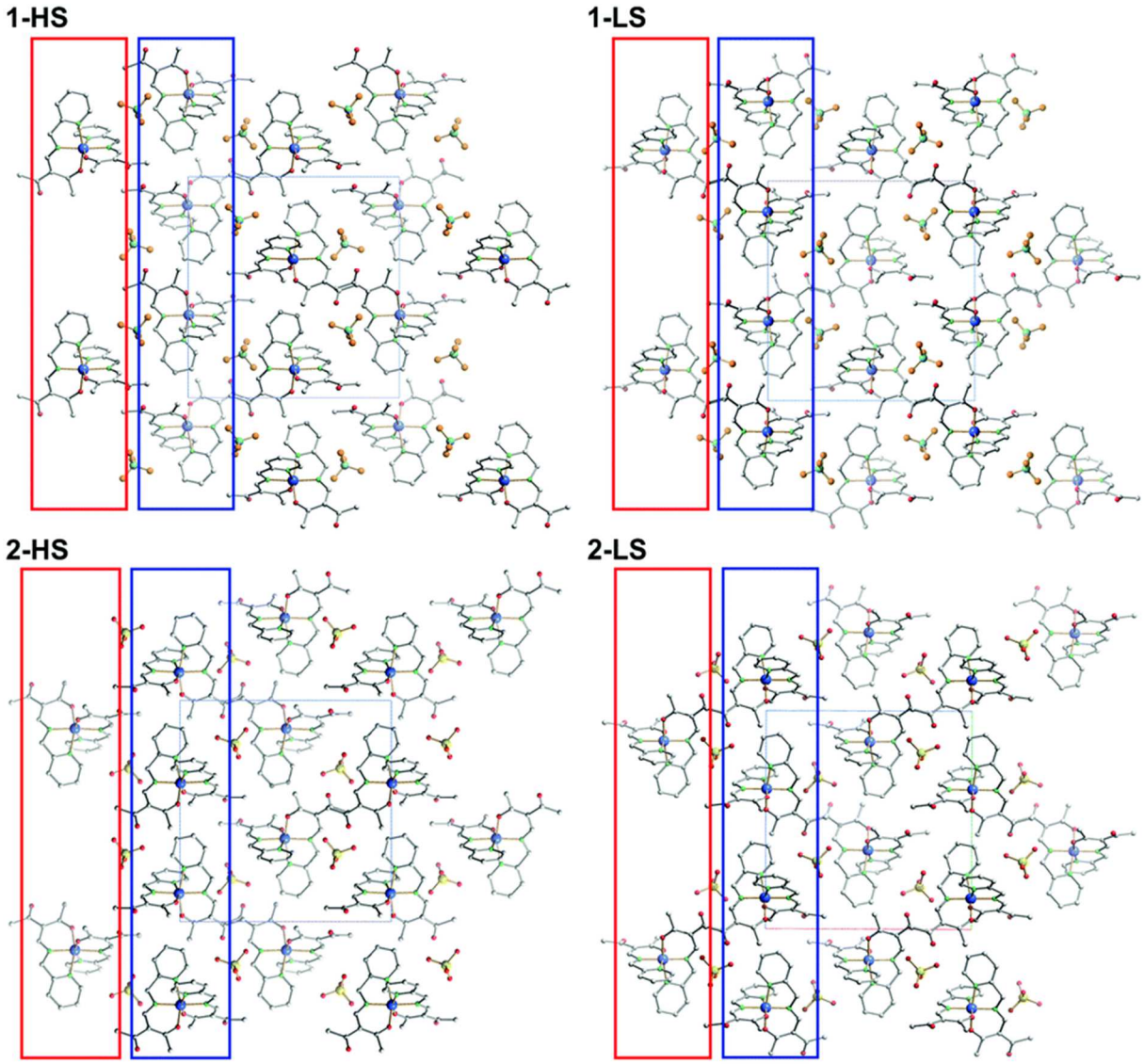

Fig. 2 Packing of **1** (HS, top left and LS, top right) and **2** (HS, bottom left and LS, bottom right) in the crystal along [100]. Hydrogen atoms were omitted for clarity. Red and blue boxes highlight the different layers discussed in the main text.

In the HS state of both complexes two C–H···π interactions are present; one between the aromatic C3–H3 of one pyridyl ring and the six-membered ring made up by the chelate cycle of one tridentate ligand and the iron(III) centre (Fe1–O21–C29–C28–C27–N22). The second one is between a methyl group of one tridentate ligand (C30–H30B for **1** and C30–H30C for **2**) and the pyridyl ring of a neighbouring ligand (N21–C21–C22– C23–C24–C25). In the LS state of both complexes, only the second C–H···π interaction can be found. Many non-classical hydrogen bonds are observed for both complexes in both spin states; mostly between C–H groups of the tridentate ligands and the fluorine or the oxygen atoms of the respective anions. Interactions between C–H groups and keto oxygens of a neighbouring ligand are observed as

well. In complex **1**, there are two hydrogen bonds which are present in the HS state, but not in the LS state, namely C1–H1···F2 and C26–H26B···F3. In case of complex **2**, C1–H1···O31 is the only interaction which can be observed in the HS, but not the LS state. Pictures of the packing of the complexes highlighting the hydrogen bonds are shown in Fig. 3.

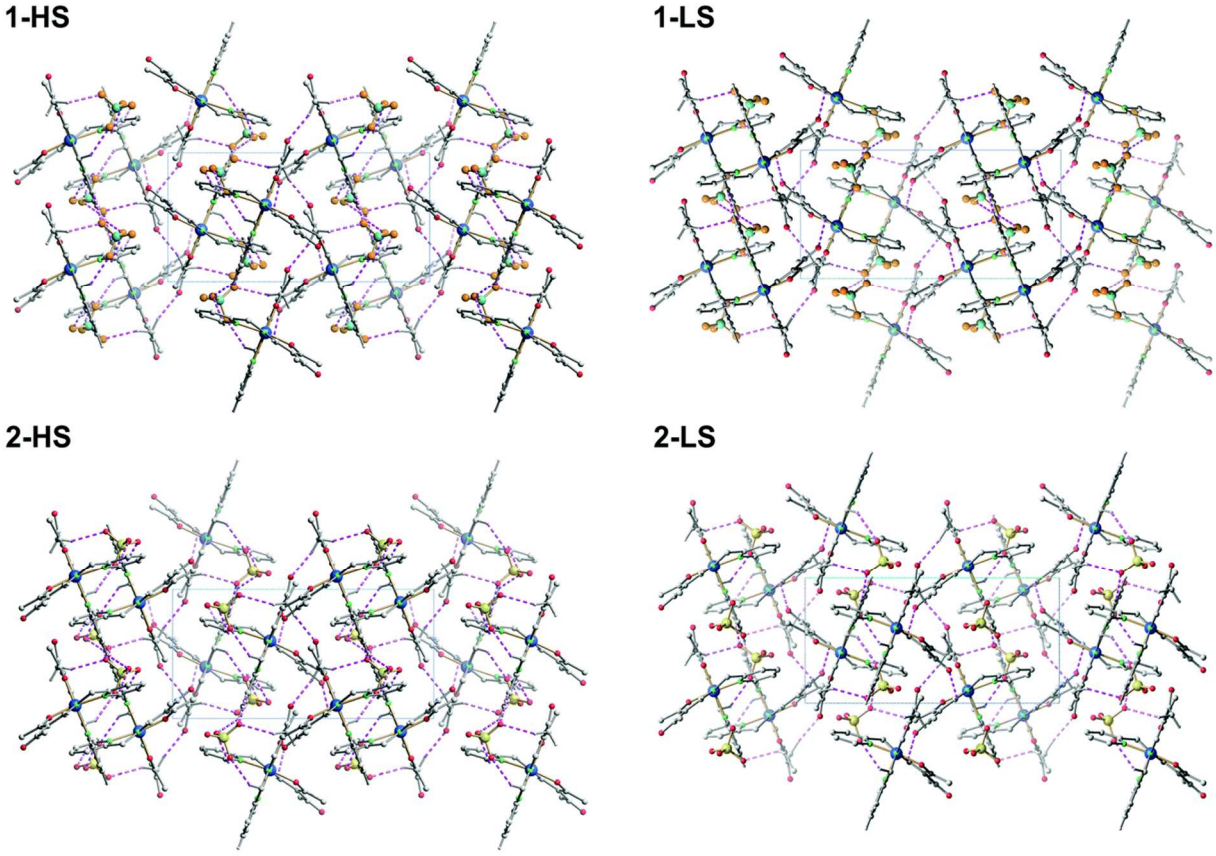

Fig. 3 Packing of **1** (HS, top left and LS, top right) and **2** (HS, bottom left and LS, bottom right) in the crystal along [010]. Hydrogen atoms not involved in any hydrogen bonds were omitted for clarity. Hydrogen bonds were drawn as pink, dashed lines.

The Hirshfeld surface, mapped over d_{norm}, of complex **1-HS** is shown in Fig. 4, top left as example. There are dominant H···O interactions between the methyl group of one ligand and the keto oxygen of another (highlighted with a red circle in Fig. 4). Those interactions appear as distinct spikes in the 2D fingerprint plot (Fig. 4, bottom left) and form a chain of complex molecules along [100]. Other visible spots in the surface are caused by H···F interactions involving the BF_4^- anion and H···H interactions. The same kind of interactions are observed for the LS state of the complex, as well as for complex **2** in both spin states. The Hirshfeld surfaces

and fingerprint plots for those structures can be found in the ESI, Fig. S3–S5. The relative contribution of the different interactions to the Hirshfeld surface was calculated and is shown in Fig. 5. It can be seen that most interactions originate form H···H contacts, H···O interactions to keto oxygen, and H···anion interactions. Please note the very similar results for both complexes in both spin states that explains nicely the very similar spin crossover curve for both samples.

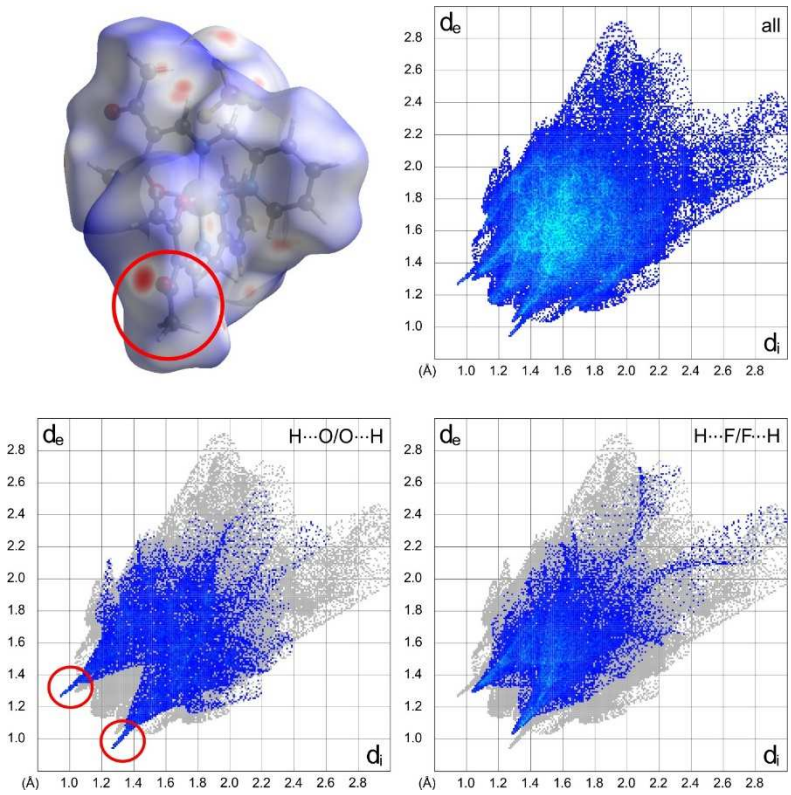

Fig. 4 Hirshfeld surface mapped with d_{norm} (top left), fingerprint plots: full (top right), resolved into H···O/O···H (bottom left), and H···F/F···H (bottom right) contacts of complex **1-HS**.

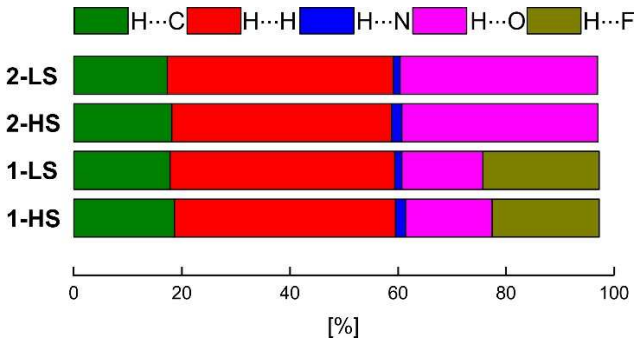

Fig. 5 Relative contributions of different intermolecular interactions to the Hirshfeld surface area.

Temperature dependent magnetic susceptibility measurements were performed using a SQUID magnetometer to investigate the possible SCO properties of the two complexes. Measurements were performed with an applied field of 5000 G and in settle mode. Both complexes show an abrupt ST below 200 K; the $\chi_M T$ vs. T plots are shown in Fig. 6. At 300 K the iron centres of both complexes are clearly in the HS state with $\chi_M T$ values of 4.60 and 4.23 cm^3 K mol^{-1} (**1** and **2**, respectively). The transition temperature $T_{1/2}$ for complex **1** is at 145 K and for complex **2** 115 K. At 50 K, the $\chi_M T$ values indicate a clear LS state for both complexes (0.57 and 0.58 cm^3 K mol^{-1}, respectively). Those values are typical for both spin states of iron(III) complexes with this ligand type.[7] A small kinetic effect can be observed for the ST, the compounds show a small (7 K wide) hysteresis when measured in sweep mode with a scan rate of 5 K min^{-1} (Fig. S6). This hysteresis disappears when the samples were measured in settle mode.

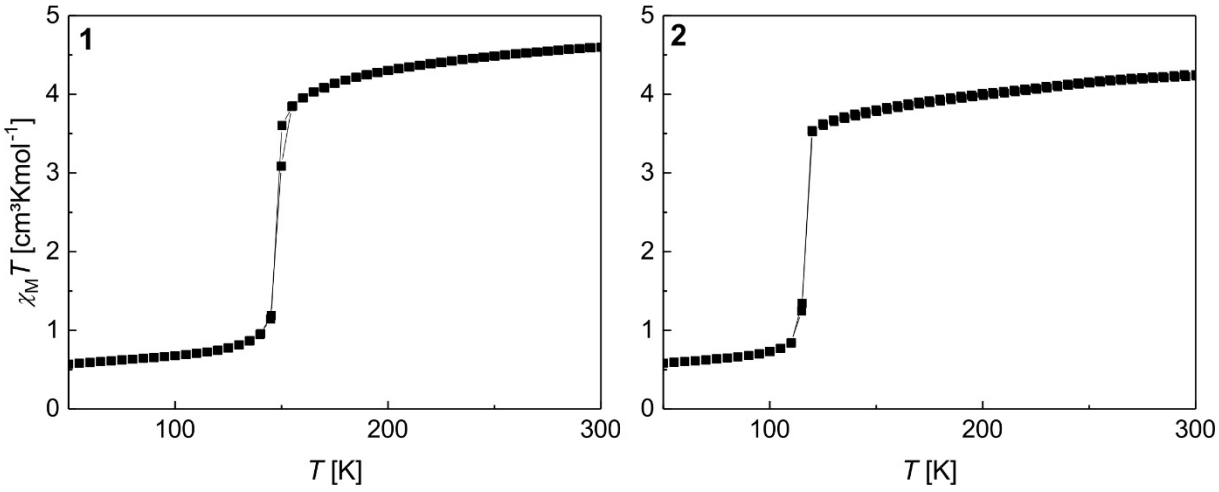

Fig. 6 Plot of the $\chi_M T$ product vs. T for complex **1** (left) and **2** (right).

The abrupt spin transition can be explained with the large number of intermolecular interactions, while the kinetic effects are most likely due to the breaking of intermolecular interactions in the crystal packing of the complexes (transition from HS to LS state). The differences in the transition temperature between the two complexes is best explained with the size of the counter ion. The smaller BF_4^- in **1** stabilises the LS state leading to a higher $T_{1/2}$ compared to **2** with the larger ClO_4^- as anion. This trend is comparable to the matrix effects observed for metal dilution experiments for iron(II) complexes, where an substitution of iron(II) by manganese(II) or zinc(II) shifts the transition temperature due to a variation of the internal pressure of the different host lattices.[14,15] For the example $[Fe/Zn/Mn(pic)_3]^{2+}$ (pic = 2-picolylamine) the smaller zinc(II) ion stabilises the LS state by increasing $T_{1/2}$ to 117 K compared to the corresponding host lattice with the larger manganese(II) ($T_{1/2}$ = 97 K) and the pure iron(II) complex ($T_{1/2}$ = 74 K).[14] A similar effect upon halogen substitution on the spin transition temperature in iron(III) complexes was recently observed for compounds bearing salicylaldehyde-2-pyridyl-hydrazone-type ligands and dicarboxylic acids as counter ion.[16]

8.3 Conclusions

We presented two isostructural iron(III) spin crossover complexes with the same tridentate ligand but different anions. Both complexes were investigated considering their magnetic behaviour and showed an abrupt, complete spin transition above 100 K. It was possible to obtain the single crystal X-ray structures of both complexes in the high spin and the low spin state. Both compounds crystallised in the orthorhombic space group $P2_12_12_1$. The packing of the two complexes in the crystal is the same, for the spin transition of complex **1** two hydrogen bonds have to be broken, whereas only one of those is missing in the low spin state of complex **2**. The transition temperature is shifted by 30 K to lower temperature for **2** with the larger anion. This can be explained with different internal pressures generated by the host lattice.

Conflicts of interest

There are no conflicts to declare.

8.4 Notes and references

[1] (a) O. Sato, J. Tao, Y.-Z. Zhang, *Angew. Chem., Int. Ed.* **2007**, *46*, 2152–2187; (b) A. B. Gaspar, M. Seredyuk, P. Gütlich, *J. Mol. Struct.* **2009**, *924–926*, 9–19; (c) P. Gütlich, *Eur. J. Inorg. Chem.* **2013**, 581–591; (d) Spin Crossover in Transition Metal Compounds I-III, ed. P. Gütlich and H. A. Goodwin, Springer, Berlin/Heidelberg, **2004**, pp. 233–235; (e) Spin-Crossover Materials, ed. M. A. Halcrow, John Wiley & Sons Ltd, Chichester, **2013**; (f) A. B. Gaspar, B. Weber, in Molecular Magnetic Materials, ed. B. Sieklucka and D. Pinkowicz, Wiley-VCH Verlag GmbH & Co. KGaA, Weinheim, Germany, **2017**, pp. 231–252; (g) K. S. Murray, *Aust. J. Chem.* **2009**, *62*, 1081–1101; (h) A. Bousseksou, G. Molnar, L. Salmon, W. Nicolazzi, *Chem. Soc. Rev.* **2011**, *40*, 3313–3335.

[2] (a) A. B. Gaspar, V. Ksenofontov, M. Seredyuk, P. Gütlich, *Coord. Chem. Rev.* **2005**, *249*, 2661–2676; (b) K. Senthil Kumar, M. Ruben, *Coord. Chem. Rev.* **2017**, *346*, 176–205; (c) C. Atmani, F. El Hajj, S. Benmansour, M. Marchivie, S. Triki, F. Conan, V. Patinec, H. Handel, G. Dupouy, C. J. Gómez-García, *Coord. Chem. Rev.* **2010**, *254*, 1559–1569.

[3] E. Collet, P. Guionneau, *C. R. Chim.* **2018**, *21*, 1133–1151.

[4] M. Nihei, T. Shiga, Y. Maeda, H. Oshio, *Coord. Chem. Rev.* **2007**, *251*, 2606–2621.

[5] D. J. Harding, P. Harding, W. Phonsri, *Coord. Chem. Rev.* **2016**, *313*, 38–61.

[6] (a) J. Tao, R.-J. Wei, R.-B. Huang, L.-S. Zheng, *Chem. Soc. Rev.* **2012**, *41*, 703–737; (b) M. A. Halcrow, *Chem. Soc. Rev.* **2011**, *40*, 4119–4142; (c) P. Guionneau, *Dalton Trans.* **2014**, *43*, 382–393; (d) S. Brooker, *Chem. Soc. Rev.* **2015**, *44*, 2880–2892.

[7] K. Dankhoff, S. Schneider, R. Nowak, B. Weber, *Z. Anorg. Allg. Chem.* **2018**, *644*, 1839–1848.

[8] W. Phonsri, L. C. Darveniza, S. R. Batten, K. S. Murray, *Inorganics* **2017**, *5*, 51.

[9] A. Tsukiashi, M. Nakaya, F. Kobayashi, R. Ohtani, M. Nakamura, J. M. Harrowfield, Y. Kim, S. Hayami, *Inorg. Chem.* **2018**, *57*, 2834–2842.

[10] S. Sundaresan, I. Kühne, C. Kelly, A. Barker, D. Salley, H. Müller-Bunz, A. Powell, G. Morgan, *Crystals* **2019**, *9*, 19.

[11] (a) T. Boonprab, P. Harding, K. S. Murray, W. Phonsri, S. G. Telfer, A. Alkaş, R. Ketkaew, Y. Tantirungrotechai, G. N. L. Jameson, D. J. Harding, *Dalton Trans.* **2018**, *47*, 12449–12458; (b) N. Phukkaphan, D. L. Cruickshank, K. S. Murray, W. Phonsri, P. Harding, D. J. Harding, *Chem. Commun.* **2017**, *53*, 9801–9804; (c) R. N. Sylva, H. A. Goodwin, *Aust. J. Chem.* **1967**, *20*, 479; (d) Y. Garcia, P. J. van Koningsbruggen, R. Lapouyade, L. Rabardel, O. Kahn, M. Wieczorek, R. Bronisz, Z. Ciunik, M. F. Rudolf, *C. R. Chim.* **1998**, *1*, 523–532.

[12] D. Sertphon, D. J. Harding, P. Harding, K. S. Murray, B. Moubaraki, J. D. Cashion, H. Adams, *Eur. J. Inorg. Chem.* **2013**, 788–795.

[13] M. Koike, K. Murakami, T. Fujinami, K. Nishi, N. Matsumoto, Y. Sunatsuki, *Inorg. Chim. Acta* **2013**, *399*, 185–192.

[14] A. Hauser, in Spin Crossover in Transition Metal Compounds I-III, ed. P. Gütlich and H. A. Goodwin, Springer, Berlin/Heidelberg, **2004**, vol. *234*, pp. 155–198.

[15] (a) P. Gütlich, A. Hauser, H. Spiering, *Angew. Chem.* **1994**, *106*, 2109–2141; (b) H. Spiering, E. Meissner, H. Köppen, E. W. Müller, P. Gütlich, *Chem. Phys.* **1982**, *68*, 65–71.

[16] T. Nakanishi, A. Okazawa, O. Sato, *Inorganics* **2017**, *5*, 53.

8.5 Supporting Information

Experimental:

The ligand HL was synthesised as published previously.[1] All other chemicals were commercially available and used without further purification. CHN analyses were measured with a Vario El III from Elementar AnalysenSysteme. Samples were prepared in a tin boat, and acetanilide was used as standard. Mass spectra were recorded with a Finnigan MAT 8500 with a data system MASPEC II. IR spectra were recorded with a Perkin Elmer Spectrum 100 FT-IR spectrometer.

$[FeL_2]BF_4$ (**1**). HL (0.2 g, 0.9 mmol, 1 eq), sodium acetate (0.05 g, 0.9 mmol, 1 eq), and iron(III) nitrate nonahydrate (0.22 g, 0.55 mmol, 0.6 eq) were dissolved in ethanol (20 mL) and the

resulting purple solution was heated to reflux for 1 h. After cooling to room temperature, approximately half of the solvent was removed under reduced pressure. Sodium tetrafluoroborate (1.14 g, 10 mmol, 25 eq) was dissolved in 20 mL water and added to the purple solution. The mixture was stirred at room temperature for 10 min, the resulting purple solid was filtrated, washed with a few mL of water and dried *in vacuo*. Yield: 0.10 g (577.15 g·mol^{-1}, 40 %). Elemental analysis ($C_{24}H_{26}BF_4FeN_4O_4$, %) measured (calcd.): C 49.32 (49.95), H 4.30 (4.54), N 9.56 (9.71). MS (EI, pos.) *m/z* (%): 490 ($C_{24}H_{26}FeN_4O_4$, 36), 93 (C_6H_6N, 100) 43 (C_2H_3O, 25). IR: ν = 1579 (s, C=O), 1568 (s, C=O) cm^{-1}.

$[FeL_2]ClO_4$ (**2**). HL (0.2 g, 0.9 mmol, 1 eq), sodium acetate (0.05 g, 0.9 mmol, 1 eq), and iron(III) nitrate nonahydrate (0.22 g, 0.55 mmol, 0.6 eq) were dissolved in ethanol (20 mL) and the resulting purple solution was heated to reflux for 1 h. After cooling to room temperature, approximately half of the solvent was removed under reduced pressure. Barium perchlorate trihydrate (5.37 g, 10 mmol, 25 eq) was dissolved in 20 mL water and added to the purple solution. The mixture was stirred at room temperature for 10 min, the resulting purple solid was filtrated, washed with a few mL of water and dried *in vacuo*. Yield: 0.14 g (589.79 g·mol^{-1}, 43 %). IR: ν = 1579 (s, C=O), 1567 (s, C=O) cm^{-1}.

Single crystal X-ray structure analysis

X-ray structure analysis of the crystals was performed with a Stoe StadiVari diffractometer using graphite-monochromated MoKα radiation. The data were corrected for Lorentz and polarization effects. The structures were solved by direct methods (SIR-97)[2] and refined by fullmatrix least-square techniques against Fo^2–Fc^2 (SHELXL-2017).[3] All hydrogen atoms were calculated in idealised positions with fixed displacement parameters. ORTEP-III[4] was used for the structure representation, SCHAKAL-99[5] to illustrate molecule packing. The Hirshfeld surfaces were mapped with d_{norm}, and 2D fingerprint plots were generated using CrystalExplorer 17.5.[6] Graphical plots of the molecular Hirshfeld surfaces use a red-white-blue colour scheme. Red highlights contacts shorter than the van der Waals separation, contacts around the van der Waals separation are white, and blue is used for longer contacts.

CCDC (1898802–1898805) contain the supplementary crystallographic data for this paper. These data can be obtained free of charge from The Cambridge Crystallographic Data Centre.

Magnetic measurements

Magnetic measurements on the compounds were carried out using a SQUID MPMS-XL5 from Quantum Design with an applied field of 5000 G, and in the temperature range from 300 to 50 K in settle and in sweep (5 K/min) mode. The sample was prepared in a gelatine capsule held in a plastic straw. The raw data were corrected for the diamagnetic part of the sample holder and the diamagnetism of the organic ligand using tabulated Pascal's constants.[7]

Table S1. Crystallographic data for the complexes at different temperatures presented in this work.

	1-HS	**1-LS**	**2-HS**	**2-LS**
CCDC	1898802	1898803	1898804	1898805
formula	$C_{24}H_{26}FeN_4O_4$, BF_4	$C_{24}H_{26}FeN_4O_4$, BF_4	$C_{24}H_{26}FeN_4O_4$, ClO_4	$C_{24}H_{26}FeN_4O_4$, ClO_4
sum formula	$C_{24}H_{26}BF_4FeN_4O_4$	$C_{24}H_{26}BF_4FeN_4O_4$	$C_{24}H_{26}ClFeN_4O_8$	$C_{24}H_{26}ClFeN_4O_8$
M/ g mol^{-1}	577.15	577.15	589.79	589.79
crystal system	orthorhombic	orthorhombic	orthorhombic	orthorhombic
space group	$P2_12_12_1$	$P2_12_12_1$	$P2_12_12_1$	$P2_12_12_1$
crystal description	purple plate	purple plate	purple plate	purple plate
a/ Å	8.6392(3)	8.6111(3)	8.6776(3)	8.6347(3)
b/ Å	16.7578(5)	16.4406(5)	16.8062(8)	16.5568(7)
c/ Å	17.6029(8)	17.5177(8)	17.6168(6)	17.5497(6)
α/ °	90	90	90	90
β/ °	90	90	90	90
γ/ °	90	90	90	90
V/ Å^3	2548.44(16)	2480.01(16)	2569.19(17)	2508.96(16)
Z	4	4	4	4
ρ_{calcd}/ g cm^{-3}	1.504	1.546	1.525	1.561
μ/ mm^{-1}	0.660	0.678	0.747	0.765
crystal size/ mm	0.115×0.052×0.029	0.115×0.052×0.029	0.087×0.078×0.038	0.087×0.078×0.038
F(000)	1188	1188	1220	1220
T/ K	175	133	150	100
λ/ Å	Mo-K$_\alpha$ 0.71073	Mo-K$_\alpha$ 0.71073	Mo-K$_\alpha$ 0.71073	Mo-K$_\alpha$ 0.71073
Θ range/ °	1.7–28.5	2.3–28.6	2.3–28.5	2.3–28.5
Reflns. collected	12870	14682	13721	13617
Indep. reflns.(R_{int})	5894 (0.054)	5782 (0.062)	6016 (0.045)	5863 (0.039)
Parameters	343	343	343	343
$R1$ (all data)	0.0461	0.0477	0.0405	0.0368
$wR2$	0.0940	0.0975	0.0705	0.0649
GooF	0.89	0.89	0.89	0.90
Flack x	−0.030(17)	−0.02(2)	−0.022(13)	−0.001(12)

Figure S1. ORTEP drawing of **1** in the HS state (top) and LS state (bottom). Ellipsoids were drawn at 50 % probability level. Hydrogen atoms were omitted for clarity.

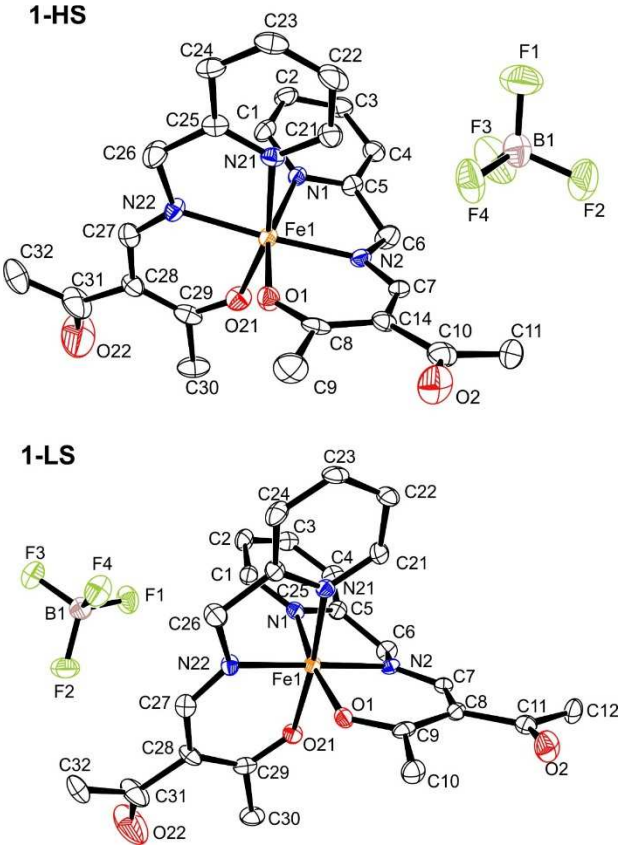

Figure S2. ORTEP drawing of **2** in the HS state (top) and LS state (bottom). Ellipsoids were drawn at 50 % probability level. Hydrogen atoms were omitted for clarity.

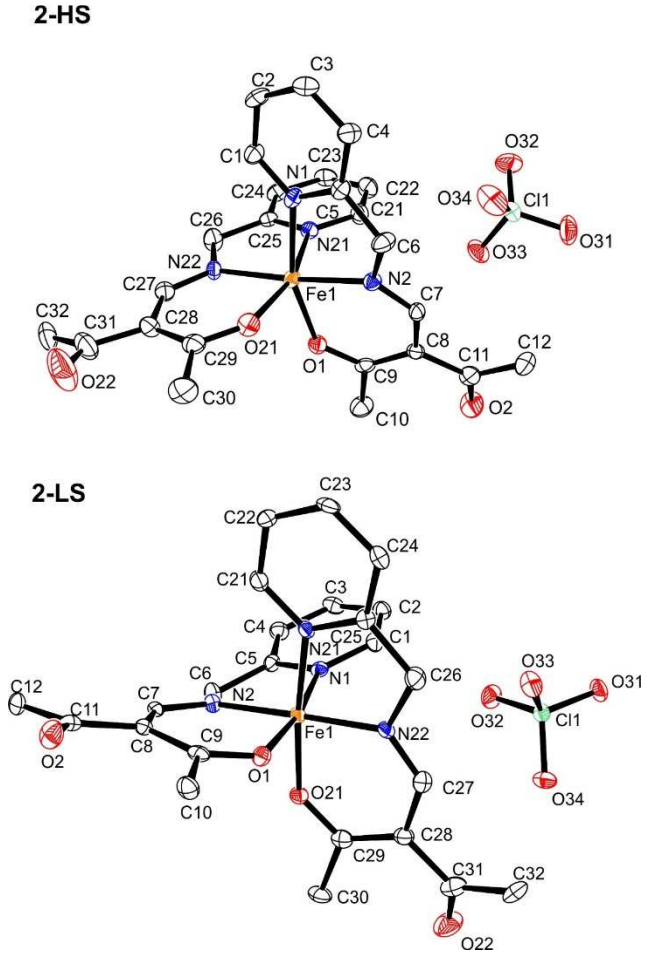

Table S2. Summary of the C–H···π interactions of the complexes presented in this work.

		C_g	H···C_g/Å Y···C_g/Å	X–H···C_g/° X–Y···C_g/°	X···C_g/Å
1-HS	C3–H3	Fe1–O21–C29–C28–C27–N22[a]	2.95	153	3.818(6)
	C30–H30B	N21–C21–C22–C23–C24–C25[b]	2.72	134	3.470(5)
1-LS	C30–H30B	N21–C21–C22–C23–C24–C25[c]	2.61	143	3.444(5)
2-HS	C3–H3	Fe1–O21–C29–C28–C27–N22[d]	2.95	153	3.824(4)
	C30–H30C	N21–C21–C22–C23–C24–C25[c]	2.73	134	3.481(4)
2-LS	C30–H30C	N21–C21–C22–C23–C24–C25[b]	2.59	148	3.465(4)

a: 3/2−x, 2−y, −1/2+z; b: 1+x, y, z; c: −1+x, y, z; d: 1/2−x, −y, 1/2+z.

Table S3. Hydrogen bonds and angles of complexes presented in this work.

	Donor	Acceptor	D–H/Å	H···A/Å	D···A/Å	D–H···A/°
1-HS	C1–H1	F2[a]	0.95	2.54	3.008(6)	111
	C7–H7	O2[b]	0.95	2.50	3.090(6)	121
	C21–H21	F4[c]	0.95	2.43	3.089(6)	126
	C23–H23	F2[d]	0.95	2.42	3.179(6)	137
	C24–H24	F1[d]	0.95	2.52	3.357(6)	146
	C26–H26B	F3[a]	0.99	2.52	3.380(6)	145
	C32–H32B	O22[e]	0.98	2.31	3.253(8)	161
	C32–H32A	F1[a]	0.98	2.49	3.320(6)	142
1-LS	C7–H7	O2[f]	0.95	2.49	3.187(6)	131
	C21–H21	F4[g]	0.95	2.47	3.346(6)	152
	C23–H23	F1[h]	0.95	2.41	3.120(6)	132
	C24–H24	F2[h]	0.95	2.48	3.340(6)	151
	C32–H32A	F2[c]	0.98	2.54	3.327(6)	137
	C32–H32B	O22[i]	0.98	2.36	3.308(7)	170
2-HS	C1–H1	O31[k]	0.95	2.60	3.039(5)	109
	C7–H7	O2[l]	0.95	2.48	3.076(5)	120
	C21–H21	O33[c]	0.95	2.53	3.135(4)	121
	C23–H23	O31[m]	0.95	2.43	3.192(5)	137
	C24–H24	O32[m]	0.95	2.55	3.384(5)	147
	C26–H26A	O34[k]	0.99	2.52	3.377(5)	145
	C32–H32B	O22[n]	0.98	2.31	3.264(6)	166
	C32–H32C	O32[k]	0.98	2.54	3.323(6)	137
2-LS	C7–H7	O2[o]	0.95	2.49	3.198(4)	132
	C21–H21	O33[p]	0.95	2.51	3.383(4)	153
	C23–H23	O32[q]	0.95	2.44	3.150(4)	131
	C24–H24	O34[q]	0.95	2.50	3.364(4)	152
	C26–H26A	O33[c]	0.99	2.58	3.395(4)	140
	C32–H32B	O22[r]	0.98	2.39	3.347(4)	165
	C32–H32C	O34[c]	0.98	2.55	3.298(4)	133

a: 1−x, −1/2+y, 3/2−z; b: 1/2+x, 5/2−y, 2−z; c: x, y, z; d: −x, −1/2+y, 3/2−z; e: −1/2+x, 3/2−y, 2−z; f: −1/2+x, 5/2−y, 2−z; g: 2−x, −1/2+y, 3/2−z; h: 1+x, y, z; i: 1/2+x, 7/2−y, 2−z; k: 1−x, 1/2+y, 3/2−z; l: −1/2+x, −1/2−y, 1−z; m: 2−x, 1/2+y, 3/2−z; n: 1/2+x, 1/2−y, 1−z; o: 1/2+x, 1/2−y, −z; p: 1−x, 1/2+y, 1/2−z; q: −1+x, y, z; r: −1/2+x, −1/2−y, −z.

Figure S3. Hirshfeld surface mapped with d_{norm} (top left), fingerprint plots: full (top right), resolved into H···O/O···H (bottom left), and H···F/F···H (bottom right) contacts of complex **1-LS**.

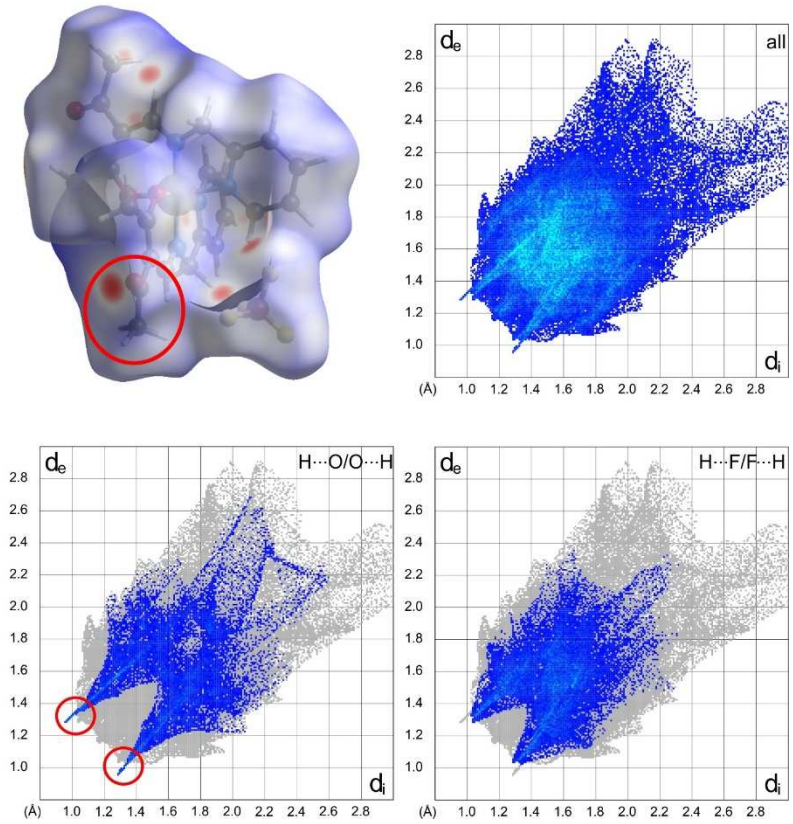

Figure S4. Hirshfeld surface mapped with d_{norm} (top left), fingerprint plots: full (top right), and resolved into H···O/O···H (bottom left) of complex **2-HS**.

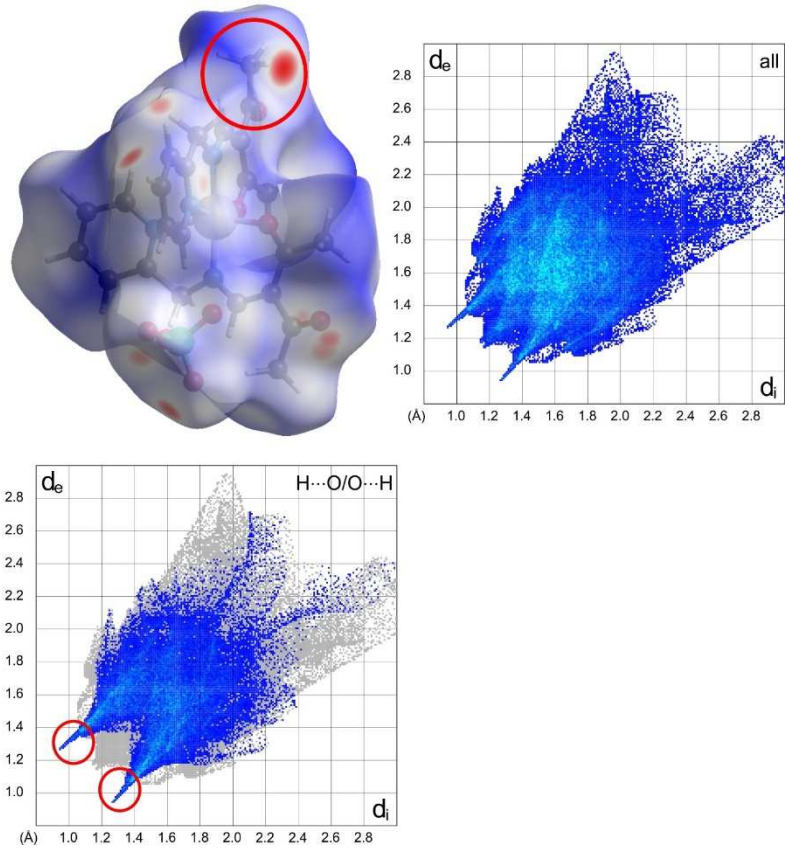

Figure S5. Hirshfeld surface mapped with d_{norm} (top left), fingerprint plots: full (top right), and resolved into H···O/O···H (bottom left) contacts of complex **2-LS**.

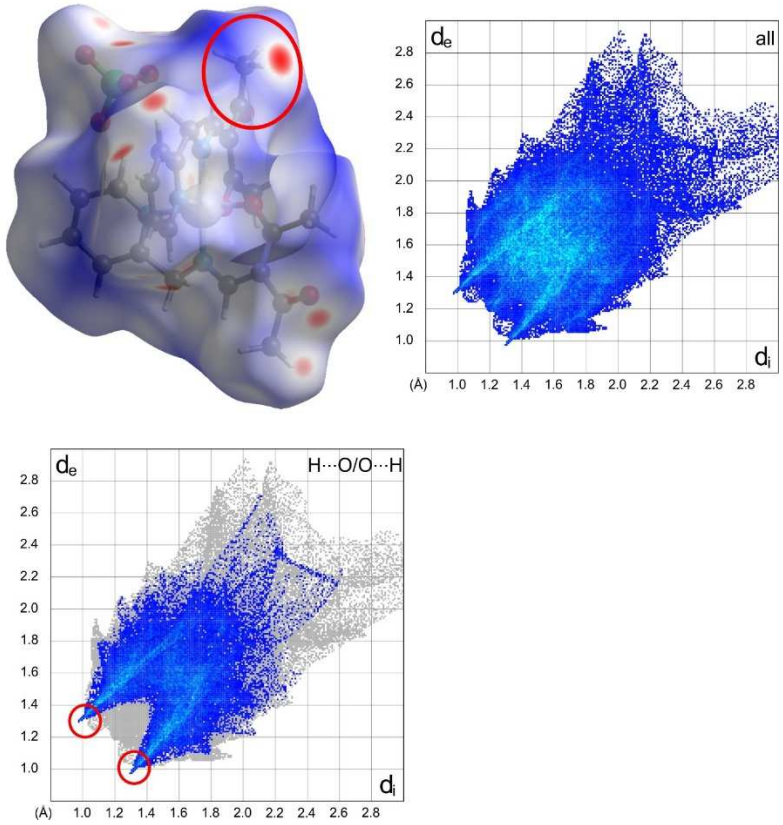

Figure S6. Plot of the $\chi_M T$ product vs. T for complex **1** (left) and **2** (right) measured in sweep mode with a scan rate of 5 K/min.

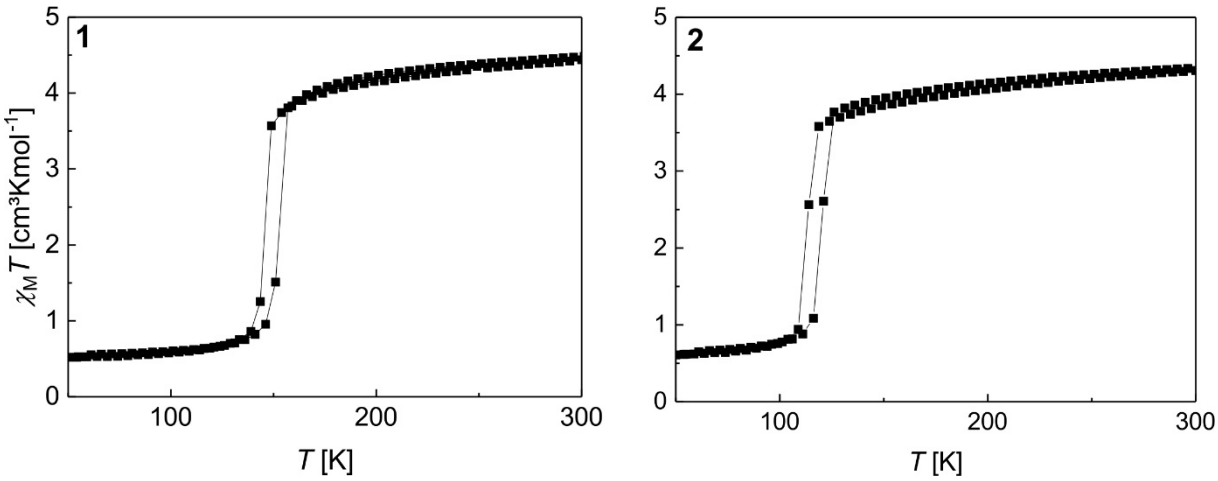

References

[1] K. Dankhoff, B. Weber, *CrystEngComm.* **2018**, *20*, 818–828.

[2] A. Altomare, M. C. Burla, M. Camalli, G. L. Cascarano, C. Giacovazzo, A. Guagliardi, A. G. G. Moliterni, G. Polidori, R. Spagna, *J. Appl. Cryst*. **1999**, *32*, 115–119.

[3] G. Sheldrick, *Acta Cryst. A* **2008**, *64*, 112–122.

[4] a) C. K. Johnson, M. N. Burnett, ORTEP-III, Oak-Ridge National Laboratory, Oak-Ridge, TN, **1996**; b) L. Farrugia, *J. Appl. Cryst*. **1997**, *30*, 565.

[5] E. Keller, Schakal-99, University of Freiburg, Freiburg, Germany, **1999**.

[6] M. J. Turner, J. J. McKinnon, S. K. Wolff, D. J. Grimwood, P. R. Spackman, D. Jayatilaka, M. A. Spackman, CrystalExplorer17 **2017**. University of Western Australia.

[7] O. Kahn, *Molecular Magnetism*, VCH, New York, N.Y, **1993**.

9. Towards new robust Zn(II) complexes for the ring-opening polymerization of lactide under industrial relevant conditions

Pascal M. Schäfer[a], Katja Dankhoff[b], Matthias Rothemund[c], Agnieszka N. Ksiazkiewicz[d,e,f], Andrij Pich[d,e,f], Rainer Schobert[c], Birgit Weber*[b] and Sonja Herres-Pawlis*[a]

[a] Institute for Inorganic Chemistry, RWTH Aachen University, Landoltweg 1, 52074 Aachen, Germany. E-mail: sonja.herres-pawlis@ac.rwth-aachen.de;
[b] Department of Chemistry, Inorganic Chemistry IV, Universität Bayreuth, Universitätsstr. 30, 95440 Bayreuth, Germany. E-Mail: weber@uni-bayreuth.de;
[c] Department of Chemistry, Organic Chemistry I, Universität Bayreuth, Universitätsstr. 30, 95440 Bayreuth, Germany;
[d] Functional and Interactive Polymers, Institute of Technical and Macromolecular Chemistry, RWTH Aachen University, Worringerweg 2, 52074 Aachen, Germany;
[e] DWI – Leibniz Institute for Interactive Materials e.V., Forckenbeckstr. 50, 52074 Aachen, Germany;
[f] Aachen Maastricht Institute for Biobased Materials (AMIBM), Maastricht University, Brightlands Chemelot Campus, Urmonderbaan 22, 6167 RD Geleen, The Netherlands

Published in: *ChemistryOpen* **2019**, *8*, 1020–1026. (DOI: 10.1002/open.201900199)

Keywords: polylactide • catalysis • biobased materials • sustainable chemistry • ring-opening polymerisation

Abstract: The synthesis of bio-based and biodegradable plastics is a hot topic in research due to growing environmental problems caused by omnipresent plastics. As a result, polylactide, which has been known for years, has seen a tremendous increase in industrial production. Nevertheless, the manufacturing process using the toxic catalyst $Sn(Oct)_2$ is very critical. As an

alternative, five zinc acetate complexes have been synthesized with Schiff base-like ligands that exhibit high activity in the ring-opening polymerization of non-purified lactide. The systems bear different side arms in the ligand scaffold. The influence of these substituents has been analyzed. For a detailed description of the catalytic activities, the rate constants k_{app} and k_p were determined using in-situ Raman spectroscopy at a temperature of 150°C. The polymers produced have molar masses of up to 71 000 $gmol^{-1}$ and are therefore suitable for a variety of applications. Toxicity measurements carried out for these complexes proved the nontoxicity of the systems.

9.1 Introduction

The rising littering of our planet with plastics and the increasing scarcity of crude oil pose new challenges for society.[1] In addition to recycling systems and natural materials, bio-based and biodegradable plastics are a good alternative.[2] A plastic that meets both criteria is polylactide.[3] Sugarcane, sugar beets or maize serve as raw material source. After a fermentation process of the material, the lactic acid is obtained, which is esterified in a subsequent condensation reaction to the cyclic dimer, being the monomer unit lactide. By a controlled ring-opening polymerization, the corresponding polymer polylactide is then synthesized.[4] The controlled ring-opening succeeds with the aid of suitable catalysts.[5] From an economic point of view, some requirements are placed on the catalyst. In addition to cost-effective production, high activities, low concentrations of use and robustness against air and moisture are in the foreground. In addition, the turnover must be ensured at temperatures beyond 130°C and colourless polymers are to be obtained.[6] The tin octanoate ($Sn(Oct)_2$) ($Oct=OCO(CH_2)_6CH_3$) fulfils these properties and is therefore currently the most widely used catalyst in the industrial production of PLA.[7] Since the catalyst is not removed after melt polymerization, it remains in the polymer and it is assumed that the tin(II) compound accumulates during the compost degradation of polylactide. For a long time, the toxicity of this tin compound has been known, so a replacement for $Sn(Oct)_2$ is strongly advised to keep the bioplastic PLA “green” even if the catalyst remains in the polymer matrix.[8] Zinc-based catalyst systems are therefore an excellent alternative. Thus, Coates *et al.* developed various zinc complexes with β-diiminates as ligand.[9] Zinc aminophenolates from Ma *et al.*,[10]

Mehrkhodavandi *et al.*,[11] Tolman *et al.*[12] showed high activities and stereoselectivities. Hayes and Wheaton *et al.* developed zinc complexes bearing phosphinimines[13] and Schulz *et al.*[14] zinc ketoiminate and β-diketiminate complexes. Different zinc alkoxides with trispyrazolyl- and trisindazolylborate ligands have been designed and tested by Chisholm *et al.*[15] Zinc complexes containing OOO-tridentate bis(phenolate) or tris(pyrazolyl) methane ligands have been applied successfully in the ROP of lactide by Mountford *et al.*[16] In 2016 Williams *et al.* presented dinuclear zinc systems, which reached the highest activity in the area of zinc catalysts up to now.[17] While the above-mentioned systems have been tested mainly in solution and with purified lactide, the activity of the catalyst with non-purified lactide, low catalyst concentrations and high temperatures is an important criterion for industrial use. Along the way, Davidson *et al.* developed titanium, zirconium and hafnium aminophenolate complexes for the polymerization in melt.[18] Jones *et al.*[19] recently presented zinc aminophenolate complexes that showed high activity in melt using singly recrystallized lactide. At a ratio of [LA]:[I]:[BnOH] = 10 000:1:100 and a temperature of 180°C a conversion of 90% as well as controlled molar masses have been reached.[20] Another attractive class of ligands in this context are guanidines.[21] As neutral donors they form stable and robust complexes in combination with zinc.[22] In the past, several hybrid and bisguanidines with N,N donors have been reported to be good catalysts in the field of non-purified lactide polymerization. In recent years, zinc hybrid guanidines with neutral N,O donors have come into the focus as they have significantly higher activity and produce molar masses up to 86 000 $gmol^{-1}$ under industrially relevant conditions.[23] Recently, iron guanidine complexes have been published, which show higher activities than pure $Sn(Oct)_2$ using non-purified *rac*-LA at 150°C.[24]

However, the search for easily accessible catalyst systems for the ROP of lactide goes on. At this point we report zinc systems containing Schiff base-like ligand scaffolds. Their synthesis succeeds starting from commercially available substances and cost-effectively in just one step. Various complexes were tested under industrial conditions and their activity was recorded *in situ* using Raman spectroscopy. An investigation of the mechanistic ring-opening was carried out by means of MALDI-ToF measurements.

9.2 Results and Discussion

Synthesis

The Zn(II) complexes were obtained by a condensation reaction between $Zn(OAc)_2 \cdot 2H_2O$ and the tridentate Schiff base-like ligands in ethanol (HL1, HL3, and HL5) or methanol (HL2 and HL4). The tridentate ligands were synthesized by a facile condensation reaction as described previously.[25] The synthesis and numbering scheme is given in Scheme 1. The acetate anion is acting as base for the deprotonation of the ligand. The coordination compounds were obtained as white, crystalline powder and their purity was confirmed by means of elemental analysis, mass spectrometry, TGA, and IR spectroscopy.

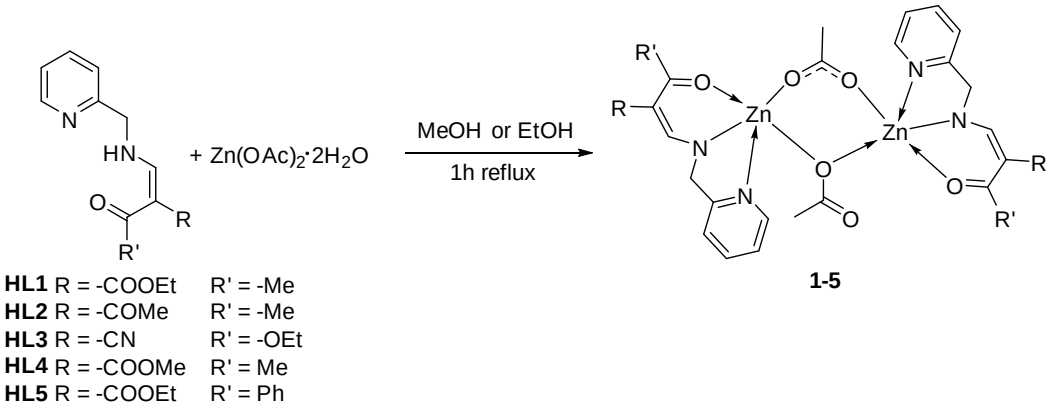

Scheme 1. General synthetic procedure for the synthesis of the Zn(II) complexes described in this work.

X-ray structure analysis

Crystals suitable for X-ray structure analysis were obtained for **1** by liquid-liquid diffusion of a methanol solution of the ligand and an aqueous solution of $Zn(OAc)_2 \cdot 2H_2O$, and for **5** from the mother liquor. The crystallographic data were collected at 133 K and are summarized in Table S1. Complex **1** crystallized in the triclinic space group $P\bar{1}$, **5** in the monoclinic space group $P2_1/c$. Both complexes crystallized as dimers, with each metal centre coordinated by one tridentate ligand and two acetate anions bridging the Zn(II) centres. One anion is coordinating with only one of the two oxygen atoms, while for the other both are coordinating. The asymmetric units of both complexes are depicted in Figure 1. The bond lengths of the first coordination sphere are given in Table S2. The Zn–N_{py} bond lengths are slightly longer (2.15 Å

in average for **1**, 2.14 Å for **5**) than the other bond lengths of the first coordination sphere of the Zn(II) atoms (average values: Zn–N_{ax} 2.03 Å [**1**], 2.04 Å [**5**]; Zn–O_{ax} 2.06 Å [**1**], 2.05 Å [**5**]; Zn–O53 2.03 Å [**1**], 2.04 Å [**5**]; Zn–O51 2.03 Å [**1**], 2.01 Å [**5**]; Zn–O52 1.98 Å [**1**], 1.97 Å [**5**]). The assignment of a single or double bond in the acetate anions is clear for the ion in which only one oxygen is bridging the Zn(II) centres (C53–1.311(5) Å / 1.307(2) Å and C53–O54 1.222(5) Å / 1.221(2) Å for **1** and **5**, respectively), whereas for the other acetate ion the delocalization of the negative charge over both oxygen atoms results in similar bond lengths (C51–O51 1.257(5) Å / 1.250(2) Å and C51–O52 1.270(5) Å and 1.263(2) Å for **1** and **5**, respectively).

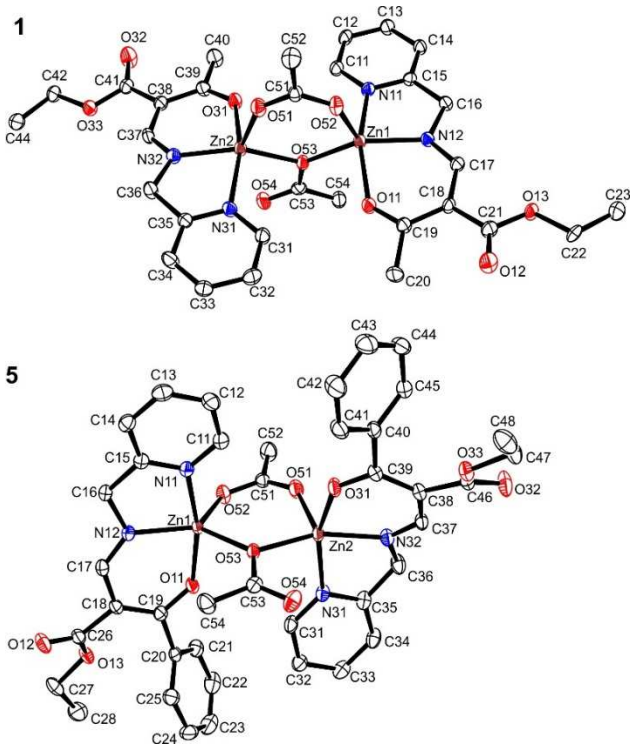

Figure 1. Molecular structures of complexes **1** (top) and **5** (bottom). Ellipsoids are drawn at 50 % probability level. Hydrogen atoms were omitted for clarity.

The distortion parameter τ helps to distinguish between a square pyramidal coordination sphere (τ close to 0) and a trigonal bipyramidal coordination sphere (τ close to 1). It is defined as $(\alpha-\beta)/60$, with the largest angle of the coordination sphere being α and the second largest β.[26] It has similar values for the both Zn(II) atoms in complex **1** (Zn1 0.15, and Zn2 0.21), this indicates a distorted square pyramidal coordination sphere. The values for complex **5** are

different for the Zn(II) atoms of this complex; 0.6 for Zn1 and 0.02 for Zn2. This indicates a nearly ideal square pyramidal geometry for Zn2. As the bond length Zn–N_{py} is still slightly longer compared to the remaining bond lengths in Zn1, the coordination geometry is likely to be square pyramidal as well. The significant differences in the τ values of complexes **5** can be explained with a C–H$\cdots\pi$ interaction between an aromatic CH group of the pyridine ring of Zn2 (C32–H32) and the phenyl ring of Zn1 (see Figure S1, right); this interaction causes the tridentate ligand of Zn2 to be more bend than for Zn1. Details of all interactions are given in Table S3–S5. Pictures of the packing of the complexes in the crystal are given in Figure S1.

Powder X-ray diffraction was performed to confirm the identical structure of the bulk and the single crystals. The diffraction patterns are given in the Supporting Information, Figure S2. It can be seen that the patterns for **1** and **5** are identical for the bulk complex and the calculated pattern for the crystal structure. Small differences can be explained with the different temperatures used for the measurements (single crystal at 133 K, powder at room temperature).

To determine the nuclearity of the complexes in solution, the conductivity of a 1.5 mM aqueous solution of compounds **2** and **4** was measured. Compared to the one of the used distilled water (1.6 µS/cm) it is enhanced (234.9 µS/cm for **2** and 217.9 µS/cm for **4**). This is an indication for the formation of monomeric species in aqueous solution. The other compounds were not fully soluble in water.

Polymerisation

All five complexes were tested regarding their activity in the ring-opening polymerization of *rac*-lactide (Tables 1 and 2). The corresponding polymerizations were carried out with nonpurified *rac*-LA at a temperature of 150°C. The [M]/[I] ratio was 500 : 1, assuming that both zinc atoms of one complex propagate a chain. An additional co-initiator has been omitted. The kinetic measurements were accomplished by *in situ* Raman spectroscopy. In a steel reactor, the reaction progress was followed in melt at a stirring speed of 260 rpm. The kinetic evaluation was carried out by a semilogarithmic plot of the lactide concentration *versus* time (determination of k_{app}). For the complexes **1**, **2**, **4** & **5** detailed results are given. Due to the intense fluorescence of complex **3**, a kinetic study was not possible. All polymers have been characterized by gel permeation chromatography (GPC) to give information regarding their molar masses.

Table 1. Polymerization data for *rac*-LA with catalyst **2**.

[M]/[I]	k_{app} (s^{-1})[b]	time (min)	conv. (%)[c]	$M_{n,theo}$ (g mol^{-1})	M_n (g mol^{-1})[d]	*PD*
500	1.14×10^{-3}	25	62	45 000	65 000	1.5
625	8.60×10^{-4}	30	78	70 000	54 000	1.8
1000	4.22×10^{-4}	27	65	94 000	81 000	1.4
1500	2.23×10^{-4}	61	57	123 000	43 000	1.8
2000	1.28×10^{-4}	112	56	161 000	21 000	2.2

[a] Conditions: 150 °C, solvent free, non-purified technical grade *rac*-LA. [b] Determined from the slope of the plots of $\ln([LA]_0/[LA]_t)$ versus time. For spectra see SI. [c] As determined by ^{1}H NMR spectroscopy. [d] Determined by GPC (in THF), $M_{n,theo}$: 72 000 g mol^{-1} for 100% conversion.

Regarding the different values for k_{app} of the four different catalysts, it is clear that **5** is the slowest with a $k_{app} = 6.08 \pm 0.1 \times 10^{-4}\ s^{-1}$. On the other hand, the other complexes **1**, **2** & **4** with values of $k_{app} = 1.22 \pm 0.15 \times 10^{-3}\ s^{-1}$ (**1**), $k_{app} = 1.14 \pm 0.04 \times 10^{-3}\ s^{-1}$ (**2**) & $k_{app} = 1.41 \pm 0.01 \times 10^{-3}\ s^{-1}$ (**4**) are of identical orders of magnitude. To understand the slower activity of **5**, it helps to look at the structure of the complex. While the complexes **1**, **2** & **4** bear short esters or an aldehyde plus a methyl group, complex **5** has an ester- and a phenyl group attached. This results in a higher steric demand and access of the lactide to the metal centre is made more difficult. To determine the polymerization rate constant k_p detailed kinetic measurements with complex **2** were performed (Figure 2). By polymerization experiments at different catalyst concentrations (up to 2000 : 1 per zinc), it was possible to obtain the rate constant k_p from the linear fit by plotting the different k_{app} values against the catalyst concentration. Compared with the k_p from the recently published zinc guanidine catalyst [$ZnCl_2$(TMG5NMe$_2$asme)] with a value of $6.10 \pm 0.34 \times 10^{-2}\ Lmol^{-1}\ s^{-1}$ [23b] complex **2** with $k_p = 8.59 \pm 0.36 \times 10^{-2}\ Lmol^{-1}\ s^{-1}$ is slightly faster.

Table 2. Polymerisation data for *rac*-LA with catalysts **1**–**5.**[a]

init.	k_p (L mol^{-1} s^{-1})[b]	k_{app} (s^{-1})[c]	time (min)	conv. (%)[d]	$M_{n,theo}$ (g mol^{-1})[e]	M_n (g mol^{-1})[f]	*PD*
1		$1.22 \pm 0.15 \times 10^{-3}$	41	79	57 000	62 000	1.6
2	$8.59 \pm 0.36 \times 10^{-2}$	$1.14 \pm 0.04 \times 10^{-3}$	25	62	45 000	65 000	1.5
4		$1.41 \pm 0.01 \times 10^{-3}$	42	78	56 000	71 000	1.5
5		$6.08 \pm 0.1 \times 10^{-4}$	49	75	54 000	57 000	1.6

[a] Conditions: solvent free, non-purified technical grade *rac*-LA, 150°C. [b] Determined by plotting k_{app} versus [init.]. k_p [I] [M]; $k_p = k_{app}/[I]$. [c] Determined from the slope of the plots of $\ln([LA]_0/[LA]_t)$ versus time for a ratio of [M]/[I] = 500:1. [d] As determined by ^{1}H NMR spectroscopy. [e] Calculated assuming that every zinc of each dinuclear complex propagates one chain $M_{n,theo}$: 72 000 g mol^{-1} for 100% conversion at a ratio of [M]/[I] = 500:1. [f] Determined by GPC (in THF).

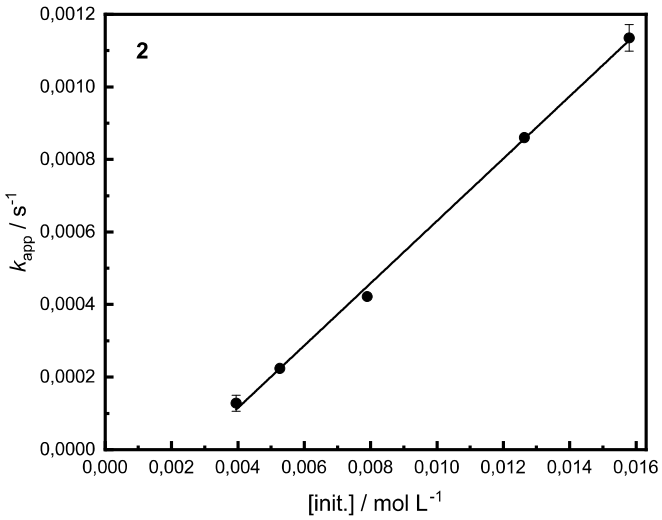

Figure 2. Plot of k_{app} versus [init.] for **2**. Conditions: *rac*-LA, 150 °C, 260 rpm, non-purified; [M]/[I] = 500:1, 625:1, 1000:1, 1500:1, 2000:1.

In a comparison to the active zinc catalyst $Zn(CH_3COO)_2$ with a conversion of 69% after 24 h ([M]/[I]= 500 : 1) the herein presented systems with a conversion of 79% after 41 min ([M]/[I]=500 : 1) are significantly faster.[22d] The analysis of the molar masses of the respective polylactides shows that all systems are able to synthesise high molar masses up to 71000 $gmol^{-1}$ (**4**). The theoretical molar masses propose that every available zinc atom propagates a chain. With polydispersities (*PD*) of 1.5–1.6, the values are very good for polymerization in melt. As mechanism, we propose the coordination-insertion mechanism which will be detailed below. First, X-ray data show that all complexes are dinuclear. However, if the kinetics of the polymerization catalyzed by complex **5** (Figure 3) are considered as example, an induction phase is conspicuous at the beginning of the polymerization. Typically, such induction phases are accounted to the formation of the active species. To investigate the reaction order, a plot of ln(k_{app}) vs. ln([init.]) was used (see Figure S9). The slope of 1.57 was obtained indicating a fractional reaction rate. In this case a dissociation of the dinuclear complex is proposed.[27] This is also supported by the obtained molar masses, which are closer to the theoretical value if based on the calculation per zinc atom. MALDI-ToF measurements also confirm that a “half” complex is attached to the chain end (see Figure S11). While acetate primarily initiates the polymerization, the propagation of the chain takes place through half a complex. Due to a decomposition of the complex caused by impurities in the monomer, smaller amounts of ligand can be found at the end of the chains. Zinc acetate as the active species can be excluded due to

its lower catalysis activity.[22d] All three observations lead to the result that by dissociation of the complex the active species is formed. Tacticity determinations by ^{1}H NMR spectroscopy showed that the catalysts produce atactic polymer. To exclude potential epimerization during the polymerization, an experiment with L-lactide using **2** has been performed. Homodecoupled ^{1}H NMR revealed purely isotactic PLA.

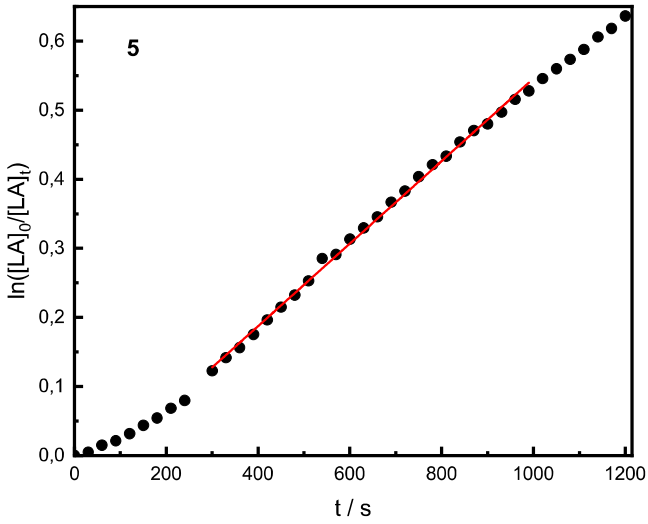

Figure 3. Semi-logarithmic plot of the polymerisation of non-purified *rac*-LA with **5** [M]/[I] = 500:1, 150 °C, 260 rpm, conversion determined by *in situ* Raman spectroscopy.

TGA measurements of all five complexes show that the catalytic active systems remain stable at temperatures up to 225°C. Therefore, they are suitable for industrial use at typical temperatures between 180 and 200°C.

Cytotoxicity

In order to identify any potential toxicity of the complexes, the catalytically active complex **2** was tested against toxin-sensitive 518A2 melanoma, HT-29 and HCT-116wt colon carcinoma, Hela cervix carcinoma cells and non-malignant human fibroblasts using the MTT proliferation assay.[30] Complex **2** showed virtually no cytotoxicity against any of these cells with 50% growth inhibitory concentrations IC_{50} > 100 µM. It may therefore be considered non-hazardous to health.

9.3 Conclusions

Dinuclear zinc acetate complexes with five different substituted Schiff base-like ligands were prepared. The ligand and complex syntheses convince by their ease of preparation and their robustness towards higher temperature and lactide impurities. Four systems were found to be highly active in the catalytic ring-opening polymerization of non-purified lactide under industrial conditions. Their kinetic behaviour has been observed *via in situ* Raman spectroscopy. Despite an anionic ligand system, the complexes show a high degree of tolerance to the impurities in the monomer and produce industrially useful PLA with molar masses of up to 71 000 $gmol^{-1}$ and a conversion of 78%. With a $k_p = 8.59 \pm 0.36 \times 10^{-2}\,Lmol^{-1}\,s^{-1}$, the systems are slightly faster than the recently published zinc guanidine complex[23b] and show that this class of ligands in combination with zinc also has a high potential to replace the currently industrially used catalyst $Sn(Oct)_2$. Mechanistic investigations have shown that the dinuclear complex is present in melt of lactide as a mononuclear unit. As such, it forms the active species in the polymerization of lactide. Cytotoxic studies with sensitive non-malignant fibroblasts and cancer cells also demonstrated the nontoxicity of the complexes, which thus represent an active, robust and green catalyst for the ROP of lactide. Together with the facile synthesis, a viable alternative for the cytotoxic $Sn(Oct)_2$ opens up new avenues for lactide polymerization.

9.4 Experimental Section

HL1–HL5 were synthesised as published.[25a] All other chemicals were commercially available and used without further purification. Elemental analysis were measured with Vario El III from Elementar AnalysenSysteme. Samples were prepared in a tin boat, and acetanilide was used as standard. Mass spectra were recorded with a Finnigan MAT 8500 with a data system MASPEC II. IR spectra were recorded with a Perkin Elmer Spectrum 100 FT-IR spectrometer. TGA was measured with a Netzsch STA 449.

[ZnL1OAc] (1). $Zn(AcO)_2 \cdot 2H_2O$ (0.2 g, 0.91 mmol) and HL1 (0.377 g, 1.52 mmol) were dissolved in EtOH (5 mL) and the light orange solution was heated to reflux for 1 h. After cooling to RT and left to stand for 1 night the white precipitate was filtered, washed with a few mL of EtOH, and dried in air. Yield: 0.21 g (743.40 $g \cdot mol^{-1}$, 31 %). Elemental analysis ($C_{30}H_{36}Zn_2N_4O_{10}$, %) found C 48.52, H 4.91, N 7.51; calcd. C 48.47, H 4.88, N 7.54. MS (EI, pos.) *m/z* (%): 370 ($C_{15}H_{18}ZnN_2O_5$, 5), 310 ($C_{13}H_{15}ZnN_2O_3$, 93), 93 (C_6H_6N, 100). IR: ν = 1680 (s, C=O), 1612 (s, C=O), 1572 (s, C=O) cm^{-1}.

[ZnL2OAc] (2). $Zn(AcO)_2 \cdot 2H_2O$ (0.2 g, 0.91 mmol) and HL2 (0.331 g, 1.52 mmol) were dissolved in MeOH (5 mL) and the light yellow solution was heated to reflux for 1 h. After cooling to RT and left to stand for 1 night the white precipitate was filtered, washed with a few mL of MeOH, and dried in air. Yield: 0.25 g (683.34 $g \cdot mol^{-1}$, 40 %). Elemental analysis ($C_{28}H_{32}Zn_2N_4O_{10}$, %) found C 48.90, H 4.94, N 8.02; calcd. C 49.21, H 4.72, N 8.20. MS (EI, pos.) *m/z* (%): 340 ($C_{14}H_{16}ZnN_2O_4$, 5), 280 ($C_{12}H_{13}ZnN_2O_2$, 100), 93 (C_6H_6N, 65). IR: ν = 1665 (s, C=O), 1567 (s, C=O) cm^{-1}.

[ZnL3OAc] (3). $Zn(AcO)_2 \cdot 2H_2O$ (0.2 g, 0.91 mmol) and HL3 (0.176 g, 1.52 mmol) were dissolved in EtOH (5 mL) and the light yellow solution was heated to reflux for 1 h. After cooling to RT and left to stand for 1 night the white precipitate was filtered, washed with a few mL of EtOH, and dried in air. Yield: 0.22 g (709.34 $g \cdot mol^{-1}$, 34 %). Elemental analysis ($C_{28}H_{30}Zn_2N_6O_8$, %) found C 46.81, H 4.13, N 11.57; calcd. C 47.41, H 4.26, N 11.85. MS (EI, pos.) *m/z* (%): 353 ($C_{14}H_{15}ZnN_3O_4$, 6), 293 ($C_{12}H_{12}ZnN_3O_2$, 100). IR: ν = 2193 (s, C≡N), 1650 (s, C=O), 1591 (s, C=O) cm^{-1}.

[ZnL4OAc] (4). $Zn(AcO)_2 \cdot 2H_2O$ (0.2 g, 0.91 mmol) and HL4 (0.356 g, 1.52 mmol) were dissolved in MeOH (5 mL) and the light orange solution was heated to reflux for 1 h. After cooling to RT and left to stand for 1 night the white precipitate was filtered, washed with a few mL of MeOH, and dried in air. Yield: 0.23 g (715.34 $g \cdot mol^{-1}$, 35 %). Elemental analysis ($C_{28}H_{32}Zn_2N_4O_{10}$, %) found C 46.86, H 4.69, N 7.71; calcd. C 47.01, H 4.51, N 7.83. MS (EI, pos.) *m/z* (%): 356 ($C_{14}H_{16}ZnN_2O_5$, 7), 296 ($C_{12}H_{13}ZnN_2O_3$, 100), 93 (C_6H_6N, 45). IR: ν = 1681 (s, C=O), 1611 (s, C=O), 1579 (s, C=O) cm^{-1}.

[ZnL5OAc] (5). $Zn(AcO)_2 \cdot 2H_2O$ (0.2 g, 0.91 mmol) and HL5 (0.471 g, 1.52 mmol) were dissolved in EtOH (5 mL) and the light orange solution was heated to reflux for 1 h. After cooling to RT and left to stand for 1 night the white precipitate was filtered, washed with a few

mL of EtOH, and dried in air. Yield: 0.32 g (867.54 g·mol^{-1}, 41 %). Elemental analysis ($C_{40}H_{40}Zn_2N_4O_{10}$, %) found C 55.30, H 4.56, N 6.41; calcd. C 55.38, H 4.65, N 6.46. MS (EI, pos.) *m/z* (%): 432 ($C_{20}H_{20}ZnN_2O_5$, 6), 372 ($C_{18}H_{17}ZnN_2O_3$, 100), 93 (C_6H_6N, 38). IR: ν = 1676 (s, C=O), 1608 (s, C=O), 1571 (s, C=O) cm^{-1}.

X-ray diffraction on single crystals

The X-ray analysis was performed with a Stoe StadiVari diffractometer using graphite-monochromated MoKα radiation. The data were corrected for Lorentz and polarization effects. The structures were solved by direct methods (SIR-97)[28] and refined by fullmatrix least-square techniques against Fo2–Fc2 (SHELXL-97).[29] All hydrogen atoms were calculated in idealised positions with fixed displacement parameters. ORTEP-III[30] was used for the structure representation, SCHAKAL-99[31] to illustrate molecule packing. CCDC 1901404 (**1**) and CCDC 1900405 (**5**) contain the supplementary crystallographic data for this paper.

Powder X-ray diffraction

Powder diffractograms were measured with a STOE StadiP Powder Diffractometer (STOE, Darmstadt) using Cu[Kα1] radiation with a Ge Monochromator, and a Mythen 1K Stripdetector in transmission geometry.

Reaction monitoring

Raman spectra were obtained under process conditions using a RXN1 spectrometer from Kaiser Optical Systems. Ten accumulated measurements with 0.5 seconds measuring time were subsumed to one spectrum. The laser was used at a wavelength 785 nm and 459 mW through an immersion probe with a short-focus sapphire lens (d = 0.1 mm). The resulting time-resolved data was processed with the *PEAXACT* 4.0 Software. The boundaries for the lactide integration were 627 – 713 cm^{-1}.

Polymerization

All polymerizations at a ratio of [M]/[I] = 500:1 and 2000:1 have been investigated twice.

Technical grade lactide: *rac*-LA from Total Corbion PLA was used for the polymerisations. Therefore, D- and L-lactide were mixed in a ratio of 1:1. Both D- and L-lactide consisted of maximum free acids of 3 meq kg^{-1} and maximum water residues of 0.01%.

Polymerisation followed by Raman spectroscopy: In a nitrogen filled glovebox, the catalyst and *rac*-LA (3,6-dimethyl-1,4-dixane-2,5-dione, 12.0 g, 83.3 mmol) were weighed separately. The catalyst and the lactide were homogenised completely in an agate mortar and the mixture filled in a glass vial. The steel reactor was heated at 150 °C under vacuum and flashed three times with argon. For polymerisation, the reaction mixture was filled in a steel reactor under argon conditions (99.998% purity). The reactor was closed with a shaft drive stirrer with agitator speed contro ("minisprint", premix reactor AG, Switzerland) and the sample collection started after the reaction mixture insertion as soon as the reactor was closed. The Raman probe was installed close to the stirrer. The shaft drive stirrer with agitator speed control was used to stir the reaction at 260 rpm. The reaction mixture was removed from the reactor at 150 °C and ^{1}H NMR was collected at room temperature on a Bruker Avance II (400 MHz) or a Bruker Avance III (400 MHz) to determine the conversion. The NMR signals were calibrated to the residual signals of the deuterated solvent [$\delta_H(CDCl_3)$ = 7.26 ppm]. The reaction mixture was dissolved in an appropriate amount of DCM, the polymer was precipitated in ethanol (r.t.), dried *in vacuo* and characterised.

Gel permeation chromatography

The average molecular masses and the mass distributions of the obtained polylactide samples were determined by GPC in THF as the mobile phase at a flow rate of 1 mL min^{-1}. The utilised GPCmax VE-2001 from Viscotek was a combination of an HPLC pump, two Malvern Viscotek T columns (porous styrene divinylbenzene co-polymer) with a maximum pore size of 500 and 5000 Å, a refractive index detector (VE-3580), and a viscometer (Viscotek 270 Dual Detector). Universal calibration was applied to evaluate the chromatographic results.

MALDI-ToF mass spectrometry: The end group analysis was performed by MALDI-ToF on a Bruker ultrafleXtreme equipped with a 337 nm smartbeam laser in the reflective mode. THF solutions of *trans*-2-[3-(4-*tert*-butylphenyl)-2-methyl-2-propenylidene]malononitrile (DCTB) (5 µL of a 20 mg/mL solution), sodium trifluoroacetate (0.1 µL of a 10 mg/mL solution), and analyte (5 µL of a 10 mg/mL) were mixed and a droplet thereof applied on the sample target. Protein 1 calibration standard is the name of the protein mixture used for calibration. For spectra 4000 laser shots with 24% laser power were collected. The laser repetition rate was 1000 Hz. The homopolymer analysis was performed using Polymerix software (Sierra analytics).

Cell culture

The human melanoma cell line 518A2, the human colon carcinoma cell lines HT-29 and HCT-116, the cervix carcinoma cell line Hela, and the non-malignant Hdfa fibroblasts were cultivated in Dulbecco's Modified Eagle Medium supplemented with 10% FBS, and 1% antibiotic-antimycotic at 37 °C, 5% CO_2 and 95% humidity. Only mycoplasma-free cultures were used.

MTT assay

The cytotoxicity of the compounds was studied via the MTT-based proliferation assay [32] on cells of 518A2 melanoma (obtained from the department of Radiotherapy and Radiobiology, University Hospital Vienna, Austria), HT29 (DSMZ ACC-299) and $HCT116^{wt}$ (DSMZ ACC-581) colon carcinomas, Hela (DSMZ ACC-57) cervix carcinoma, and Hdfa fibroblasts (Thermo Fisher). Briefly, cells (100 µL/well; 5×10^4 cells/mL for the four tumour cell lines, 1×10^5 for the Hdfa cells) were grown in 96-well plates for 24 h and then treated with varying concentrations of the test compound or solvent control (DMSO) for 72 h. After centrifugation of the plates (300 g, 5 min, 4 °C), the supernatant was discarded and 50 µL/well of a 0.05% MTT solution in PBS was added to the wells and incubated for 2 h. After another centrifugation step the supernatant was discarded and the formazan precipitate was dissolved in 25 µL DMSO containing 10% SDS and 0.6% acetic acid for at least 1 h at 37 °C and the absorbance of formazan (570 nm) and background (630 nm) was measured with a microplate reader (Tecan). The IC_{50} values were calculated as the mean ± standard deviation of four independent experiments.

Acknowledgements

P.M.S. thanks the Hanns-Seidel-Foundation (fellowship) for funding (Bundesministerium für Bildung und Forschung, BMBF). The authors thank Total Corbion PLA for lactide donations. KD thanks the BayNAT graduate school for financial support. F. Puchtler and M. Schwarzmann (AC I, University of Bayreuth) are thanked for the PXRD measurements and the TGA.

9.5 References

[1] a) F. Wikström, K. Verghese, R. Auras, A. Olsson, H. Williams, R. Wever, K. Grönman, M. K. Pettersen, H. Møller, R. Soukka, *J. Ind. Ecol.*, *0*; b) J. L. Lavers, A. L. Bond, *Proc. Natl. Acad. Sci. USA* **2017**, *114*, 6052–6055; c) R. Geyer, J. R. Jambeck, K. L. Law, *Sci. Adv.* **2017**, *3*.

[2] G. L. Gregory, E. M. Lopez-Vidal, A. Buchard, *Chem. Commun.* **2017**, *53*, 2198–2217.

[3] Y. Zhu, C. Romain, C. K. Williams, *Nature* **2016**, *540*, 354–362.

[4] a) E. Castro-Aguirre, F. Iñiguez-Franco, H. Samsudin, X. Fang, R. Auras, *Adv. Drug Delivery Rev.* **2016**, *107*, 333–366; b) R. Auras, B. Harte, S. Selke, *Macromol. Biosci.* **2004**, *4*, 835–864; c) R. E. Drumright, P. R. Gruber, D. E. Henton, *Adv. Mater.* **2000**, *12*, 1841–1846.

[5] a) A. P. Dove, *Chem. Commun.* **2008**, 6446–6470; b) M. J. Stanford, A. P. Dove, *Chem. Soc. Rev.* **2010**, *39*, 486–494; c) O. Dechy-Cabaret, B. Martin-Vaca, D. Bourissou, *Chem. Rev.* **2004**, *104*, 6147–6176; d) Y. Sarazin, J.-F. Carpentier, *Chem. Rev.* **2015**, *115*, 3564–3614; e) I. dos Santos Vieira, S. Herres-Pawlis, *Eur. J. Inorg. Chem.* **2012**, 765–774.

[6] Z. Zhong, P. J. Dijkstra, J. Feijen, *Angew. Chem.* **2002**, *114*, 4692–4695.

[7] a) J. W. Leenslag, A. J. Pennings, *Makromol. Chem.* **1987**, *188*, 1809–1814; b) A. J. Nijenhuis, D. W. Grijpma, A. J. Pennings, *Macromolecules* **1992**, *25*, 6419–6424; c) H. R. Kricheldorf, R. Dunsing, *Makromol. Chem.* **1986**, *187*, 1611–1625; d) H. R. Kricheldorf, R. Dunsing, A. Serra, *Macromolecules* **1987**, *20*, 2050–2057.

[8] a) H. R. Kricheldorf, *Chemosphere* **2001**, *43*, 49–54; b) A. Stjerndahl, A. Finne-Wistrand, A. C. Albertsson, C. M. Bäckesjö, U. Lindgren, *J. Biomed. Mater. Res., Part A* **2008**, *87A*, 1086–1091.

[9] B. M. Chamberlain, M. Cheng, D. R. Moore, T. M. Ovitt, E. B. Lobkovsky, G. W. Coates, *J. Am. Chem. Soc.* **2001**, *123*, 3229–3238.

[10] Y. Yang, H. Wang, H. Ma, *Inorg. Chem.* **2015**, *54*, 5839–5854.

[11] T. Ebrahimi, E. Mamleeva, I. Yu, S. G. Hatzikiriakos, P. Mehrkhodavandi, *Inorg. Chem.* **2016**, *55*, 9445–9453.

[12] C. K. Williams, L. E. Breyfogle, S. K. Choi, W. Nam, V. G. Young, M. A. Hillmyer, W. B. Tolman, *J. Am. Chem. Soc.* **2003**, *125*, 11350–11359.

[13] C. A. Wheaton, P. G. Hayes, *Chem. Commun.* **2010**, *46*, 8404–8406.

[14] a) C. Scheiper, D. Dittrich, C. Wölper, D. Bläser, J. Roll, S. Schulz, *Eur. J. Inorg. Chem.* **2014**, 2230–2240; b) C. Scheiper, S. Schulz, C. Wölper, D. Bläser, J. Roll, *Z. Anorg. Allg. Chem.* **2013**, *639*, 1153–1159; c) C. Scheiper, C. Wölper, D. Bläser, J. Roll, S. Schulz, *Z. Naturforsch.* **2014**, *69b*, 1365–1374; d) P. Steiniger, P. M. Schäfer, C. Wölper, J. Henkel, A. N. Ksiazkiewicz, A. Pich, S. Herres-Pawlis, S. Schulz, *Eur. J. Inorg. Chem.* **2018**, *2018*, 4014–4021.

[15] M. H. Chisholm, N. W. Eilerts, J. C. Huffman, S. S. Iyer, M. Pacold, K. Phomphrai, *J. Am. Chem. Soc.* **2000**, *122*, 11845–11854.

[16] Y. Huang, W. Wang, C.-C. Lin, M. P. Blake, L. Clark, A. D. Schwarz, P. Mountford, *Dalton Trans.* **2013**, *42*, 9313–9324.

[17] A. Thevenon, C. Romain, M. S. Bennington, A. J. P. White, H. J. Davidson, S. Brooker, C. K. Williams, *Angew. Chem. Int. Ed.* **2016**, *55*, 8680–8685.

[18] A. J. Chmura, M. G. Davidson, C. J. Frankis, M. D. Jones, M. D. Lunn, *Chem. Commun.* **2008**, 1293–1295.

[19] a) T. R. Forder, M. F. Mahon, M. G. Davidson, T. Woodman, M. D. Jones, *Dalton Trans.* **2014**, *43*, 12095–12099; b) S. L. Hancock, M. F. Mahon, M. D. Jones, *Dalton Trans.* **2013**, *42*, 9279–9285; c) M. D. Jones, L. Brady, P. McKeown, A. Buchard, P. M. Schäfer, L. H. Thomas, M. F. Mahon, T. J. Woodman, J. P. Lowe, *Chem. Sci.* **2015**, *6*, 5034–5039; d) M. D. Jones, M. G. Davidson, C. G. Keir, L. M. Hughes, M. F. Mahon, D. C. Apperley, *Eur. J. Inorg. Chem.* **2009**, 635–642; e) M. D. Jones, S. L. Hancock, P. McKeown, P. M. Schäfer, A. Buchard, L. H. Thomas, M. F. Mahon, J. P. Lowe, *Chem. Commun.* **2014**, *50*, 15967-15970; f) P. McKeown, M. G. Davidson, G. Kociok-Kohn, M. D. Jones, *Chem. Commun.* **2016**, *52*, 10431–10434.

[20] P. McKeown, S. N. McCormick, M. F. Mahon, M. D. Jones, *Polym. Chem.* **2018**, *9*, 5339–5347.

[21] a) O. Bienemann, A.-K. Froin, I. dos Santos Vieira, R. Wortmann, A. Hoffmann, S. Herres-Pawlis, *Z. Anorg. Allg. Chem.* **2012**, *638*, 1683–1690; b) S. Herres-Pawlis, A. Neuba, O. Seewald, T. Seshadri, H. Egold, U. Flörke, G. Henkel, *Eur. J. Org. Chem.* **2005**, 4879–4890; c) T. Rösener, O. Bienemann, K. Sigl, N. Schopp, F. Schnitter, U. Flörke, A. Hoffmann, A. Döring, D. Kuckling, S. Herres-Pawlis, *Chem. Eur. J.* **2016**, *22*, 13550–13562; d) T. Rösener, A. Hoffmann, S. Herres-Pawlis, *Eur. J. Inorg. Chem.* **2018**, 3164–3175; e) J. Stanek, T. Rösener, A. Metz, J. Mannsperger, A. Hoffmann, S.

Herres-Pawlis, in *Topics in Heterocyclic Chemistry*, Springer Berlin Heidelberg, Berlin, Heidelberg, **2015**, pp. 1–70.

[22] a) A. Metz, J. Heck, C. Gohlke, K. Kröckert, Y. Louven, P. McKeown, A. Hoffmann, M. Jones, S. Herres-Pawlis, *Inorganics* **2017**, *5*, 85; b) A. Metz, P. McKeown, B. Esser, C. Gohlke, K. Kröckert, L. Laurini, M. Scheckenbach, S. N. McCormick, M. Oswald, A. Hoffmann, M. D. Jones, S. Herres-Pawlis, *Eur. J. Inorg. Chem.* **2017**, 5557–5570; c) A. Metz, R. Plothe, B. Glowacki, A. Koszalkowski, M. Scheckenbach, A. Beringer, T. Rösener, J. Michaelis de Vasconcellos, R. Haase, U. Flörke, A. Hoffmann, S. Herres-Pawlis, *Eur. J. Inorg. Chem.* **2016**, 4974–4987; d) J. Börner, U. Flörke, K. Huber, A. Döring, D. Kuckling, S. Herres-Pawlis, *Chem. Eur. J.* **2009**, *15*, 2362–2376.

[23] a) P. M. Schäfer, M. Fuchs, A. Ohligschläger, R. Rittinghaus, P. McKeown, E. Akin, M. Schmidt, A. Hoffmann, M. A. Liauw, M. D. Jones, S. Herres-Pawlis, *ChemSusChem* **2017**, *10*, 3547–3556; b) P. M. Schäfer, P. McKeown, M. Fuchs, R. D. Rittinghaus, A. Hermann, J. Henkel, S. Seidel, C. Roitzheim, A. N. Ksiazkiewicz, A. Hoffmann, A. Pich, M. D. Jones, S. Herres-Pawlis, *Dalton Trans.* **2019**, 10.1039/C8DT04938F.

[24] S. Herres-Pawlis, R. D. Rittinghaus, P. M. Schäfer, P. Albrecht, C. Conrads, A. Hoffmann, A. Ksiazkiewicz, O. Bienemann, A. Pich, *ChemSusChem* **2019,** 10.1002/cssc.201900481.

[25] a) K. Dankhoff, B. Weber, *CrystEngComm* **2018**, *20*, 818–828; b) K. Dankhoff, S. Schneider, R. Nowak, B. Weber, *Z. Anorg. Allg. Chem.* **2018**, *644*, 1839–1848.

[26] L. Yang, D. R. Powell, R. P. Houser, *Dalton Trans.* **2007**, 955–964.

[27] W. A. Munzeiwa, V. O. Nyamori, B. Omondi, *Appl. Organomet. Chem.* **2018**, *32*, e4247.

[28] A. Altomare, M. C. Burla, M. Camalli, G. L. Cascarano, C. Giacovazzo, A. Guagliardi, A. G. G. Moliterni, G. Polidori, R. Spagna, *J. Appl. Crystallogr.* **1999**, *32*, 115–119.

[29] G. Sheldrick, *Acta Cryst. A* **2008**, *64*, 112–122.

[30] M. N. Burnett, C. K. Johnson, ; Oak Ridge National Lab., TN (United States), **1996**, p. 176.

[31] E. Keller, Schakal-99, University of Freiburg, Germany, Freiburg, **1999**.

[32] T. Mosmann, *J. Immunol. Methods* **1983**, *65*, 55–63.

9.6 Supporting Information

Table S1. Crystallographic data of **1** and **5**.

	1	**5**
CCDC	1901404	1901405
formula	$C_{30}H_{36}N_4O_{10}Zn_2$	$C_{40}H_{40}N_4O_{10}Zn_2$
sum formula	$C_{30}H_{36}N_4O_{10}Zn_2$	$C_{40}H_{40}N_4O_{10}Zn_2$
M/ g mol^{-1}	743.41	867.50
crystal system	triclinic	monoclinic
space group	$P-1$	$P2_1/c$
crystal description	colourless plate	colourless plate
a/ Å	9.4692(4)	16.9724(5)
b/ Å	13.2391(6)	14.5261(5)
c/ Å	13.1893(6)	17.2695(6)
α/ °	96.547(4)	90
β/ °	93.463(3)	115.352(2)
γ/ °	106.449(4)	90
V/ Å^3	1567.97(13)	3847.6(2)
Z	2	4
ρ_{calcd}/ g cm^{-3}	1.575	1.498
μ/ mm^{-1}	1.593	1.311
crystal size/ mm	0.136×0.050×0.046	0.120×0.106×0.075
F(000)	768	1792
T/ K	133(2)	133(2)
λ/ Å	Mo-Kα 0.71073	Mo-Kα 0.71073
Θ range/ °	2.09–28.47	1.9–28.1
Reflns. collected	8917	22994
Indep. reflns.(R_{int})	7320 (0.071)	8714 (0.033)
Parameters	415	505
$R1$ (all data)	0.0464	0.0295
$wR2$	0.1134	0.0662
GooF	0.89	0.94

Table S2. Selected bond lengths/ Å of **1** and **5**.

	Zn–N_{py}	Zn–N_{ax}	Zn–O_{ax}	Zn–O53	Zn2–O51	Zn1–O52	O51–C51	O52–C51	O53–C53	O54–C53
1	2.134(3)	2.031(3)	2.059(3)	2.024(3)	2.031(3)	1.978(3)	1.257(5)	1.270(5)	1.311(5)	1.222(5)
	2.159(3)	2.021(3)	2.054(3)	2.035(3)						
5	2.1189(11)	2.0330(15)	2.0435(15)	2.0396(13)	2.0086(16)	1.9708(15)	1.250(2)	1.263(2)	1.307(2)	1.221(2)
	2.1662(19)	2.0424(16)	2.0500(16)	2.0499(13)						

Table S3. Hydrogen bonds and angles of **1** and **5**.

		D–H/Å	H···A/Å	D···A/Å	D–H···A/°
1	C14–H14···O54[a]	0.95	2.34	3.140(5)	142
5	C13–H13···O33[b]	0.95	2.43	3.287(3)	150
	C14–H14···O54[b]	0.95	2.43	3.309(3)	154
	C27–H27A···O32[c]	0.99	2.57	3.205(3)	122
	C33–H33···O54[d]	0.95	2.46	3.175(3)	132
	C44–H44···O51[e]	0.95	2.50	3.393(3)	157
	C52–H52B···O12[f]	0.98	2.52	3.454(3)	160

a: −1+x, y, z; b: x, 1/2−y, 1/2+z; c: 1+x, y, 1+z; d: 2−x, −y, 1−z; e: 1−x, −y, 1−z; f: 2−x, −y, 2−z.

Table S4. Summary of the C–H···π interactions of **1** and **5**.

		C_g	H···C_g/Å	X–H···C_g/°	X···C_g/Å
1	C6–H6B	Zn2–N31–C35–C36–N32[a]	2.769	147	3.626(4)
	C36–H36A	Zn1–N11_C15–C16–N12[b]	2.95	135	3.718(4)
	C42–H42B	Zn2–O31–C39–C38–C37–N32[c]	2.68	138	3.479(5)
5	C32–H32	C20–C21–C22–C23–C24–C25[d]	2.67	142	3.467(2)
	C16–H16B	Zn1–O11–C19–C18–C17–N12[e]	2.48	153	3.388(2)
	C44–H44	Zn2–O31–C39–C38–C37–N32[f]	2.85	126	3.493(2)

a: −1+x, y, z; b: 1+x, y, z; c: 2−x, −y, 1−z; d : x, y, z; e: 2−x, −y, 2−z; f: 1−x, −y, 1−z.

Table S5. Selected distances and angles of the π– π and M– π interactions of **1** and **5**. C_g(I) is the centroid of the ring number I, α is the dihedral angle between the rings, β is the angle between the vector C_g(I) → C_g(J) and the normal to ring I, γ is the angle between the vector C_g(I) → C_g(J) and the normal to ring J.

	C_g(I)	C_g(J)	C_g–C_g/Å	α/°	β/°	γ/°
1	N31–C31–C32–C33–C34–C35	N31–C31–C32–C33–C34–C35[a]	3.721(2)	0.00(19)	22.1	22.1
5	N31–C31–C32–C33–C34–C35	N31–C31–C32–C33–C34–C35[b]	3.4814(12)	0.00(10)	18.0	18.0

a: 2−x, −y, 2−z; b: 2−x, −y, 1−z.

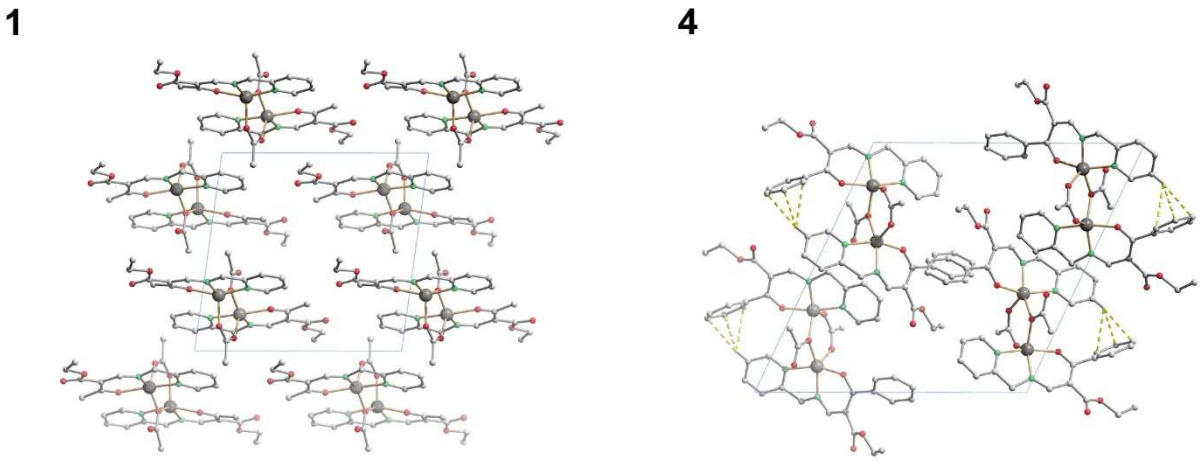

Figure S1. Molecular packing of **1** (left, along [100]) and **5** (right, along [010]). Discussed C–H···π interactions of **5** are drawn as yellow, dashed lines. Hydrogen atoms not involved in intermolecular interactions were omitted for clarity.

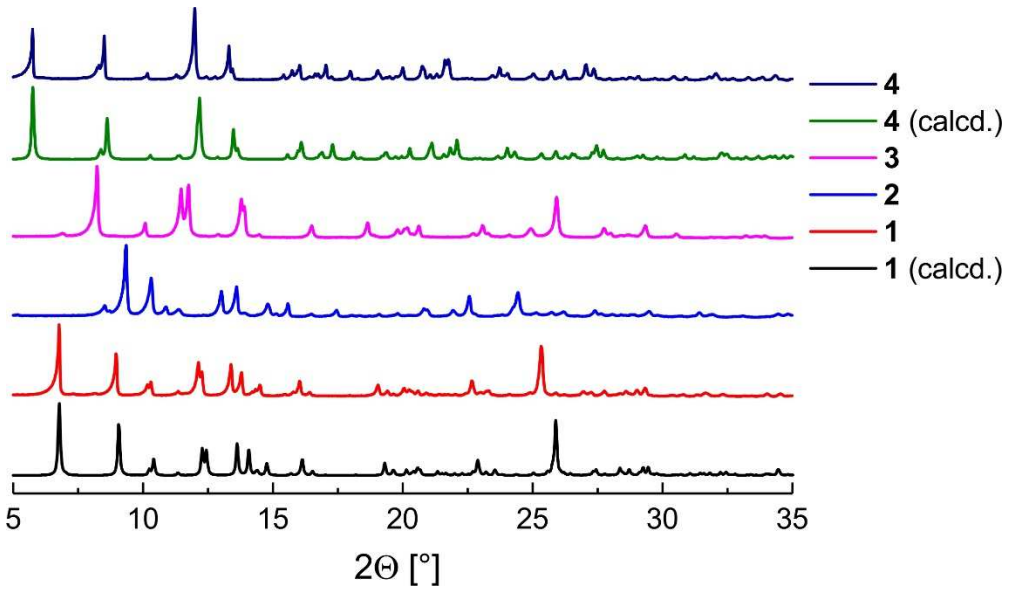

Figure S2. Powder X-ray diffraction patterns of **1**–**5**, measured and calculated. The calculated patterns were obtained at 133 K, the measured ones at room temperature.

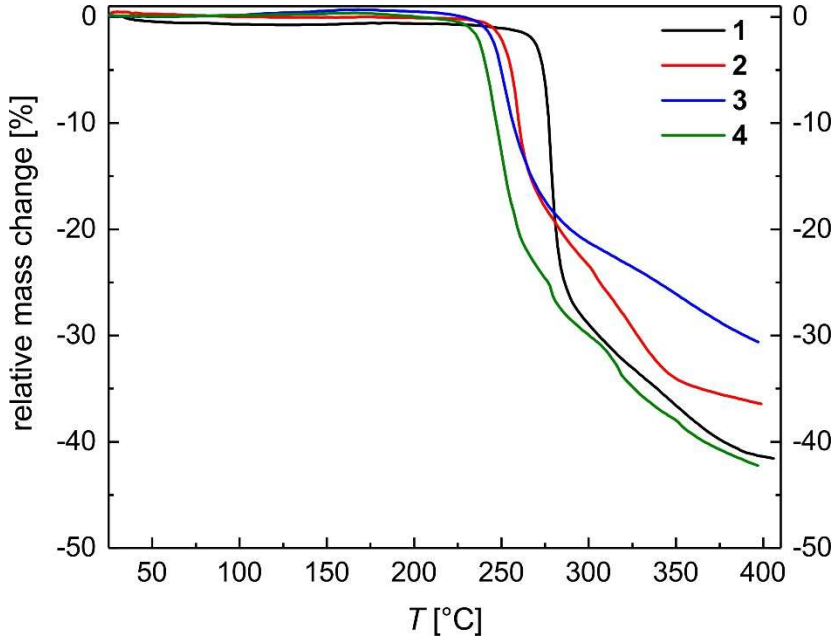

Figure S3. TGA measurements of complexes **1**–**5**.

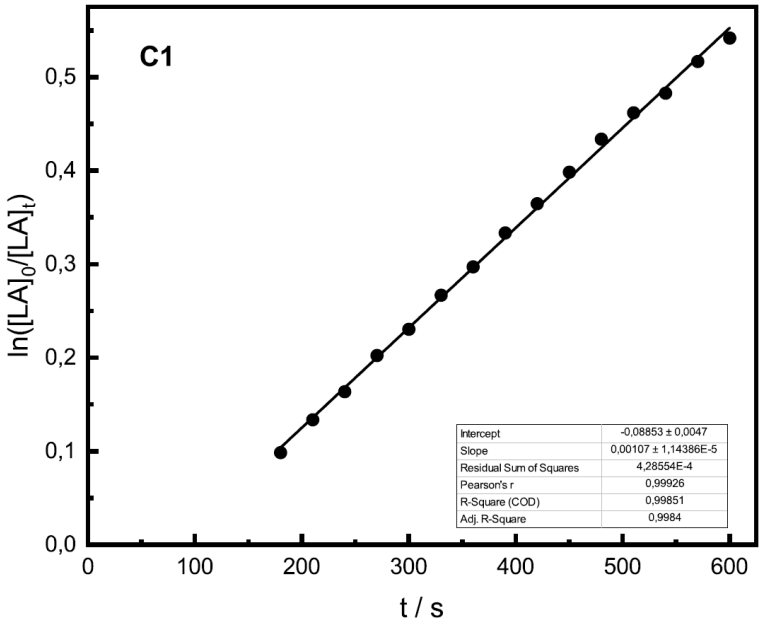

Figure S4. Semi-logarithmic plot of the polymerization of non-purified *rac*-LA with **1** [M]/[I] = 500:1, 150 °C, 260 rpm, conversion determined by *in situ* Raman spectroscopy.

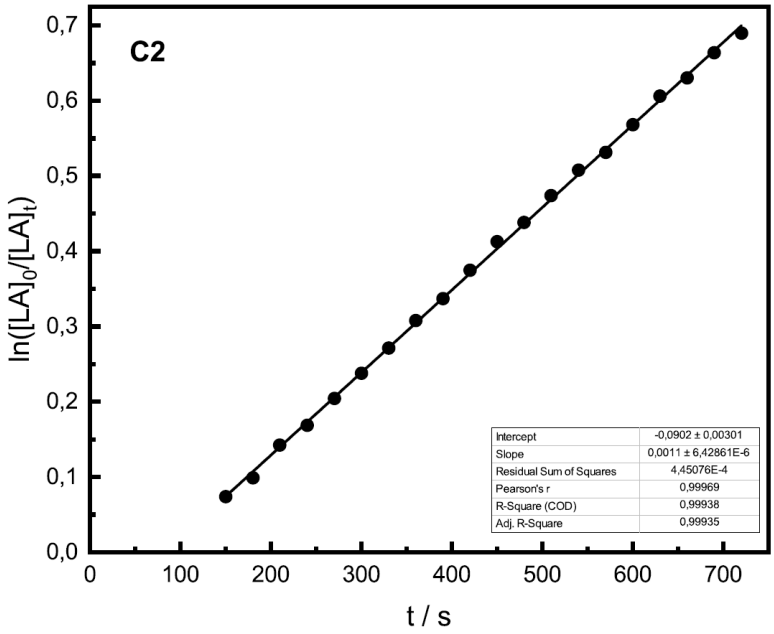

Figure S5. Semi-logarithmic plot of the polymerization of non-purified *rac*-LA with **2** [M]/[I] = 500:1, 150 °C, 260 rpm, conversion determined by *in situ* Raman spectroscopy.

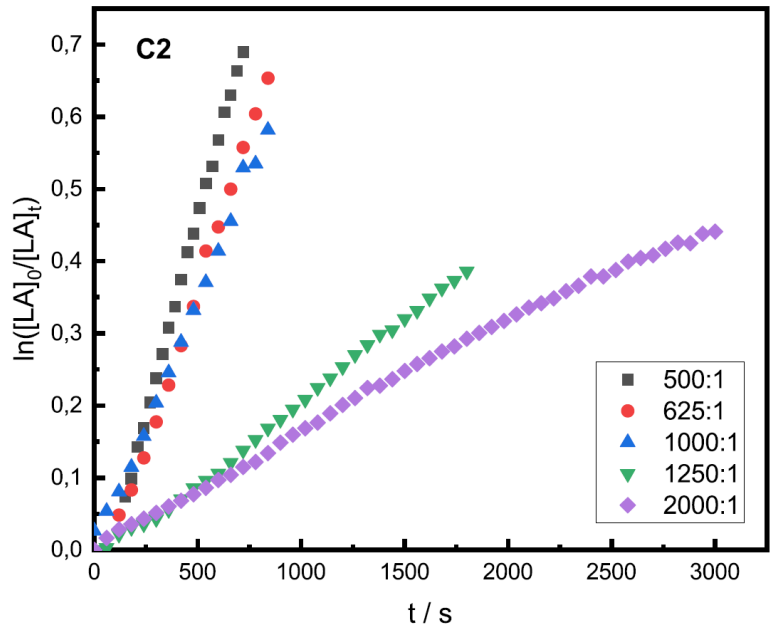

Figure S6. Semi-logarithmic plot of the polymerization of non-purified *rac*-LA with **2** [M]/[I] = 500:1 (*k*app =), [M]/[I] = 625:1 (*k*app =), [M]/[I] = 1000:1 (*k*app =), [M]/[I] = 1250:1 (*k*app =), [M]/[I] = 2000:1 (*k*app =), 150 °C, 260 rpm, conversion determined by *in situ* Raman spectroscopy.

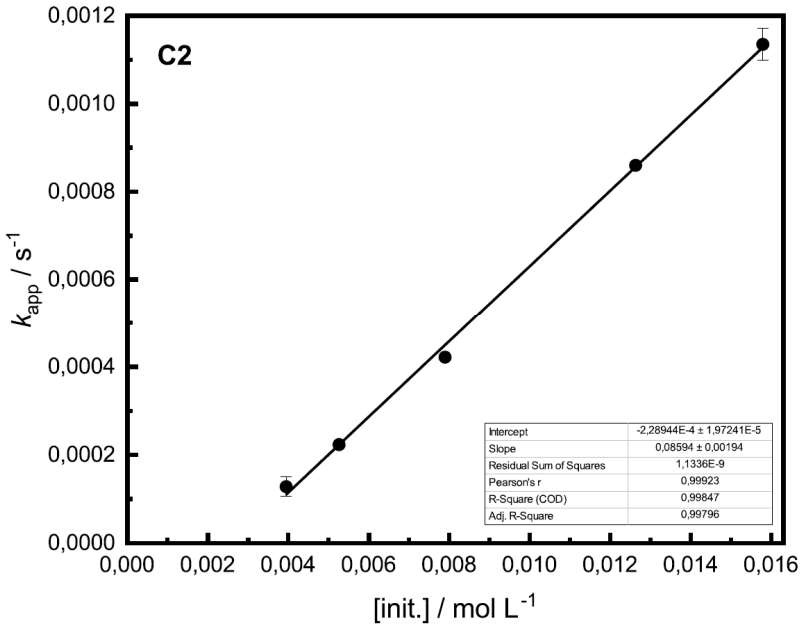

Figure S7. Plot of k_{app} versus [init.] for **2**. Conditions: rac-LA, 150 °C, 260 rpm, non-purified; [M]/[I] = 500:1, 625:1, 1000:1, 1500:1, 2000:1.

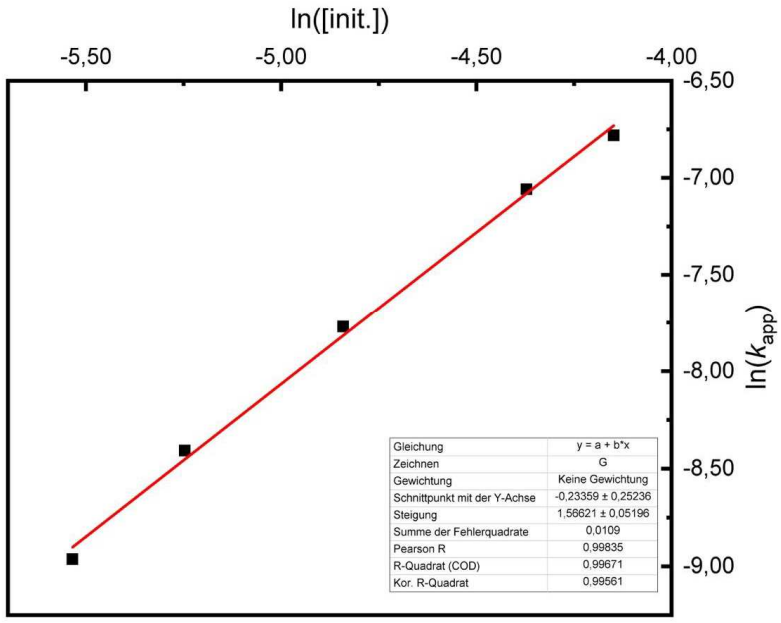

Figure S8. Logarithmic plot of ln(k_{app}) versus ln([init.]) for the polymerization of non-purified *rac*-LA with **4** [M]/[I] = 500:1, 150 °C, 260 rpm.

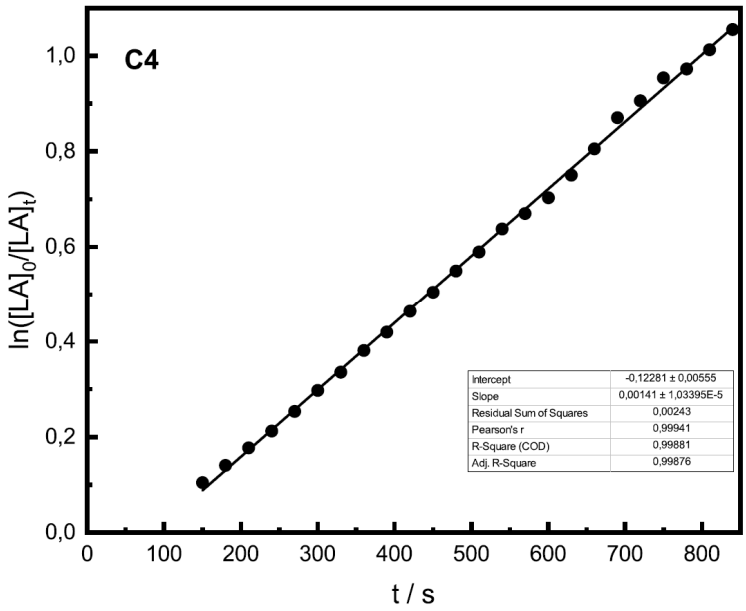

Figure S9. Semi-logarithmic plot of the polymerization of non-purified *rac*-LA with **4** [M]/[I] = 500:1, 150 °C, 260 rpm, conversion determined by *in situ* Raman spectroscopy.

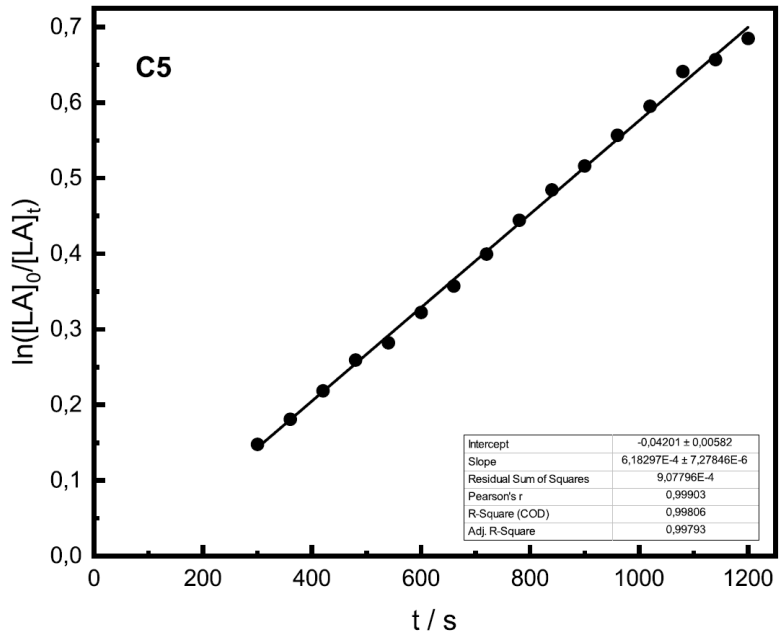

Figure S10. Semi-logarithmic plot of the polymerization of non-purified *rac*-LA with **5** [M]/[I] = 500:1, 150 °C, 260 rpm, conversion determined by *in situ* Raman spectroscopy.

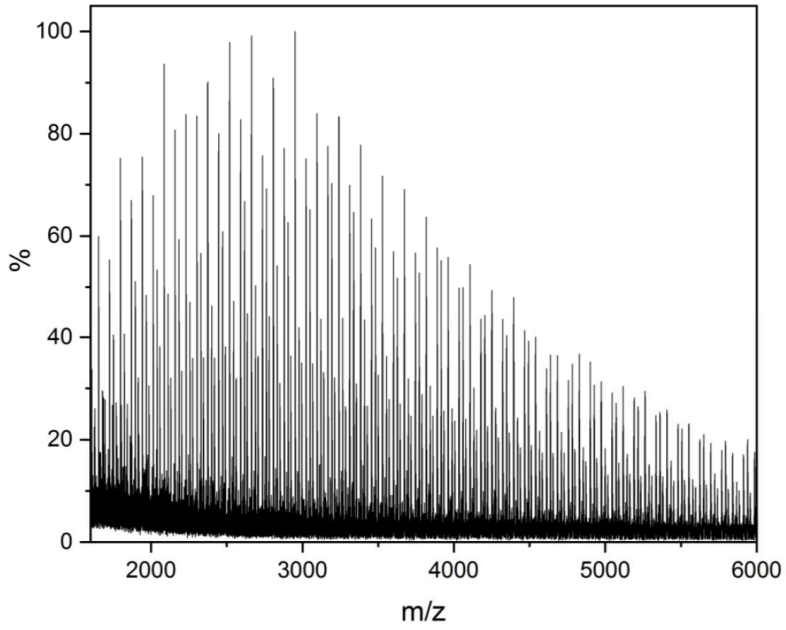

Figure S11. Stack of MALDI-ToF spectra obtained for a polymerisation with **4** [M]/[I] = 70:1, 150 °C, 260 rpm, *rac*-LA.

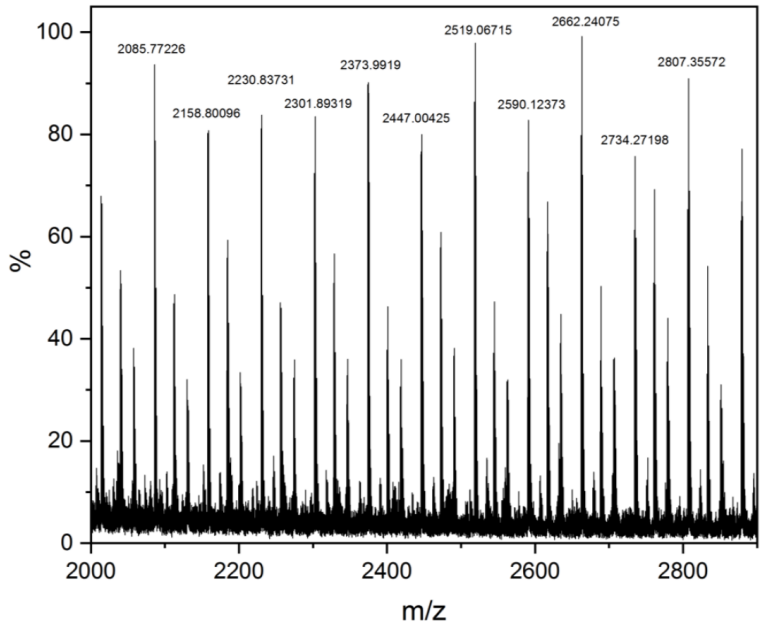

Figure S12. Stack of MALDI-ToF spectra obtained for a polymerisation with **4** [M]/[I] = 70:1, 150 °C, 260 rpm, *rac*-LA. For m/z 2807.35572:

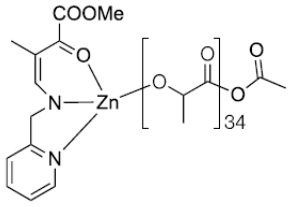

Table S6. Possible end-groups for the obtained polymer initiated by **4** [M]/[I] = 70:1, 150 °C, 260 rpm, *rac*-LA.

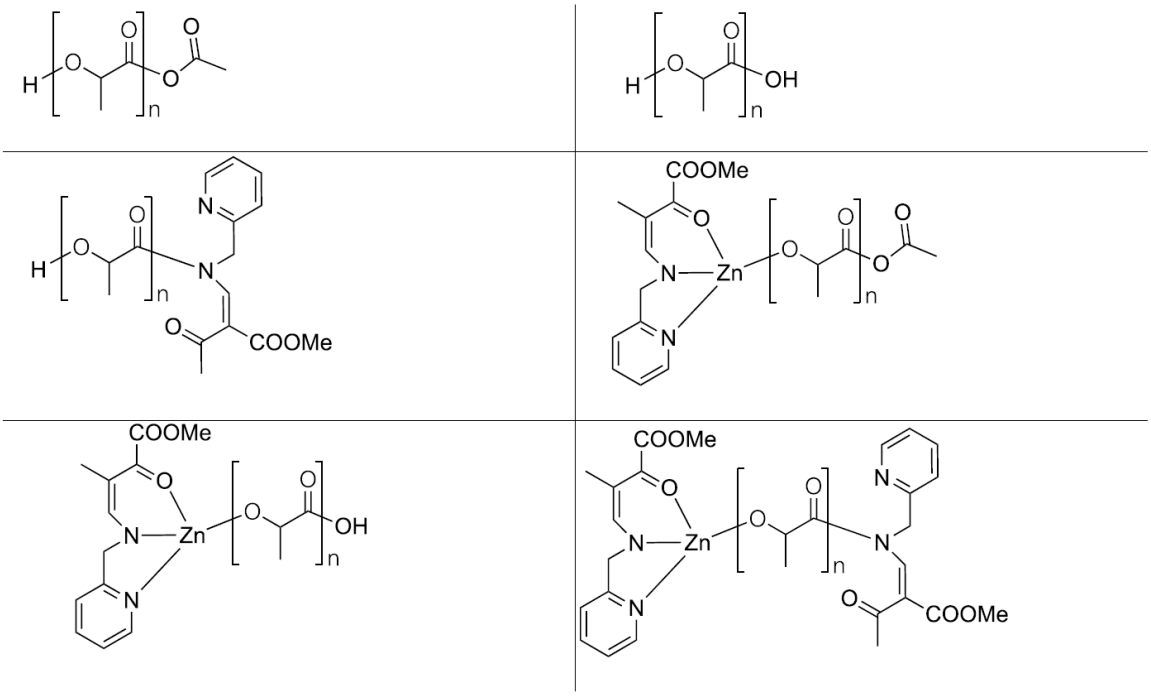

Results of the MALDI-ToF analysis for all series of the spectrum:

Ligand-Zn-PLA: 26.77%

Ligand-PLA: 10.59%

Acetate-PLA: 22.94%

OH: 10.53%

H: 17.29%

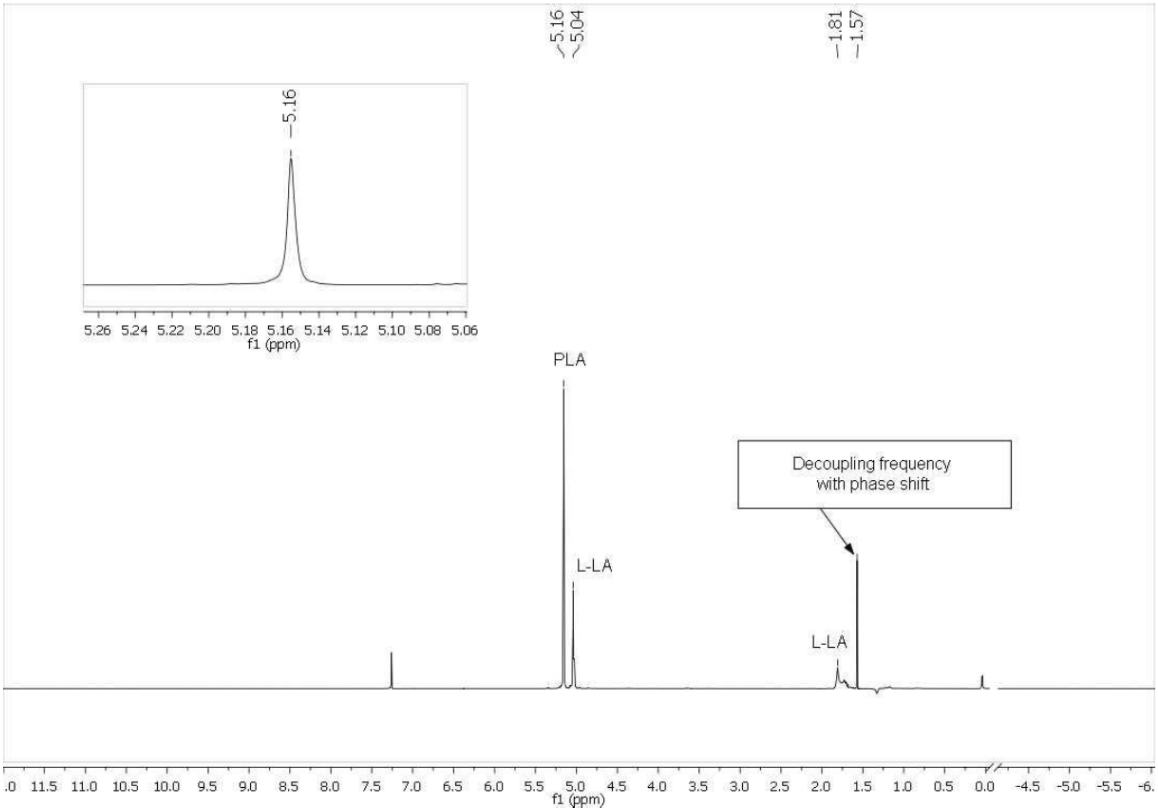

Figure S13. Homonuclear decoupled ^{1}H NMR spectrum ($CDCl_3$, 400 MHz) of PLA prepared by polymerization of L-lactide with **2** at 150 °C.

10. Copper(II) complexes with tridentate Schiff base-like ligands: solid state and solution structures and anticancer effects

Katja Dankhoff[+],[a] Madeleine Gold[+],[b] Luisa Kober,[b] Florian Schmitt,[b] Lena Pfeifer,[a] Andreas Dürrmann,[a] Hana Kostrhunova,[c] Matthias Rothemund,[b] Viktor Brabec,[c] Rainer Schobert,*[b] and Birgit Weber*[a]

[a] Department of Chemistry, Inorganic Chemistry IV, Universität Bayreuth, Universitätsstr. 30, 95440 Bayreuth, Germany. E-Mail: weber@uni-bayreuth.de;
[b] Department of Chemistry, Organic Chemistry I, Universität Bayreuth, Universitätsstr. 30, 95440 Bayreuth, Germany;
[c] Czech Academy of Sciences, Institute of Biophysics, Kralovopolska 135, CZ-61265 Czech Republic.
[+] These authors contributed equally to this work.

Published in *Dalton Trans.* **2019**, *48*, 15220–15230. (DOI: 10.1039/c9dt02571e)

Abstract: We report 15 new Cu(II) complexes with tridentate NNO β-acylenamino ligands derived from 2-picolylamine and bearing up to three alkyl, alkoxy, alkoxycarbonyl, or (pseudo)halide substituents. The structures of nine complexes were elucidated by single crystal X-ray diffraction analysis. Complexes with an unsubstituted pyridine ring crystallised with a square pyramidal coordination sphere, whereas substitution of the pyridine ring led to a square planar coordination sphere around the metal centre. The solution structures and properties of the complexes were characterised by UV-Vis spectroscopy and cyclic voltammetry. They were also tested for their cytotoxic effect on four human cancer cell lines. Two complexes were identified that were highly active with single-digit IC_{50} values, exceeding those of cisplatin by far. A tentative structure–activity relationship was proposed as well as topoisomerase I inhibition as a possible mode of action, while any significant interference with DNA and the level of reactive oxygen species could be excluded.

10.1 Introduction

The incidence and economic burden of cancer rise at an alarming rate. While the field of medicinal inorganic chemistry could in principle offer many avenues for the development of new therapeutic agents against cancer, the research is still dominated by platinum and ruthenium complexes.[1] Cisplatin, carboplatin, and oxaliplatin are customarily used for the treatment of various cancer entities such as testicular or colon cancer. These three complexes share a similar structure and mechanism of action. Despite their high efficacy, their clinical applicability is limited by serious side effects, originating from their high toxicity, and by the frequent occurrence of intrinsic or acquired resistance of tumours to platinum compounds.[2]

However, anti-cancer active complexes of metals other than platinum, including copper, became the focus of research interest in recent years.[3] Copper is essential for the development of organisms as it plays an important role as part of the active site of various metalloproteins such as tyrosinase, catecholase, or hemocyanin.[4] Therefore its complexes have been investigated under the assumption that endogenous metals may be less toxic to normal cells than to cancer cells. Nevertheless, copper is toxic at higher concentrations as it is redox-active and can displace other metal ions.[5] Anti-cancer active copper complexes may act in various ways, *e.g.* by DNA binding, apoptosis induction *via* reactive oxygen species (ROS) generation, and by inhibition of topoisomerase I.[6]

Cu(II) complexes with tridentate NNO-chelating Schiff base ligands were only occasionally evaluated for biological activity, and mostly for antibacterial effects.[7] For a few of them an interaction with DNA was observed.[8] However, to the best of our knowledge, there are no studies on their antiproliferative impact on cancer cells, in contrast to the related, yet well-investigated tridentate NNS-chelated thiosemicarbazone complexes.[9]

Here we present a series of 18 Cu(II) complexes with tridentate Schiff base-like ligands that bear different substituents (R, R′, and R″) to alter the electronic environment of the metal centre. The impact of the substituents on the properties of the corresponding complexes was already successfully demonstrated for the corresponding Fe(II/III) and Zn(II) complexes.[10] Here, single crystal X-ray structures of nine Cu(II) complexes were obtained and are discussed. All

compounds were tested with regard to their cytotoxic activity against different cancer cell lines. The underlying modes of action were investigated.

10.2 Results and Discussion

Synthesis.

The complexes were synthesised in three steps (Scheme 1). First, the tridentate ligands were synthesised by a condensation reaction between the amine and the respective β-acylenol ether. The synthesis of **HL1–HL6** was carried out as described previously.[10a] The substituted 2-picolylamines were synthesised using the synthetic procedures described by Karlin *et al*.[11] In order to obtain the corresponding Cu(II) complexes, $CuSO_4$, sodium methoxide, which acts as a base for the deprotonation of the ligand, and the respective tridentate ligand were heated to reflux in methanol, resulting in a dark blue or dark green solution.

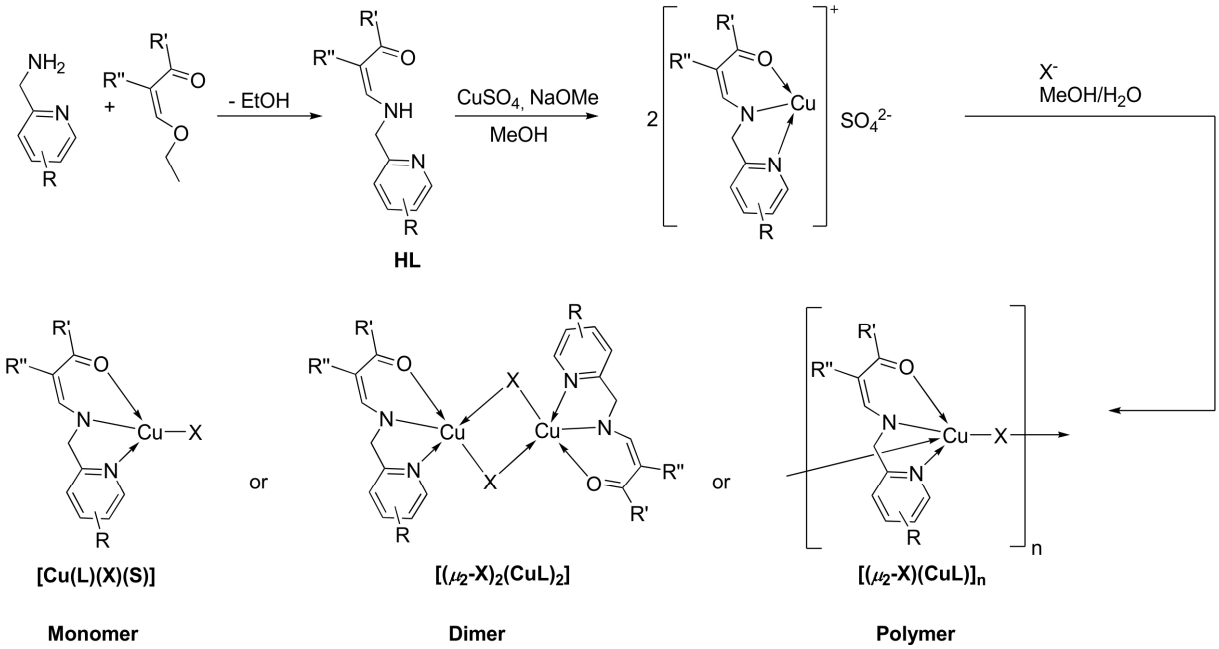

Scheme 1. General synthesis of the tridentate ligands **HL1-15** and their Cu(II) complexes **1**–**18**. The organic substituents R, R', and R'' and the anions X^- are specified in Table 1. Complexes **1**–**3** were obtained as described previously.[10a]

The use of a water-free base is important to avoid the formation of $Cu(OH)_2$/CuO during synthesis. The Cu(II) complexes **1–18** were precipitated with an aqueous solution of the sodium salt of the anion. They were obtained as crystalline, blue to green powders and their purity was confirmed by means of elemental analysis, mass spectrometry, and IR spectroscopy. Complexes **1–3** were described previously.[10a] An overview of all complexes described in this work is given in Table 1.

Table 1. Overview of the structures of copper complexes **1–18**. Complexes **1–3** were described previously.[10a]

Complex	Ligand	R	R‘	R‘‘	X^-	Solid state structure
1	HL1	-4-H	-Me	-COOEt	NO_3^-	Dimer[10a]
2	HL1	-4-H	-Me	-COOEt	Cl^-	Dimer[10a]
3	HL1	-4-H	-Me	-COOEt	NCS^-	Polymer[10a]
4	HL1	-4-H	-Me	-COOEt	Br^-	Dimer
5	HL2	-4-H	-Me	-COMe	Br^-	Dimer
6	HL3	-4-H	-OEt	-COOEt	Br^-	unknown
7	HL4	-4-H	-OEt	-CN	Br^-	Polymer
8	HL5	-4-H	-Ph	-COOEt	Br^-	Dimer
9	HL6	-4-H	-Me	-COOMe	Br^-	Dimer
10	HL7	-4-OMe	-OEt	-COOEt	Br^-	unknown
11	HL8	-4-OMe	-OEt	-CN	Br^-	unknown
12	HL9	-4-Cl	-OEt	-COOEt	Br^-	Monomer
13	HL10	-4-Cl	-OEt	-CN	Br^-	unknown
14	HL11	-4-Me	-OEt	-COOEt	Br^-	unknown
15	HL12	-4-Me	-OEt	-CN	Br^-	Monomer
16	HL13	-6-Me	-OEt	-CN	Br^-	unknown
17	HL14	-5-Me	-OEt	-COOEt	Br^-	Monomer
18	HL15	-5-Me	-OEt	-CN	Br^-	Monomer

X-ray structure analysis.

Crystals suitable for single crystal X-ray structure analysis were obtained for compounds **4**, **5**, **7**, **8**, **9**, **12**, **15**, **17**, and **18** by liquid–liquid diffusion of the precursor complex solution and an aqueous sodium bromide solution at room temperature. The crystallographic data were obtained at 133 K and are summarised in Table S1. Selected bond lengths and angles of the coordination sphere are given in Table S2. All complexes crystallised with one anion and one tridentate ligand per metal centre. The structures of **4**, **7**, and **17** are shown in Fig. 1 as representative examples, the remaining structures can be found in the ESI, Fig. S1. Complexes **4**, **5**, **8**, and **9**

crystallised as μ-bridged dimers, with the bromide ions connecting the two Cu(II) centres and the ligands orientated *trans* to one another. Complex **7** crystallised as a one dimensional coordination polymer with the anions bridging the metal centres to form an infinite chain, as described previously by us for complexes of this type.[10a] The metal centre has a square pyramidal coordination sphere. Complexes **12**, **15**, **17**, and **18** show a square planar coordination of the Cu(II) centre, yet do not form dimers or polymers, or coordinate additional solvent molecules, unlike previously described complexes. For all square planar Cu(II) complexes M···π and π···π interactions involving the centroids (5-ring and 6-ring) around the metal centre were observed, leading to a stacking of the planar complexes. Details on all intermolecular interactions can be found in the ESI, Tables S3–S5. Interactions between keto oxygen and aromatic C–H groups were also observed for all complexes.

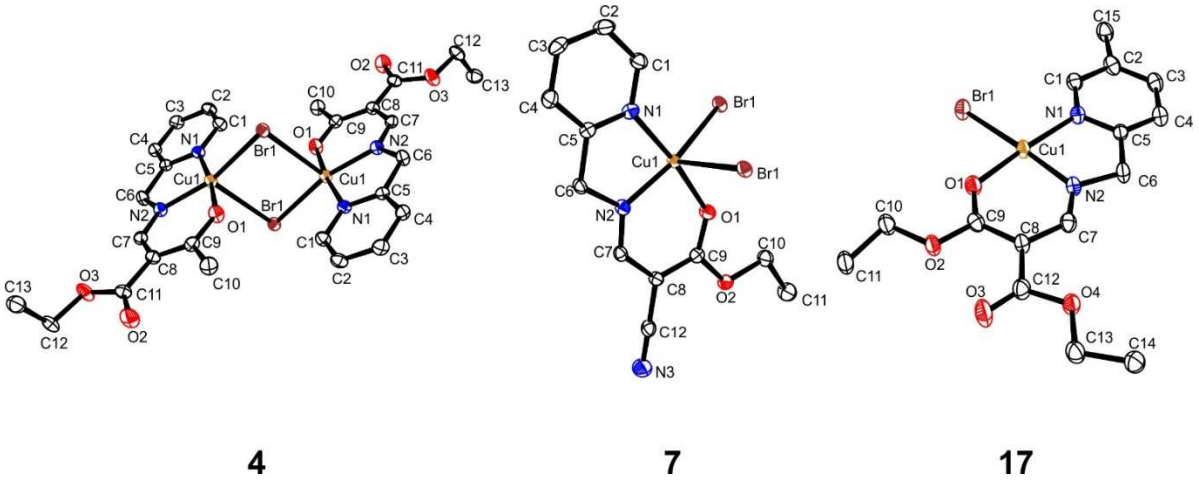

Fig. 1. Structures of **4** (left), **7** (middle), and **17** (right). Thermal ellipsoids were drawn at 50% probability level. Hydrogen atoms were omitted for clarity.

Powder X-ray diffraction analyses were done to confirm that the complexes obtained from synthesis and the single crystals had the same structure. The diffraction patterns are given in the ESI, Fig. S2 and S3. Except for complexes **5** and **12**, the patterns are identical. Small differences visible in the patterns of the other complexes can be explained with the different temperatures and methods used for the measurements.

The magnetism of compounds **4**–**18** was investigated, the magnetic behaviour of complexes **1**–**3** was described previously.[10a] Measurements down to 2 K were performed for the dimeric

complexes **4** and **9** and for the monomeric compound **15**. The other substances were investigated down to 50 K. The $\chi_M T$ *vs.* *T* plots are presented in Fig. S4–S6, the magnetic moments are summarised in Table S6. The room temperature moment is within the expected range for dimeric or monomeric copper(II) complexes. Only weak ferromagnetic interactions ($J < 10$ cm^{-1}) are observed in case of the dimeric complexes. This is in agreement with previously described complexes of this type.[10a] In the case of the monomeric complex **15** very weak antiferromagnetic interactions are observed that were not analysed any further.

UV-Vis spectroscopy and cyclic voltammetry.

UV-Vis spectra of the complexes were recorded in water (**1**) and DMSO (**2**–**18**); they can be found in the ESI, Fig. S7–S9, the absorption maxima and the logarithm of the extinction coefficient are summarised in Table 2. Complex **1** is not stable in DMSO solution with its colour quickly changing from light blue to dark red/brown. Absorption maxima (in DMSO) between 624 and 676 nm were observed for all complexes except **16** (764 nm), possibly due to the 6-methyl group on the pyridine ring being rather close to the metal centre. Complexes **11**–**18** featured a second absorption maximum between 390 and 442 nm. In aqueous solution the absorption maxima are slightly blue-shifted. The complexes **3**, **8**, and **11** were not completely soluble in water. The extinction coefficient ε indicates a d–d transition and no charge transfer responsible for the colour. The spectra were recorded over 72 h to investigate the stability of the compounds in solution (**1** in water, the remaining in DMSO).

No change of the position of the absorption maxima was seen, however, for complexes **2**, **3**, **4**, **5**, **8**, **9**, **12**, and **13** a decrease of extinction took place. In order to determine whether or not the anion still coordinates the Cu(II) centre conductivity measurements were carried out (Table 2). This is especially of interest regarding the dimeric or polymeric species. The conductivity of the solution used for the UV-Vis measurements was measured three times to obtain a mean value. The observed values indicate that the anion is no longer coordinated to the metal centre but is most likely replaced by a solvent molecule. This indicates that in solution probably only monomeric species exist, unlike in the solid state.

Table 2. Absorption maxima λ_{max}, log ε, molar conductivity σ, and electrochemical properties (in acetonitrile, 0.1 M NBu_4PF_6, vs. $Ag/AgNO_3$, 50 mV s^{-1}) of the complexes discussed in this work.

	λ_{max} [nm] (log ε)		σ [$10^3 \cdot \mu S \cdot cm^{-1} \cdot M^{-1}$]		E_{red} [V]	E_{ox} [V]
	Water	DMSO	Water	DMSO		
1	624 (2.07)	Not stable	89	Not stable	−0.71	1.42
2	630 (2.06)	668 (2.18)	85	17	−0.8	1.01
						1.39
3	Not completely	639 (2.17)	Not completely	19	−0.71	−0.55
	soluble		soluble		0.24	0.67
						0.81
4	626 (2.04)	638 (2.17)	89	30	−0.66	0.76
					0.43	
					0.65	
5	626 (2.06)	640 (2.17)	101	29	−0.62	0.86
						1.38
6	641 (1.90)	661 (2.05)	97	29	−0.6	0.86
					0.43	
7	656 (1.85)	674 (1.99)	97	29	−0.46	0.72
					0.45	1.35
8	Not completely	644 (2.15)	Not completely	27	−0.62	0.82
	soluble		soluble		0.44	
					0.66	
9	624 (2.06)	640 (2.13)	96	28	−0.64	0.84
					0.43	
10	636 (2.04)	654 (2.08)	95	27	−0.64	0.84
	372 (2.56)				0.43	
11	Not completely	673 (2.01)	Not completely	29	−0.48	0.62
	soluble	411 (2.09)	soluble		0.44	0.76
						1.38
12	645 (2.01)	664 (2.04)	102	27	−0.54	0.86
	391 (2.18)	409 (2.15)			0.47	
13	655 (1.94)	676 (2.00)	101	27	−0.42	0.78
	401 (2.09)	407 (2.12)				1.44
14	639 (2.03)	650 (1.82)	100	17	−0.59	0.84
	386 (2.34)	395 (2.06)			0.45	
15	659 (2.03)	667 (1.99)	110	19	−0.46	0.75
	398 (2.16)	408 (2.14)				1.37
16	698 (1.95)	746 (1.96)	98	27	−0.26	0.75
	429 (2.11)	442 (2.06)				1.36
17	638 (2.03)	659 (2.06)	96	29	−0.62	0.77
	390 (2.19)	406 (2.17)			0.38	1.17
18	647 (1.98)	674 (2.00)	97	29	−0.5	0.7
	401 (2.11)	412 (2.09)				1.3

The electrochemical behaviour of the compounds was investigated using cyclic voltammetry. The voltammograms are presented in the ESI, Fig. S10–S12, the reduction and oxidation potentials are summarised in Table 2. All complexes show irreversible reduction peaks between −0.4 and −0.8 V corresponding to the reduction of Cu(II) to Cu(I). The exception is again compound **16** with a reduction potential of −0.26 V. The anodic processes are not very well-defined and correspond to oxidation processes of the ligand, taking place above 0.7 V.

Cytotoxicity.

All complexes were tested for their structure-dependent antiproliferative activity against cells of human 518A2 melanoma, HT-29, HCT-116^{wt}, and HCT-116$^{p53-/-}$ colon carcinoma, and the cervix carcinoma cell line HeLa using the standard MTT assay (Table 3 and Fig. 2). The complexes **1**–**4** share the same chelate ligand **HL1**, yet differ in their counter anions. The other complexes own the same counter anion (Br^-) but carry different substituents either on the β-acylenamino fragment (**5**–**9**) or on the latter and the pyridine ring (**10**–**18**). The free ligand **HL11** and $CuSO_4$ were investigated as well. The solubility of compounds **3**, **8**, and **11** (not fully soluble in water) in PBS was confirmed by diluting a 2 mM DMSO solution to 100 μM in PBS. No precipitate occurred and the UV-Vis spectra are presented in Fig. S13.

All compounds showed dose-dependent growth inhibition of all cell lines, exceeding that of $CuSO_4$ in most cases. Complexes **11**–**13** and **15** proved least active against all cell lines with IC_{50} values greater 40 μM on average. Complexes **1**–**4**, differing only in their counter anions, were of comparable, moderate activity. Also, the spread in the IC_{50} values for complexes **4**–**9**, sharing an unsubstituted pyridine ring while differing in substituents R′ and R″, was only marginal. In contrast, complexes **10** (R = 4-OMe) and **14** (R = 4-Me) which both have electron donating substituents R in 4-position of the pyridine ring and are identical in substituents R′ (= OEt), R″ (= COOEt) and counter anion (= Br^-) showed the highest activity of all tested compounds, including the clinical established drug cisplatin, with single-digit micromolar IC_{50} values against all cancer cell lines. Interestingly, the couple of complexes **11** (R = 4-OMe) and **15** (R = 4-Me), identical to **10**/**14** in terms of substituents R and R′ yet carrying a cyanide instead of a COOEt substituent R″ were virtually inactive against all cell lines. So, a tentative SAR assumption is that the cytotoxicity of such copper complexes might be enhanced by sticking electron donors on the pyridine ring and by avoiding strongly electron withdrawing substituents R″ such as cyanide.

Table 3. Growth inhibitory concentrations IC_{50} (μM; 72 h) of complexes **1**–**18**, ligand **HL11**, $CuSO_4$, and cisplatin for cells of human melanoma 518A2, colon carcinomas HT-29, HCT-116^{wt} and HCT-116$^{p53-/-}$, cervix carcinoma HeLa, as well as non-cancerous human dermal fibroblasts (adult) HDFa. Selectivity index (SI) was calculated as IC_{50}(HDFa)/øIC_{50} (all tested cancer cell lines).

	518A2	**HT-29**	**HCT-116^{wt}**	**HCT-116$^{p53-/-}$**	**HeLa**	**HDFa**	**SI**
$CuSO_4$	34.0 ± 1.3	>50	49.8 ± 3.0	>50	>50		
cisplatin[13]	7.8 ± 1.1	8.5 ± 0.3	12.0 ± 1.1	27.0 ± 4.1		41.0 ± 4.0	3.0
1	8.2 ± 0.5	17.2 ± 0.1	8.7 ± 0.5	20.1 ± 2.6	38.8 ± 1.2	15.6 ± 1.9	0.8
2	13.8 ± 2.4	18.2 ± 4.8	20.4 ± 1.9	34.1 ± 0.7	17.3 ± 0.5		
3	15.2 ± 1.7	15.8 ± 1.3	7.7 ± 1.3	17.6 ± 1.0	18.0 ± 1.7		
4	15.1 ± 0.2	19.4 ± 1.2	27.8 ± 1.6	18.1 ± 1.4	15.8 ± 2.5		
5	17.1 ± 1.1	23.2 ± 1.1	38.0 ± 4	27.5 ± 1.2	30.0 ± 1.2		
6	17.6 ± 1.6	25.1 ± 0.5	21.0 ± 1.9	18.6 ± 1.5	22.0 ± 2.2		
7	18.4 ± 2.3	17.5 ± 1.7	19.5 ± 0.7	25.6 ± 2.6	18.4 ± 1.1		
8	11.4 ± 0.7	27.7 ± 3.7	9.7 ± 0.8	10.0 ± 0.4	15.1 ± 1.8		
9	23.7 ± 1.3	27.0 ± 1.7	14.5 ± 1.2	19.3 ± 0.7	20.1 ± 0.6		
10	5.9 ± 0.4	2.2 ± 0.3	4.7 ± 0.1	2.2 ± 0.3	4.0 ± 0.3	18.4 ± 0.4	4.8
11	>50	>50	44.0 ± 1.0	34.9 ± 1.2	>50		
12	>50	>50	49.7 ± 2.1	16.9 ± 0.8	47.7 ± 1.6		
13	>50	>50	49.5 ± 3.7	>50	>50		
14	8.3 ± 0.5	4.0 ± 0.2	8.1 ± 0.9	2.3 ± 0.2	9.0 ± 0.8	18.3 ± 1.1	2.9
15	>100	>50	>50	>50	>50		
16	15.9 ± 0.6	40.8 ± 4.9	16.7 ± 0.6	20.1 ± 1.4	43.7 ± 5.5		
17	15.1 ± 1.2	30.7 ± 2.4	11.0 ± 0.7	20.8 ± 1.4	17.8 ± 0.6		
18	17.4 ± 0.8	26.4 ± 2.7	50.5 ± 3.9	29.1 ± 9.8	37.4 ± 5.4		
HL11	>100	>100	>100	>100	>100		
$CuSO_4$ + HL11 (1 : 1)	23.5 ± 1.3	16.8 ± 1.2	9.9 ± 0.1	7.6 ± 0.3	38.8 ± 6.4		

The free ligand **HL11** of compound **14** was also tested inactive. Mixtures of ligand **HL11** and $CuSO_4$ (1 : 1) were less cytotoxic against all cancer cell lines in comparison to the corresponding complex **14**. What little activity we found for these mixtures can probably be ascribed to a spontaneous, partial complex formation, as solutions of **HL11** and $CuSO_4$ turned immediately greenish (like solutions of pure complex **14**) after mixing.

The selectivity for tumour cells of the most active complexes **1**, **10**, and **14** can be estimated by comparison of their cytotoxicities against cancer cell lines and non-cancerous cells (HDFa). In this context, complex **10** showed a very high selectivity with a selectivity index (SI = 4.8) higher than that of cisplatin (SI = 3.0). The stability of those compounds in PBS solution (100 μM)

was investigated at 37 °C over 72 h using UV-Vis spectroscopy (Fig. S14). No change can be seen indicating that the complexes are stable under these conditions.

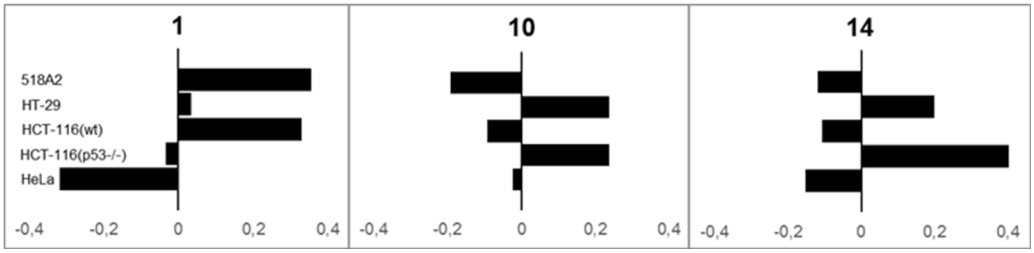

Fig. 2. Cell line specificities of copper complexes **1** (left), **10** (middle) and **14** (right) as deviations of the log(IC_{50}) for individual cells lines from the mean log(IC_{50}) value over all cell lines. Negative values indicate lower and positive values higher than average activities. Mean log(IC_{50}) values are 1.3 for complex **1**, 0.58 for complex **10**, and 0.80 for complex **14**.

Moreover, the uptake of the most active complexes **1**, **10** and **14** into HCT-116^{wt} colon carcinoma cells was quantified using ICP-MS (Table 4). These three complexes appear to have about the same intrinsic cytotoxic activity against this particular cancer cell line. The differences in their IC_{50} values nicely correlate with their intracellular concentrations. It is remarkable that the structurally different couple **1** and **14** exhibit very similar uptake rates and IC_{50} values, while the structurewise closely related pair **10** and **14** differ by a factor of circa 2 in both. The cellular copper content in cells after treatment with $CuSO_4$ alone was significantly lower compared to that of cells treated with complexes **1**, **10** or **14**.

Table 4. Copper content in HCT-116^{wt} colon carcinoma cells (ng/10^6 cells) after treatment with 4 µM of the test compounds **1**, **10** and **14**, as well as $CuSO_4$ and mixtures of the latter with ligand **HL11** for 24 h under standard cell culture conditions. The copper content of untreated cells (0.76 ± 0.31 ng Cu/10^6 cells) has already been subtracted from the presented values.

compound	**copper content in cell lysates [ng/10^6 cells]**	**IC_{50} values for HCT-116^{wt} [µM]**
1	5.70 ± 1.08	8.7 ± 0.5
10	11.78 ± 0.77	4.7 ± 0.1
14	7.94 ± 1.65	8.1 ± 0.9
$CuSO_4$	3.96 ± 0.79	49.8 ± 3.0
$CuSO_4$ + HL11 (1 : 1)	4.46 ± 0.71	9.9 ± 0.1

Treatment with mixtures of $CuSO_4$ and ligand **HL11** led to values between those of $CuSO_4$ and the corresponding complex **14**, confirming the assumption of spontaneous, partial formation of complex **14** in solution. It should be noted, though, that this might be different for cell lines other than HCT-116^{wt}. As the cytotoxic effect of copper complexes may originate from DNA binding[5,12] we investigated the interaction of complexes **1**, **10**, and **14** both with linear salmon sperm DNA using an ethidium bromide intercalation assay (*cf.* ESI, Fig. S15) and with circular pBR322 plasmid DNA in electrophoretic mobility shift assays (EMSA, Fig. S16). No significant effects were observed in either assay. An alternative mode of action is the generation of reactive oxygen species (ROS).[12,14] Therefore the complexes, $CuSO_4$, and free ligand **HL11** were investigated with respect to their influence on the ROS level in 518A2 melanoma cells using NBT assays after 24 h incubation (Fig. S17). The cells were treated with the test compounds (1 and 10 μM) or vehicle. All compounds including $CuSO_4$ and **HL11** led to a small rise in cellular ROS levels. There is no stringent correlation between the rise in ROS and the cytotoxicity exhibited by the complexes, indicating the generation of ROS not to be the dominant mode of action.

Another type of clinical important targets for anticancer drugs are the topoisomerase enzymes[6] which catalyse the supercoiling of the DNA. As copper complexes have been shown to be able to inhibit these enzymes,[5] complexes **1**, **10**, **14**, and $CuSO_4$ were tested for inhibition of topoisomerase I (Fig. 3). Compounds **1** and **10** showed a similar inhibition of the enzyme (setting in from 25 μM), whereas **14** inhibited topoisomerase I only at concentrations of at least 50 μM. Addition of $CuSO_4$ to the reaction mixture had no influence on the activity of topoisomerase I. This confirms that the inhibitory effect stems from the intact complexes rather than copper salts from decomposition.

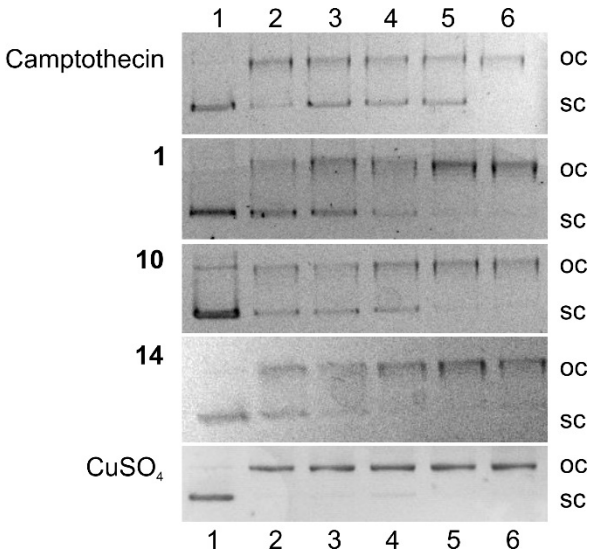

Fig. 3. Inhibition of topoisomerase I by Camptothecin, complexes **1**, **10**, **14**, and $CuSO_4$. Lane 1: 100 µM substance without enzyme; lane 2–6: 100, 50, 25, 10, and 0 µM with enzyme. Top: open circular form (oc) generated by active topoisomerase I, bottom: supercoiled form (sc).

10.3 Experimental Section

Complexes **1**–**3**, ligands **HL1**–**HL6**, 2-aminomethyl-4-methoxypyridine, 2-aminomethyl-4-chloropyridine, 2-amino-methyl-4-methylpyridine, 2-aminomethyl-5-methylpyridine, and 2-aminomethyl-6-methylpyridine were synthesised by previously described procedures.[10,11] Methanol used for the complex synthesis was distilled over magnesium under argon. All other chemicals were commercially available and used as received. ^{1}H NMR spectra were measured at room temperature and 300 MHz with a Varian INOVA 300. Elemental analysis were measured with a Vario EL III from Elementar Analysen-Systeme with acetanilide as standard. The samples were placed in a small tin boat. Mass spectra were recorded with a Finnigan MAT 8500 with a data system MASPEC II. IR spectra were recorded with a PerkinElmer Spectrum 100 FT-IR spectrometer. Conductivity was measured with a FiveGo F3 portable meter from Mettler Toledo.

HL7. 2-Aminomethyl-4-methoxypyridine (0.6 g, 4.3 mmol, 1 eq.) was diluted in ethanol (5 mL) and diethylethoxymethylenemalonate (1.2 g, 5.2 mmol, 1.2 eq.) was added, resulting in an orange solution. This mixture was heated to reflux for 1 h. After cooling to room temperature, the solvent was removed under reduced pressure, yielding a dark orange oil. After one week at

−28 °C, the now orange solid was suspended in icecold diethyl ether (3 mL), filtered, washed with ice-cold diethyl ether (5 mL), and dried in air. Yield: 0.86 g (308.33 g mol^{-1}, 64%). Elemental analysis ($C_{15}H_{20}N_2O_5 \cdot 0.3H_2O$, %) found C 57.17, H 6.84, N 8.57; calcd C 57.32, H 6.63, N 8.91. ^{1}H NMR (298 K, $CDCl_3$, 300 MHz): δ = 9.6 (1 H, m, –NH), 8.42 (1 H, m, 6-PyH), 8.11 (1 H, d, ^3J = 14.1 Hz, =CH), 6.78 (2 H, m, 2-&4-PyH), 4.62 (2 H, d, ^3J = 6.1 Hz, 2-Py–CH_2), 4.23 (4 H, m, –O–CH_2–CH_3), 3.87 (3 H, s, –O–CH_3), 1.34 (6 H, m, –O–CH_2–CH_3) ppm. MS (EI, pos.) *m/z* (%): 308 ($C_{15}H_{20}N_2O_5$, 20), 262 ($C_{13}H_{15}N_2O_4$, 100), 123 (C_7H_8NO, 85). IR: ν = 3275 (m, N–H), 1684 (s, C=O), 1630 (s, C=O) cm^{-1}.

HL8. 2-Aminomethyl-4-methoxypyridine (0.5 g, 3.6 mmol, 1 eq.) was diluted in ethanol (5 mL) and ethyl(ethoxymethylene)cyanoacetate (0.73 g, 4.3 mmol, 1.2 eq.) was added, resulting in a yellow suspension. This mixture was heated to reflux for 1 h. After cooling to room temperature white needles precipitated. Those were filtered, washed with ethanol, and dried in air. Yield: 0.34 g (261.28 g mol^{-1}, 36%). Elemental analysis ($C_{13}H_{15}N_3O_3$, %) found C 59.60, H 5.50, N 16.00; calcd C 59.76, H 5.79, N 16.08. ^{1}H NMR (298 K, $CDCl_3$, 300 MHz): δ = 9.43 (1 H, m, –NH), 8.43 (1 H, d, ^3J = 5.8 Hz, 6-PyH), 7.48 (1 H, d, ^3J = 13.8 Hz, =CH), 6.85 (2 H, m, 3-&5-PyH), 4.63 (2 H, d, ^3J = 5.9 Hz, 2-Py–CH_2), 4.22 (2 H, q, ^3J = 7.3 Hz, –O–CH_2–CH_3), 3.92 (3 H, s, –O–CH_3), 1.29 (3 H, t, ^3J = 7.1 Hz, –O–CH_2–CH_3) ppm. MS (EI, pos.) *m/z* (%): 261 ($C_{13}H_{15}N_3O_3$, 100), 232 ($C_{11}H_{10}N_3O_3$, 25), 215 ($C_{11}H_{10}N_3O_2$, 65), 188 ($C_{10}H_{10}N_3O$, 45), 149 ($C_8H_{10}N_2O$, 60), 123 (C_7H_8NO, 100). IR: ν = 3202 (m, N–H), 2206 (s, C≡N), 1683 (s, C=O) cm^{-1}.

HL9. 2-Aminomethyl-4-chloropyridine (0.5 g, 3.5 mmol, 1 eq.) was diluted in ethanol (5 mL) and diethylethoxymethylenemalonate (0.91 g, 4.2 mmol, 1.2 eq.) was added, resulting in a yellow solution. The mixture was heated to reflux for 1 h. After cooling to room temperature approximately half of the solvent was removed under reduced pressure. A light yellow solid precipitated, which was filtered, washed with ethanol, and dried in air. Yield: 0.7 g (312.75 g mol^{-1}, 63%). Elemental analysis ($C_{14}H_{17}ClN_2O_4$, %) found C 53.71, H 5.32, N 8.94; calcd C 53.77, H 5.48, N 8.96. ^{1}H NMR (298 K, $CDCl_3$, 300 MHz): δ = 9.62 (1 H, m, –NH), 8.52 (1 H, m, 6-PyH), 8.09 (1 H, d, ^3J = 13.8 Hz, =CH), 7.37 (2 H, m, 2-&4-PyH), 4.75 (2 H, d, ^3J = 6.2 Hz, 2-Py–CH_2), 4.22 (4 H, m, –O–CH_2–CH_3), 1.33 (6 H, m, –O–CH_2–CH_3) ppm. MS (EI, pos.) *m/z* (%): 312 ($C_{14}H_{17}ClN_2O_4$, 30), 266 ($C_{12}H_{12}ClN_2O_3$, 100), 153 ($C_7H_7ClN_2$, 100), 127 (C_6H_5ClN, 100). IR: ν = 3281 (m, N–H), 1680 (s, C=O), 1640 (s, C=O) cm^{-1}.

HL10. 2-Aminomethyl-4-chloropyridine (0.5 g, 3.5 mmol, 1 eq.) was diluted in ethanol (5 mL) and ethyl(ethoxymethylene)cyanoacetate (0.71 g, 4.2 mmol, 1.2 eq.) was added, resulting in a yellow solution. This mixture was heated to reflux for 1 hour. After cooling to room temperature and storing at −28 °C, a solid was isolated by filtration, washed with ice-cold diethyl ether, and recrystallised in methanol (5 mL). The white, crystalline precipitate was filtered, washed with methanol, and dried in air. Yield: 0.42 g (265.70 g mol^{-1}, 46%). Elemental analysis ($C_{12}H_{12}ClN_3O_2$, %) found C 54.05, H 4.49, N 15.83; calcd C 54.25, H 4.55, N 15.82. ^{1}H NMR (298 K, $CDCl_3$, 300 MHz): δ = 9.43 (1 H, m, –NH), 8.52 (1 H, d, ^3J = 5.3 Hz, 6-PyH), 7.46 (1 H, d, ^3J = 13.8 Hz, =CH), 7.30 (1 H, dd, ^3J = 5.3 Hz, ^4J = 2.0 Hz, 5-PyH), 7.27 (1 H, d, ^3J = 1.7 Hz, 3-PyH), 4.61 (2 H, d, ^3J = 6.1 Hz, 2-Py–CH_2), 4.23 (2 H, q, ^3J = 7.1 Hz, –O–CH_2–CH_3), 1.32 (3 H, t, ^3J = 7.1 Hz, –O–CH_2–CH_3) ppm. MS (EI, pos.) *m/z* (%): 265 ($C_{12}H_{12}ClN_3O_2$, 75), 219 ($C_{10}H_7ClN_3O$, 80), 153 ($C_7H_7ClN_2$, 100), 127 (C_6H_5ClN, 100). IR: ν = 3288 (m, N–H), 2208 (s, C≡N), 1679 (s, C=O) cm^{-1}.

HL11. 2-Aminomethyl-4-methylpyridine (0.75 g, 6.1 mmol, 1 eq.) was diluted in ethanol (5 mL) and diethylethoxymethylenemalonate (1.59 g, 7.4 mmol, 1.2 eq.) was added, resulting in a yellow solution. This mixture was heated to reflux for 1 hour. After cooling to room temperature the solvent was removed under reduced pressure resulting in an orange oil. This was stored at −28 °C for 1 day. The now orange solid was suspended in ice-cold diethyl ether (5 mL), filtered, washed with ice cold diethyl ether (5 mL), and dried in air. Yield: 0.71 g (292.14 g mol^{-1}, 39%). Elemental analysis ($C_{15}H_{20}N_2O_4 \cdot H_2O$, %) found C 57.84, H 7.19, N 8.73; calcd C 58.05, H 7.15, N 9.03. ^{1}H NMR (298 K, $CDCl_3$, 300 MHz): δ = 9.55 (1 H, m, –NH), 8.45 (1 H, d, ^3J = 5.1 Hz, 6-PyH), 8.09 (1 H, d, ^3J = 13.8 Hz, =CH), 7.21 (2 H, m, 2-&4-PyH), 4.77 (2 H, d, ^3J = 6.0 Hz, 2-Py–CH_2), 4.21 (4 H, m, –O–CH_2–CH_3), 2.44 (3 H, s, 4-Py–CH_3), 1.30 (6 H, m, –O–CH_2–CH_3) ppm. MS (EI, pos.) *m/z* (%): 292 ($C_{15}H_{20}N_2O_4$, 45), 246 ($C_{13}H_{14}N_2O_3$, 100), 219 ($C_{12}H_{15}N_2O_2$, 55), 133 ($C_8H_9N_2$, 100), 107 (C_7H_9N, 100). IR: ν = 3262 (m, N–H), 1675 (s, C=O), 1636 (s, C=O) cm^{-1}.

HL12. 2-Aminomethyl-4-methylpyridine (0.5 g, 4.1 mmol, 1 eq.) was diluted in ethanol (5 mL) and ethyl(ethoxymethylene)cyanoacetate (0.68 g, 4.9 mmol, 1.2 eq.) was added, resulting in a yellow solution. The mixture was heated to reflux for 1 hour. After cooling to room temperature the solvent was removed under reduced pressure and the dark yellow oil was stored at −28 °C for 3 days. The now yellow solid was suspended in ice-cold diethyl ether (5 mL), filtered, and washed with ice cold diethyl ether (5 mL). The crude product was recrystallised from methanol

to yield a white, crystalline solid. Yield: 0.51 g (245.12 g mol^{-1}, 50%). Elemental analysis ($C_{13}H_{15}N_3O_2 \cdot 0.25\ H_2O$, %) found C 62.84, H 6.17, N 16.84; calcd C 62.51, H 6.25, N 16.82. ^{1}H NMR (298 K, $CDCl_3$, 300 MHz): δ = 9.43 (1 H, m, –NH), 8.48 (1 H, d, ^3J = 5.1 Hz, 6-PyH), 7.48 (1 H, d, ^3J = 13.8 Hz, =CH), 7.17 (2 H, m, 3-&5-PyH), 4.67 (2 H, d, ^3J = 5.7 Hz, 2-Py–CH_2), 4.25 (2 H, m, –O–CH_2–CH_3), 2.43 (3 H, s, 4-Py–CH_3), 1.32 (3 H, t, ^3J = 7.1 Hz, –O–CH_2–CH_3) ppm. MS (EI, pos.) *m/z* (%): 245 ($C_{13}H_{15}N_3O_2$, 80), 199 ($C_{11}H_{10}N_3O$, 50), 172 ($C_{10}H_{10}N_3$, 55), 133 ($C_7H_9N_2$, 100), 107 (C_7H_7N, 100). IR: ν = 3280 (m, N–H), 2204 (s, C≡N), 1673 (s, C=O) cm^{-1}.

HL13. 2-Aminomethyl-6-methylpyridine (1 g, 8.2 mmol, 1 eq.) was diluted in ethanol (5 mL) and ethyl(ethoxymethylene)cyanoacetate (1.66 g, 9.8 mmol, 1.2 eq.) was added, resulting in a yellow solution. The mixture was heated to reflux for 1 hour. After cooling to room temperature the solvent was removed under reduced pressure, yielding a dark yellow oil. After 3 days at −28 °C the now dark yellow solid was suspended in ice-cold diethyl ether (5 mL), filtered, and washed with ice-cold diethyl ether (10 mL). Recrystallisation from methanol gave a white solid. Yield: 0.27 g (245.12 g mol^{-1}, 14%). Elemental analysis ($C_{13}H_{15}N_3O_2 \cdot 0.5\ H_2O$, %) found C 62.25, H 6.86, N 16.34; calcd C 61.40, H 6.34, N 16.52. ^{1}H NMR (298 K, $CDCl_3$, 300 MHz): δ = 9.42 (1 H, m, –NH), 8.43 (1 H, d, ^3J = 5.8 Hz, 6-PyH), 7.48 (1 H, d, ^3J = 13.8 Hz, =CH), 6.85 (2 H, m, 3-&5-PyH), 4.63 (2 H, d, ^3J = 5.9 Hz, 2-Py–CH_2), 4.22 (2 H, q, ^3J = 7.3 Hz, –O–CH_2–CH_3), 3.92 (3 H, s, –O–CH_3), 1.29 (3 H, t, ^3J = 7.1 Hz, –O–CH_2–CH_3) ppm. MS (EI, pos.) *m/z* (%): 245 ($C_{13}H_{15}N_3O_2$, 100), 199 ($C_{11}H_{10}N_3O$, 65), 172 ($C_{10}H_{10}N_3$, 55), 133 ($C_7H_9N_2$, 100), 107 (C_7H_7N, 100). IR: ν = 3269 (m, N–H), 2204 (s, C≡N), 1694 (s, C=O) cm^{-1}.

HL14. 2-Aminomethyl-5-methylpyridine (1 g, 8.2 mmol, 1 eq.) was diluted in ethanol (5 mL) and diethylethoxymethylenemalonate (2.13 g, 9.8 mmol, 1.2 eq.) was added, resulting in a yellow solution. This mixture was heated to reflux for 1 hour. After cooling to room temperature the solvent was removed under reduced pressure yielding a yellow oil. This oil was stored at −28 °C for 1 week. The now yellow solid was suspended in ice-cold diethyl ether (5 mL), filtered, washed with ice-cold diethyl ether (10 mL), and dried in air. Yield: 1.36 g (292.14 g mol^{-1}, 57%). Elemental analysis ($C_{15}H_{20}N_2O_4 \cdot 0.5EtOH \cdot 0.5H_2O$, %) found C 59.47, H 7.34, N 8.23; calcd C 59.24, H 7.46, N 8.64. ^{1}H NMR (298 K, $CDCl_3$, 300 MHz): δ = 9.6 (1 H, m, –NH), 8.43 (1 H, m, 6-PyH), 8.11 (1 H, d, ^3J = 14.0 Hz, =CH), 7.60 (1 H, m, 4-PyH), 7.22 (1 H, d, ^3J = 7.9 Hz, 3-PyH), 4.68 (2 H, d, ^3J = 6.1 Hz, 2-Py–CH_2), 4.21 (4 H, m, –O–CH_2–CH_3), 2.36 (3 H, s, 5-Py–CH_3), 1.29 (6 H, m, –O–CH_2–CH_3) ppm. MS (EI, pos.) *m/z* (%): 292

($C_{15}H_{20}N_2O_4$, 45), 246 ($C_{13}H_{15}N_2O_3$, 100), 133 ($C_8H_{10}N_2$, 100), 107 (C_7H_8N, 100). IR: ν = 3307 (m, N–H), 1682 (s, C=O), 1617 (s, C=O) cm^{-1}.

HL15. 2-Aminomethyl-5-methylpyridine (1 g, 8.2 mmol, 1 eq.) was diluted in ethanol (5 mL) and ethyl(ethoxymethylene)cyanoacetate (1.66 g, 9.8 mmol, 1.2 eq.) was added, resulting in a yellow solution. This mixture was heated to reflux for 1 hour. After cooling to room temperature the solvent was removed under reduced pressure, yielding an orange oil. This was stored at −28 °C for 1 day, suspended in ice-cold diethyl ether (5 mL), filtered, and washed with ice-cold diethyl ether (10 mL). Recrystallisation from THF gave a white, crystalline solid. Yield: 0.38 g (245.12 g mol^{-1}, 19%). Elemental analysis ($C_{13}H_{15}N_3O_2$, %) found C 63.52, H 6.33, N 17.13; calcd C 63.66, H 6.16, N 17.13. ^{1}H NMR (298 K, $CDCl_3$, 300 MHz): δ = 8.41 (1 H, d, ^4J = 0.7 Hz, 6-PyH), 8.03 (1 H, d, ^3J = 15.2 Hz, =CH), 7.43 (1 H, dd, ^3J = 7.82 Hz, ^4J = 0.86 Hz, 4-PyH), 7.15 (1 H, d, ^3J = 8.0 Hz, 3-PyH), 7.01 (1 H, m, –NH), 4.61 (2 H, d, ^3J = 5.6 Hz, 2-Py–CH_2), 4.21 (2 H, q, ^3J = 7.3 Hz, –O–CH_2–CH_3), 2.35 (3 H, s, 5-Py–CH_3), 1.29 (3 H, t, ^3J = 7.1 Hz, –O–CH_2–CH_3) ppm. MS (EI, pos.) *m/z* (%): 245 ($C_{13}H_{15}N_3O_2$, 100), 199 ($C_{11}H_{10}N_3O$, 70), 133 ($C_8H_{10}N_2$, 100), 107 (C_7H_8N, 100). IR: ν = 3269 (m, N–H), 2204 (s, C≡N), 1694 (s, C=O) cm^{-1}.

General procedure for the synthesis of the Cu(II) complexes

0.2 g of the corresponding ligand, $CuSO_4$ (1.2 eq.), and sodium methoxide (1.2 eq.) were dissolved in methanol (20 mL) under argon atmosphere and heated to reflux for 1 h, resulting in a dark blue or green solution. After cooling to RT the excess of $CuSO_4$ and sodium methoxide was removed by filtration. All further steps were carried out in air. The Cu(II) complexes were precipitated with an aqueous solution of the corresponding sodium or potassium salt of the anion (4 eq. in 20 mL). If no precipitate occurred, the solvent was removed under reduced pressure until a solid could be isolated. This solid was washed with water and methanol and dried in air.

[(μ-Br)$_2$(CuL1)$_2$] (4). Yield: 0.20 g green, crystalline powder (781.45 g mol^{-1}, 32%). Elemental analysis ($C_{26}H_{30}Br_2Cu_2N_4O_6$, %) found C 40.07, H 3.72, N 7.20; calcd C 39.96, H 3.87, N 7.17. MS (EI, pos.) *m/z* (%): 391 ($C_{15}H_{18}BrCuN_2O_3$, 14), 309 ($C_{13}H_{15}CuN_2O_3$, 52), 248 ($C_{13}H_{15}N_2O_3$, 14), 93 (C_6H_6N, 100). IR: ν = 1685 (s, C=O), 1604 (s, C=O) cm^{-1}.

[(μ-Br)$_2$(CuL2)$_2$] (5). Yield: 0.12 g green needles (721.40 g mol^{-1}, 18%). Elemental analysis ($C_{24}H_{26}Br_2Cu_2N_4O_4$, %) found C 39.96, H 3.88, N 7.74; calcd C 39.96, H 3.63, N 7.77. MS (EI, pos.) *m/z* (%): 361 ($C_{12}H_{13}BrCuN_2O_2$, 1), 279 ($C_{12}H_{13}CuN_2O_2$, 9), 218 ($C_{12}H_{13}$N2O2, 42), 93 (C_6H_6N, 100). IR: ν = 1649 (s, C=O), 1613 (s, C=O) cm^{-1}.

[CuL3Br] (6). Yield: 0.16 g green powder (420.75 g mol^{-1}, 13%). Elemental analysis ($C_{14}H_{17}BrCuN_2O_4$, %) found C 39.99, H 4.28, N 6.91; calcd C 39.97, H 4.07, N 6.66. MS (EI, pos.) *m/z* (%): 421 ($C_{14}H_{17}BrCuN_2O_4$, 25), 340 ($C_{14}H_{17}CuN_2O_4$, 29), 93 (C_6H_6N, 100). IR: ν = 1685 (s, C=O), 1623 (s, C=O) cm^{-1}.

[(μ-Br)(CuL4)]$_n$ (7). Yield: 0.14 g green powder (373.70 g mol^{-1}, 43%). Elemental analysis ($C_{12}H_{12}CuN_3O_2$, %) found C 38.70, H 3.48, N 11.26; calcd C 38.57, H 3.24, N 11.24. MS (EI, pos.) *m/z* (%): 374 ($C_{12}H_{12}CuBrN_3O_2$, 2), 293 ($C_{12}H_{12}CuN_3O_2$, 4), 231 ($C_{12}H_{12}N_3O_2$, 23), 93 (C_6H_6N, 100). IR: ν = 2201 (s, C≡N), 1627 (s, C=O) cm^{-1}.

[(μ-Br)$_2$(CuL5)$_2$] (8). Yield: 0.20 g dark green needles (905.59 g mol^{-1}, 35%). Elemental analysis ($C_{36}H_{34}Br_2Cu_2N_4O_6$, %) found C 48.09, H 3.98, N 6.23; calcd C 47.75, H 3.78, N 6.19. MS (EI, pos.) *m/z* (%): 310 ($C_{18}H_{17}N_2O_3$, 16), 93 (C_6H_6N, 100). IR: ν = 1671 (s, C=O), 1602 (s, C=O) cm^{-1}.

[(μ-Br)$_2$(CuL6)$_2$] (9). Yield: 0.20 g dark blue, crystalline powder (753.39 g mol^{-1}, 31%). Elemental analysis ($C_{24}H_{26}Br_2Cu_2N_4O_6$, %) found C 38.19, H 3.18, N 7.22; calcd C 38.26, H 3.48, N 7.44. MS (EI, pos.) *m/z* (%): 376 ($C_{12}H_{13}BrCuN_2O_3$, 6), 295 ($C_{12}H_{13}CuN_2O_3$, 24), 234 ($C_{12}H_{13}N_2O_3$, 22), 93 (C_6H_6N, 100). IR: ν = 1687 (s, C=O), 1613 (s, C=O) cm^{-1}.

[CuL7Br] (10). Yield: 0.09 g dark green powder (450.78 g mol^{-1}, 31%). Elemental analysis ($C_{15}H_{19}BrCuN_2O_5$, %) found C 39.43, H 4.27, N 6.38; calcd C 39.97, H 4.25, N 6.21. MS (EI, pos.) *m/z* (%): 451 ($C_{15}H_{19}BrCuN_2O_5$, 5), 370 ($C_{15}H_{19}CuN_2O_5$, 5), 308 ($C_{15}H_{19}N_2O_5$, 52), 262 ($C_{13}H_{14}N_2O_4$, 100), 123 (C_7H_8NO, 100). IR: ν = 1662 (s, C=O), 1618 (s, C=O) cm^{-1}.

[CuL8Br] (11). Yield: 0.25 dark green, crystalline powder (403.72 g mol^{-1}, 81%). Elemental analysis ($C_{13}H_{14}BrCuN_3O_3$, %) found C 39.27, H 3.98, N 10.63; calcd C 38.68, H 3.50, N 10.41. MS (EI, pos.) *m/z* (%): 404 ($C_{13}H_{14}BrCuN_3O_3$, 5), 323 ($C_{13}H_{14}CuN_3O_3$, 15), 261 ($C_{13}H_{14}N_3O_3$, 100), 123 (C_7H_8NO, 100). IR: ν = 2207 (s, C≡N), 1616 (s, C=O) cm^{-1}.

[CuL9Br] (12). Yield: 0.12 g dark green, crystalline powder (455.19 g mol^{-1}, 41%). Elemental analysis ($C_{14}H_{16}BrClCuN_2O_4$, %) found C 37.03, H 3.52, N 6.13; calcd C 36.94, H 3.54, N 6.15. MS (EI, pos.) *m/z* (%): 455 ($C_{14}H_{16}BrClCuN_2O_4$, 15), 375 ($C_{14}H_{16}ClCuN_2O_4$, 15), 266 ($C_{12}H_{12}ClN_2O_3$, 100), 127 (C_6H_5ClN, 100). IR: ν = 1664 (s, C=O), 1596 (s, C=O) cm^{-1}.

[CuL10Br] (13). Yield: 0.18 g dark green, crystalline powder (408.14 g mol^{-1}, 59%). Elemental analysis ($C_{12}H_{11}BrClCuN_3O_2$, %) found C 35.18, H 2.55, N 10.27, calcd C 35.31, H 2.72, N 10.30. MS (EI, pos.) *m/z* (%): 408 ($C_{12}H_{11}BrClCuN_3O_2$, 10), 327 ($C_{11}H_{12}ClCuN_3O_2$, 20), 265 ($C_{11}H_{12}ClN_3O_2$, 60), 219 ($C_{10}H_6ClN_3O$, 80), 127 (C_6H_5ClN, 100). IR: ν = 2209 (s, C≡N), 1616 (s, C=O) cm^{-1}.

[CuL11Br] (14). Yield: 0.13 g dark green, crystalline powder (434.78 g mol^{-1}, 35%). Elemental analysis ($C_{15}H_{19}BrCuN_2O_4 \cdot MeOH$, %) found C 40.26, H 4.40, N 6.27; calcd C 39.79, H 4.67, N 6.19. MS (EI, pos.) *m/z* (%): 435 ($C_{15}H_{19}BrCuN_2O_4$, 15), 354 ($C_{15}H_{19}CuN_2O_4$, 20), 246 ($C_{13}H_{14}N_2O_3$, 100), 133 ($C_8H_9N_2$, 100), 107 (C_7H_9N, 100). IR: ν = 1673 (s, C=O), 1599 (s, C=O) cm^{-1}.

[CuL12Br] (15). Yield: 0.20 g dark green, crystalline powder (387.72 g mol^{-1}, 65%). Elemental analysis ($C_{13}H_{14}BrCuN_3O_2$, %) found C 40.37, H 3.63, N 10.68; calcd C 40.27, H 3.64, N 10.84. MS (EI, pos.) *m/z* (%): 388 ($C_{13}H_{14}BrCuN_3O_2$, 10), 307 ($C_{13}H_{14}CuN_3O_2$, 20), 245 ($C_{13}H_{14}N_3O_2$, 80), 107 (C_7H_9N, 100). IR: ν = 2208 (s, C≡N), 1620 (s, C=O) cm^{-1}.

[CuL13Br] (16). Yield: 0.09 g dark green, crystalline powder (387.72 g mol^{-1}, 29%). Elemental analysis ($C_{13}H_{14}BrCuN_3O_2 \cdot H_2O$, %) found C 38.38, H 4.01, N 10.31; calcd C 38.48, H 3.97, N 10.36. MS (EI, pos.) *m/z* (%): 245 ($C_{13}H_{14}N_3O_2$, 100), 199 ($C_{11}H_9N_3O$, 85), 133 ($C_8H_9N_2$, 100), 107 (C_7H_8N, 100). IR: ν = 2216 (s, C≡N), 1635 (s, C=O) cm^{-1}.

[CuL14Br] (17). Yield: 0.15 g dark green, crystalline powder (434.78 g mol^{-1}, 50%). Elemental analysis ($C_{15}H_{19}BrCuN_2O_4$, %) found C 41.51, H 4.45, N 6.37; calcd C 41.44, H 4.41, N 6.44. MS (EI, pos.) *m/z* (%): 435 ($C_{15}H_{19}BrCuN_2O_4$, 20), 353 ($C_{15}H_{19}CuN_2O_4$, 20), 292 ($C_{15}H_{19}N_2O_4$, 20), 246 ($C_{13}H_{14}N_2O_3$, 100), 133 ($C_8H_9N_2$, 100), 107 (C_7H_8N, 100). IR: ν = 1684 (s, C=O), 1606 (s, C=O) cm^{-1}.

[CuL15Br] (18). Yield: 0.17 g dark green, crystalline powder (387.72 g mol^{-1}, 54%). Elemental analysis ($C_{13}H_{14}BrCuN_3O_2$, %) found C 40.18, H 3.50, N 10.72; calcd C 40.27, H

3.64, N 10.84. MS (EI, pos.) *m/z* (%): 388 ($C_{13}H_{14}BrCuN_3O_2$, 5), 307 ($C_{13}H_{14}CuN_3O_2$, 10), 245 ($C_{13}H_{14}N_3O_2$, 70), 133 ($C_8H_9N_2$, 100), 107 (C_7H_8N, 100). IR: ν = 2204 (s, C≡N), 1622 (s, C=O) cm^{-1}.

X-ray diffraction on single crystals

The X-ray analysis of all crystals was performed with a Stoe StadiVari diffractometer using graphite-monochromated MoKα radiation. The data were corrected for Lorentz and polarisation effects. The structures were solved by direct methods (SIR-2014)[15] and refined by fullmatrix least-square techniques against $F_o^2 - F_c^2$ (SHELXL-97).[16] All hydrogen atoms were calculated in idealised positions with fixed displacement parameters. ORTEP-III[17] was used for the structure representation. CCDC 1566628–1566632 and 1915614–1915617 contain the supplementary crystallographic data for this paper.

Powder X-ray diffraction

Powder diffractograms were measured with a STOE StadiP Powder Diffractometer (STOE, Darmstadt) using Cu[Kα1] radiation with a Ge Monochromator, and a Mythen 1K Stripdetector in transmission geometry.

Magnetic measurements

Magnetic measurements on the compounds were carried out using a SQUID MPMS-XL5 from Quantum Design with an applied field of 5000 G, and in the temperature range from 300 to 50 K (or 2 K). The sample was prepared in a gelatine capsule held in a plastic straw. The raw data were corrected for the diamagnetic part of the sample holder and the diamagnetism of the organic ligand using tabulated Pascal's constants.[18]

Optical properties

Absorbance spectra were obtained using an Agilent UV-Vis spectrophotometer 8453 (Agilent Technologies, USA) operating in a spectral range of 190–1100 nm. The spectra were measured at 298 K in quartz cells with 1 cm lightpath (Hellma, Germany).

Cyclic voltammetry

Redox potentials were obtained using a CH Instruments Electrochemical Analyser (610E) in 0.1 M NBu_4PF_6/MeCN with a platinum electrode, referenced to 0.01 M $AgNO_3$ at room temperature with a scan rate of 50 mV s^{-1}.

Cell culture

The human melanoma cell line 518A2, and the human colon carcinoma cell lines HT-29, HCT-116^{wt}, and HCT-116$^{p53-/-,}$ and the cervix carcinoma cell line HeLa were cultivated in Dulbecco's Modified Eagle Medium supplemented with 10% FBS, and 1% antibiotic–antimycotic at 37 °C, 5% CO_2 and 95% humidity. Only mycoplasma-free cultures were used.

MTT assay

The cytotoxicity of the compounds was studied via the MTT based proliferation assay[19] on cells of 518A2 melanoma (obtained from the department of Radiotherapy and Radiobiology, University Hospital Vienna, Austria), HT-29 (DSMZ ACC-299) and HCT-116^{wt} (DSMZ ACC-581) colon carcinomas, HeLa (DSMZ ACC-57) cervix carcinoma, and human dermal fibroblasts (adult) HDFa (ATCC® PCS-201-012™). Briefly, cells (100 µL per well; 5×10^4 cells per mL) were grown in 96-well plates for 24 h and then treated with varying concentrations of the test compound or solvent control (DMSO) for 72 h. After centrifugation of the plates (300*g*, 5 min, 4 °C), the supernatant was discarded and 50 µL per well of a 0.05% MTT solution in PBS was added to the wells and incubated for 2 h. After another centrifugation step the supernatant was discarded and the formazan precipitate was dissolved in 25 µL DMSO containing 10% SDS and 0.6% acetic acid for at least 1 h at 37 °C and the absorbance of formazan (570 nm) and background (630 nm) was measured with a microplate reader (Tecan). The IC_{50} values were calculated as the mean ± standard deviation of four independent experiments.

Cellular uptake

For measurement of the cellular uptake of the copper complexes into colon carcinoma cells ICP-MS analysis of cell lysates was carried out. Therefore, HCT-116^{wt} cells were seeded at a density of 2×10^6 cells per dish and grown over night. The cells were subsequently treated with 4 µM of the test compounds under cell culture conditions. After 24 h the cells were washed

with 1 × PBS, harvested, counted and pelleted. The cells were lysed using the microwave acid (HCl) digestion system (CEM Mars®). Copper content was determined using ICP-MS (Agilent 7000, Japan). The copper content of untreated cells (0.76 ± 0.31 ng Cu per 10^6 cells) has already been subtracted from the presented values.

Ethidium bromide saturation assay

Salmon sperm DNA (SS-DNA, Sigma-Aldrich) was pipetted into a black 96-well plate in TE buffer (10 mM Tris-HCl, 1 mM EDTA, pH 8.5) to reach a final amount of 1 μg per 100 μL and incubated with varying concentrations of complexes **1**, **10**, **14** and $CuSO_4$ for 2 h at 37 °C. Afterwards, 100 μL of a 10 μg mL^{-1} ethidium bromide solution in TE buffer was added to each well. After 5 min of incubation, the fluorescence (λ_{ex} = 535 nm, λ_{em} = 595 nm) was detected using a microplate reader (Tecan F200). Each fluorescence value was corrected by possible intrinsic compound and ethidium bromide background fluorescence. As all experiments were carried out in triplicate, the relative ethidium bromide fluorescence was calculated as mean ± SD with solvent controls set to 100%.

Electrophoretic mobility shift assay

Circular plasmid DNA pBR322 (1.5 μg, Thermo Scientific) in TE buffer (10 mM Tris-HCl, 1 mM EDTA, pH 8.5) was incubated with dilution series of cisplatin (CDDP) or complexes **1**, **10**, and **14** (0, 5, 10, 25, 50 μM) at 37 °C for 24 h (20 μL total sample volume). Then, samples were subjected to gel electrophoresis using 1% agarose gels in 0.5× TBE buffer (89 mM Tris, 89 mM boric acid, 25 mM EDTA, pH 8.3). After staining the gels with ethidium bromide (10 μg mL^{-1}), DNA bands were documented using UV excitation. Experiments were carried out at least in duplicate.

NBT assay

The effect of the test compounds on the relative levels of reactive oxygen species (ROS) was studied by using the NBT assay.[20] 518A2 melanoma cells (100 μL per well, 1 × 10^5 cells per mL) were seeded in 96 well plates and allowed to adhere for 24 h. Then, the cells were treated with the test compounds (1 and 10 μM) or vehicle (DMSO) for 24 h. After centrifugation (300*g*, 5 min, 4 °C) the supernatant was discarded and the cells were incubated with 25 μL of a 0.1% NBT solution in PBS for 4 h at 37 °C. Then, the cells were centrifuged again (300*g*, 5 min, 4 °C) and the NBT solution was withdrawn. The precipitated formazan was dissolved for 30 min

by adding first 25 µL of a 2 M KOH solution and then 33 µL DMSO. Then, the absorbance of formazan (630 nm) and background (405 nm) was measured with a microplate reader (Tecan). The formazan absorbance of the vehicle treated control cells was set as 100% ROS generation. All experiments were performed in sextuplicate resulting in the relative ROS generation as the mean ± standard deviation.

Topoisomerase I inhibition assay

To detect a potential inhibition of topoisomerase I a relaxation assay with supercoiled plasmid DNA was performed. Therefore, nuclear extracts containing topoisomerase type I and II enzymes were prepared from HT-29 colon carcinoma cells by differential centrifugation. Briefly, 0.5 µg pBR322 supercoiled plasmid DNA (Carl Roth) was incubated with the nuclear enzyme extracts in assay buffer (50 mM Tris/HCl, 100 mM KCl, 1 mM DTT, 1 mM EDTA, 5 µg mL^{-1} acetylated bovine serum albumin, pH 7.5) with varying concentrations of the test compounds for 30 min at 37 °C. The absence of ATP in the reaction mixture prevented the activity of topoisomerase type II enzymes and the DMSO concentration was standardised to 1% for all samples to exclude influence of the solvent. Reaction products were extracted with phenol–chloroform–isoamyl alcohol mixture (49.5 : 49.5 : 1; Sigma Aldrich), mixed with 5 µL of 5× loading dye, loaded onto a 1% agarose gel and electrophoresis was carried out at 66 V for 3.5 h. Gels were stained with ethidium bromide (10 µg mL^{-1}) for 30 min, washed with ddH_2O and photographed under UV light.

10.4 Conclusions

We presented 15 new Cu(II) complexes with different tridentate Schiff base-like ligands bearing varying substituents on the pyridine ring and the chelate cycle. Single crystal X-ray structures of nine complexes were obtained and discussed. Compounds with no substituents on the pyridine ring crystallised as dimeric or polymeric complexes, with the metal centres being bridged by the anions. The introduction of substituents on the pyridine ring led to the crystallisation of square planar compounds with short M···π and π···π interactions. The compounds were tested for their cytotoxic activity towards various cancer cell lines. Three previously described complexes with the same tridentate ligand (**HL1**) but different anions were

investigated as well to rule out a potential influence of the anion. Most compounds were moderately active with IC_{50} values > 10 μM. Two complexes (**10** and **14**) bearing only ester side chains on the chelate perimeter and electronreleasing methoxy or methyl groups in 4-position of the pyridine ring showed IC_{50} values in the low single-digit micromolar range. The respective complexes with a cyanide side chain instead of an ester group (**11** and **15**) were inactive (IC_{50} > 50 μM). The counter anion of the complexes does not seem to be crucial for the antiproliferative effect. These observations provide an entry point for future drug optimisations. In terms of the mode of action and the biological targets of the active copper complexes we could exclude the involvement of reactive oxygen species and any significant DNA interaction, but confirmed the inhibition of topoisomerase I to at least contribute to their anticancer effect. This sets them apart from other known topoisomerase I inhibitory Cu(II) complexes that already carry anticancer active ligands such as plumbagin,[6b] and that interfere with ROS levels and bind to DNA.

Conflicts of interest

There are no conflicts to declare.

Acknowledgements

RS thanks the Deutsche Forschungsgemeinschaft (DFG) for a grant (Scho 402/12-2), HK and VB were supported by the Czech Science Foundation (Grant 17-05302S). KD thanks the University of Bayreuth Graduate School (BayNAT program) for financial support. Florian Puchtler (ACI, Department of Chemistry, University of Bayreuth) is thanked for the powder X-ray diffraction.

10.5 Notes and references

[1] (a) T. C. Johnstone, K. Suntharalingam, S. J. Lippard, *Chem. Rev.* **2016**, *116*, 3436–3486; (b) D. Wang, S. J. Lippard, *Nat. Rev. Drug Discovery* **2005**, *4*, 307–320; (c) L. Kelland, *Nat. Rev. Cancer* **2007**, *7*, 573–584; (d) E. Alessio, G. Mestroni, A. Bergamo, G. Sava, *Curr. Top. Med. Chem.* **2004**, *4*, 1525–1535; (e) J. Hildebrandt, H. Görls, N.

Häfner, G. Ferraro, M. Dürst, I. B. Runnebaum, W. Weigand, A. Merlino, *Dalton Trans.* **2016**, *45*, 12283–12287; (f) C. G. Hartinger, M. A. Jakupec, S. Zorbas-Seifried, M. Groessl, A. Egger, W. Berger, H. Zorbas, P. J. Dyson, B. K. Keppler, *Chem. Biodiversity* **2008**, *5*, 2140–2155; (g) A. Casini, J. Reedijk, *Chem. Sci.* **2012**, *3*, 3135–3144.

[2] Y. Jung, S. J. Lippard, *Chem. Rev.* **2007**, *107*, 1387–1407.

[3] (a) S. Tardito, L. Marchiò, *Curr. Med. Chem.* **2009**, *16*, 1325–1348; (b) M. Tacke, *J. Organomet. Chem.* **2015**, *782*, 17–21; (c) D. M. Griffith, B. Szőcs, T. Keogh, K. Y. Suponitsky, E. Farkas, P. Buglyó, *J. Inorg. Biochem.* **2011**, *105*, 763–769; (d) M. Buczkowskar, A. Bodtke, U. Lindequist, M. Gdaniec, P. J. Bednarski, *Arch. Pharm. Chem. Life Sci.* **2011**, *344*, 605–616; (e) L. Oehninger, R. Rubbiani, I. Ott, *Dalton Trans.* **2013**, *42*, 3269–3284.

[4] (a) E. I. Solomon, D. E. Heppner, E. M. Johnston, J. W. Ginsbach, J. Cirera, M. Qayyum, M. T. Kieber-Emmons, C. H. Kjaergaard, R. G. Hadt, L. Tian, *Chem. Rev.* **2014**, *114*, 3659–3853; (b) C. Citek, S. Herres-Pawlis, T. D. P. Stack, *Acc. Chem. Res.* **2015**, *48*, 2424–2433; (c) J. N. Hamann, B. Herzigkeit, R. Jurgeleit, F. Tuczek, *Coord. Chem. Rev.* **2017**, *334*, 54–66; (d) A. Hoffmann, S. Binder, A. Jesser, R. Haase, U. Flörke, M. Gnida, M. Salomone Stagni, W. Meyer-Klaucke, B. Lebsanft, L. E. Grünig, S. Schneider, M. Hashemi, A. Goos, A. Wetzel, M. Rübhausen, S. Herres-Pawlis, *Angew. Chem.* **2014**, *126*, 305–310; (e) C. Wilfer, P. Liebhäuser, A. Hoffmann, H. Erdmann, O. Grossmann, L. Runtsch, E. Paffenholz, R. Schepper, R. Dick, M. Bauer, M. Dürr, I. Ivanović-Burmazović, S. Herres-Pawlis, *Chem. – Eur. J.* **2015**, *21*, 17639–17649.

[5] C. Santini, M. Pellei, V. Gandin, M. Porchia, F. Tisato, C. Marzano, *Chem. Rev.* **2014**, *114*, 815–862.

[6] (a) F. Tisato, C. Marzano, M. Porchia, M. Pellei, C. Santini, *Med. Res. Rev.* **2010**, *30*, 708–749; (b) Z.-F. Chen, M.-X. Tan, L. M. Liu, Y.-C. Liu, H.-S. Wang, B. Yang, Y. Peng, H.-G. Liu, H. Liang, C. Orvig, *Dalton Trans.* **2009**, 10824–10833; (c) Z. Yu, J. A. Cowan, *Chem. – Eur. J.* **2017**, *23*, 14113–14127.

[7] (a) Z. H. Chohan, S. Kausar, *Chem. Pharm. Bull.* **1993**, *41*, 951–953; (b) M. K. Panda, M. M. Shaikh, R. J. Butcher, P. Ghosh, *Inorg. Chim. Acta* **2011**, *372*, 145–151.

[8] (a) B.-T. Ko, C.-C. Chang, S.-L. Lai, F.-J. Lai, C.-C. Lin, *Polyhedron* **2012**, *45*, 49–54; (b) L. H. A. Rahman, A. M. Abu-Dief, S. K. Hamdan, A. A. Seleem, *Int. J. Nano. Chem.* **2015**, *1*, 65–77.

[9] J. Easmon, G. Pürstinger, G. Heinisch, T. Roth, H. H. Fiebig, W. Holzer, W. Jäger, M. Jenny, J. Hofmann, *J. Med. Chem.* **2001**, *44*, 2164–2171.

[10] (a) K. Dankhoff, B. Weber, *CrystEngComm* **2018**, *20*, 818–828; (b) K. Dankhoff, S. Schneider, R. Nowak, B. Weber, *Z. Anorg. Allg. Chem.* **2018**, *644*, 1839–1848; (c) K. Dankhoff, B. Weber, *Dalton Trans.* **2019**, DOI:10.1039/C9DT00846B; (d) P. M. Schäfer, K. Dankhoff, M. Rothemund, A. N. Ksiazkiewicz, A. Pich, R. Schobert, B. Weber, S. Herres-Pawlis, *ChemistryOpen* **2019**, *8*, 1020–1026.

[11] (a) A. Nanthakumar, S. Fox, N. M. Murthy, K. D. Karlin, *J. Am. Chem. Soc.* **1997**, *119*, 3898–3906; (b) C. X. Zhang, S. Kaderli, M. Costas, E. Kim, Y.-M. Neuhold, K. D. Karlin, A. D. Zuberbühler, *Inorg. Chem.* **2003**, *42*, 1807–1824.

[12] D. Denoyer, S. Masaldan, S. La Fontaine. M. A. Cater, *Metallomics* **2015**, *7*, 1459–1476.

[13] T. Rehm, M. Rothemund, J. K. Muenzner, A. Noor, R. Kempe, R. Schobert, *Dalton Trans.* **2016**, *45*, 15390–15398.

[14] (a) C. Duncan, A. R. White, *Metallomics* **2012**, *4*, 127–138; (b) Z.-Y. Ma, X. Qiao, C.-Z. Xie, J. Shao, J.-Y. Xu, Z.-Y. Qiang, J.-S. Lou, *J. Inorg. Biochem.* **2012**, *117*, 1–9; (c) A. Sîrbu, O. Palamarciuc, M. V. Babak, J. M. Lim, K. Ohui, E. A. Enyedy, S. Shova, D. Darvasiová, P. Rapta, W. H. Ang, V. B. Arion, *Dalton Trans.* **2017**, *46*, 3833–3847.

[15] A. Altomare, M. C. Burla, M. Camalli, G. L. Cascarano, C. Giacovazzo, A. Guagliardi, A. G. G. Moliterni, G. Polidori, R. Spagna, *J. Appl. Crystallogr.* **1999**, *32*, 115–119.

[16] G. Sheldrick, *Acta Crystallogr., Sect. A: Found. Crystallogr.* **2008**, *64*, 112–122.

[17] (a) C. K. Johnson, M. N. Burnett, ORTEP-III, Oak-Ridge National Laboratory, Oak-Ridge, TN, **1996**; (b) L. Farrugia, *J. Appl. Crystallogr.* **1997**, *30*, 565.

[18] O. Kahn, Molecular Magnetism, VCH, New York, N.Y, **1993**.

[19] T. Mosmann, *J. Immunol. Methods* **1983**, *65*, 55–63.

[20] J. K. Muenzner, B. Biersack, A. Albrecht, T. Rehm, U. Lacher, W. Milius, A. Casini, J.-J. Zhang, I. Ott, V. Brabec, O. Stuchlikova, I. C. Andronache, L. Kaps, D. Schuppan, R. Schobert, *Chem. – Eur. J.* **2016**, *22*, 18953–18962.

10.6 Supporting Information

Table S1. Crystallographic data of the complexes discussed in this work.

	4	**5**	**7**	**8**	**9**
CCDC	1566628	1566629	1566630	1566631	1566632
formula	$[(\mu_2\text{–Br})_2(CuL1)_2]$	$[(\mu_2\text{–Br})_2(CuL2)_2]$	$[(\mu_2\text{–Br})(CuL4)]_n$	$[(\mu_2\text{–Br})_2(CuL5)_2]$	$[(\mu_2\text{–Br})_2(CuL6)_2]$
sum formula	$C_{26}H_{30}Br_2Cu_2N_4O_6$	$C_{24}H_{26}Br_2Cu_2N_4O_4$	$C_{12}H_{12}BrCuN_3O_2$	$C_{36}H_{34}Br_2Cu_2N_4O_6$	$C_{24}H_{26}Br_2Cu_2N_4O_6$
M/ g mol^{-1}	781.44	721.39	373.70	905.57	753.38
crystal system	triclinic	triclinic	monoclinic	monoclinic	triclinic
space group	$P\bar{1}$	$P\bar{1}$	$P2_1/c$	$P2_1/n$	$P\bar{1}$
crystal description	blue green block	blue block	green plate	green block	blue green prism
a/ Å	7.7302(4)	7.9933(7)	7.6905(4)	10.5383(6)	8.0566(4)
b/ Å	9.2879(5)	9.2785(11)	24.3476(14)	9.5476(5)	8.4259(4)
c/ Å	10.2517(5)	9.4396(10)	7.7833(4)	17.4636(12)	11.1094(5)
α/ °	94.782(4)	90.031(9)	90	90	75.675(4)
β/ °	94.310(4)	98.575(7)	113.207(4)	100.791(5)	86.846(4)
γ/ °	108.849(4)	111.440(8)	90	90	68.045(4)
V/ Å^3	690.07(6)	643.21(12)	1339.46(13)	1726.04(18)	677.12(6)
Z	1	1	4	2	1
ρ_{calcd}/ g cm^{-3}	1.880	1.862	1.853	1.742	1.848
μ/ mm^{-1}	4.485	4.798	4.614	3.600	4.567
crystal size/ mm	0.090×0.070×0.065	0.110×0.105×0.097	0.110×0.102×0.093	0.104×0.097×0.093	0.099×0.084×0.075
F(000)	390	358	740	908	374
T/ K	133(2)	133(2)	133(2)	133(2)	133(2)
λ/ Å	Mo-K_α 0.71073	Mo-K_α 0.71073	Mo-K_α 0.71073	Mo-K_α 0.71073	Mo-K_α 0.71073
Θ range/ °	2.00–28.50	2.2–28.6	1.68–28.67	2.11–28.47	1.9–28.4
Reflns. collected	3242	7822	3151	4145	3198
Indep. reflns.(R_{int})	2709 (0.0317)	3021 (0.1611)	2226 (0.0608)	2693 (0.1860)	2677 (0.0299)
Parameters	181	163	172	226	172
R1 (all data)	0.0266 (0.0361)	0.0814 (0.1116)	0.0404 (0.0654)	0.0733 (0.1115)	0.0241 (0.0332)
wR2	0.0628	0.2878	0.1099	0.2261	0.0560
GooF	0.985	1.064	0.960	1.011	0.997

Table S1. (continued)

	12	**15**	**17**	**18**
CCDC	1915615	1915614	1915617	1915616
formula	[CuL9Br]	[CuL12Br]	[CuL14Br]	[CuL15Br]
sum formula	$C_{14}H_{16}BrClCuN_2O_4$	$C_{13}H_{14}BrCuN_3O_2$	$C_{15}H_{19}BrCuN_2O_4$	$C_{13}H_{14}BrCuN_3O_2$
M/ g mol^{-1}	455.19	387.72	434.77	387.72
crystal system	triclinic	triclinic	monoclinic	triclinic
space group	$P-1$	$P-1$	$P2_1/a$	$P-1$
crystal description	green cube	green plate	green plate	green plate
a/ Å	8.0351(3)	7.8986(4)	7.9002(3)	7.5494(2)
b/ Å	9.6830(3)	8.2689(3)	18.0037(6)	8.2358(3)
c/ Å	11.4547(4)	11.3892(4)	11.3870(5)	12.3671(4)
α/ °	98.869(3)	85.890(3)	90	107.000(3)
β/ °	102.321(3)	78.823(3)	94.962(4)	96.398(3)
γ/ °	104.864(3)	81.476(3)	90	102.191(3)
V/ Å^3	820.70(5)	720.98(5)	1613.54(11)	706.30(4)
Z	2	2	4	2
ρ_{calcd}/ g cm^{-3}	1.842	1.786	1.790	1.823
μ/ mm^{-1}	3.947	4.289	3.851	4.378
crystal size/ mm	0.095×0.076×0.065	0.119×0.117×0.098	0.079×0.052×0.037	0.085×0.045×0.032
F(000)	454	386	876	386
T/ K	133(2)	133(2)	133(2)	133(2)
λ/ Å	Mo-K_α 0.71073	Mo-K_α 0.71073	Mo-K_α 0.71073	Mo-K_α 0.71073
Θ range/ °	1.9–28.5	1.8–29.1	1.6–28.4	1.8–28.5
Reflns. collected	12083	8912	12531	10623
Indep. reflns.(R_{int})	3966 (0.030)	3350 (0.028)	3900 (0.058)	3406 (0.027)
Parameters	208	181	208	181
$R1$ (all data)	0.0368 (0.0504)	0.0296 (0.0431)	0.0430 (0.0642)	0.0272 (0.0400)
$wR2$	0.0995	0.0741	0.1137	0.0659
GooF	1.04	1.034	1.04	1.05

Table S2. Selected bond lengths/Å and angles/° of the complexes discussed in this work.

	$Cu–N_{py}$	Cu–N	Cu–O	Cu–X	Cu–X–Cu	X–Cu–X
4	2.0126(19)	1.928(2)	1.9363(18)	2.4316(4)	91.15(1)	88.85(1)
				2.8919(4)		
5	1.993(7)	1.924(8)	1.926(6)	2.4419(14)	91.16(4)	88.84(4)
				2.9264(15)		
7	1.995(3)	1.949(3)	1.951(3)	2.4153(6)	95.92(2)	96.08(2)
				2.8131(6)		
8	1.994(6)	1.945(5)	1.918(4)	2.4330(12)	86.70(4)	93.30(3)
				2.9152(12)		
9	2.0001(17)	1.9316(17)	1.9256(17)	2.4281(3)	91.17(1)	88.83(1)
				2.9752(4)		
12	1.995(3)	1.930(3)	1.923(3)	2.3787(5)	/	/
15	2.026(2)	1.976(2)	1.9730(18)	2.4174(4)	/	/
17	1.990(3)	1.936(3)	1.940(2)	2.3770(6)	/	/
18	2.005(2)	1.928(3)	1.9481(16)	2.3588(4)	/	/

Figure S1. Structures of **5**(top left), **8** (top middle), **9** (top right), **12** (bottom left), **15** (bottom middle), and **18** (bottom right). Ellipsoids were drawn at 50 % probability level. Hydrogen atoms were omitted for clarity.

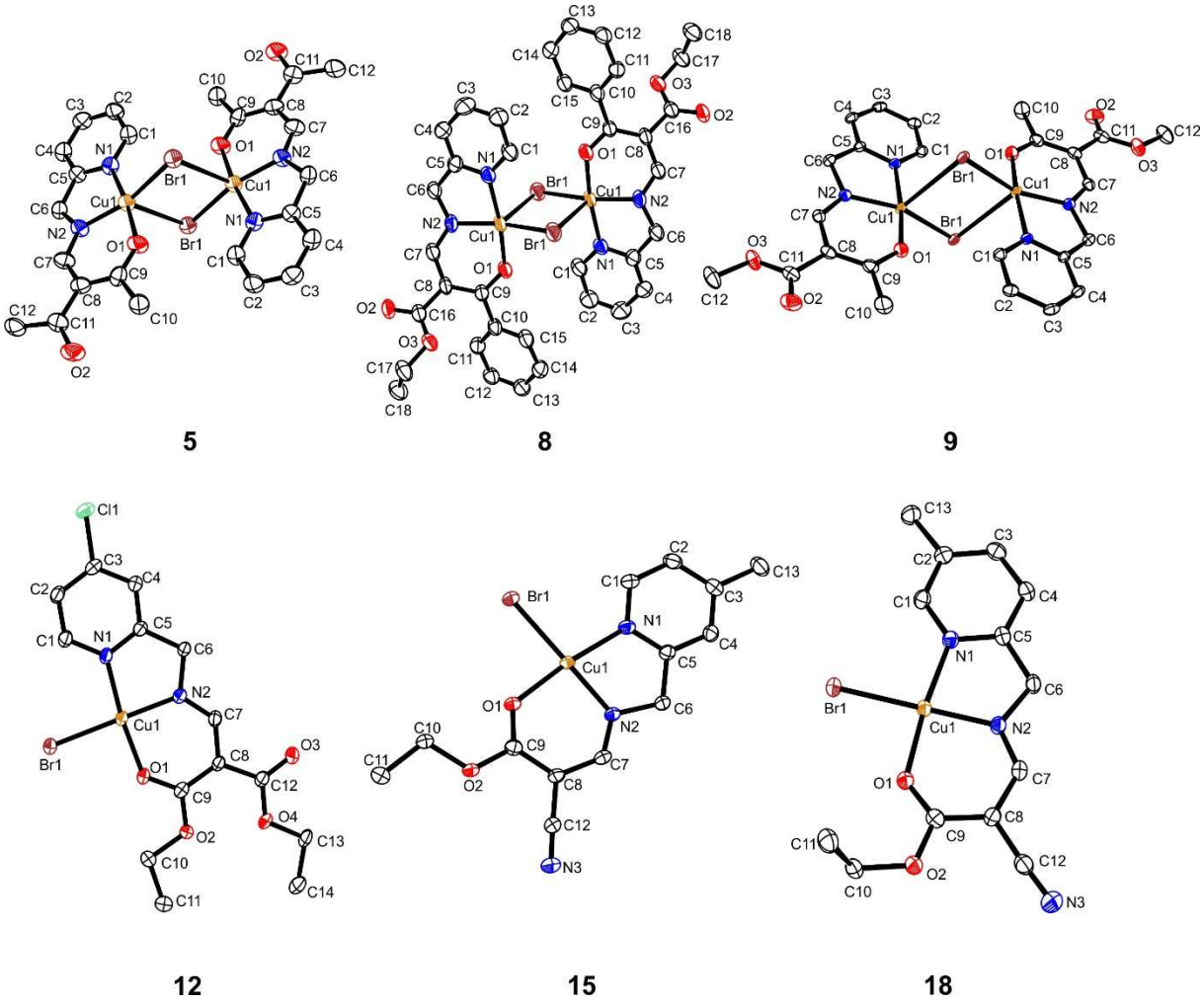

Table S3. Summary of the C–H···π / X–Y···π interactions of the complexes presented in this work.

		C_g	H···C_g/Å Y···C_g/Å	X–H···C_g/° X–Y···C_g/°	X···C_g/Å
5	C12–H12A	Cu1–O1–C9–C8–C7–N2[a]	2.83	141	3.644(11)
7	C6–H6A	Cu1–O1–C9–C8–C7–N2[b]	2.66	141	3.485(4)
	C10–H10B	N1–C1–C2–C3–C4–C5[c]	2.81	141	3.634(5)
12	C3–Cl1	Cu1–N1–C5–C6–N2[d]	3.3478(14)	84.40(11)	3.614(3)
17	C10–H10A	N1–C1–C2–C3–C4–C5[e]	2.98	132	3.709(4)
	Cu1–Br1	Cu1–N1–C5–C6–N2[f]	3.3662(14)	83.37(3)	3.8900(14)
	Cu1–Br1	N1–C1–C2–C3–C4–C5[f]	3.8784(15)	118.56(3)	5.4320(15)

a: −3−x, −y, −z; b: x, 3/2−y, 1/2+z; c: x, 3/2−y, −1/2+z; d: 1−x, −y, 2−z; e: −1/2+x, 1/2−y, z; f: 1/2+x, 1/2−y, z.

Table S4. Selected distances and angles of the π– π and M– π interactions of the complexes presented in this work. $C_g(I)$ is the centroid of the ring number I, α is the dihedral angle between the rings, β is the angle between the vector $C_g(I) \rightarrow C_g(J)$ and the normal to ring I, γ is the angle between the vector $C_g(I) \rightarrow C_g(J)$ and the normal to ring J.

	$C_g(I)$	$C_g(J)$	C_g–C_g/Å	α/°	β/°	γ/°
4	Cu1–O1–C9–C8–C7–N2	N1–C1–C2–C3–C4–C5[a]	3.9305(14)	2.29(11)	25.5	24.0
9	N1–C1–C2–C3–C4–C5	Cu1[b]	3.982	0	29.86	0
12	Cu1–N1–C5–C6–N2	Cu1–O1–C9–C8–C7–N2[b]	3.3580(16)	2.53(12)	9.6	9.8
	N1–C1–C2–C3–C4–C5	N1–C1–C2–C3–C4–C5[c]	3.4951(18)	0.02(15)	17.4	17.4
	Cu1–N1–C5–C6–N2	Cu1[b]	3.544	0	22.30	0
	Cu1–O1–C9–C8–C7–N2	Cu1[b]	3.707	0	28.89	0
15	Cu1–N1–C5–C6–N2	Cu1–O1–C9–C8–C7–N2[d]	3.2977(14)	3.99(10)	11.6	11.9
	Cu1–N1–C5–C6–N2	N1–C1–C2–C3–C4–C5[a]	3.6338(14)	0.81(12)	19.5	18.7
	Cu1–N1–C5–C6–N2	Cu1[d]	3.635	0	30.33	0
	Cu1–O1–C9–C8–C7–N2	Cu1[d]	3.423	0	20.86	0
	N1–C1–C2–C3–C4–C5	Cu1[a]	3.570	0	16.69	0
17	Cu1–N1–C5–C6–N2	Cu1–O1–C9–C8–C7–N2[e]	3.5852(18)	4.02(14)	21.8	18.6
	Cu1–N1–C5–C6–N2	Cu1[f]	3.890	0	32.59	0
	Cu1–O1–C9–C8–C7–N2	Cu1[f]	3.444	0	16.48	0
18	Cu1–N1–C5–C6–N2	Cu1–N1–C5–C6–N2[g]	3.5980(14)	0.02(11)	20.0	20.0
	Cu1–N1–C5–C6–N2	Cu1–O1–C9–C8–C7–N2[h]	3.4963(13)	1.40(10)	22.6	23.6
	Cu1–N1–C5–C6–N2	N1–C1–C2–C3–C4–C5[g]	3.6748(13)	3.91(11)	22.6	22.3
	Cu1–O1–C9–C8–C7–N2	N1–C1–C2–C3–C4–C5[g]	3.5589(13)	2.74(10)	17.7	18.0
	Cu1–N1–C5–C6–N2	Cu1[h]	3.650	0	28.30	0
	Cu1–N1–C5–C6–N2	Cu1[g]	3.907	0	30.19	0
	Cu1–O1–C9–C8–C7–N2	Cu1[h]	3.322	0	14.07	0
	N1–C1–C2–C3–C4–C5	Cu1[g]	3.548	0	21.11	0

a: 1−x, 1−y, −z; b: 1−x, 1−y, 2−z; c: 1−x, −y, 2−z; d: 1−x, −y, −z; e: 1/2+x, 1/2−y, z; f: −1/2+x, 1/2−y, z; g: 2−x, −y, 1−z; h: 1−x, −y, 1−z.

Table S5. Hydrogen bonds and angles of the complexes presented in this work.

	Donor	Acceptor	D–H/Å	H···A/Å	D···A/Å	D–H···A/°
4	C3–H3	Br1[a]	0.95	2.82	3.606(3)	140
	C6–H6B	Br1[b]	0.99	2.77	3.652(3)	149
5	C2–H2	O2[c]	0.95	2.48	3.203(12)	133
	C6–H6A	Br1[d]	0.99	2.83	3.730(9)	151
	C6–H6B	O2[e]	0.99	2.56	3.378(11)	140
7	C6–H6B	Br1[f]	0.99	2.88	3.766(4)	149
	C7–H7	Br1[g]	0.95	2.84	3.744(4)	159
8	C7–H7	O2[h]	0.95	2.39	3.318(9)	164
9	C3–H3	Br1[i]	0.95	2.90	3.602(2)	132
	C6–H6B	Br1[j]	0.99	2.92	3.829(2)	153
12	C2–H2	Br1[k]	0.95	2.91	3.842(3)	167
	C4–H4	O3[l]	0.95	2.30	3.142(4)	148
15	C6–H6A	Br1[m]	0.99	2.88	3.747(3)	147
17	C4–H4	O3[o]	0.95	2.42	3.370(5)	173
18	C7–H7	Br1[a]	0.95	2.85	3.622(2)	139
	C13–H13C	Br1[p]	0.98	2.91	3.832(3)	157

a: x, −1+y, z; b: 1−x, 1−y, −z; c: 1+x, 1+y, 1+z; d: −3−x, −y, 1−z; e: −3−x, −y, −z; f: 1+x, 3/2−y, 1/2+z; g: 1+x, y, 1+z; h: 2−x, −y, 1−z; i: −1+x, 1+y, z; j: 1−x, 1−y, 2−z; k: −x, −y, 2−z; l: 2−x, 1−y, 2−z; m: 1+x, y, z; o: −1/2−x, 1/2+y, −z; p: 2−x, 1−y, 1−z.

Figure S2. Powder X-ray diffraction patterns and calculated pattern of **4**, **5**, **7**, **8**, and **9**. Calculated patterns were obtained at 133 K, measured at room temperature.

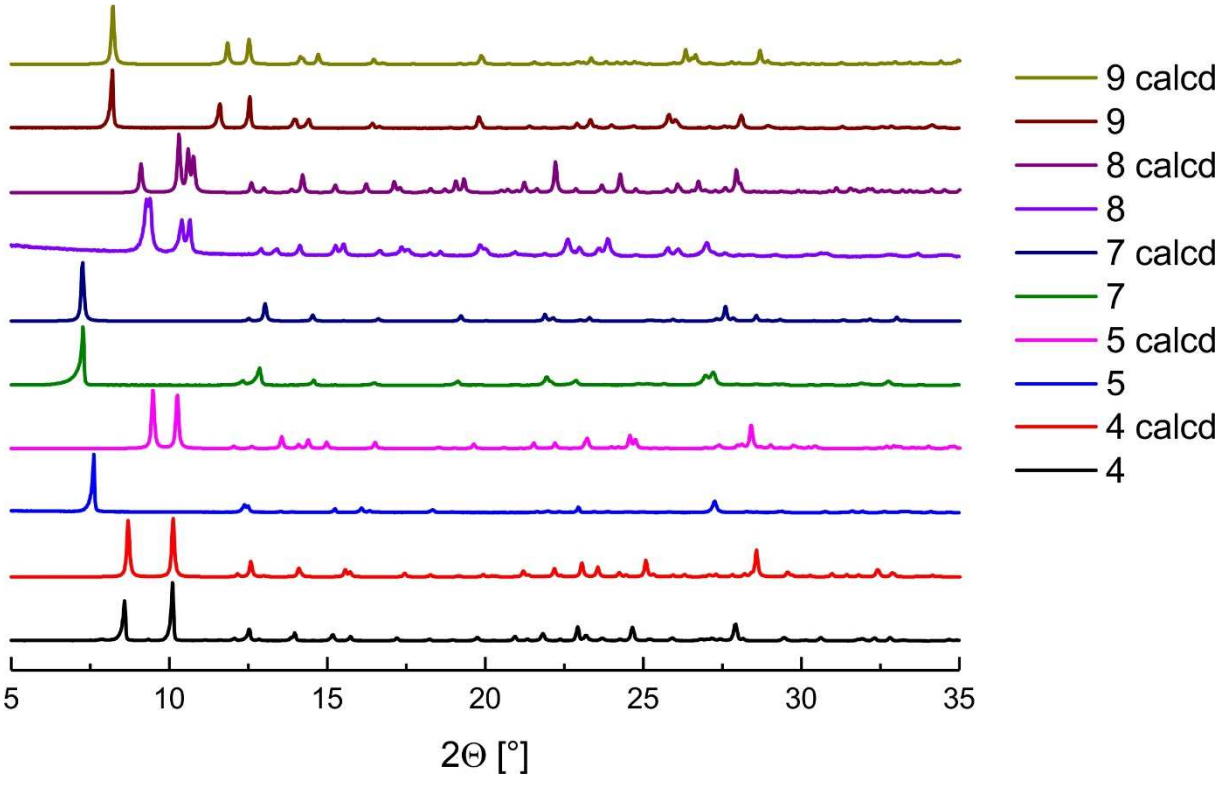

Figure S3. Powder X-ray diffraction patterns and calculated patterns of **12**, **15**, **17**, and **18**. Calculated patterns were obtained at 133 K, measured at room temperature.

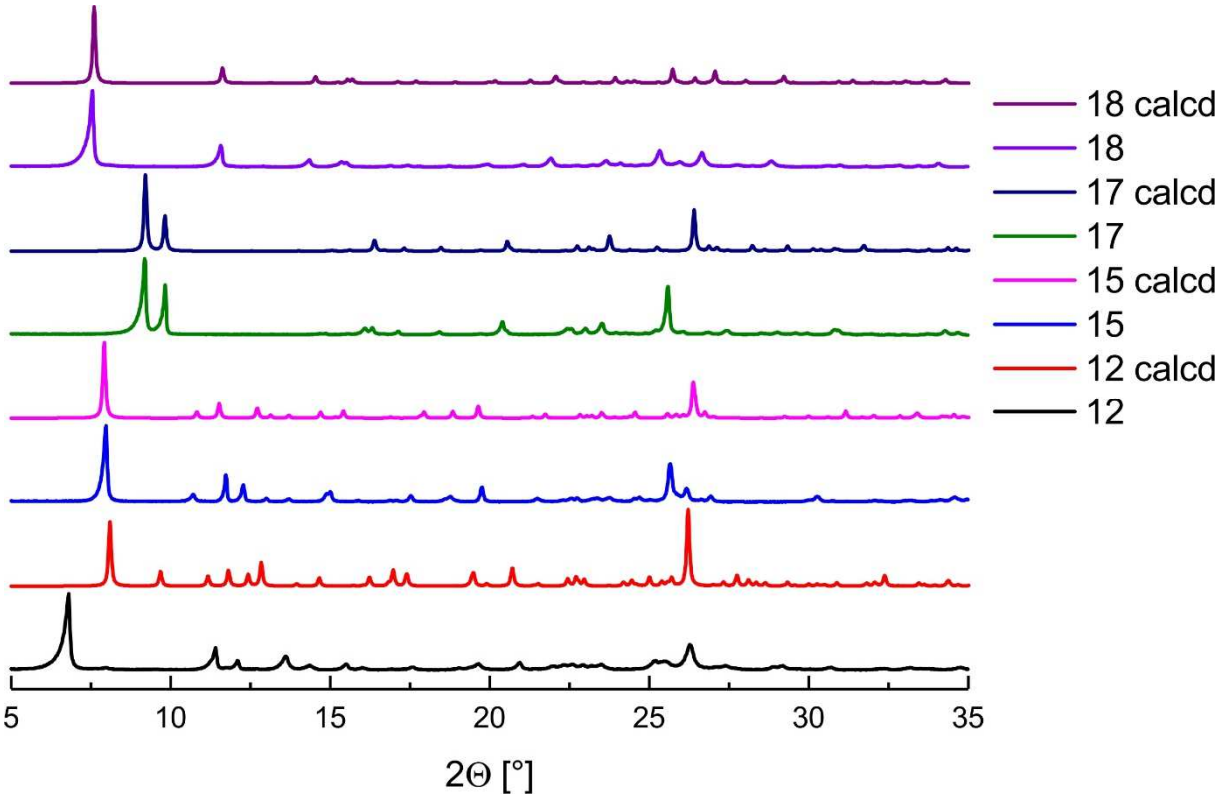

Figure S4. $\chi_M T$ vs. T plots of compounds **4**, **5**, **6**, **7**, **8**, and **9**.

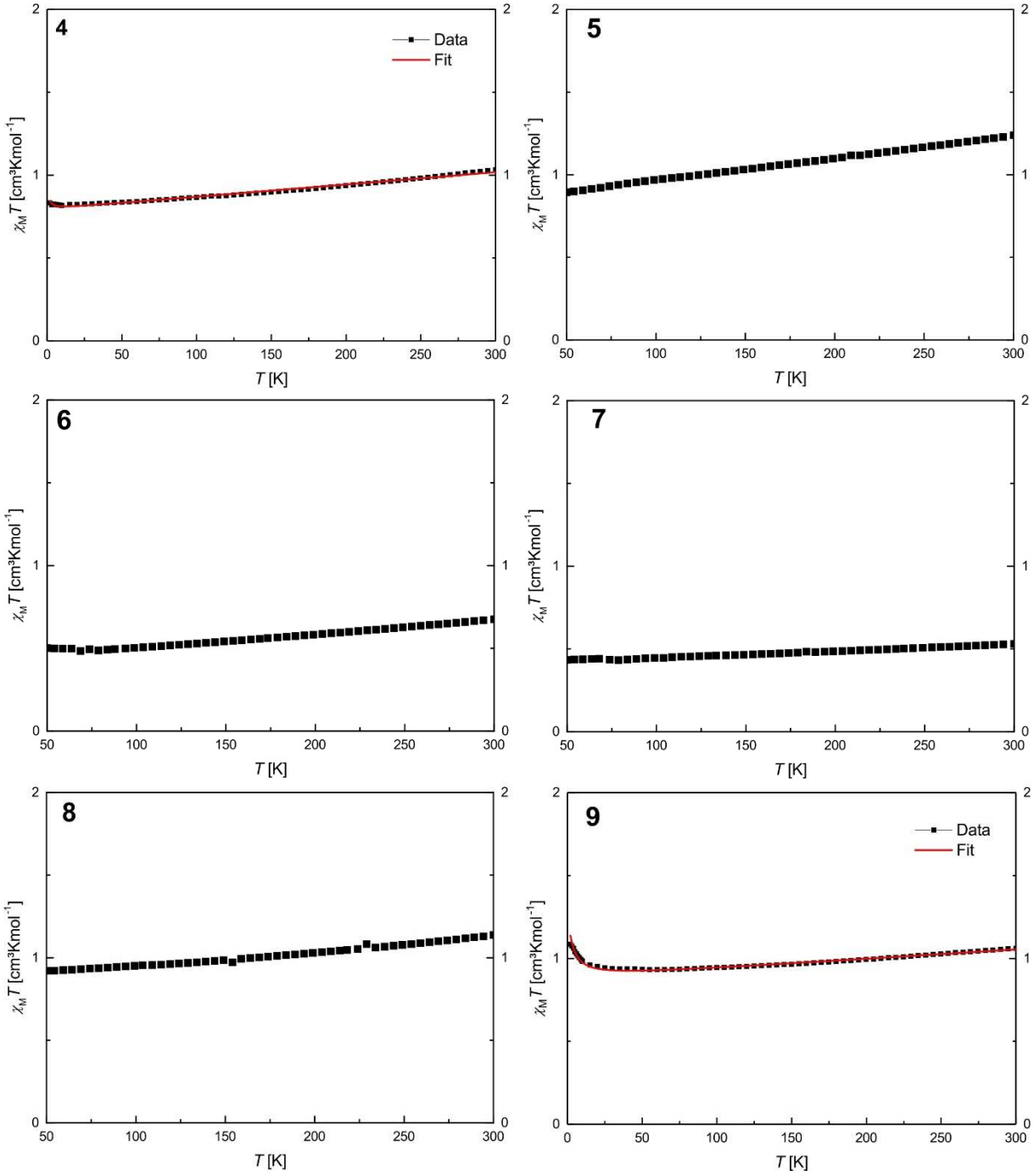

Figure S5. $\chi_M T$ vs. T plots of compounds **10**, **11**, **12**, **13**, **14**, and **15**.

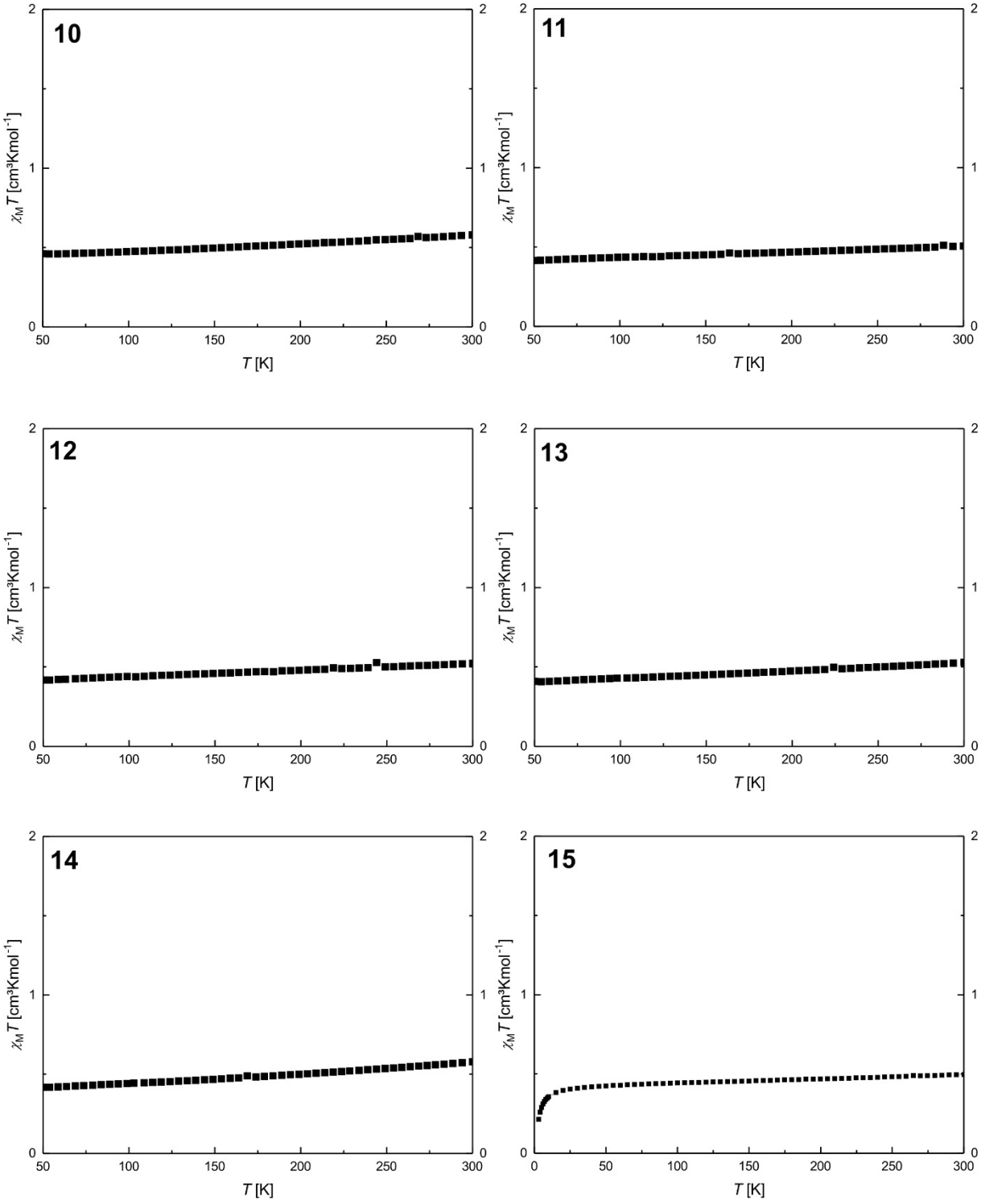

Figure S6. $\chi_M T$ vs. T plots of compounds **16**, **17**, and **18**.

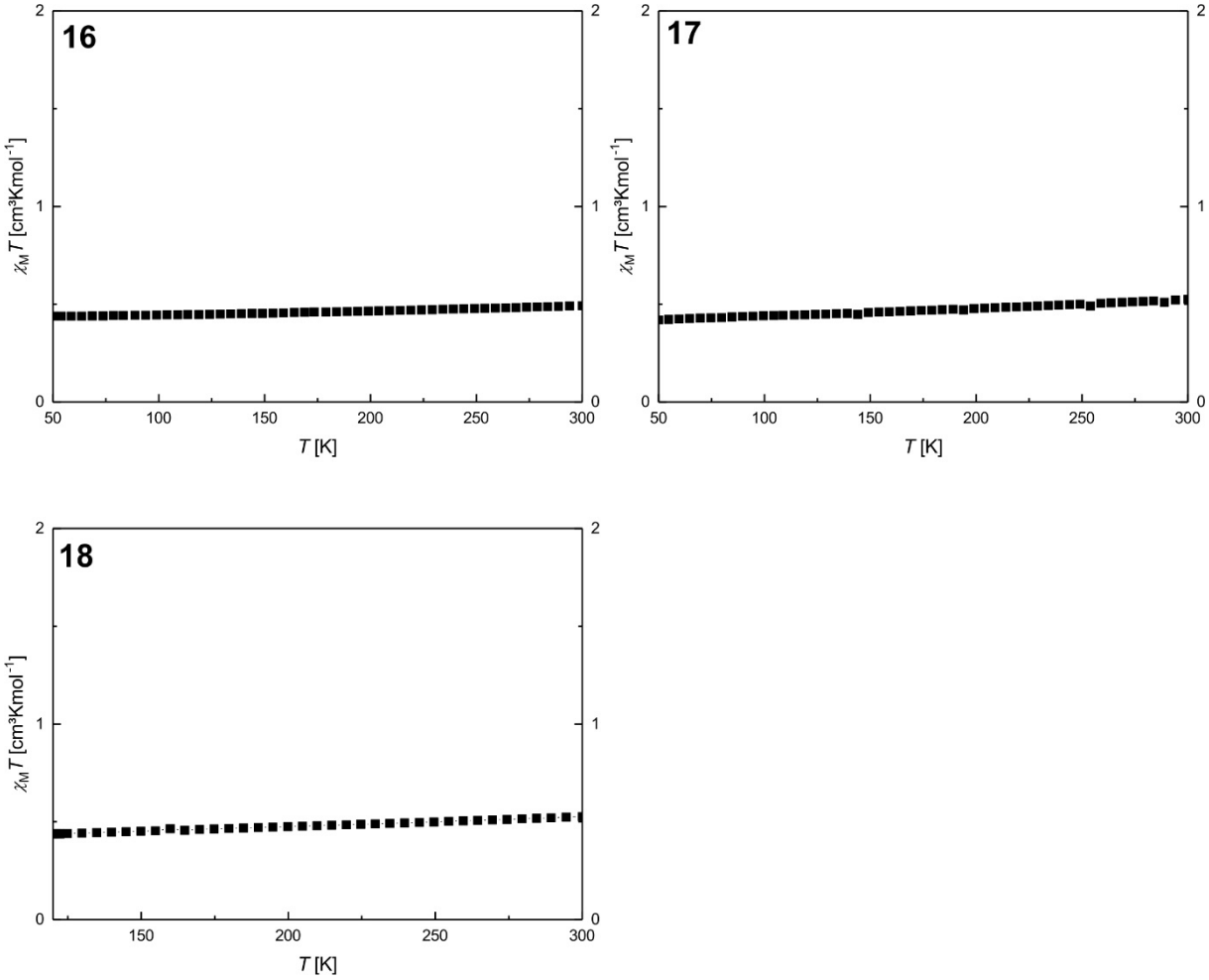

Table S6. Data of the magnetic measurements with μ_{eff} at 300 K, $\chi_M T$ at 300 K, 50 K, and, if measured, 2 K, and, if determined, the coupling constant *J*, *g*, and TIP.

	μ_{eff} [μ_B] (300 K)	$\chi_M T$ [$cm^3K^{-1}mol^{-1}$] (300 K)	$\chi_M T$ [$cm^3K^{-1}mol^{-1}$] (50 K)	$\chi_M T$ [$cm^3K^{-1}mol^{-1}$] (2 K)	*J* [cm^{-1}]	*g*	TIP [cm^3mol^{-1}]
4	2.88	1.04	0.84	0.83	0.38(5)	2.057(3)	$7.45(11)\cdot10^{-4}$
5	3.15	1.24	0.89				
6	2.33	0.68	0.50				
7	2.06	0.53	0.43				
8	3.02	1.14	0.92				
9	2.90	1.05	0.93	1.09	3.38(19)	2.163(4)	$5.79(17)\cdot10^{-4}$
10	2.16	0.58	0.46				
11	2.01	0.51	0.42				
12	2.05	0.52	0.42				
13	2.06	0.53	0.41				
14	2.15	0.58	0.42				
15	1.99	0.50	0.42	0.21			
16	1.99	0.49	0.44				
17	2.05	0.53	0.42				
18	2.05	0.53	0.44 (120 K)*				

*due to technical difficulties this complex could only be measured until 120 K.

Figure S7. UV-Vis spectra of **1**–**6** (**1** in H_2O, **2**–**6** in DMSO) at the indicated time points.

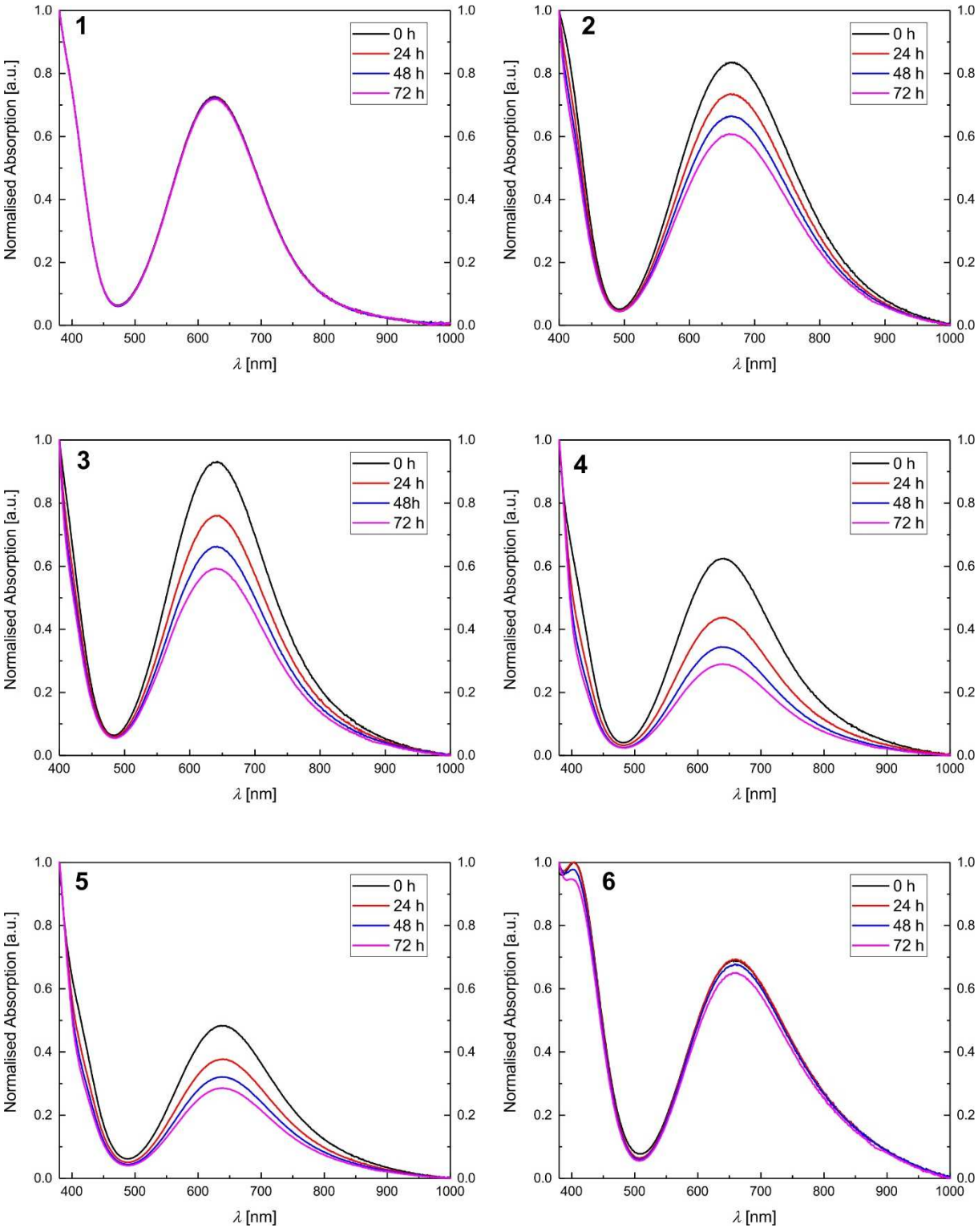

Figure S8. UV-Vis spectra of **7**–**12** (DMSO) at the indicated time points.

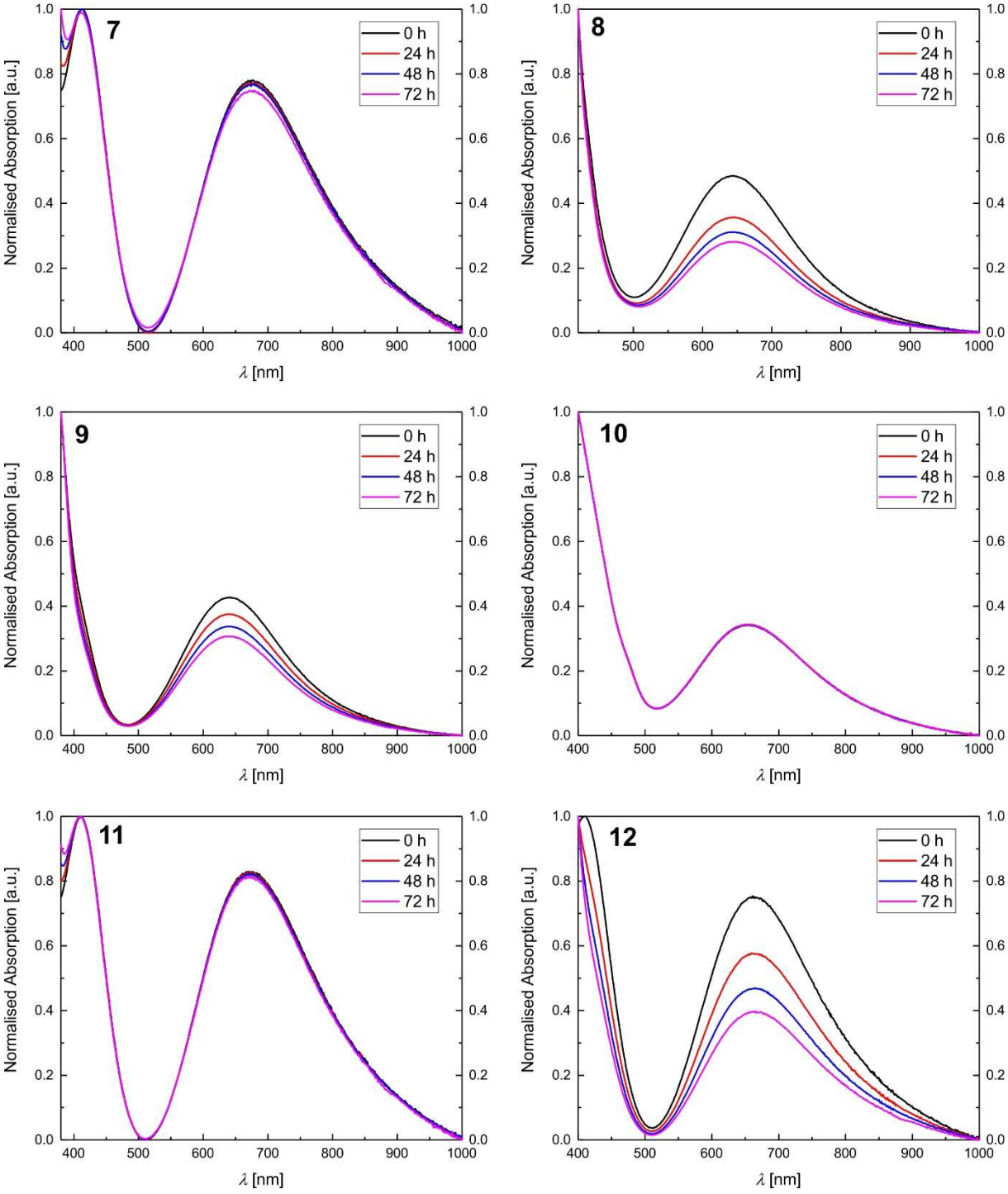

Figure S9. UV-Vis spectra of **13**–**18** (DMSO) at the indicated time points.

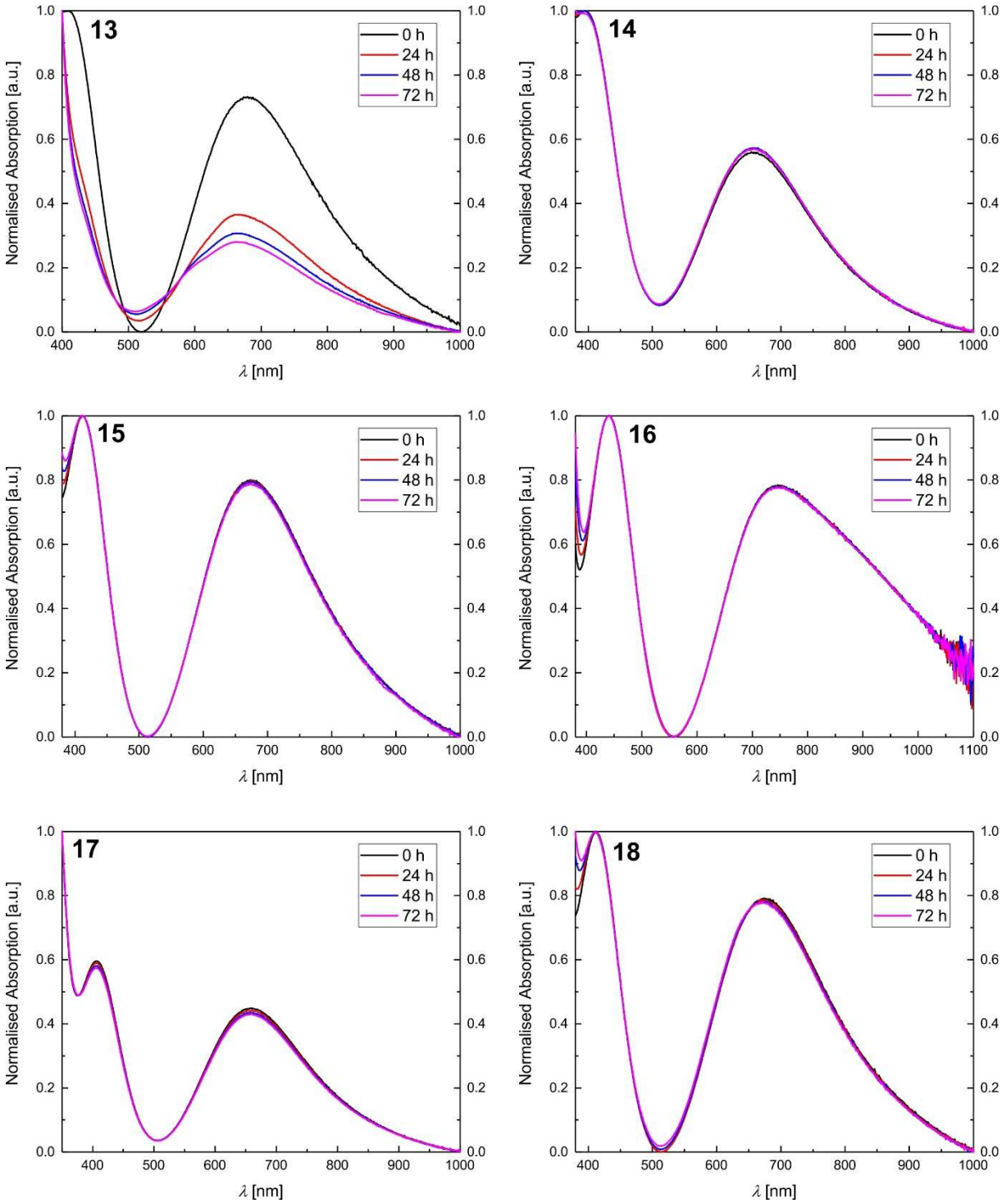

Figure S10. Cyclic voltammograms (MeCN, 0.1 M NBu_4PF_6, vs. $Ag/AgNO_3$, 50 mV/s) of **1**–**6**.

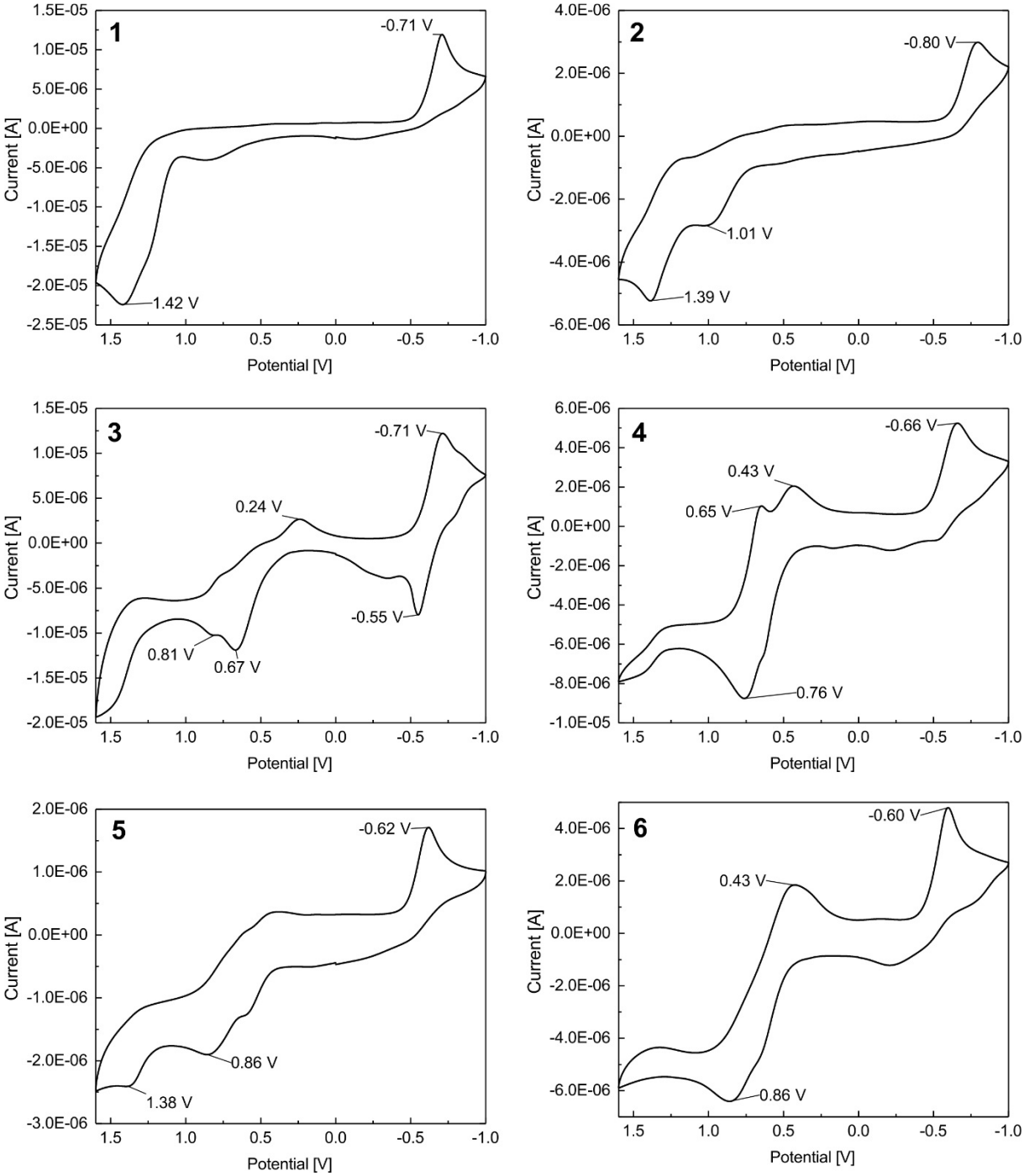

Figure S11. Cyclic voltammograms (MeCN, 0.1 M NBu_4PF_6, vs. $Ag/AgNO_3$, 50 mV/s) of **7**–**12**.

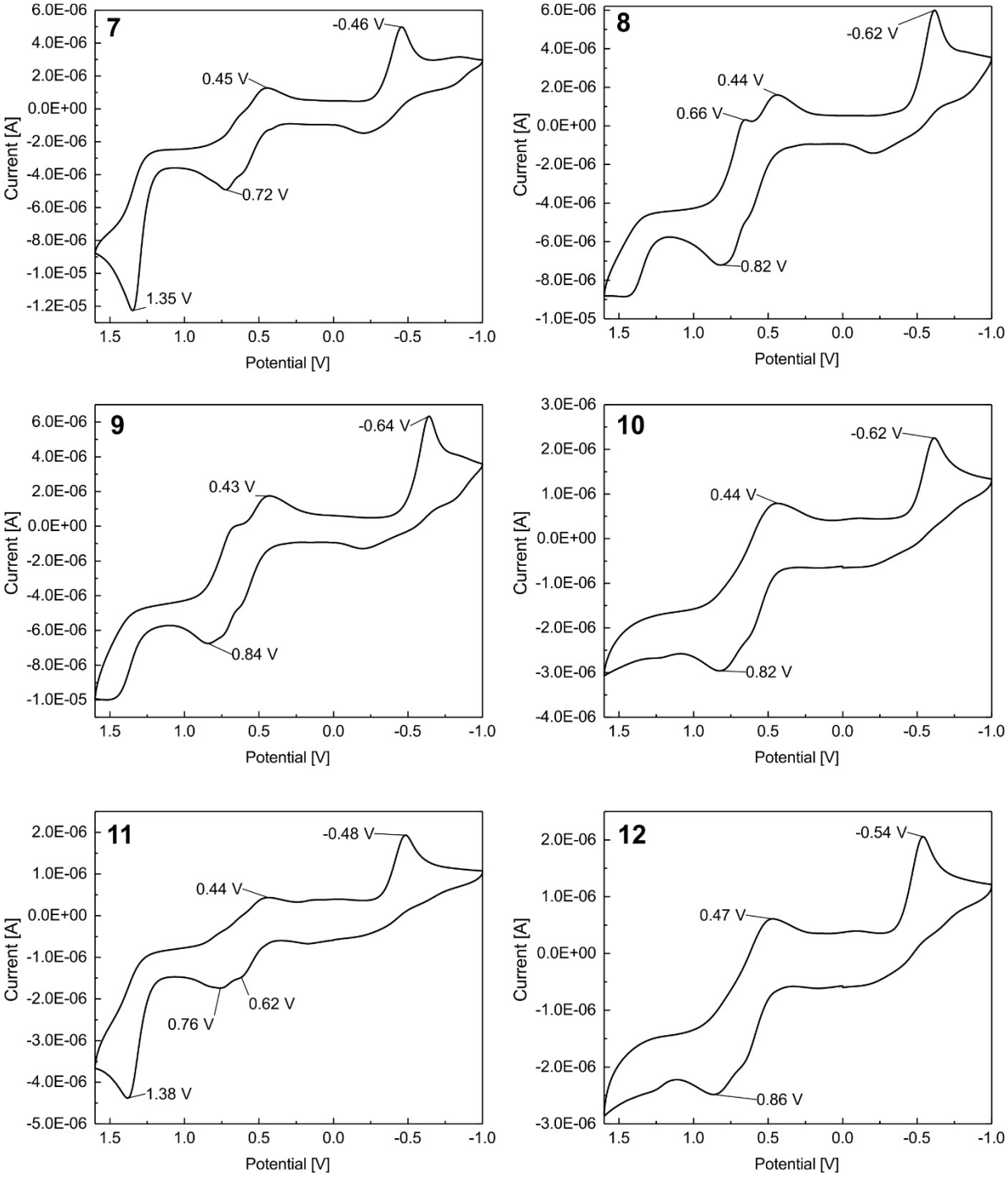

Figure S12. Cyclic voltammograms (MeCN, 0.1 M NBu_4PF_6, vs. $Ag/AgNO_3$, 50 mV/s) of **13**–**18**.

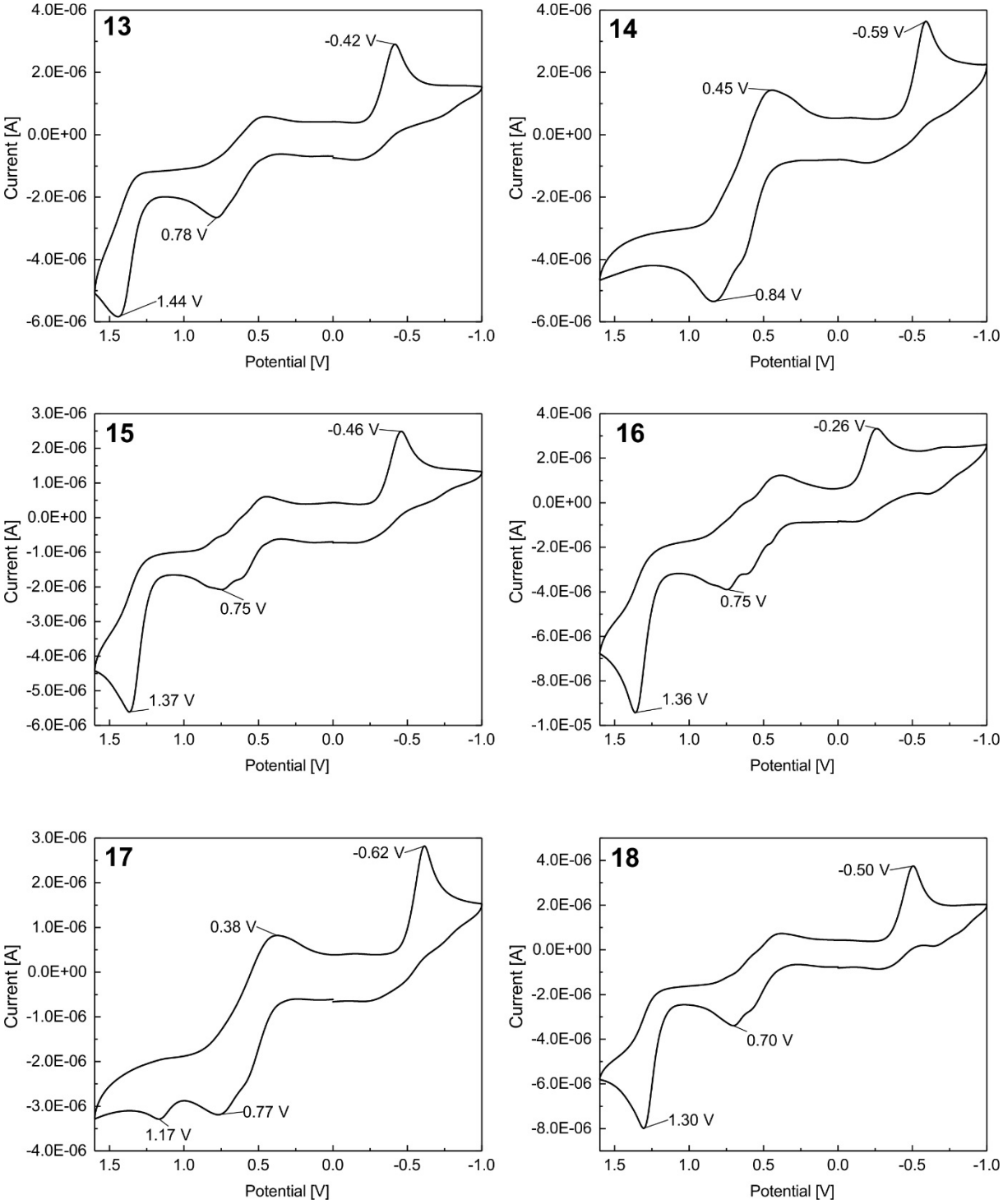

Figure S13. UV-Vis spectra of **3**, **8**, and **11** in PBS.

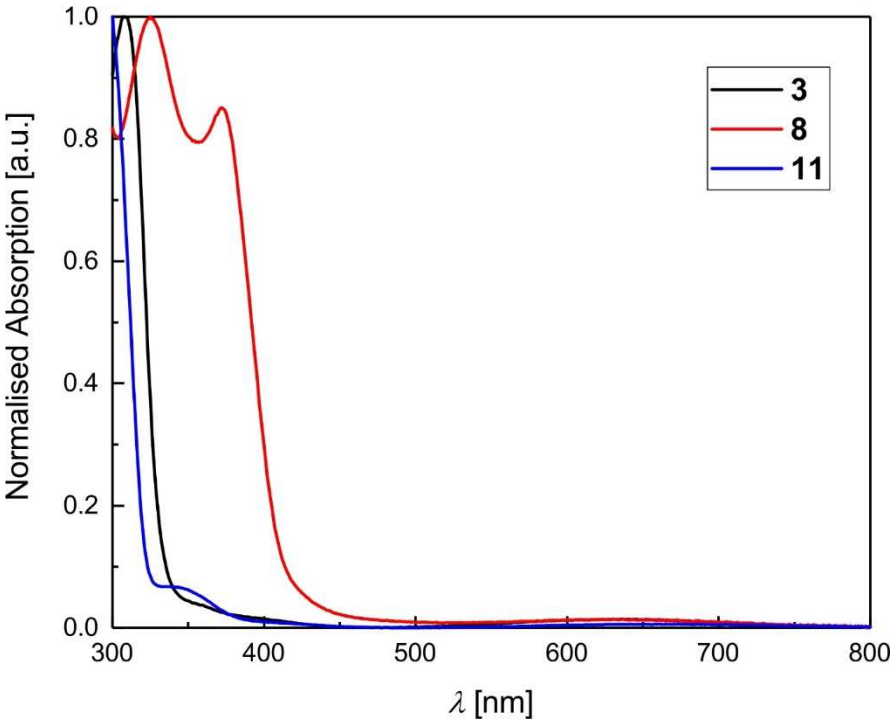

Figure S14. UV-Vis spectra of compounds **1**, **10**, and **14** (100 µM) in PBS at 37 °C at the indicated time points.

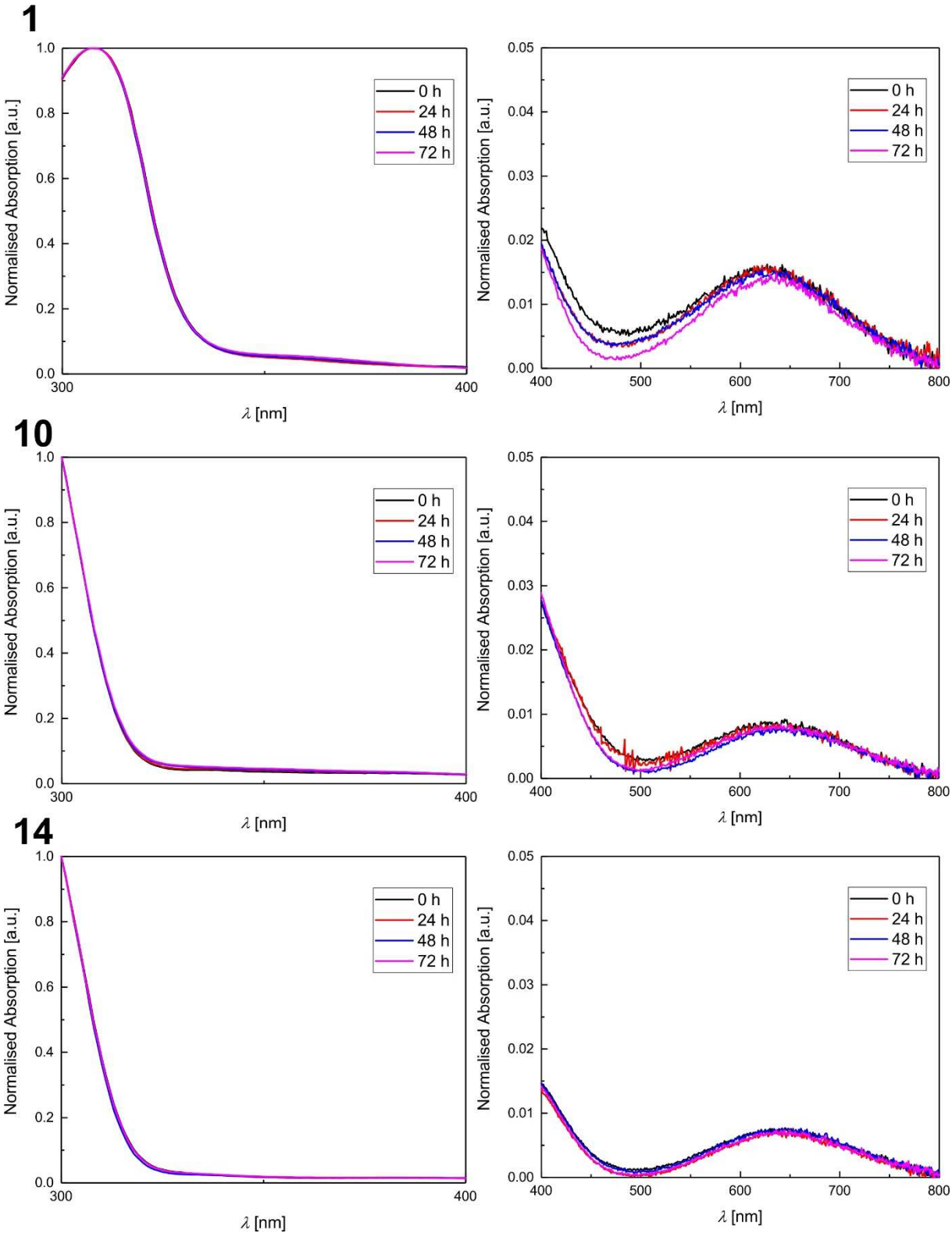

Figure S15. Relative ethidium bromide–DNA adduct fluorescence after pre-incubation with vehicle (0 µM) of **1**, **10**, **14**, and $CuSO_4$ (25, 50, 75, 100 µM) for 2 h. A decreased fluorescence indicates an interaction between DNA and test compound which prevents the intercalation of ethidium bromide molecules between the double-stranded SS-DNA. Values ± SD derived from at least three independent experiments with controls set to 100 %.

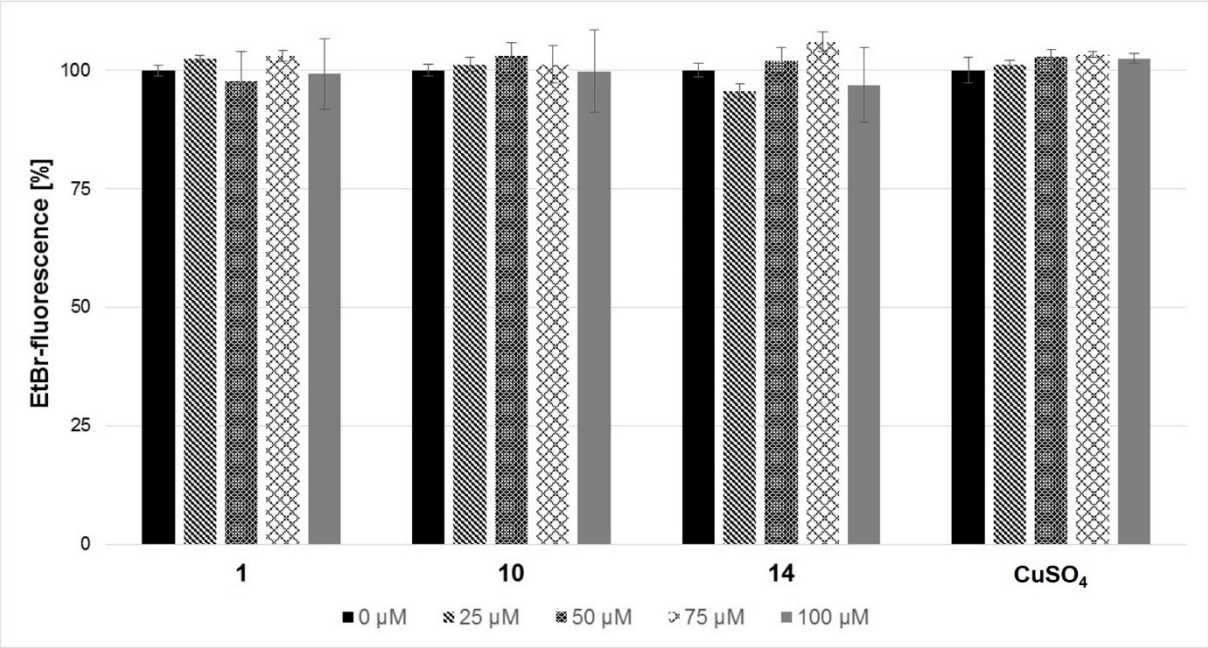

Figure S16. Electrophoretic mobility shift assay (EMSA) with circular pBR322 DNA. DNA was incubated with cis-platin (CDDP, top left), **1** (top right), **10** (bottom left), or **14** (bottom right) (0, 5, 10, 25, 50 µM) for 24 h and subjected to agarose gel electrophoresis followed by ethidium bromide staining. Supercoiled form (top) and open circular form (bottom). Pictures are representative for at least two independent experiments.

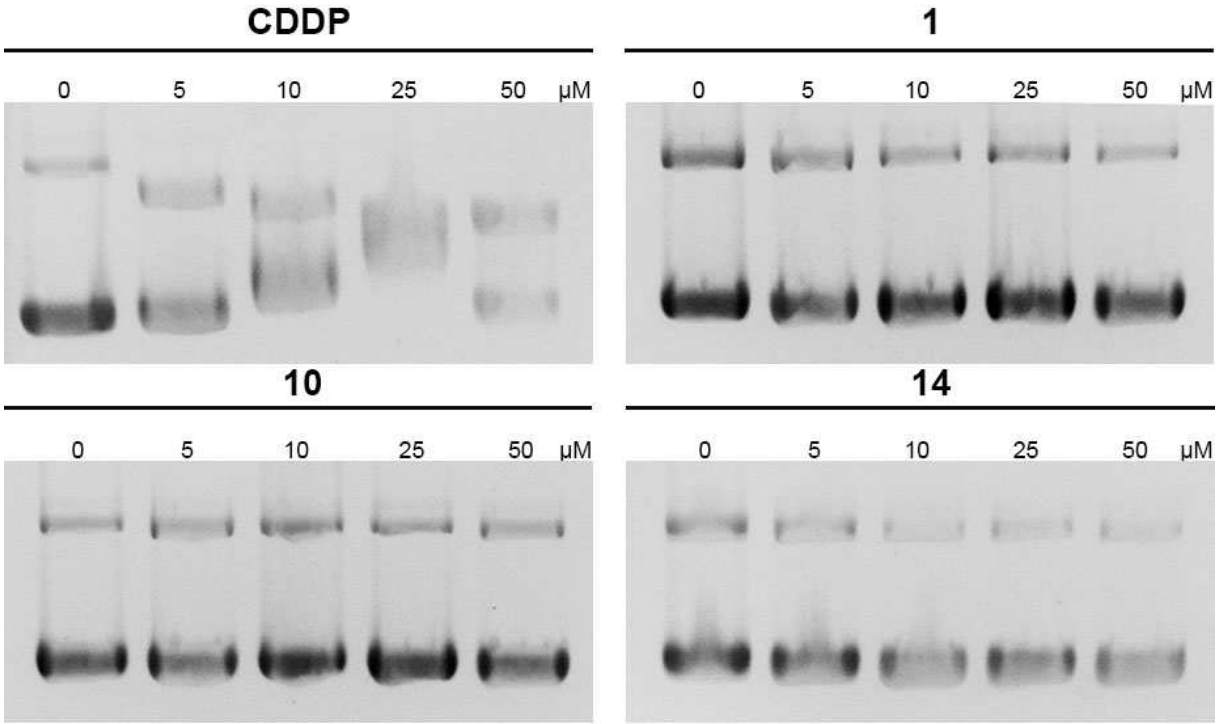

Figure S17. Effect of copper complexes **1**–**18**, $CuSO_4$, and HL11 on the relative superoxide levels in 518A2 melanoma cells after 24 h incubation as determined by NBT assays. The ROS production (%) was obtained as the mean ± standard deviation of six independent experiments with respect to untreated control cells set to 100 %.

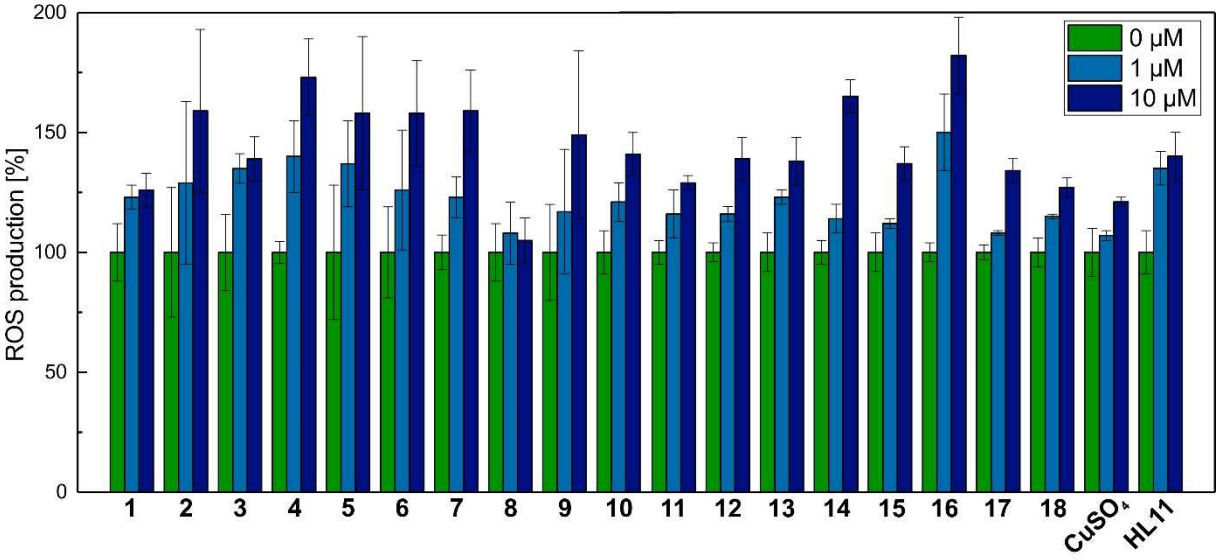

Figure S18. Mass spectrum (DIP, EI, pos.) of **4**.

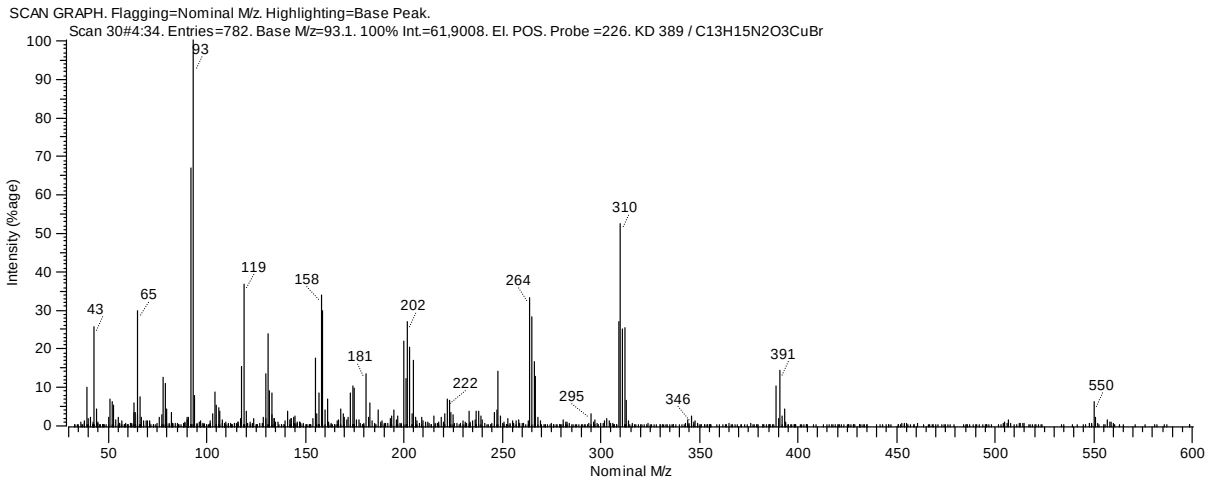

Figure S19. Mass spectrum (DIP, EI, pos.) of **5**.

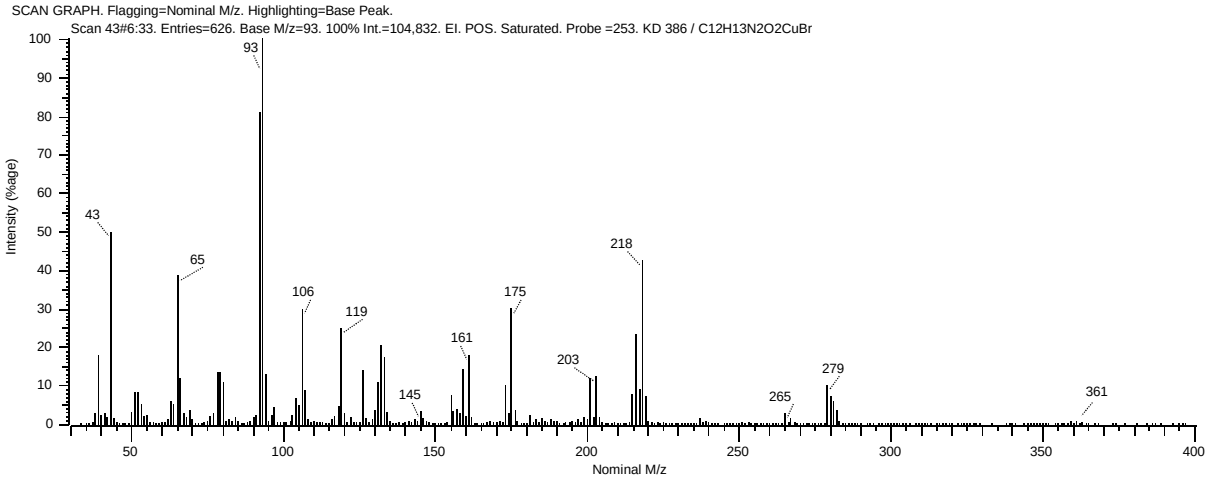

Figure S20. Mass spectrum (DIP, EI, pos.) of **6**.

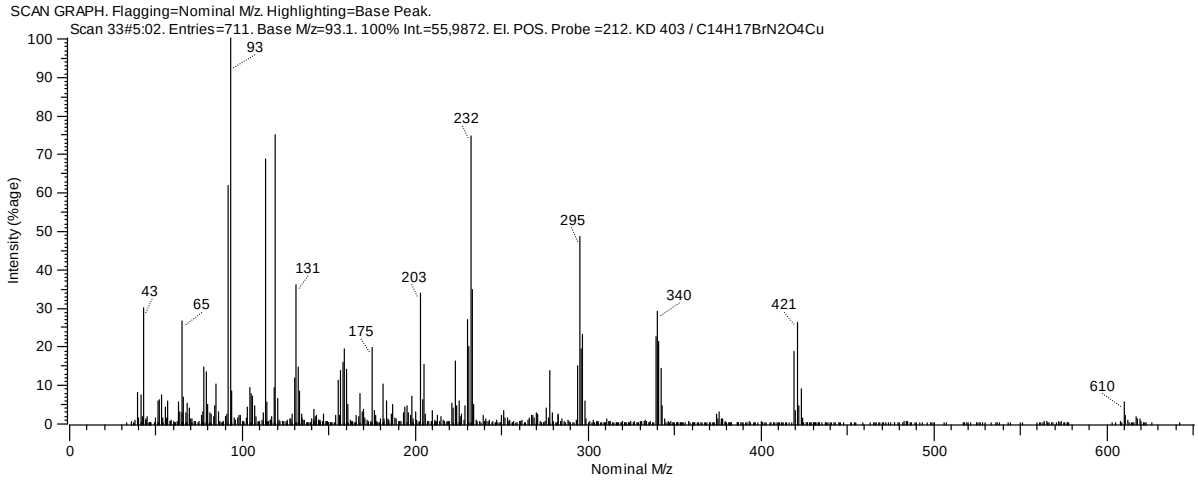

Figure S21. Mass spectrum (DIP, EI, pos.) of **7**.

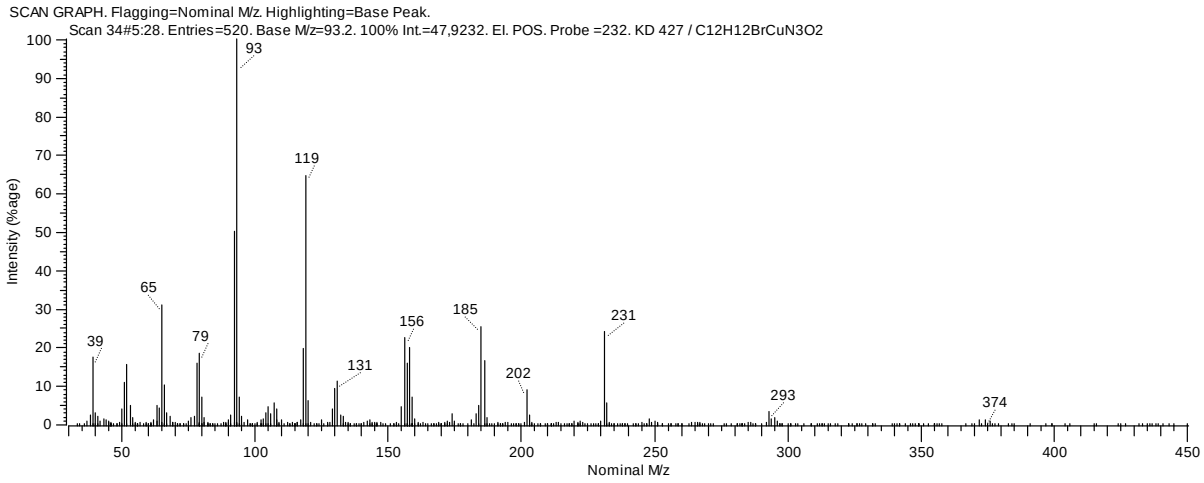

Figure S22. Mass spectrum (DIP, EI, pos.) of **8**.

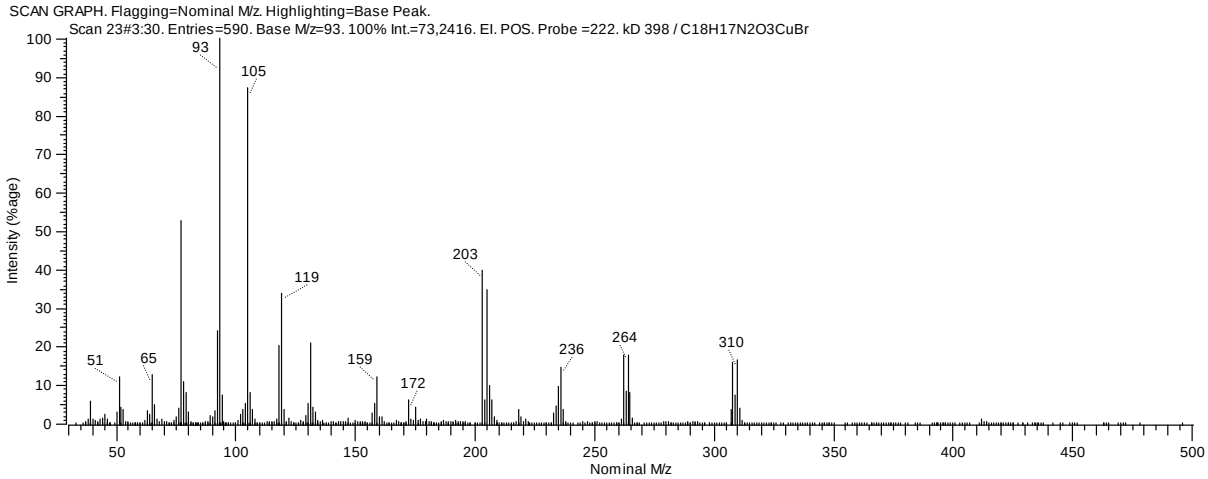

Figure S23. Mass spectrum (DIP, EI, pos.) of **9**.

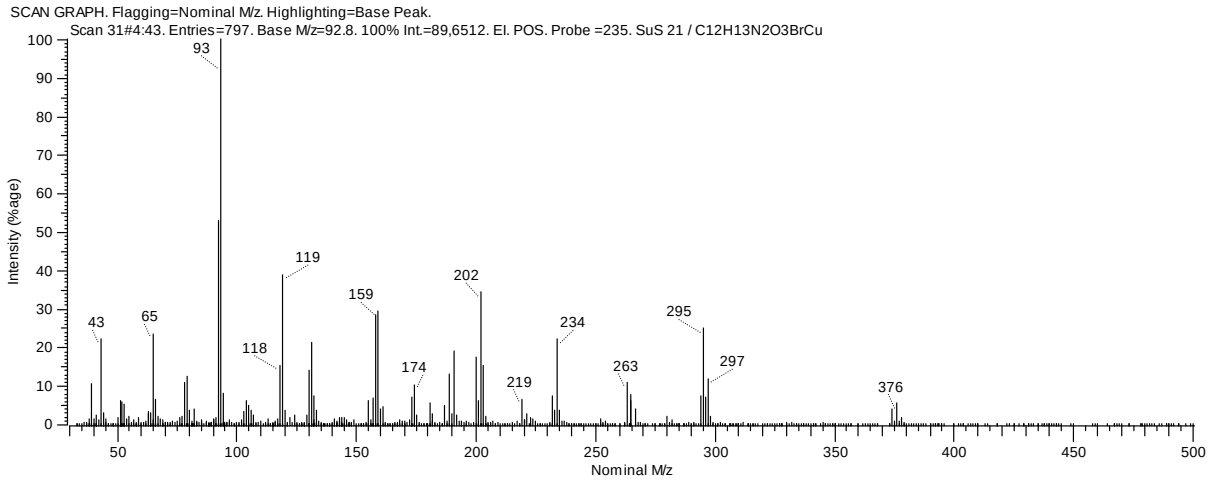

Figure S24. Mass spectrum (DIP, EI, pos.) of **10**.

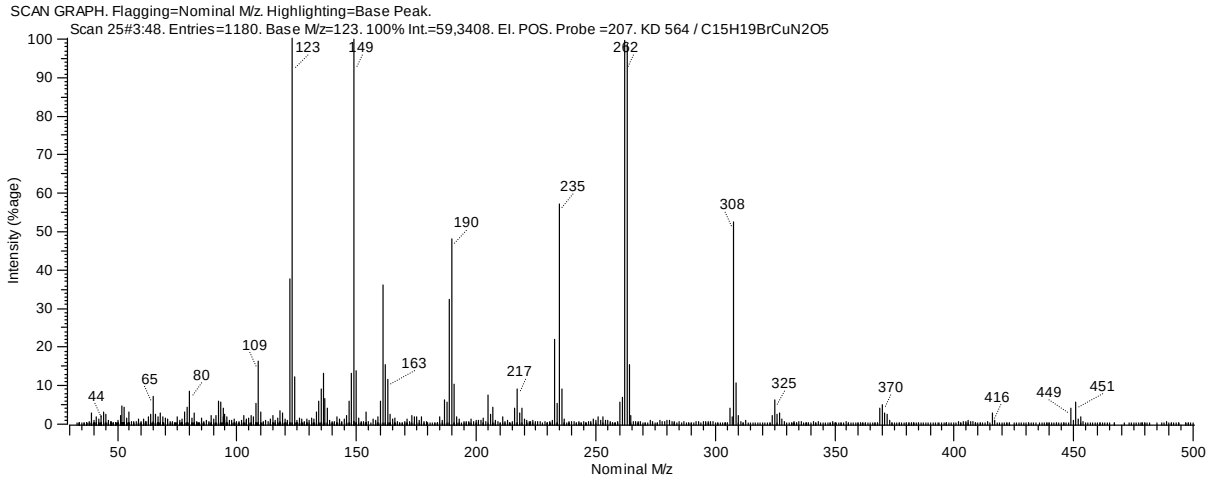

Figure S25. Mass spectrum (DIP, EI, pos.) of **11**.

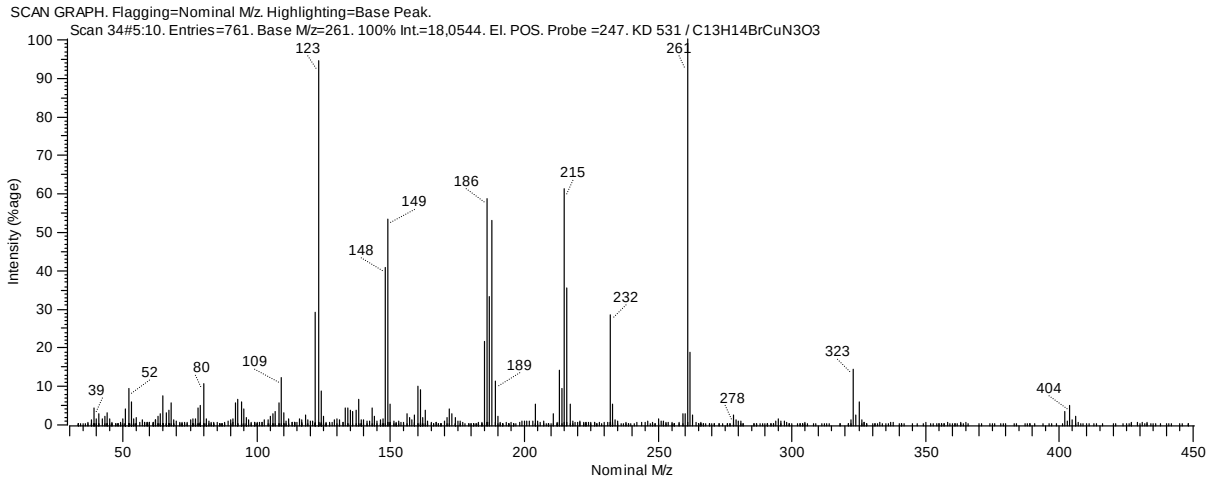

Figure S26. Mass spectrum (DIP, EI, pos.) of **12**.

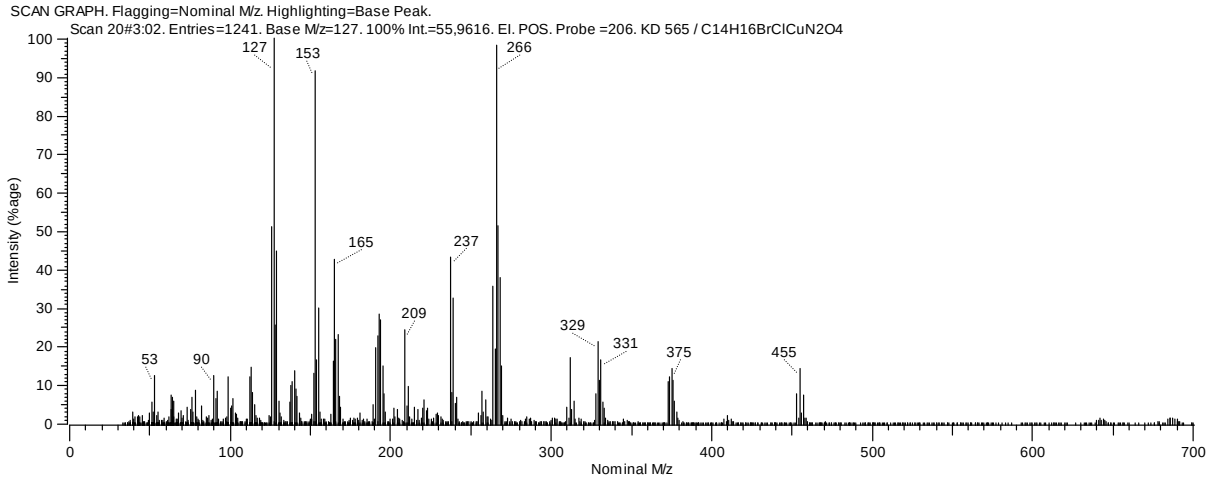

Figure S27. Mass spectrum (DIP, EI, pos.) of **13**.

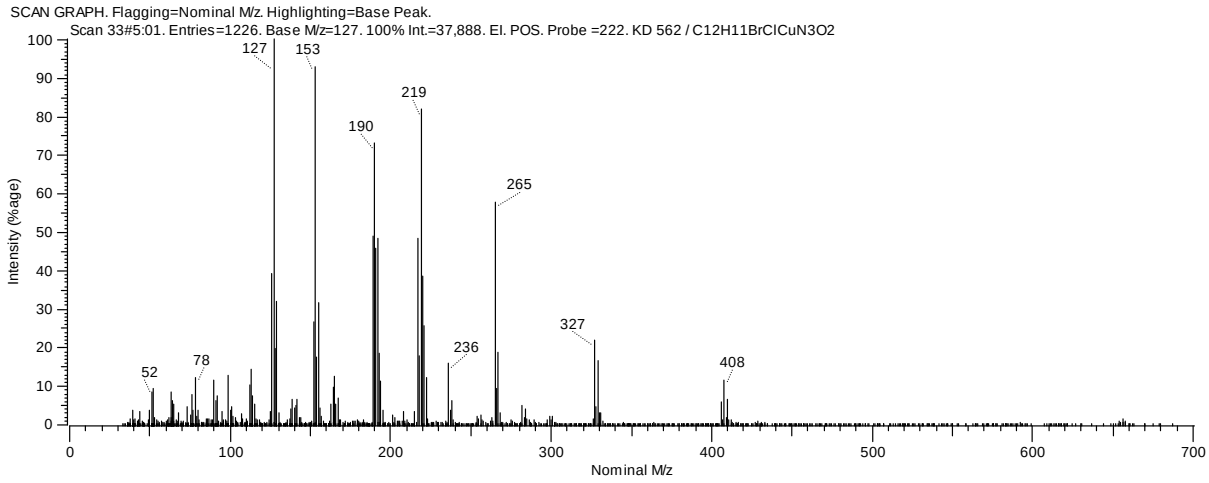

Figure S28. Mass spectrum (DIP, EI, pos.) of **14**.

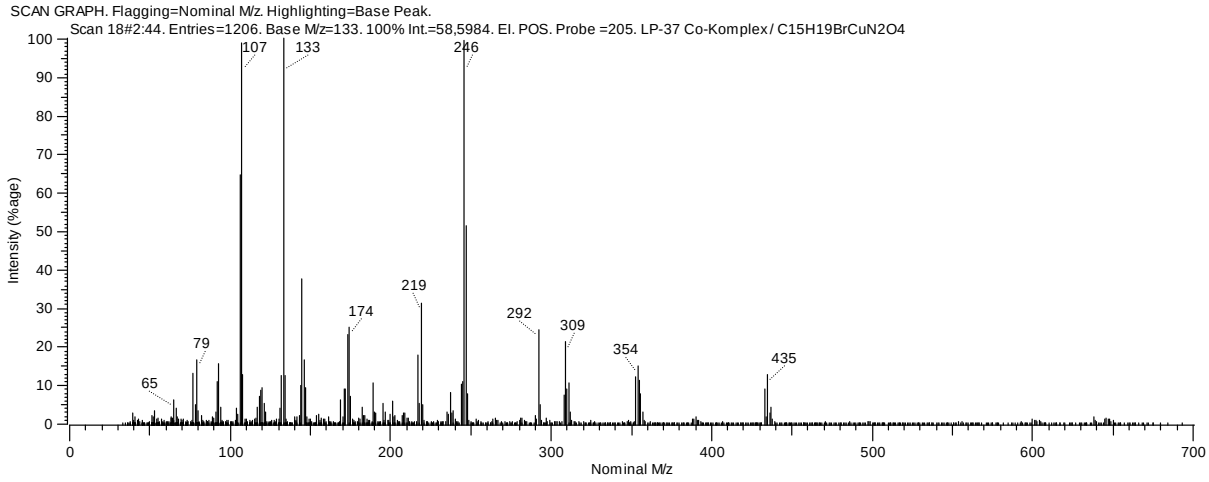

Figure S29. Mass spectrum (DIP, EI, pos.) of **15**.

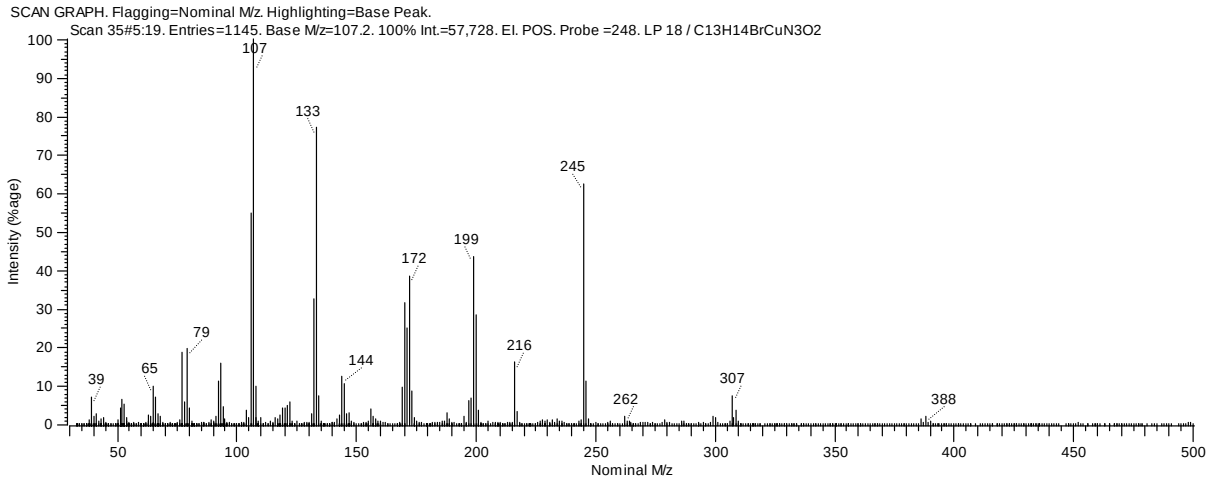

Figure S30. Mass spectrum (DIP, EI, pos.) of **16**.

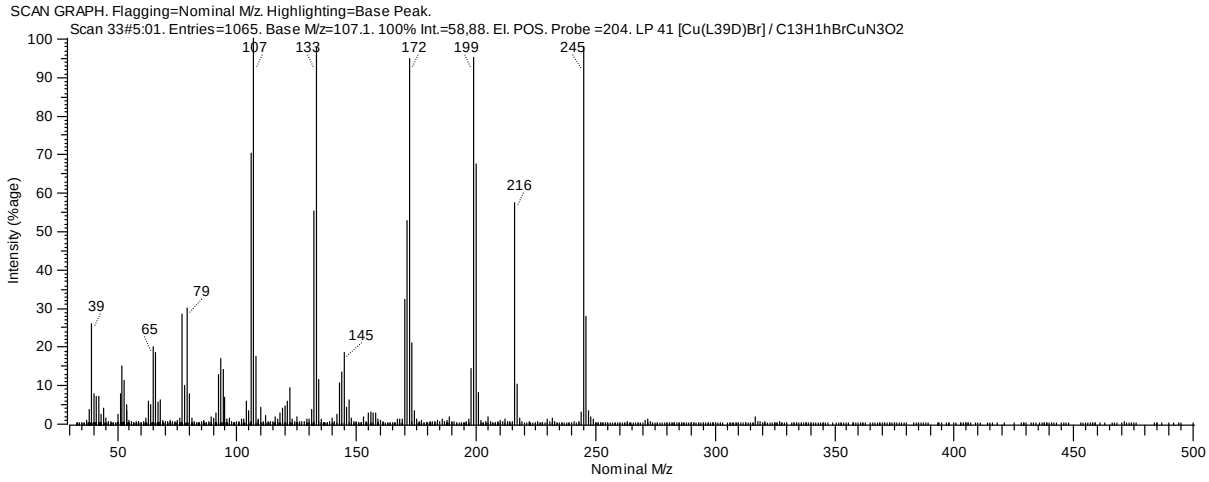

Figure S31. Mass spectrum (DIP, EI, pos.) of **17**.

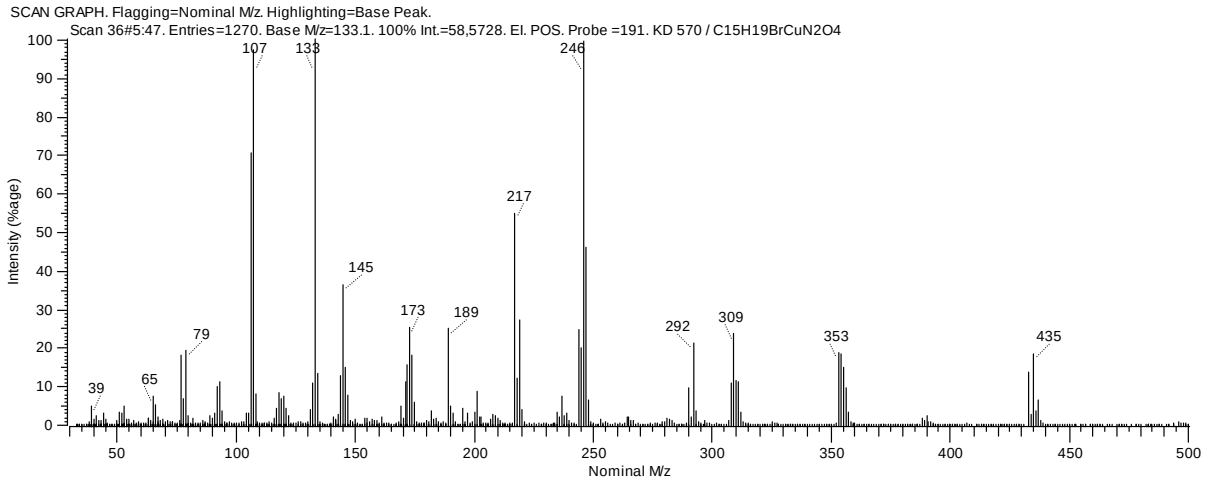

Figure S32. Mass spectrum (DIP, EI, pos.) of **18**.

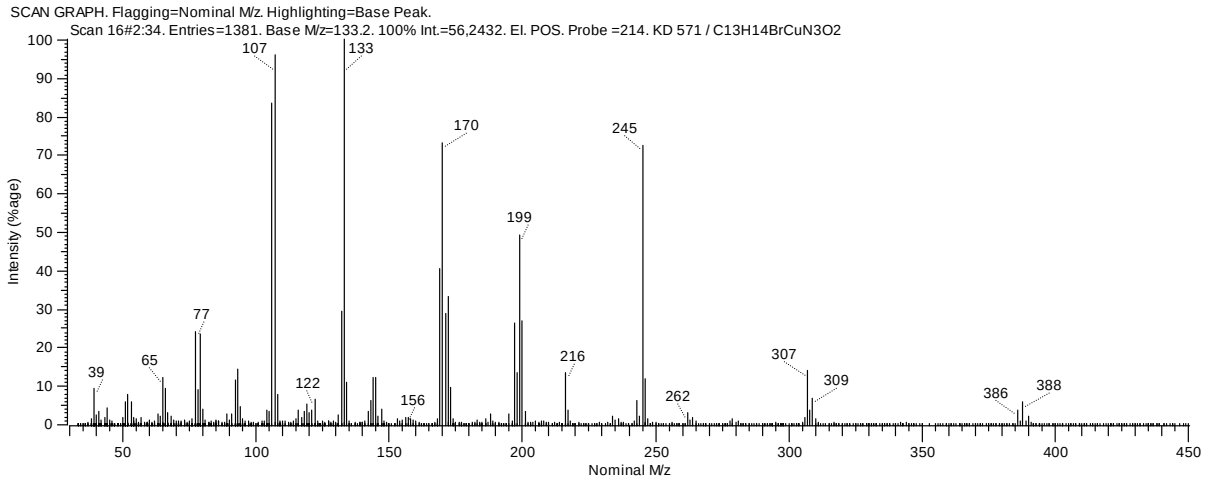

11.List of publications

K. Dankhoff, M. Gold, L. Kober, F. Schmitt, L. Pfeifer, A. Dürrmann, H. Kostrhunova, M. Rothemund, V. Brabec, R. Schobert, B. Weber: „Copper(II) complexes with tridentate Schiff base-like ligands: solid state and solution structures“, *Dalton Trans.* **2019**, *48*, 15220–15230.

P. M. Schäfer, K. Dankhoff, M. Rothemund, A. N. Ksiazkiewicz, A. Pich, R. Schobert, B. Weber, S. Herres-Pawlis; „Towards new robust Zn(II) complexes for the ring-opening polymerization of lactide under industrial relevant conditions”, *ChemistryOpen* **2019**, *8*, 1020–1026.

K. Dankhoff, B. Weber: „Isostructural iron(III) spin crossover complexes with a tridentate Schiff base-like ligand: X-ray structures and magnetic properties”, *Dalton Trans.* **2019**, DOI: 10.1039/C9DT00846B.

K. Dankhoff, A. Ahmad, B. Weber, B. Biersack, R. Schobert: „Anticancer properties of a new non-oxido vanadium(IV) complex with a catechol-modified 3,3′-diindolylmethane ligand”, *J. Inorg. Biochem.* **2019**, *194*, 1–6.

K. Dankhoff, S. Schneider, R. Nowak, B. Weber: „Iron(II) and Iron(III) Complexes of Tridentate NNO Schiff Base-like Ligands – X-ray Structures and Magnetic Properties“, *Z. Anorg. Allg. Chem.* **2018**, *644*, 1839–1848.

H. L. C. Feltham, K. Dankhoff, C. J. Meledandri, S. Brooker: „Towards Dual-Functionality Spin-Crossover Complexes”, *ChemPlusChem* **2018**, *83*, 582–589.

K. Dankhoff, B. Weber: „Novel Cu(II) complexes with NNO-Schiff base-like ligands : structures and magnetic properties“, *CrystEngComm* **2018**, *20*, 818–828.

B. Weber, E. Kaps, K. Dankhoff: „Synthesis of a New Schiff Base-like Trinucleating Ligand and its Copper, Vanadyl, and Iron Complexes : Influence of the Bridging Ligand on the Magnetic Properties”, *Z. Anorg. Allg. Chem.* **2017**, *643*, 1593–1599.

K. Dankhoff, C. Lochenie, F. Puchtler, B. Weber: „Solvent Influence on the Magnetic Properties of Iron(II) Spin-Crossover Coordination Compounds with 4,4'-Dipyridylethyne as Linker“, *Eur. J. Inorg. Chem.* **2016**, 2136–2143.

S. Schlamp, K. Dankhoff, B. Weber: „Amphiphilic iron(II) complexes with short alkyl chains : crystal packing and spin transition properties“, *New J. Chem.* **2014**, *38*, 1965–1972.

12.(Eidesstattliche) Versicherungen und Erklärungen

(§ 9 Satz 2 Nr. 3 PromO BayNAT)

Hiermit versichere ich eidesstattlich, dass ich die Arbeit selbstständig verfasst und keine anderen als die von mir angegebenen Quellen und Hilfsmittel benutzt habe (vgl. Art. 64 Abs. 1 Satz 6 BayHSchG).

(§ 9 Satz 2 Nr. 3 PromO BayNAT)

Hiermit erkläre ich, dass ich die Dissertation nicht bereits zur Erlangung eines akademischen Grades eingereicht habe und dass ich nicht bereits diese oder eine gleichartige Doktorprüfung endgültig nicht bestanden habe.

(§ 9 Satz 2 Nr. 4 PromO BayNAT)

Hiermit erkläre ich, dass ich Hilfe von gewerblichen Promotionsberatern bzw. -vermittlern oder ähnlichen Dienstleistern weder bisher in Anspruch genommen habe noch künftig in Anspruch nehmen werde.

(§ 9 Satz 2 Nr. 7 PromO BayNAT)

Hiermit erkläre ich mein Einverständnis, dass die elektronische Fassung meiner Dissertation unter Wahrung meiner Urheberrechte und des Datenschutzes einer gesonderten Überprüfung unterzogen werden kann.

(§ 9 Satz 2 Nr. 8 PromO BayNAT)

Hiermit erkläre ich mein Einverständnis, dass bei Verdacht wissenschaftlichen Fehlverhaltens Ermittlungen durch universitätsinterne Organe der wissenschaftlichen Selbstkontrolle stattfinden können.

…….

Ort, Datum, Unterschrift